

Copyright
by
Georgios Zalachoris
2014

The Dissertation Committee for Georgios Zalachoris certifies that this is the approved version of the following dissertation:

Evaluation of One-Dimensional Site Response Methodologies using Borehole Arrays

Committee:

Ellen M. Rathje, Supervisor

Kenneth H. Stokoe II

Robert B. Gilbert

John L. Tassoulas

Stephen P. Grand

Brady R. Cox

**Evaluation of One-Dimensional Site Response Methodologies using
Borehole Arrays**

by

Georgios Zalachoris, Dipl.; M.S.E.

Dissertation

Presented to the Faculty of the Graduate School of

The University of Texas at Austin

in Partial Fulfillment

of the Requirements

for the Degree of

Doctor of Philosophy

The University of Texas at Austin

May 2014

Dedication

To my wonderful parents,

Maria and Vasilis

for the opportunities they gave me to explore boundaries
without losing my point of reference

Στην Λένγκω λοιπόν

Acknowledgements

Concentrating a 6-year graduate school experience in an “acknowledgement” page is by definition an impossible task, something that often leads to formalities I would like to avoid. Being no exception to the norm of graduate studies in UT, I was blessed to be surrounded by numerous professors, colleagues and friends who served as an inspirational source of support in all levels; academic, moral or personal. Nonetheless, if I had to personify my life in UT for the past 4 years, Professor Ellen M. Rathje would stand out. With her professionalism and energetic involvement, she generously guided me to my academic adulthood. Now that our unavoidably hierarchical relationship is over, I will be honored if she could offer me her friendship as well.

Evaluation of One-Dimensional Site Response Methodologies using Borehole Arrays

Georgios Zalachoris, Ph.D.

The University of Texas at Austin, 2014

Supervisor: Ellen M. Rathje

Numerical modeling techniques commonly used to compute the response of soil and rock media under earthquake shaking are evaluated by analyzing the observations provided by instrumented borehole arrays. The NIED Kik-Net database in Japan is selected as the main source of borehole array data for this study. The stiffness of the site and the availability of high intensity motions are the primary factors considered towards the selection of appropriate Kik-Net borehole arrays for investigation. Overall, 13 instrumented vertical arrays are investigated using over 750 recorded ground motions characterized by low (less than $0.05 g$) to high (greater than $0.3 g$) recorded peak ground accelerations at the downhole sensor. Based on data from the selected borehole arrays, site response predictions using 1-D linear elastic (LE) analysis, equivalent linear (EQL) analysis, equivalent linear analysis with frequency-dependent soil properties (EQL-FD), and fully nonlinear analysis (NL) are compared with the borehole observations.

Initially, the low intensity motions are used to evaluate common assumptions regarding 1-D site response analysis. First, we identify the borehole wavefield best simulating the actual boundary condition at depth by comparing the theoretical

linear-elastic (LE) and observed responses. Then, we identify the best-fit small-strain damping profiles that can incorporate the additional in-situ attenuation mechanisms. Finally, we assess the validity of the one-dimensional modeling assumption. Our analyses indicate that the appropriate boundary condition for analysis of a borehole array depends on the depth of the borehole sensor and that, for most of the considered vertical arrays, the one-dimensional assumption reasonably simulates the actual wave propagation pattern.

In the second part of this study, we evaluate the accuracy of the EQL, EQL-FD and NL site response methods by quantifying the misfit (i.e., residual) between the simulations and observations at different levels of shaking. The evaluation of the performance of the theoretical models is made both on a site-by-site basis and in an aggregated manner. Thereafter, the variability in the predicted response from the three site response methods is assessed. Comparisons with the observed responses indicate that the misfit of simulations can be significant at short periods and large strains. Moreover, all models seem to be characterized by the same level of variability irrespectively of the level of shaking.

Finally, several procedures that can be used to improve the accuracy of the one-dimensional EQL, EQL-FD and NL site response analyses, are investigated. First, an attempt to take into account the shear strength of the soil materials at large shear strains is made. Additionally, several modifications to the EQL-FD approach are proposed. The proposed modifications are evaluated against recordings from the borehole arrays. Our analyses indicate that the accuracy of the theoretical models can be, partly, increased by incorporating the proposed modifications.

Table of Contents

Acknowledgements	v
Abstract	vi
List of Tables	xii
List of Figures	xv
Chapter 1 Introduction	1
1.1. Problem Significance	1
1.2. Research Objectives.....	2
1.3. Organization of Dissertation	3
Chapter 2 One-Dimensional Site Response Methodologies	5
2.1. Introduction	5
2.2. Equivalent-Linear Site Response Method	7
2.3. Fully Nonlinear Site Response Method	21
2.4. Summary	27
Chapter 3 Validation Studies of One-Dimensional Site Response Methods	29
3.1. Introduction	29
3.2. Studies Comparing Equivalent-Linear and Nonlinear Analyses	29
3.2.1. Silva <i>et al.</i> , 2000.....	30
3.2.2. Park <i>et al.</i> , 2004.....	31
3.2.3. Stewart <i>et al.</i> , 2008	34
3.2.4. Kwak <i>et al.</i> , 2008.....	35
3.2.5. Kottke, 2010	36
3.3. Studies using Borehole Arrays.....	37
3.3.1. Borja <i>et al.</i> , 2000	37
3.3.2. Lee <i>et al.</i> , 2006.....	38
3.3.3. Stewart <i>et al.</i> , 2008	40

3.3.4. Kottke, 2010	42
3.3.5. Kaklamanos <i>et al.</i> , 2013	42
3.4. Summary of Observations	44
3.5. Summary	46
Chapter 4 Borehole Strong-Motion Arrays	47
4.1. Introduction	47
4.2. Available Geotechnical Borehole Arrays	47
4.3. Site and Ground-Motion Selection	48
4.4. Material Property Characterization of the Selected Sites	59
4.5. Signal Processing of Recorded Motions	68
4.6. Summary	70
Chapter 5 Assessment of Common Assumptions of One-Dimensional Site Response Analysis	72
5.1. Introduction	72
5.2. Uncertainty in the Borehole Wavefield	73
5.2.1. Previous Studies on the Identification of Borehole Wavefields	73
5.2.2. Linear-Elastic Transfer Functions.....	79
5.2.3. Selection of Appropriate Wavefield	84
5.3. Uncertainty in the Small-Strain Damping	89
5.3.1. Selection of Best-Fit Small-Strain Damping Profiles.....	92
5.3.2. Best-Fit Amplification Factors.....	95
5.4. Uncertainty in the One-Dimensional Assumption	99
5.5. Summary	112
Chapter 6 Assessment of Performance of of One-Dimensional Site Response Methodologies	114
6.1. Introduction	114
6.2. General Framework - Example of Site Response Validation.....	115
6.3. Results from Analyses on a Site-by-Site Basis.....	126
6.4. Aggregated Results.....	137

6.4.1. Strain and Period Dependence of Residuals	138
6.4.2. Effect of T_{site}	147
6.4.3. Comparison of Results with Kaklamanos <i>et al.</i> (2013).....	151
6.5. Summary	153
Chapter 7 Variability Evaluation.....	155
7.1. Introduction	155
7.2. Identification of Sources of Variability	155
7.3. Quantification of Site Response Variability	159
7.4. Effect of T_{site} and T_m	170
7.4.1. Effect of T_{site}	170
7.4.2. Effect of T_m	172
7.5. Comparison of Variability Estimates with Previous Studies	178
7.6. Summary	181
Chapter 8 Improvement of Performance of the One-Dimensional Site Response Methodologies.....	183
8.1. Introduction	183
8.2. Strength Correction at Large Strains.....	184
8.2.1. Example Application of Shear Strength Correction Procedure	189
8.2.2. Overall Results.....	196
8.3. Proposed Modifications to EQL-FD Algorithm.....	207
8.3.1. Performing EQL-FD Computations After EQL Iterations ..	208
8.3.2. Utilization of Complete Shear-Strain Spectrum.....	211
8.4. Discussion of Results	226
8.5. Summary	234
Chapter 9 Summary and Conclusions.....	236
9.1. Summary and Conclusions	236
9.2. Recommendations for Future Work.....	239

Appendix	242
A.1. Boring Logs for the Selected Kik-Net Vertical Arrays	242
A.2. Strong Ground Motions Utilized	253
A.3. Supplementary Documentation.....	263
A.4. Strength Corrected Soil Layers at Each Site.....	266
Bibliography	275
Vita	286

List of Tables

Table 2.1: Computer codes for equivalent-linear site response analysis	21
Table 2.2: Common nonlinear soil models.....	24
Table 2.3: Computer codes for 1-D nonlinear site response analysis	26
Table 3.1: Comparative studies of one-dimensional site response methods..	30
Table 3.2: Verification studies of site response methodologies against recordings.....	37
Table 4.1: Categorization of geotechnical strong-motion arrays in the U.S.A.(information from Steidl, 2006)	49
Table 4.2: Borehole array databases	50
Table 4.3: Site locations, surface altitude, approximate valley length and width for the selected sites from Kik_net database.....	55
Table 4.4: Site characteristics and downhole sensor depth for the selected borehole arrays.....	56
Table 4.5: Number of recordings per PGA_{base} range.....	57
Table 4.6: Darendeli (2001) parameters for the La Cienega array (after Kottke, 2010)	64
Table 4.7: Locations of ground water table (GWT)	66
Table 4.8: Shear modulus reduction and damping ratio curves for the Lotung array (EPRI, 1993).....	68
Table 5.1: Grouping of arrays based on site characteristics and appropriate wavefield boundary condition.....	85

Table 5.2: Tabulated factors applied on D_{min} for the best-fit damping profile for each array	94
Table 5.3: Frequency range, <i>median</i> σ_{ln} and correlation coefficient, r , for each array.....	107
Table 6.1: Number of motions per PGA_{base} range for all vertical arrays	116
Table 6.2: Defined γ_{max} ranges and associated number of motions for all site response methods	139
Table 6.3: Percentage contribution of each individual array to the overall <i>mean</i> residual depicted in <i>FIGURE 6.14</i>	145
Table 6.4: Site periods (T_{site}) and corresponding ranges in T/T_{site} for all vertical arrays - $T_{min} = 0.05$ s and $T_{max} = 2.0$ s	148
Table 7.1: Number of input motions per borehole array and γ_{max} range	160
Table 8.1: Maximum shear strains (γ_{max}) in %, computed before and after the strength correction for all site response models, and for a input motion recorded on 06/14/2008, 08:43 at IWTH26 array	194
Table 8.2: Information regarding the four single-events recorded at IBRH13 vertical array used for the exemplified evaluation of the proposed modification to the EQL-FD approach	215
Table A.1: Utilized strong motion records at each vertical array.....	253
Table A.2: Percentage contribution of each array to the overall residual depicted in <i>FIGURE 6.16</i> - <u>EQL method</u>	263
Table A.3: Percentage contribution of each array to the overall residual depicted in <i>FIGURE 6.16</i> - <u>EQL-FD method</u>	264

Table A.4: Percentage contribution of each array to the overall residual depicted in <i>FIGURE 6.16</i> – <u>NL method</u>	265
---	-----

List of Figures

Figure 2.1: Schematic representation of the considered one-dimensional site response methodologies	7
Figure 2.2: Hysteresis loop of soil under cyclic loading and the corresponding equivalent damping (D). ΔE is the dissipated energy during one cycle of loading and E is the maximum strain energy	9
Figure 2.3: Typical shape of modulus reduction (G/G_{max}) and damping (D) curves	9
Figure 2.4: Example of equivalent-linear computations for a single layer: (a) input motion time history, (b) Fourier Amplitude Spectrum of the input motion, (c) transfer function, (d) computed Fourier Amplitude of the output motion, and (e) output motion time history	11
Figure 2.5: Nomenclature of layered medium in equivalent-linear formulation	12
Figure 2.6: Schematic illustration of iterative procedure implemented in “traditional” equivalent-linear (EQL) algorithm	13
Figure 2.7: Small strain and large strain hysteresis loops for soils under cyclic loading (after Yoshida et al., 2002).....	14
Figure 2.8: Strain Fourier spectra from various earthquakes. (a) Yoshida et al., 2002; (b) Assimaki and Kausel, 2002; (c) Kwak et al., 2008	16
Figure 2.9: Smoothing of strain Fourier spectra used in EQL-FD algorithms (from Kwak <i>et al.</i> , 2008).....	18
Figure 2.10: Mapping of soil properties in the frequency domain.....	20

Figure 2.11: Typical calculation steps on hysteretic behavior implemented in nonlinear site response models (after Stewart <i>et al.</i> , 2008).....	23
Figure 2.12: Curve fitting of MRDF and MRD models to target, empirical curves	25
Figure 3.1: Amplification factors predicted by equivalent-linear and nonlinear models, for NEHRP category C (from Silva <i>et al.</i> , 2000)	32
Figure 3.2: Amplification factors predicted by equivalent-linear and nonlinear models, for NEHRP category E (from Silva <i>et al.</i> , 2000)	33
Figure 3.3: Comparison of surface response spectra: (a) $PGA = 0.1 g$, and (b) $PGA = 0.65 g$ (from Park <i>et al.</i> , 2004)	34
Figure 3.4: Comparison of surface acceleration response spectra produced by different models (from Kwak <i>et al.</i> (2008)	36
Figure 3.5: Acceleration response spectra at 5% damping: Lotung LSST12 case study (Borja <i>et al.</i> , 1999)	38
Figure 3.6: Bias in the response as obtained by Lee <i>et al.</i> (2006). Positive bias corresponds to underprediction; negative to overprediction.....	39
Figure 3.7: Acceleration response spectra for data and simulation results compared through prediction residuals: (a) La Cienega, (b) KGWH02, and (c) Lotung. Positive residual corresponds to underprediction; negative to overprediction (from Stewart <i>et al.</i> , 2008)	41
Figure 3.8: Prediction residuals for different site response methodologies. Positive residual shows underprediction; negative residual corresponds to overprediction (from Kottke, 2010)	43

Figure 3.9: Illustration of the period dependence of the accuracy of LE and EQL analysis with respect to the maximum calculated shear strain, γ_{max} (from Kaklamanos <i>et al.</i> , 2013)	44
Figure 4.1: Distribution of (a) maximum PGA_{base} , (b) number of records, and (c) depth to downhole sensor with respect to V_{s30} , for the Kik-Net vertical arrays	52
Figure 4.2: (a) Number of sites per NEHRP site classification, and (b) number of records per PGA_{base} range.....	53
Figure 4.3: Shear wave (V_s) profiles of the considered borehole arrays	58
Figure 4.4: Unit Weight (γ_t) profiles of the considered borehole arrays	60
Figure 4.5: Comparison between the selected Darendeli (2001) shear-modulus reduction curves with data from laboratory testing (from Kottke, 2010)	62
Figure 4.6: Comparison between the selected Darendeli (2001) damping curves with data from laboratory testing (from Kottke, 2010)	63
Figure 4.7: Shear (V_s) and Compression (V_p) wave velocity profiles.....	65
Figure 4.8: Mean confining pressure (σ'_m) variation with depth	67
Figure 4.9: Nonlinear soil properties at Lotung site established through laboratory testing (from EPRI, 1993)	69
Figure 4.10: Transfer function of 5 th order Butterworth filter applied to all recorded time histories	70
Figure 5.1: Common assumptions regarding wavefield pattern throughout a 1-D layered system (after Kottke, 2010).....	74

Figure 5.2: Comparison of empirical (shaded area) and theoretical transfer functions evaluated at different depths of Garber Valley borehole array (CA). “Outcrop Response” refers to the “incoming only” wavefield and “Borehole Response” corresponds to a “within” wavefield assumption. (from Bonilla <i>et al.</i> , 2002)	75
Figure 5.3: Observed and computed transfer functions assuming a “within” wavefield (from Thompson et al., 2009)	77
Figure 5.4: Observed and computed transfer functions assuming an “incoming only” wavefield (from Thompson et al., 2009).....	78
Figure 5.5: Minimum damping (D_{min}) profiles considered	81
Figure 5.6: Comparison of theoretical linear-elastic transfer functions and observed transfer functions for low intensity motions ($PGA_{base} < 0.05 g$).....	83
Figure 5.7: Comparison of <i>median</i> linear-elastic amplification factors and observed amplification factors for low intensity motions ($PGA_{base} < 0.05 g$).....	88
Figure 5.8: Damping structures of 5 KiK-Net arrays obtained from empirical correlations (dashed lines), and from the Assimaki and Steidl (2007) inversion technique (solid line) (<u>Note:</u> $\xi = D_{min}$) (from Assimaki and Steidl, 2007).....	92
Figure 5.9: Factor applied on D_{min} for the best-fit damping profile vs base sensor depth of each array.....	94
Figure 5.10: Damping profiles based on D_{min} and on the best-fit damping profile.....	96

Figure 5.11: Amplification Factors based on D_{min} and on the best-fit damping profile.....	97
Figure 5.12: Calculated <i>mean</i> residuals for all sites based on the best-fit damping profile.....	100
Figure 5.13: Variability associated with the residual in the predictions based on the best-fit damping profile.....	101
Figure 5.14: Illustration of: (a) a <u>high</u> σ_{ln} array, (b) a <u>low</u> σ_{ln} array, (c) an array with a <u>good</u> fit between the theoretical and the observed transfer functions, and (d) an array with a <u>poor</u> fit between the theoretical and the empirical transfer functions (from Thompson <i>et al.</i> , 2012)..	104
Figure 5.15: Inter-event variability (σ_{ln}) and comparison between the observed and computed amplification factor, for <i>Group 1</i> sites.....	108
Figure 5.16: Inter-event variability (σ_{ln}) and comparison between the observed and computed amplification factor, for <i>Group 2</i> sites.....	109
Figure 5.17: Inter-event variability (σ_{ln}) and comparison between the observed and computed amplification factor, for <i>Group 3</i> sites.....	110
Figure 6.1: Observed and computed Amplification Factors, for the IBRH13 borehole array.....	118
Figure 6.2: Calculated Residuals for all site response methods, for IBRH13 borehole array.....	119
Figure 6.3: Observed and compute acceleration time series at the surface of the IBRG13 site using an input motion recorded on 08/04/03, 20: 57....	120

Figure 6.4: Observed and compute acceleration time series at the surface of the IBRG13 site using an input motion recorded on 03/11/11, 14: 54...	121
Figure 6.5: Calculated maximum shear strain (γ_{max}) for all sites and input intensities.....	122
Figure 6.6: Relationship between the calculated maximum shear strains (γ_{max}) and the peak shear strain estimates ($PGV_{surf}/V_{s,min}$) for all sites, input motions and site response models.....	124
Figure 6.7: Amplification residuals ($y = \ln(AF^{obs}/AF^{calc})$) computed at 6 distinct spectral periods versus calculated maximum shear strain, for IBRH13 site.....	125
Figure 6.8: Residuals vs maximum calculated shear strains (γ_{max}) for all sites and site response methods - $T = 0.05 s$	127
Figure 6.9: Residuals vs maximum calculated shear strains (γ_{max}) for all sites and site response methods - $T = 0.1 s$	129
Figure 6.10: Residuals vs maximum calculated shear strains (γ_{max}) for all sites and site response methods - $T = 0.3 s$	130
Figure 6.11: Residuals vs maximum calculated shear strains (γ_{max}) for all sites and site response methods - $T = 0.5 s$	133
Figure 6.12: Residuals vs maximum calculated shear strains (γ_{max}) for all sites and site response methods - $T = 1.0 s$	134
Figure 6.13: Residuals vs maximum calculated shear strains (γ_{max}) for all sites and site response methods - $T = 2.0 s$	135

Figure 6.14: Combined *average* prediction residuals vs maximum calculated shear strains (γ_{max}) for all sites and site response methods, within 5 different spectral period bins - $0.05\text{ s} < T < 0.32\text{ s}$ - *grey* dots represent the average residual from 27 spectral periods included within each of the 5 spectral period bins depicted, *black dot/line* represents the *mean* residual within a narrow γ_{max} range, *black dotted line* represents the corresponding 90 % confidence intervals..... 140

Figure 6.15: Combined *average* prediction residuals vs maximum calculated shear strains (γ_{max}) for all sites and site response methods, within 5 different spectral period bins - $0.32\text{ s} < T < 2.0\text{ s}$ - *grey* dots represent the average residual from 27 spectral periods included within each of the 5 spectral period bins depicted, *black dot/line* represents the *mean* residual within a narrow γ_{max} range, *black dotted line* represents the corresponding 90 % confidence intervals..... 141

Figure 6.16: Contour plots of *mean* prediction residuals vs maximum calculated shear strains (γ_{max}) vs spectral period (T) for all site response methods..... 143

Figure 6.17: Selection of appropriate range of T/T_{site} for the computation of the mean prediction residuals across all sites.... 148

Figure 6.18: Contour plots of *mean* prediction residuals vs maximum calculated shear strains (γ_{max}) vs normalized period (T/T_{site}) for all site response methods..... 150

Figure 6.19: Comparison of <i>mean</i> prediction residuals vs γ_{max} vs T , for the EQL and NL site response methods, with recommendations from Kaklamanos <i>et al.</i> (2013) (black lines).....	152
Figure 7.1: Schematic definition of inter and intra-site residuals (reproduced based on Figure 1 in Al Atik <i>et al.</i> (2011))....	157
Figure 7.2: Results from Kaklamanos <i>et al.</i> (2013) in terms of : (a) fixed effect, α , (b) total standard deviation, σ_y , (c) intra-site standard deviation, σ , and (d) inter-site standard deviation, τ_s . (from Kaklamanos <i>et al.</i> , 2012).....	158
Figure 7.3: (a) Mean residuals, and (b) standard deviations for amplification factors computed by the <u>EQL approach</u>	160
Figure 7.4: (a) Mean residuals, and (b) standard deviations for amplification factors computed by the <u>EQL-FD approach</u>	162
Figure 7.5: (a) Mean residuals, and (b) standard deviations for amplification factors computed by the <u>NL approach</u>	163
Figure 7.6: (a) Mean residuals, μ_y , and (b) total standard deviations, σ_y , across different induced shear strain levels, for all site response models... ..	167
Figure 7.7: (a) Mean residuals, μ_y , and (b) total standard deviations, σ_y , versus normalized period (T/T_{site}) across different induced shear strain levels....	171
Figure 7.8: Mean period (T_m) of the input motions versus their respective PGA_{base}	173

Figure 7.9: Mean intra-site residuals, $\varepsilon_{i,j}$, for all site response models computed using motions with $T_m < 0.33$ s (solid line) and motions with $T_m > 0.33$ s (dashed line), for: (a) $\gamma_{max} < 0.01$ %, (b) 0.1 % $< \gamma_{max} < 0.01$ %t, and (c) $\gamma_{max} > 0.1$ %..... 175

Figure 7.10: Amplification residuals for all site response models computed using two single events recorded at IWTH26 site.... 177

Figure 7.11: Schematic explanation of the dependence of the amplification residuals on the frequency content of the input motion, for EQL method..... 177

Figure 7.12: Comparison of across-site uncertainty estimated for EQL approach with Kaklamanos *et al.* (2013), in terms of : (a) fixed effect, α , (b) total standard deviation, σ_y , (c) intra-site standard deviation, σ , and (d) inter-site standard deviation, τ_s 179

Figure 8.1: Example application of the Hashash *et al.* (2010) procedure for the modification of the G/G_{max} curve to account for the shear strength at large strains..... 187

Figure 8.2: Original and modified modulus reduction and damping curves as well as the derived stress strain relationships for the strength corrected layer at IWTH26 array..... 190

Figure 8.3: Relationship between the computed maximum shear strain (γ_{max}) before and after the strength correction, for all site response models – IWTH26 array..... 192

Figure 8.4: (a) Surface response spectra, and (b) amplification factor residuals before and after the strength correction for all site response models, at IWTH26 array..... 193

Figure 8.5: Frequency-dependence of: (a) modulus reduction, and (b) damping for EQL and EQL-FD, for an input motion recorded on 06/14/08, 08: 43 with $PGA_{base} = 0.21 g$ 195

Figure 8.6: Relationship between the computed maximum shear strain (γ_{max}) before and after the strength correction, for all site response models..... 197

Figure 8.7: Contour plots of *mean* prediction residuals vs maximum calculated shear strains (γ_{max}) vs spectral period (T) obtained before and after the strength correction procedure – EQL method..... 199

Figure 8.8: Contour plots of *mean* prediction residuals vs maximum calculated shear strains (γ_{max}) vs spectral period (T) obtained before and after the strength correction procedure – EQL-FD method..... 200

Figure 8.9: Contour plots of *mean* prediction residuals vs maximum calculated shear strains (γ_{max}) vs spectral period (T) obtained before and after the strength correction procedure – NL method..... 201

Figure 8.10:Contour plots of *mean* prediction residuals vs maximum calculated shear strains (γ_{max}) vs T/T_{site} obtained before and after the strength correction procedure – EQL method..... 203

Figure 8.11: Contour plots of *mean* prediction residuals vs maximum calculated shear strains (γ_{max}) vs T/T_{site} obtained before and after the strength correction procedure – EQL-FD method..... 205

Figure 8.12:Contour plots of *mean* prediction residuals vs maximum calculated shear strains (γ_{max}) vs T/T_{site} obtained before and after the strength correction procedure – NL method..... 206

Figure 8.13: Comparison of maximum shear strains (γ_{max}) computed using the original and the modified EQL-FD algorithm, for IBRH13 borehole array..... 210

Figure 8.14: Mean prediction residuals for the original and for the modified EQL-FD models, for IBRH13 borehole array..... 211

Figure 8.15: Example illustration of the two approaches to scaling the complete shear strain spectrum..... 213

Figure 8.16: Evaluation of the performance of the site response models at IBRH13 site using Motion 1 (see *TABLE 8.2*); (a) computed and observed spectral accelerations, (b) incorporated shear strain spectra ($\gamma(f)$), and (c) corresponding frequency dependence of the damping..... 215

Figure 8.17: Evaluation of the performance of the site response models at IBRH13 site using Motion 2 (see *TABLE 8.2*); (a) computed and observed spectral accelerations, (b) incorporated shear strain spectra ($\gamma(f)$), and (c) corresponding frequency dependence of the damping..... 217

Figure 8.18: Evaluation of the performance of the site response models at IBRH13 site using Motion 3 (see *TABLE 8.2*); (a) computed and observed spectral accelerations, (b) incorporated shear strain spectra ($\gamma(f)$), and (c) corresponding frequency dependence of the damping..... 218

Figure 8.19:Evaluation of the performance of the site response models at IBRH13 site using Motion 4 (see *TABLE 8.2*); (a) computed and observed spectral accelerations, (b) incorporated shear strain spectra ($\gamma(f)$), and (c) corresponding frequency dependence of the damping..... 219

Figure 8.20:Contour plots of *mean* prediction residuals vs maximum calculated shear strains (γ_{max}) vs spectral period (T) obtained using the original and the modified EQL-FD approaches..... 222

Figure 8.21:Comparison of computed maximum shear strains (γ_{max}) between: (a) the original (Assimaki and Kausel, 2002) and the modified EQL-FD approaches, and (b) the EQL and the modified EQL-FD approaches 224

Figure 8.22:*Mean* residuals vs T vs γ_{max} contour plots obtained using the EQL, the original EQL-FD (Assimaki and Kausel, 2002) and the modified EQL-FD models 225

Figure 8.23:*Mean* residuals vs T/T_{site} vs γ_{max} contour plots obtained using the EQL, the EQL-FD (Assimaki and Kausel, 2002) and the modified EQL-FD models 227

Figure 8.24:Earthquake record used for the evaluation of the 1-D modeling approach..... 229

Figure 8.25:Schematic illustration of the determination of the maximum shear stress (τ_{max}) at depth of a one-dimensional soil column 230

Figure 8.26:(a) Computed and predicted $PGA_{surface}$ versus PGA_{base} , and (b) surface spectral accelerations, for the EQL and NL site response methods 231

Figure 8.27: Surface spectral accelerations for the EQL-FD method	233
Figure 8.28: Effect of the different minimum damping (D_{min}) definitions on the computed response by the modified EQL-FD method at the IBRH13 site and for an input motion recorded on 3/19/2011, 18: 56 (motion 4 in <i>TABLE 8.2</i>)	234
Figure A.1: Boring log reported by NIED Kik-Net database, for the FKSH19 array (<u>translated</u> from the original Japanese version).....	242
Figure A.2: Boring log reported by NIED Kik-Net database, for the FKSH20 array (<u>translated</u> from the original Japanese version).....	243
Figure A.3: Boring log reported by NIED Kik-Net database, for the IBRH11 array (<u>translated</u> from the original Japanese version).....	244
Figure A.4: Boring log reported by NIED Kik-Net database, for the IBRH13 array (<u>translated</u> from the original Japanese version).....	245
Figure A.5: Boring log reported by NIED Kik-Net database, for the IWTH26 array (<u>translated</u> from the original Japanese version).....	246
Figure A.6: Boring log reported by NIED Kik-Net database, for the KSRH06 array (<u>translated</u> from the original Japanese version).....	247
Figure A.7: Boring log reported by NIED Kik-Net database, for the KSRH07 array (<u>translated</u> from the original Japanese version).....	248
Figure A.8: Boring log reported by NIED Kik-Net database, for the KSRH10 array (<u>translated</u> from the original Japanese version).....	249
Figure A.9: Boring log reported by NIED Kik-Net database, for the MYGH05 array (<u>translated</u> from the original Japanese version).....	250

Figure A.10:Boring log reported by NIED Kik-Net database, for the MYGH10 array (translated from the original Japanese version)..... 251

Figure A.11:Boring log reported by NIED Kik-Net database, for the TTRH02 array..... 252

Figure A.12:Original and modified modulus reduction and damping curves and the associated stress strain relationships for the strength corrected layers: (a) $V_S = 170\text{ m/s}$ and $\sigma'_v = 17\text{ kPa}$, and (b) $V_S = 270\text{ m/s}$ and $\sigma'_v = 175\text{ kPa}$ - FKSH19 array..... 266

Figure A.13:Original and modified modulus reduction and damping curves and the associated stress strain relationships for the strength corrected layers: (a) $V_S = 350\text{ m/s}$ and $\sigma'_v = 55.5\text{ kPa}$, (b) $V_S = 350\text{ m/s}$ and $\sigma'_v = 200\text{ kPa}$, and (c) $V_S = 500\text{ m/s}$ and $\sigma'_v = 432\text{ kPa}$ - FKSH20 array..... 267

Figure A.14: Original and modified modulus reduction and damping curves and the associated stress strain relationships for the strength corrected layers: (a) $V_S = 130\text{ m/s}$ and $\sigma'_v = 25\text{ kPa}$, (b) $V_S = 180\text{ m/s}$ and $\sigma'_v = 158\text{ kPa}$, and (c) $V_S = 240\text{ m/s}$ and $\sigma'_v = 238\text{ kPa}$ - IBRH11 array..... 268

Figure A.15: Original and modified modulus reduction and damping curves and the associated stress strain relationships for the strength corrected layers: (a) $V_S = 170\text{ m/s}$ and $\sigma'_v = 25.5\text{ kPa}$, (b) $V_S = 280\text{ m/s}$ and $\sigma'_v = 89.8\text{ kPa}$, (c) $V_S = 280\text{ m/s}$ and $\sigma'_v = 153.4\text{ kPa}$, and (d) $V_S = 400\text{ m/s}$ and $\sigma'_v = 292\text{ kPa}$ - IBRH13 array.... 269

Figure A.16: Original and modified modulus reduction and damping curves and the associated stress strain relationships for the strength corrected layer with $V_S = 130 \text{ m/s}$ and $\sigma'_v = 59.5 \text{ kPa}$ - IWTH26 array....270

Figure A.17: Original and modified modulus reduction and damping curves and the associated stress strain relationships for the strength corrected layers: (a) $V_S = 90 \text{ m/s}$ and $\sigma'_v = 16.5 \text{ kPa}$, (b) $V_S = 340 \text{ m/s}$ and $\sigma'_v = 155.5.8 \text{ kPa}$, (c) $V_S = 490 \text{ m/s}$ and $\sigma'_v = 345.4 \text{ kPa}$, and (d) $V_S = 370 \text{ m/s}$ and $\sigma'_v = 549.8 \text{ kPa}$ - KSRH06 array..... 271

Figure A.18: Original and modified modulus reduction and damping curves and the associated stress strain relationships for the strength corrected layers: (a) $V_S = 100 \text{ m/s}$ and $\sigma'_v = 33 \text{ kPa}$, (b) $V_S = 140 \text{ m/s}$ and $\sigma'_v = 90.7 \text{ kPa}$, and (c) $V_S = 140 \text{ m/s}$ and $\sigma'_v = 127.8 \text{ kPa}$ - KSRH07 array..... 272

Figure A.19: Original and modified modulus reduction and damping curves and the associated stress strain relationships for the strength corrected layers: (a) $V_S = 190 \text{ m/s}$ and $\sigma'_v = 43.8 \text{ kPa}$, (b) $V_S = 210 \text{ m/s}$ and $\sigma'_v = 167.7 \text{ kPa}$, and (c) $V_S = 300 \text{ m/s}$ and $\sigma'_v = 362 \text{ kPa}$ - KSRH10 array.... 273

Figure A.20: Original and modified modulus reduction and damping curves and the associated stress strain relationships for the strength corrected layers: (a) $V_S = 120 \text{ m/s}$ and $\sigma'_v = 24.75 \text{ kPa}$, (b) $V_S = 560 \text{ m/s}$ and $\sigma'_v = 68.8 \text{ kPa}$, (c) $V_S = 300 \text{ m/s}$ and $\sigma'_v = 144.9 \text{ kPa}$, and (d) $V_S = 360 \text{ m/s}$ and $\sigma'_v = 271 \text{ kPa}$ - MYGH05 array.... 274

Chapter 1

Introduction

1.1. Problem Significance

One of the most important and most commonly encountered problems in geotechnical earthquake engineering is the evaluation of ground response under earthquake shaking. Local soil conditions play a significant role in the nature and characteristics of ground motions at the surface of a site. The influence of local soil conditions on ground shaking is typically evaluated using numerical modeling techniques. These techniques are used to predict ground surface time histories for the development of design response spectra, to evaluate dynamic stresses and strains for the purposes of liquefaction assessment and to determine earthquake induced forces that can lead to instability of earth slopes and earth-retaining structures. The existing site response approaches differ predominantly from each other based on the way they address: 1) the complexity of the seismic wave propagation pattern, and 2) the nonlinearity of the soil response. Thus, 1-D, 2-D and 3-D models have been developed to simulate the directional effects of the passing seismic waves on the soil response, while equivalent-linear (EQL) and fully nonlinear (NL) models provide the numerical approaches by which the nonlinear soil behavior may be approximated.

In cases where major topographic and basin effects are minimal, one-dimensional ground response analysis has been considered adequate to represent the actual wave propagation conditions. However, limited data have been available

to fully evaluate the one-dimensional approximation. Most commonly, the nonlinear and inelastic soil behavior is modeled either by an equivalent-linear (EQL) or by a fully nonlinear (NL) approach. More recently, a new formulation, namely an equivalent-linear analysis with frequency dependent soil properties (EQL-FD) (e.g. Assimaki and Kausel, 2002; Yoshida *et al.*, 2001) has been proposed. This approach attempts to remedy one of the shortcomings of EQL analysis, the overdamping of high frequencies at large strains. Nevertheless, the dynamic responses computed via these models may differ substantially, and therefore their ability to accurately predict the ground response strongly depends on the characteristics of each theoretical model.

1.2. Research Objectives

The main objective of the present study is to compare and evaluate the 1-D equivalent-linear (EQL), equivalent-linear with frequency dependent soil properties (EQL-FD), and nonlinear (NL) time series site response methodologies. To investigate the accuracy of the modeling techniques with respect to recorded ground motions during earthquake shaking, recordings from borehole arrays are utilized.

The dissertation is divided in three main sections. First, one-dimensional linear-elastic (LE) analyses are performed to evaluate key assumptions typically associated with one-dimensional site response. The evaluation is achieved by comparing theoretically computed responses with observations obtained from vertical strong motion borehole arrays. Second, we investigate the ability of 1-D equivalent-linear (EQL and EQL-FD) and nonlinear (NL) formulations to accurately predict the ground response under moderate to strong shaking. Again, this

evaluation is achieved by comparing theoretically computed responses with observations obtained from vertical strong motion borehole arrays. Our ultimate goal is to: 1) evaluate the performance of the numerical algorithms at different levels of earthquake shaking, and 2) quantify the variability associated with the theoretical models. Finally, an attempt is made to provide recommendations for the optimization of the performance of EQL and NL site response analyses, and to identify improvements to the EQL-FD approach, based on the comparisons with the recorded data.

1.3. Organization of Dissertation

This dissertation consists of nine chapters. After this introductory chapter, *Chapter 2* introduces the theoretical aspects of the most commonly utilized one-dimensional site response methodologies and discusses their perceived advantages and disadvantages.

In *Chapter 3*, previous studies that deal with the evaluation of various one-dimensional site response models both relative to each other as well as relative to existing recordings from instrumented vertical arrays are presented. The observations from these research efforts are categorized and documented.

In *Chapter 4*, available data from borehole strong-motion arrays are introduced. Furthermore, the criteria set towards the selection of the most appropriate borehole arrays for use in this study are discussed and the site characteristics of the corresponding selected sites are presented.

In *Chapter 5*, an evaluation of key assumptions associated with one-dimensional site response analysis is presented. First, an assessment of the existing wavefield at the base of each borehole array is provided. That is, linear-elastic

analysis results are compared with the observed recordings to select and physically justify the appropriate wavefield assumption at the location of the base sensor. Second, an assessment of the uncertainty regarding the damping values at small-strain levels is provided. A series of linear-elastic analysis are performed by assuming different values of small strain damping and the results are evaluated against the recordings. Finally, an attempt to investigate whether the wave propagation pattern at the selected borehole arrays can be sufficiently represented by a one-dimensional model is made.

In *Chapter 6*, a thorough evaluation of the considered site response methodologies is presented. The accuracy of the theoretical models at different levels of ground shaking is discussed and physical explanations of the observed performance are provided.

In *Chapter 7*, an assessment of the model variability across the considered sites is undertaken. The various sources of variability are identified and variability is quantified for different levels of induced shear strains.

In *Chapter 8*, improvements to EQL, EQL-FD and NL site response approaches, are proposed in accordance with the findings from *Chapter 7*. The accuracy of the theoretical models is, then, reassessed.

Conclusions of the present research and recommendations for refinement of future studies are presented in *Chapter 9*.

Chapter 2

One-Dimensional Site Response Methodologies

2.1. Introduction

One-dimensional site response analysis has been an essential tool in engineering practice for simulating ground shaking during major earthquakes. One dimensional ground response models are based on the assumption that all boundaries are horizontal and extend infinitely, and thus the response is dominated by vertically propagating and horizontally polarized shear waves (SH-waves) (*FIGURE 2.1*). The simplicity of the assumed wave propagation pattern has played a significant role in reducing the computational cost of site response analysis, and yet the results have been shown to be in reasonable agreement with measured responses in many cases (i.e. EPRI, 1993). Even though the one-dimensional assumption is overly simplistic, it can be - in most cases - physically justified by the fact that when a fault ruptures, the associated body waves travel away from the source tending to bend towards a nearly vertical direction due to multiple refractions as the waves encounter lower velocity layers closer to the ground surface.

Most one-dimensional site response formulations involve the propagation of SH-waves from the base rock through a model of the soil layers to the ground surface. Typical inputs for the theoretical models are the shear wave velocity and unit weight of the layers within the soil profile, as well as information concerning the nonlinear behavior of the soil materials under shear deformation. The manner

by which the latter is specified is the factor of major distinction between the various models. That is, the nonlinear and inelastic response of the soil materials can be approximated by either an equivalent-linear (EQL) or a fully nonlinear (NL) approach (*FIGURE 2.1*). The nonlinearity of the soil stress-strain behavior implies that the shear modulus of the materials is changing. Furthermore, the inelasticity means that the soil unloads along a different path than its loading path, thereby producing energy dissipation and damping.

Rigorous analysis of the mechanical response of soils during dynamic loading requires tracking of the stress-strain behavior in the time domain. Fully nonlinear (NL) site response algorithms are typically characterized by such an approach. Nonetheless, the equivalent-linear formulation (EQL) is commonly used to approximate the nonlinear and inelastic aspects of soil response. The EQL approximation is typically achieved in the frequency domain through linear elastic analyses with soil properties that are iteratively adjusted to be consistent with an effective level of shear strain induced in the soil (*FIGURE 2.1*). Equivalent-linear analysis with frequency dependent soil properties (EQL-FD) (e.g. Assimaki and Kausel, 2002; Yoshida *et al.*, 2002) is a phenomenologically-based approach that attempts to address the inability of the traditional EQL formulation to accurately predict the amplification of high frequency soil response at large strains. Rather than using a single value of effective shear strain, the EQL-FD approach takes advantage of the complete shear strain frequency Fourier Amplitude spectrum and uses it to define strain-compatible properties at each frequency (*FIGURE 2.1*).

The following chapter introduces and briefly discusses the details of the various one-dimensional site response methodologies considered (EQL, EQL-FD and

NL). The most significant advantages and disadvantages of each of the theoretical models are also presented.

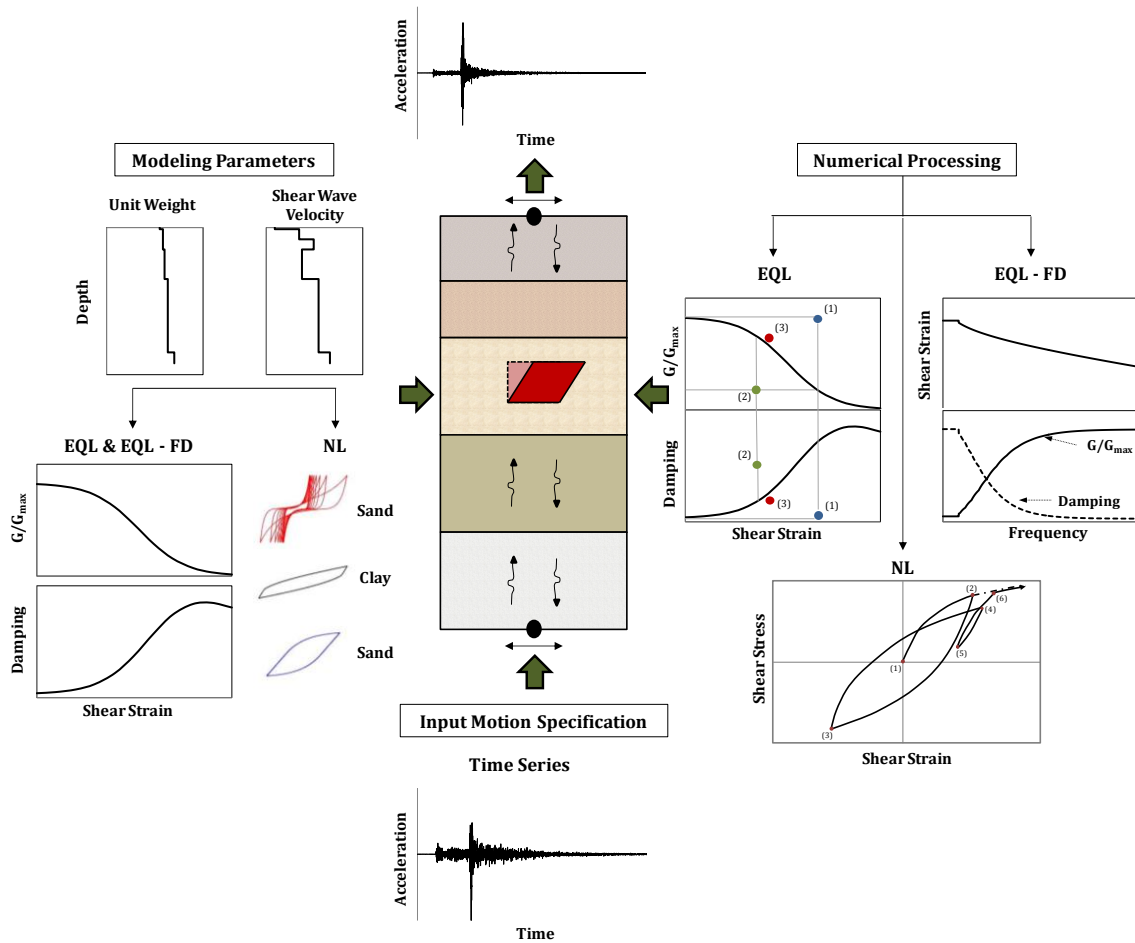


Figure 2.1: Schematic representation of the considered one-dimensional site response methodologies

2.2. Equivalent-Linear Site Response Method

Equivalent-linear site response analysis utilizes one-dimensional, linear-elastic wave propagation theory through layered media to simulate the mechanical response of soil deposits under strong shaking. The typical hysteretic stress-strain

relationship characterizing soil behavior under cyclic loading is modeled through an equivalent shear modulus (G) and an equivalent damping ratio (D) for a given level of induced shear strain. The equivalent shear modulus (G) corresponds to the secant modulus which approximates an “average” shear modulus over the entire cycle of loading, while the equivalent damping ratio corresponds to the energy dissipation encapsulated by the entire area within the hysteresis loop, as shown in *FIGURE 2.2*. Generally, as shear strain increases, the shear modulus (G) decreases and the damping ratio (D) increases. The relationship between the shear modulus and the magnitude of shear strain is usually depicted by a modulus reduction curve, i.e. the normalized secant shear modulus (G/G_{max} , where G_{max} is the small strain shear modulus) versus the logarithm of shear strain ($\log \gamma$). The small strain shear modulus (G_{max}) is computed via the small strain shear wave velocity (V_S) of any given soil material and its mass density (ρ) ($G_{max} = \rho \cdot V_S^2$). Correspondingly, the relationship between the equivalent hysteretic damping ratio (D) and shear strain is depicted by the damping curve, i.e. damping ratio versus the logarithm of shear strain ($\log \gamma$). Because the stress-strain loop (*FIGURE 2.2*) only represents the hysteretic behavior of a material, a measure of small strain, viscous energy dissipation (D_{min}) is also included in the damping curves. Modulus reduction and damping curves have been well established for many soils through various research efforts (Darendeli, 2001; Vucetic and Dobry 1991; EPRI 1993 etc.). The typical shapes of these material curves are illustrated in *FIGURE 2.3*.

Equivalent-linear computations are performed in the frequency domain. The one-dimensional wave equation for layered media is solved using complex valued transfer functions and the principle of superposition. To be compatible with such

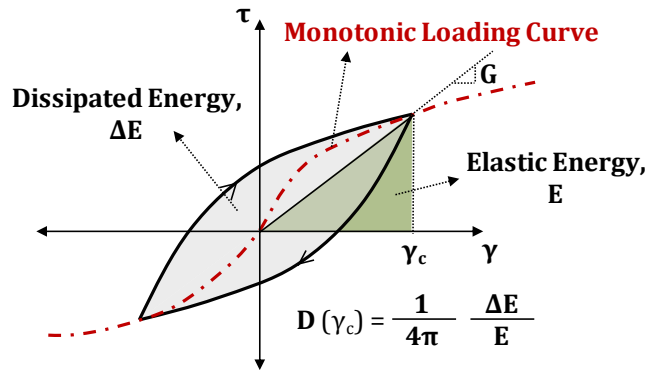


Figure 2.2: Hysteresis loop of soil under cyclic loading and the corresponding equivalent damping (D). ΔE is the dissipated energy during one cycle of loading and E is the maximum strain energy.

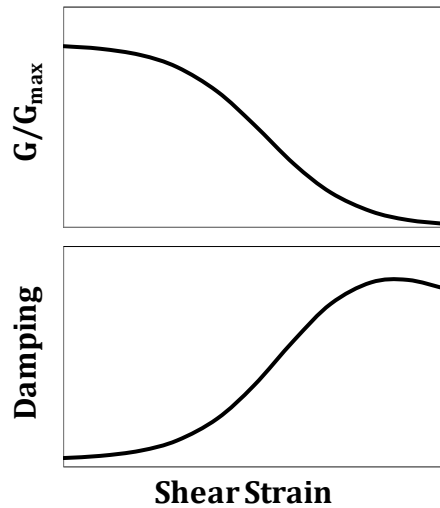


Figure 2.3: Typical shape of modulus reduction (G/G_{max}) and damping (D) curves

assumptions, all materials are assumed to be linear elastic. A schematic of the steps to an EQL analysis is shown in *FIGURE 2.4*. The input motion time series is converted to the frequency domain using the Fast Fourier Transform (FFT). Multiplication of the complex valued Fourier amplitude spectrum of the input motion with the complex valued transfer function for the site provides the Fourier amplitude spectrum of the surface motion. Using the Inverse Fast Fourier Transform (IFFT),

the Fourier amplitude spectrum of the surface motion is converted to the time domain.

The general framework of the equivalent-linear formulation, applied in the case of a layered medium, involves an iterative procedure in which material properties (G and D) are selected for each soil layer. These material properties must be consistent with the level of shear strain induced by the input motion. Thus, an iterative process is implemented to determine strain-compatible soil properties (G and D) from the empirical modulus reduction and damping curves.

Schnabel *et al.* (1972) introduced the equivalent-linear algorithm. The basis of the traditional EQL approach is the approximation of the actual nonlinear and inelastic response of the soil by performing linear analyses with soil properties that are iteratively adjusted to be compatible with an *effective* level of shear strain. This procedure is undertaken for each soil layer in the layered medium (*FIGURE 2.5*), and its key components can be described as follows:

1. Initial estimates of material properties (G and D) are selected for each layer. Small strain properties are typically utilized as an initial estimate.
2. The estimated G and D values are used to compute the response of the site, as schematically shown in *FIGURE 2.4*.
3. An *effective* level of shear strain (γ_{eff}) in each layer is determined. A fraction of the computed peak shear strain (γ_{max}) for each layer is used:

$$\gamma_{eff}^{(i)} = \alpha \cdot \gamma_{max}^{(i)} \quad (2.1)$$

where i is the iteration step and α is the fraction of the maximum shear strain considered. α can be related to earthquake magnitude (M) (Idriss and

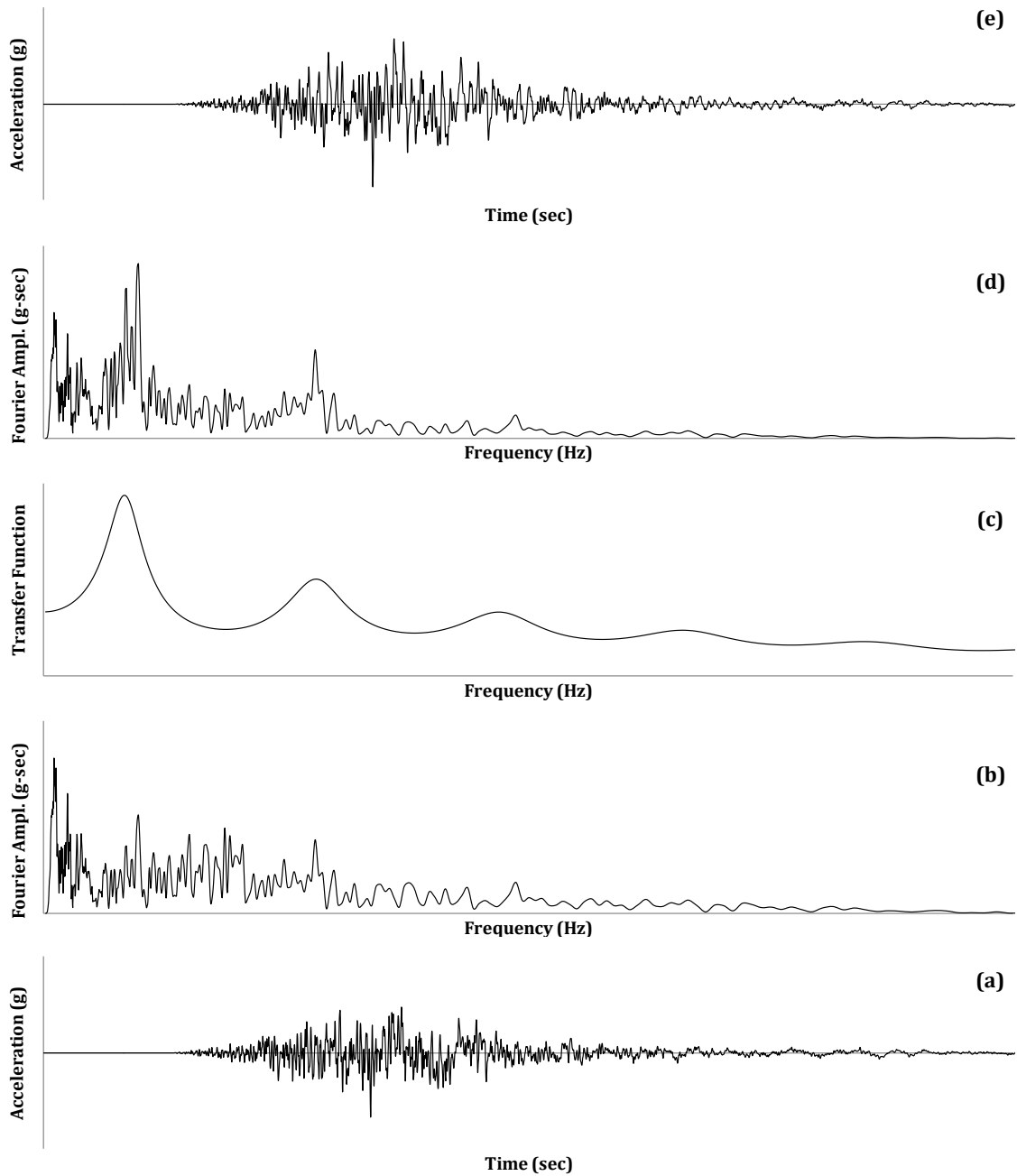


Figure 2.4: Example of equivalent-linear computations for a single layer: (a) input motion time history, (b) Fourier Amplitude Spectrum of the input motion, (c) transfer function, (d) computed Fourier Amplitude of the output motion, and (e) output motion time history

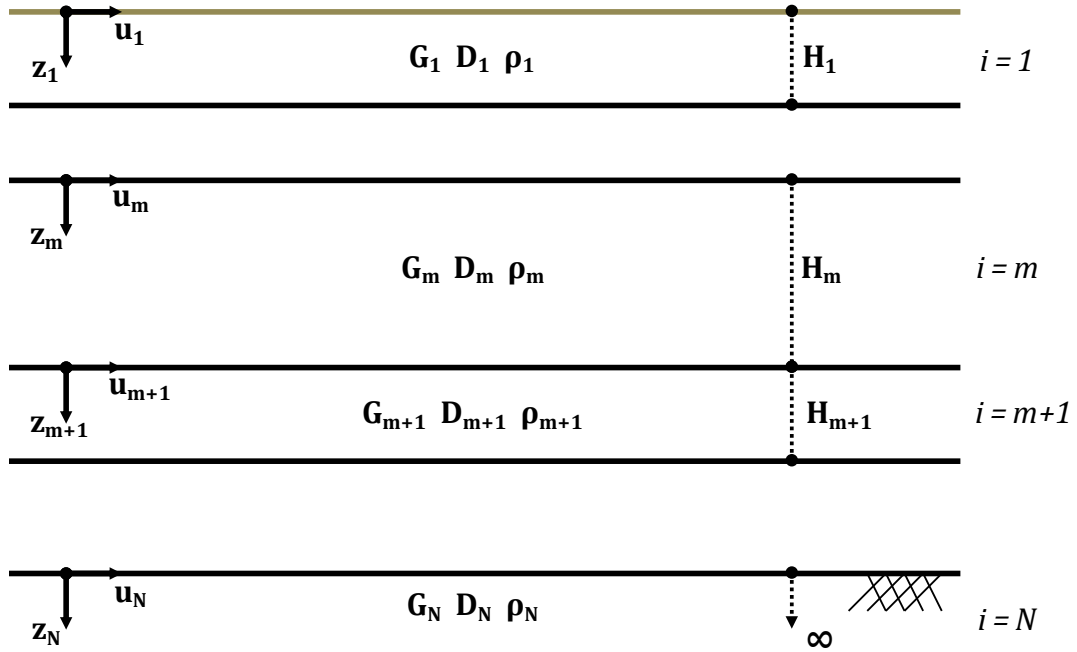


Figure 2.5: Nomenclature of layered medium in equivalent-linear formulation

Sun, 1992), as:

$$\alpha = \frac{M - 1}{10} \quad (2.2)$$

A value of 0.65 is most commonly utilized for α .

4. Based on the calculated effective level of shear strain, new values for the material properties are selected from the modulus reduction and damping curves.
5. Steps 2 to 4 are repeated until the difference between the computed material properties (G and D) of two successive iteration steps falls below a convergence criterion (FIGURE 2.6).

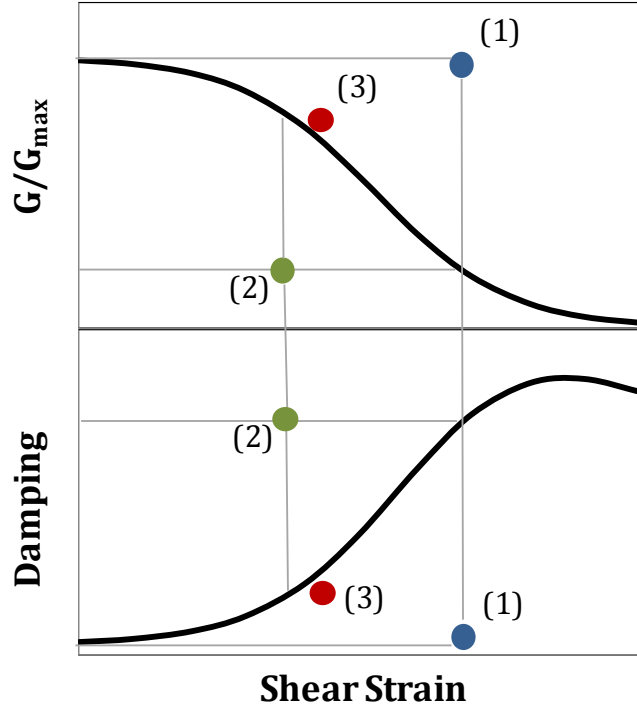


Figure 2.6: Schematic illustration of iterative procedure implemented in “traditional” equivalent-linear (EQL) algorithm

EQL analysis is the most widely used method for seismic ground response studies because of its low computational cost, its robustness and the fact that it simply requires the specification of well understood and meaningful input parameters such as the shear wave velocity as well as modulus reduction and damping curves. Nevertheless, the iterative process incorporated in its algorithm targets solely a single, peak value of shear strain. Therefore, the utilized strain-compatible soil properties remain constant throughout the duration of any strong motion time history, independent of the actual level of straining at a particular point in time. Consequently, the traditional EQL method poorly represents the time-dependent changes in soil stiffness and damping that actually occur during earthquake loading. This issue is most important at larger strains where the strain-

compatible damping becomes large. As a result the EQL approach generates poor predictions of high frequency soil response at large strains (e.g. Assimaki and Kausel, 2002).

To overcome the main limitations of the traditional EQL site response model at large strains, equivalent-linear algorithms with frequency-dependent material properties (EQL-FD) have been proposed (e.g. Furumoto *et al.*, 2000; Assimaki and Kausel, 2002; Yoshida *et al.*, 2002). These phenomenologically-based algorithms incorporate an iterative procedure in which the complete shear strain frequency spectrum is utilized to select strain-compatible properties at each frequency.

The physical mechanism behind the development of the EQL-FD site response method is schematically shown in *FIGURE 2.7*, where hysteresis loops for small (A) and large (B) strains are illustrated. Understandably, the shear modulus is large and damping ratio is small at low amplitude hysteretic loops (A), while the shear modulus is small and the damping ratio is large when large strains (B) are experienced.

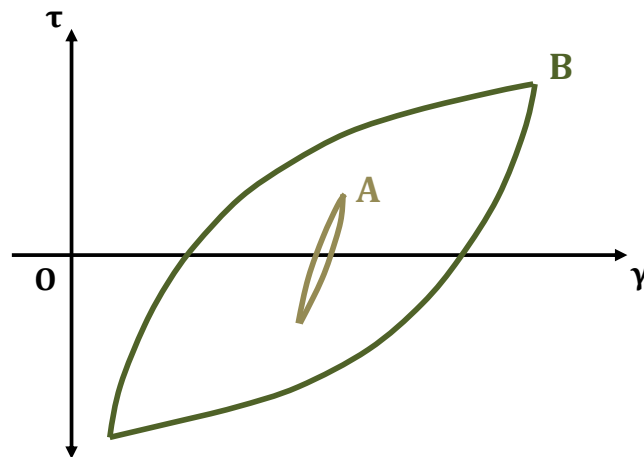


Figure 2.7: Small strain and large strain hysteresis loops for soils under cyclic loading (after Yoshida *et al.*, 2002)

Therefore, the frequency dependence of the material properties can be related to the frequency and amplitude-dependence of the induced shear strains, although the material itself is considered rate independent when loaded cyclically. Various researchers (e.g. Yoshida *et al.*, 2002; Assimaki and Kausel, 2002; Kwak *et al.*, 2008) have computed the Fourier amplitude spectra of induced shear strain time histories from several earthquake events (*FIGURE 2.8*). The results show that the high excitation frequencies are associated with secondary loops of smaller amplitude shear strains, while low excitation frequencies typically are associated with primary, higher-amplitude loops. In fact, at frequencies above 10 Hz the shear strains can be several orders of magnitude smaller than those of lower frequencies.

By acknowledging the aforementioned phenomenon, Furumoto *et al.* (2000) developed a frequency-dependent equivalent-linearized technique for site response analysis. Their work was based primarily on a previous research effort by Sugito *et al.* (1994). The key aspect of the proposed method by Furumoto *et al.* (2000) was the definition of a frequency-dependent *equivalent strain*, $\gamma_f(\omega)$, as:

$$\gamma_f(\omega) = C \cdot \gamma_{max} \cdot \frac{F_\gamma(\omega)}{F_{\gamma_{max}}} \quad (2.3)$$

where γ_{max} is the maximum shear strain, $F_\gamma(\omega)$ is the Fourier spectrum of shear strain, $F_{\gamma_{max}}$ is the maximum of $F_\gamma(\omega)$, and C is a constant. Furumoto *et al.* (2000) introduced the constant C to control the level of equivalent strain uniformly along the frequency axis. They proposed a value of C equal to 0.65 to be consistent with the definition of the *effective* level of shear strain (γ_{eff} in Equation 2.1) typically used in conventional equivalent-linear site response analysis (EQL).

The methodology proposed by Furumoto *et al.* (2000) utilizes the frequency-dependent *equivalent strain*, $\gamma_f(\omega)$ to perform equivalent-linear site response com-

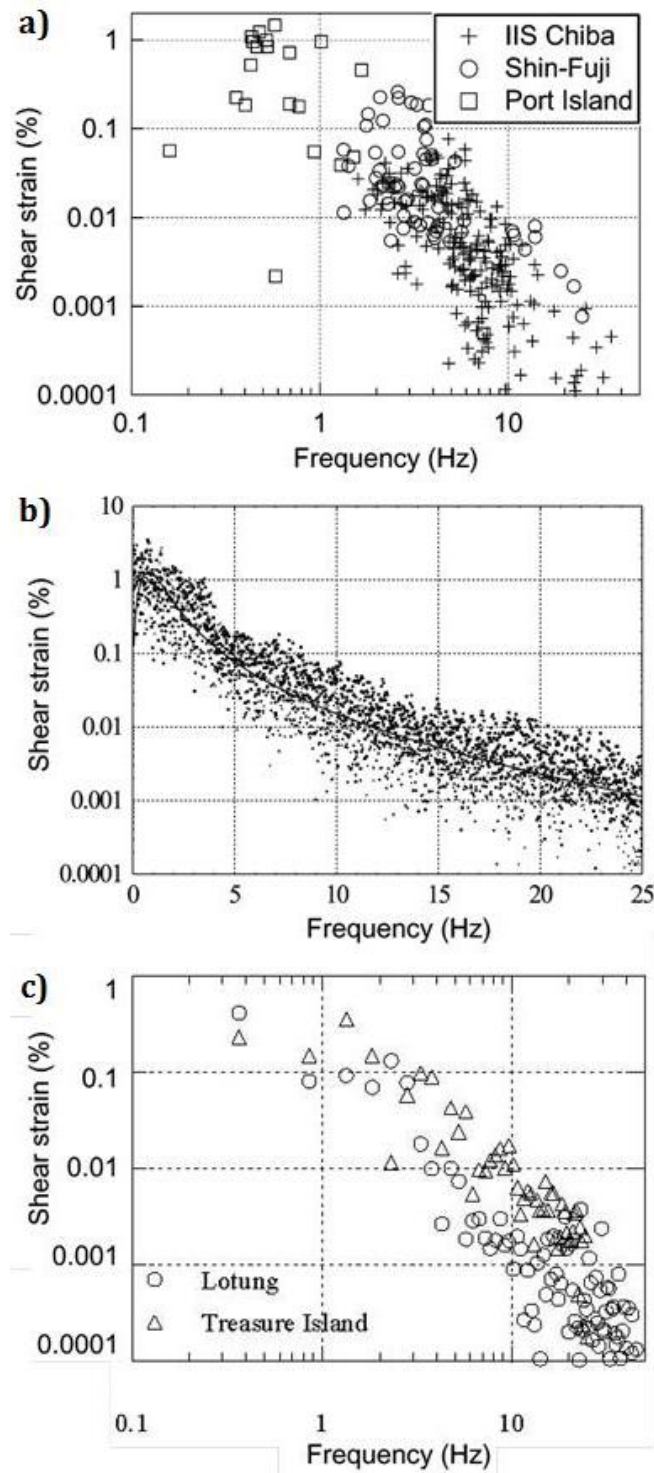


Figure 2.8: Strain frequency spectra from various earthquakes. (a) Yoshida et al., 2002; (b) Assimaki and Kausel, 2002; (c) Kwak et al., 2008

putations. An iterative procedure is adopted, in which the equivalent strain at each frequency is compared with the corresponding equivalent strain obtained in the previous iteration. Given the large range of frequencies at which the calculations are performed, the error estimates are categorized into three distinct frequency ranges: (1) low frequency range ($f < 1 \text{ Hz}$), (2) intermediate frequency range ($1 \text{ Hz} < f < 5 \text{ Hz}$), and (3) high frequency range ($f > 5 \text{ Hz}$). The average error within each frequency range is computed. The iterations are completed when a predefined convergence criterion is met.

To avoid numerical instabilities (Kausel and Assimaki, 2002) possibly associated with the convergence of the model when the highly irregular, complete shear strain frequency spectrum is used, Yoshida *et al.* (2002) and Assimaki and Kausel (2002) developed EQL-FD algorithms which incorporate a smoothed shear strain frequency spectrum, such as the ones shown in *FIGURE 2.9*, to perform site response calculations. The basic distinction between the different EQL-FD algorithms (Yoshida *et al.*, 2002 vs Assimaki and Kausel, 2002) is the approach used to smooth the strain Fourier spectrum.

Yoshida *et al.* (2002) developed a functional shape of the shear strain amplitude spectrum by stating that: (i) the maximum effective strain should be equal to the peak shear strain in a strain time history, and (ii) nonlinear soil behavior need not be considered at frequencies corresponding to shear strain levels less than 0.001 %. Therefore, they developed the following functional form:

$$\begin{cases} \gamma_{eff} = \gamma_{max} & , & f_p > f \\ \gamma_{eff} = \gamma_{max} \left\{ 1 - \left(\frac{\log f - \log f_p}{\log f_e - \log f_p} \right)^m \right\} & , & f_p \leq f \leq f_e \\ \gamma_{eff} = 0 & , & f > f_e \end{cases} \quad (2.4)$$

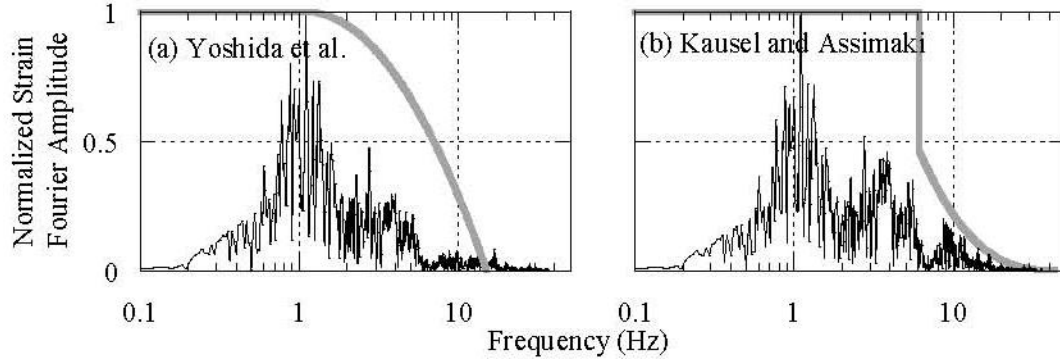


Figure 2.9: Smoothing of strain Fourier spectra used in EQL-FD algorithms (from Kwak *et al.*, 2008)

where f_p is the frequency corresponding to the maximum shear strain level (γ_{max}), f_e is the frequency above which nonlinear behavior is not considered, and m is a fitting parameter. The parameters f_e and m can be custom defined and adjusted to optimize the predictive results. Yoshida *et al.* (2002) proposed the utilization of $m = 2$ and $f_e = 15$ Hz.

Assimaki and Kausel (2002) smoothed the strain Fourier amplitude spectrum by taking the strain equal to a constant value at frequencies less than the mean angular frequency (ω_0) and exponentially decreasing the strains at frequencies greater than ω_0 . The Fourier amplitude spectrum is normalized by the average Fourier amplitude (γ_0) at frequencies less than ω_0 and fit with the following functional form:

$$\left| \frac{\gamma(\omega)}{\gamma_0} \right| = \begin{cases} 1, & \omega \leq \omega_0 \\ \frac{\exp\left(-\alpha \frac{\omega}{\omega_0}\right)}{\left(\frac{\omega}{\omega_0}\right)^\beta}, & \omega > \omega_0 \end{cases} \quad (2.5)$$

where α and β are optimization parameters determined by least squares regression. The normalized shear strain spectrum is multiplied by the peak time domain shear

strain to generate the shear strain spectrum used to select the frequency-dependent soil properties. The average Fourier amplitude, γ_0 , and the mean angular frequency, ω_0 , are computed as:

$$\omega_0 = \frac{\int_0^{\infty} \omega \gamma(\omega) d\omega}{\int_0^{\infty} \gamma(\omega) d\omega} \quad (2.6)$$

$$\gamma_0 = \frac{1}{\omega_0} \int_0^{\infty} \gamma(\omega) d\omega \quad (2.7)$$

In both EQL-FD algorithms mentioned above (Yoshida *et al.*, 2002; Assimaki and Kausel, 2002) the frequency dependent soil properties are the result of mapping of the frequency dependence of the shear strains to the strain-dependence of the modulus reduction and damping curves. Thus, smooth plots of modulus reduction and damping versus frequency are produced (*FIGURE 2.10*).

The main numerical procedures of the EQL-FD site response method are similar to those described for the traditional EQL method. The key difference between the two models lies in the way the EQL-FD approach addresses the frequency dependence of the material properties. The same one-dimensional wave propagation solution in the frequency domain is used in EQL and EQL-FD approaches, but EQL-FD uses different properties at each frequency to compute the site transfer function.

EQL-FD provides a simple, robust and fast computational tool for seismic site response studies. Contrary to the traditional EQL method, it takes into account the complete frequency content of the induced shear strains and better simulates the wide range of shear strains within the duration of seismic loading. Thus, it can po-

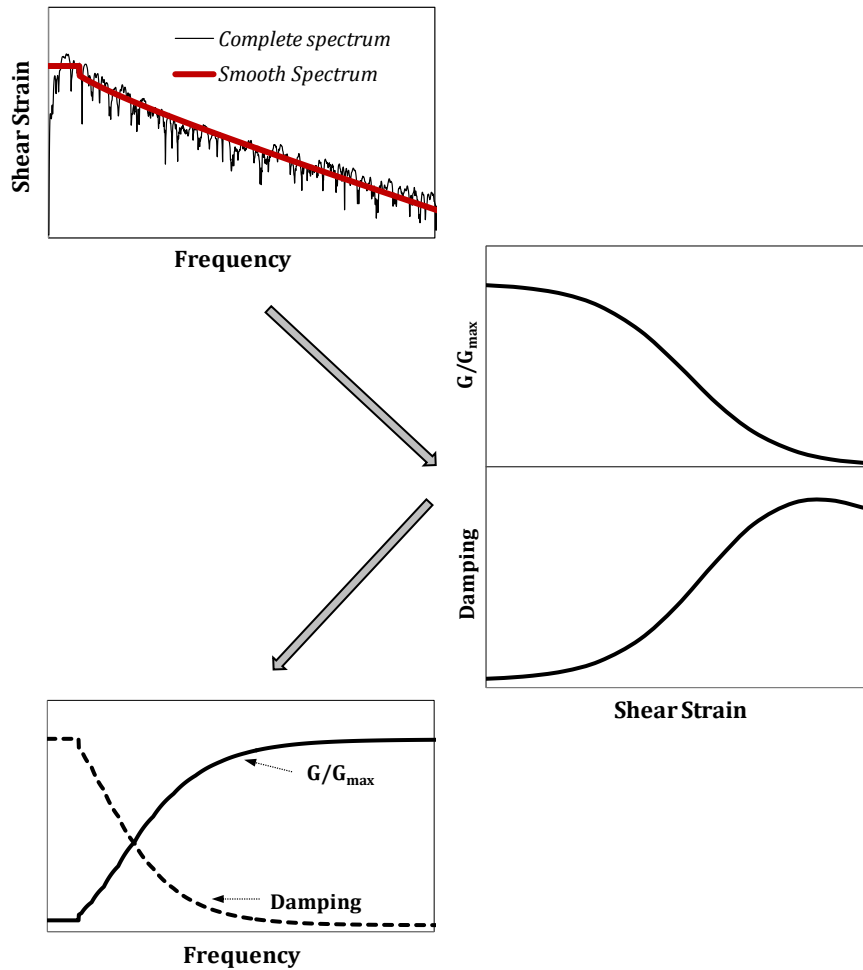


Figure 2.10: Mapping of soil properties in the frequency domain

tentially lead to a more accurate approximation of the actual nonlinear and inelastic soil behavior which otherwise could only be simulated by fully nonlinear site response methods. Nevertheless, the effectiveness of the method has not been fully verified via extensive and comprehensive validation studies.

The aforementioned equivalent-linear algorithms have been implemented in several commercially available or open-source computer codes (*TABLE 2.1*). The lack of verification for the effectiveness of EQL-FD method is partially explained by the limited number of existing codes that have implemented such a formulation. For the

present study, the equivalent-linear site response computer program *Strata* (Kottke and Rathje, 2008) was used both for EQL and EQL-FD analyses.

Table 2.1: Computer codes for equivalent-linear site response analysis

<i>"Traditional" EQL</i>		<i>EQL-FD</i>	
Computer Code	Code Developer	Computer Code	Code Developer
SHAKE	Schnabel, 1972	Strata	Kottke and Rathje, 2008
SHAKE91	Idriss and Sum, 1993	DYNEQ	Yoshida N. and Suetomi I., 1996
SHAKE2000	Ordóñez, 2002		
SHAKE04	Youngs, 2004		
Strata	Kottke and Rathje, 2008		
EERA	Bardet et al., 2000		
RASCALS	Silva and Lee, 1987		
P-SHAKE	Bechtel, 2006		

2.3. Fully Nonlinear Site Response Method

Equivalent-linear models are still the most commonly used methods for seismic ground response analyses. Even though the development of fast personal computers have made the low computational cost of EQL analysis irrelevant, the simplicity of the input parameters, the robustness of the method and the relative insensitivity to modeling errors have played a significant role in making it the dominant computational tool in engineering applications. Nonetheless, equivalent-linear models remain a, sometimes, crude approximation of the complexity of nonlinear soil response, especially under strong shaking. A more realistic representation of soil behavior can be achieved through the utilization of fully nonlinear site response models.

Fully nonlinear site response models (NL) incorporate the actual nonlinear stress-strain relationships that characterize the response of soil materials under

cyclic loading. These models involve the computation of the dynamic response of a one-dimensional soil column. The soil column typically consists of layers described by either lumped masses or discretized elements with appropriate boundary conditions, and nonlinear shear springs. Nonlinear analysis involves the solution of the differential equation of motion in the time domain using numerical time stepping methods, in which the input motion at the base of the soil column is used as the forcing function. By integrating the equation of motion in small time steps, the stress-strain relationship of the soil material is fully followed at every point in time. Thus, the key component of all nonlinear models is the backbone stress-strain curve and the unloading/reloading rules used to define the hysteretic behavior of the soil materials. A schematic example of the backbone curve and the corresponding unloading/reloading rules is shown in *FIGURE 2.11*.

The main points of differentiation between the various existing nonlinear site response models are the solution scheme for the wave equation and the implemented nonlinear soil model. The finite element method, implicit or explicit finite difference methods and the method of characteristics have all been considered for the numerical scheme for NL analysis (Stewart *et al.*, 2008). Moreover, the soil models can vary from simple, empirically based, stress-strain relationships to advanced constitutive models. A list of several commonly considered nonlinear soil models is presented in *TABLE 2.2*.

One of the most widely used nonlinear soil models is the modified Kondner-Zelasko (MKZ) model (Matasovic, 1993), which consists of an extension of the hyperbolic model (Hardin and Drnevich, 1972). The backbone curve of the model is defined, as:

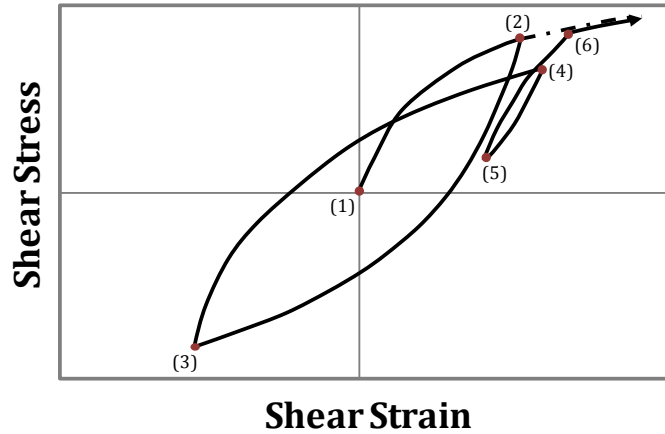


Figure 2.11: Typical calculation steps on hysteretic behavior implemented in nonlinear site response models (after Stewart *et al.*, 2008)

$$\tau = \frac{\gamma \cdot G_{max}}{1 + \beta \cdot \left(\frac{\gamma}{\gamma_r}\right)^s} \quad (2.8)$$

where τ and γ are the shear stress and shear strain respectively, γ_r is the reference shear strain, and β and s are dimensionless fitting parameters. Because the hysteretic behavior gives essentially zero small strain damping, a measure of small strain energy dissipation is incorporated by the addition of viscous damping (D_{min}). The original formulation for the small strain viscous damping (Rayleigh and Lindsay, 1945) is frequency dependent, something inconsistent with observations. Phillips and Hashash (2009) developed an algorithm which provides frequency-independent viscous damping, which in many cases better agrees with the available data.

The parameters β , s , and γ_r typically are defined by fitting the equivalent modulus reduction and damping curves to empirically based curves (e.g. Darendeli, 2001). The unload/reload rules that are used to model hysteretic behavior based on the backbone curve have a significant effect on the computed damping ratio, parti-

Table 2.2: Common nonlinear soil models

Simple Models	Advanced Constitutive Models
Ramberg and Osgood, 1943	Roscoe and Scofield, 1963
Kodner and Zelasko, 1963	Roscoe and Burland, 1968
Hyperbolic model (Hardin and Drnevich, 1972)	Mroz, 1967
Iwan type (Joyner and Chen, 1975)	Prevost, 1977
Finn et al., 1977	Dafalias and Popov, 1979
Pyke, 1979 (Extended hyperbolic)	Multiyield surface plasticity (Ragheb, 1994; Parra, 1996; Yang, 2000)
Vucetic 1990	Bounding surface plasticity (Wang, 2000)
Matasovic and Vucetic - MKZ, 1993 (Extended hyperbolic)	Gerolymos and Gazetas, 2002
Hashash and Park, 2001	

cularly at large strains. Traditional unload/reload behavior based on extended Masing rules generally overestimate damping at large strains. The need to better fit the experimentally developed damping curves at large strains lead to the development of a modulus reduction and damping curve fitting procedure (MRDF - Phillips and Hashash, 2009) which modifies the unload/reload rules to control the size of the hysteresis loops and thus the damping. *FIGURE 2.12* shows the equivalent damping curves generated from the MRDF unload/reload rules. The MRDF curve predicts significantly less damping at larger strains and is in good agreement with the target empirical curve. Contrary, the fitting procedure based on the traditional unload/reload Masing rules (MRD curve in *FIGURE 2.12*) provides much higher dam-

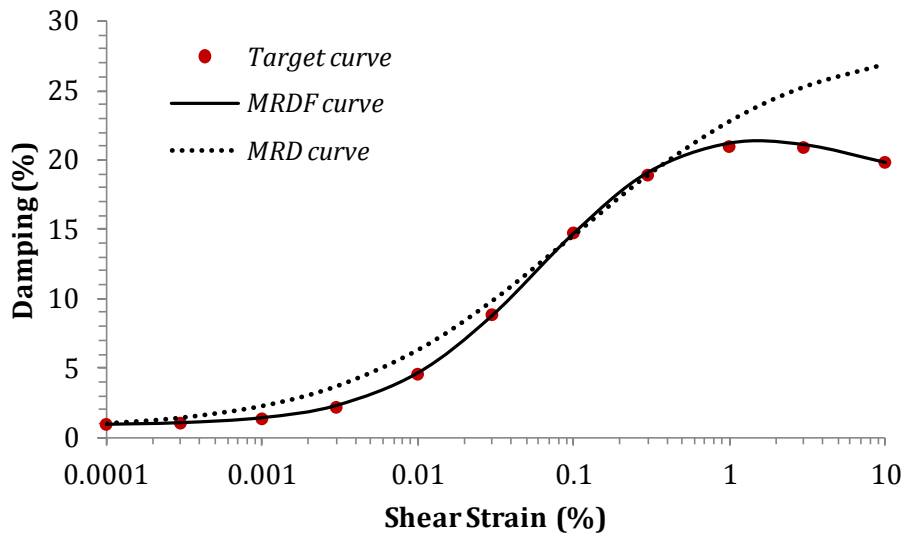


Figure 2.12: Curve fitting of MRDF and MRD models to target, empirical curves

ping ratio values at large strains.

Nonlinear site response analysis more accurately models the nonlinear and inelastic behavior of soil deposits under strong shaking, and therefore should produce more accurate estimates of the soil response. Nevertheless, the vast majority of NL algorithms require more complex soil characterization and a large number of input parameters. Additionally, substantial variability exists between different NL simulation codes (Kwok *et al.*, 2006). Finally, in some cases (deep soil deposits and large intensity and long input motions), nonlinear analysis is characterized by high computational cost.

One-dimensional nonlinear site response analysis is incorporated in several commercially available or open-source computer codes. These computer codes are based on different nonlinear wave propagation techniques (Finite Element / Finite Difference) and different nonlinear soil models. A list of several NL computer programs is provided by Stewart *et al.* (2008), which, supplemented, is also shown in *TABLE 2.3*. In the present study, the program **DeepSoil v5.1** (Hashash, 2012) was

used for the nonlinear site response analysis. The modified MKZ model, as described in the previous paragraphs, is implemented within *DeepSoil v5.1* as well as the MRDF unload/reload rules.

Table 2.3: Computer codes for 1-D nonlinear site response analysis

Computer Code	Code Developer	Computational Scheme	Nonlinear Soil Model
<i>DESRA-2C</i>	Lee and Finn, 1991	Finite Element (distributed mass)	Konder and Zelasko, 1963
<i>SUMDES</i>	Li et al., 1992	Finite Element (distributed mass)	Bounding Surface Plasticity (Wang, 2000)
<i>TESS</i>	Pyke, 1992	Explicit Finite Difference (distributed mass)	Pyke, 1979 (hyperbolic model with Cundal-Pyke hypothesis)
<i>D-MOD_2</i>	Matasovic, 2006	Finite Difference (lumped mass)	MKZ
<i>DEEPSOIL</i>	Hashash and Park, 2001, 2002	Finite Difference (lumped mass)	Hashash and Park (2001, 2002) - (modified MKZ)
<i>OpenSees</i>	McKenna and Fenves, 2001 (opensees.berkeley.edu)	Finite Element	Multi-surface Plasticity (Yang, 2000)
<i>DESRAMOD</i>	Vucetic and Dobry, 2986	Finite Element (distributed mass)	Konder and Zelasko, 1963 (with pore water pressure model by Dobry et al., 1985)
<i>MARDESRA</i>	Mok, 1990	Finite Element (distributed mass)	Martin (1975) - (modified hyperbolic)
<i>SPECTRA</i>	Borja et al., 1999a, 2000, 2002	Finite Element	Bounding Surface Plasticity (Wang, 2000)
<i>NERA</i>	Bardet and Tobita, 2001	Finite Difference	Iwan, 1967; Mroz, 1967
<i>NONLI3</i>	Joyner and Chen, 1975	Finite Difference	MKZ
<i>NL-DYAS</i>	Gerolymos and Gazetas, 2002	Explicit Finite Difference	Gerolymos and Gazetas, 2002 (BWGG)

2.4. Summary

In this chapter, a detailed overview of the most common one-dimensional site response models is provided. Traditional equivalent-linear (EQL), equivalent-linear with frequency-dependent soil properties (EQL-FD) and fully nonlinear (NL) site response analysis were discussed. The theoretical frameworks of these models, some of the details about the solution procedures, and their most significant advantages and disadvantages were discussed.

The traditional EQL method is based on an approximate iterative numerical procedure that targets an *effective* level of induced shear strain to select strain-compatible soil properties. EQL site response has been proven to be a very convenient and easily implemented tool in seismic ground response studies, but it tends to overdamp high frequency components of motion when the induced strains are large. The EQL-FD approach was developed to address the overdamping observed in traditional EQL analysis. EQL-FD analysis utilizes the complete frequency strain spectrum to select appropriate soil properties for the dynamic analysis. This approach assigns frequency-dependent shear modulus and damping values based on the frequency dependence of the generated strains, even though the properties themselves are rate-independent. EQL-FD approach provides a more realistic representation of soil behavior under strong motion shaking without losing the simplicity and low computation cost of the traditional EQL method. The site response methodology that most accurately represents the true nonlinear and inelastic characteristics of soil response is the fully nonlinear (NL) approach. In NL analysis the nonlinear stress-strain relationship is truly followed at every point in time during the entire duration of an earthquake. Nonlinear site response method is especially useful in predicting the response of soils at large strains. Nonetheless, the

analysis requires the specification of a large number of input parameters, something that makes the modeling prone to simulation errors.

Chapter 3

Validation Studies of One-Dimensional Site Response Methods

3.1. Introduction

During the past two decades, numerous validation studies of one-dimensional site response methodologies have been undertaken. These studies include either 1) comparative studies between various models for the purposes of providing insight into the results each type of analysis produces, or 2) verification research efforts through the evaluation of predictive results against recordings from instrumented vertical arrays. Validation studies for one-dimensional site response modeling techniques have been primarily focused on examining the relative benefits/shortcomings of the traditional equivalent-linear formulation (EQL) with respect to the more complex fully nonlinear (NL) approach. Within this context, different computer codes have been utilized and evaluated. In this chapter, the results and observations from a sampling of these studies are summarized. By analyzing and documenting the observations arising from various previous studies, results of the present research effort can be better evaluated.

3.2. Studies Comparing Equivalent Linear and Nonlinear Analyses

A list of the major research efforts dealing with the relative comparison of the theoretical solutions from various one-dimensional site response models is given in *TABLE 3.1*. The specifications and findings of some of the studies tabulated in *TABLE 3.1* are briefly discussed in the following paragraphs.

Table 3.1: Comparative studies for one-dimensional site response methods

Reference	Comparison Between	Sites - Soil Conditions - Recording Locations	Utilized Computer codes
Idriss (1990); Dickenson (1994)	NL / traditional EQL	Bay mud - San Francisco bay area (11 sites)	SHAKE - MARDESRA
Chang et al., (1990); Beresnev et al. (1995); Borja et al. (1999)	NL / "traditional" EQL	Soft silt (vertical array)	SHAKE - SUMDES, DESRA2, SPECTRA, unnamed code
EPRI, 1993	NL / RVT-based EQL	Gilroy 2, Treasure Island, Lotung	RASCAL - DESRA, SUMPES, TESS
Matasovic et al., (1995)	NL / traditional EQL	Oil Landfill - Monterey Park	SHAKE - D-MOD_2
Chang (1996); Darragh and Idriss (1997)	NL / traditional EQL	Deep stiff clay - Oakland, Emeryville; Gilroy (4 sites)	SHAKE - D-MOD_2
Chang et al., 1996	NL / traditional EQL	Deep alluvium - Sylmar, Hollywood, Santa Monica (3 sites)	SHAKE - D-MOD_2
Elgamal et al., (1996); Wang et al., (2001);	NL codes	Liquefiable sand - Kobe Port Island (vertical array)	SUMDES - unnamed code
Matasovic and Vucetic (1996)	NL code	Liquefiable sand - Wildlife site (vertical array)	D-MOD_2
Silva et al., 2000	NL / RVT-based EQL	Theoretical sites: a) NEHPR class site C and b) NEHPR class site E	RASCAL - DESRA-MUSC
Hashash et al., 2003	NL / traditional EQL	Deep Desposits in West Tennessee	SHAKE - DEEPSOIL
Park et al., 2004	NL / RVT-based EQL	Deep Deposits of Mississippi Embayment	SHAKE - DEEPSOIL
Foerster and Modaressi, 2007	NL / traditional EQL	Treasure Island	SHAKE - CyberQuake, DEEPSOIL, SUMDES
Deng and Ostadan, 2008	traditional EQL / RVT-based EQL	Theoretical profile	SHAKE - P-SHAKE
Kwak et al. (2008)	NL / traditional EQL / EQL-FD	Theoretical profile	GeoSHAKE
Kwok et al., 2008	NL / traditional EQL	Turkey Flat site (shallow stiff)	SHAKE04 - D-MOD_2, DEEPSOIL, TESS, SUMDES, OpenSees
Stewart et al., 2008	NL / traditional EQL	Simi Valley Knolls School (Shallow stiff), Treasure Island (Soft clay medium depth), La Cienega (Deep Stiff)	SHAKE04 - D-MOD_2, DEEPSOIL, TESS, SUMDES
Visone and Billotta, 2008	NL / traditional EQL	Theoretical profile	NERA - EERA, DEEPSOIL
Kottke, 2010	NL / traditional EQL / RVT-based EQL	Turkey Flat site, Sylmar County Hospital site, Calver cliffs site	Strata - DEEPSOIL

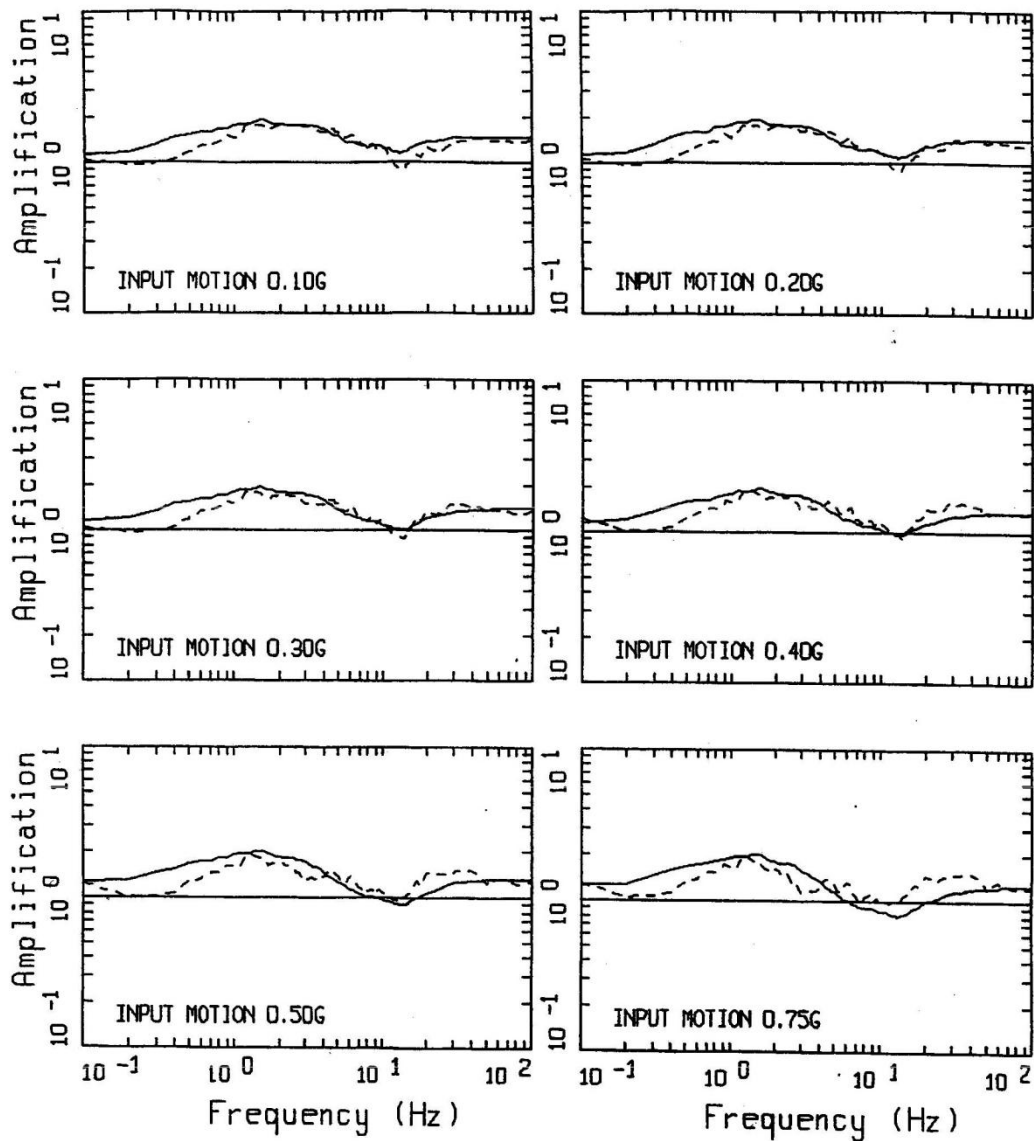
3.2.1. Silva *et al.*, 2000

Silva *et al.* (2000) studied the differences in the predictions between equivalent-linear (EQL) and fully nonlinear (NL) models, using the codes *RASCAL*

and *DESRA-MUSC*, respectively. Simulated motions with a wide range of amplitudes were used as input to the analyses. The authors developed two theoretical sites for the purposes of their study, i.e. a NEHPR class site C and a NEHPR class site E. Silva *et al.* (2000) concluded that there is generally good agreement over most of the frequency range (*FIGURES 3.1* and *3.2*). At higher loading levels, high frequency ($> 10 \text{ Hz}$) amplification is larger from the nonlinear than from the equivalent linear method. Moreover, for soft soils (NEHPR class site E – *FIGURE 3.2*), the nonlinear codes give smaller amplification factors than equivalent linear, for high levels of shaking.

3.2.2. Park *et al.*, 2004

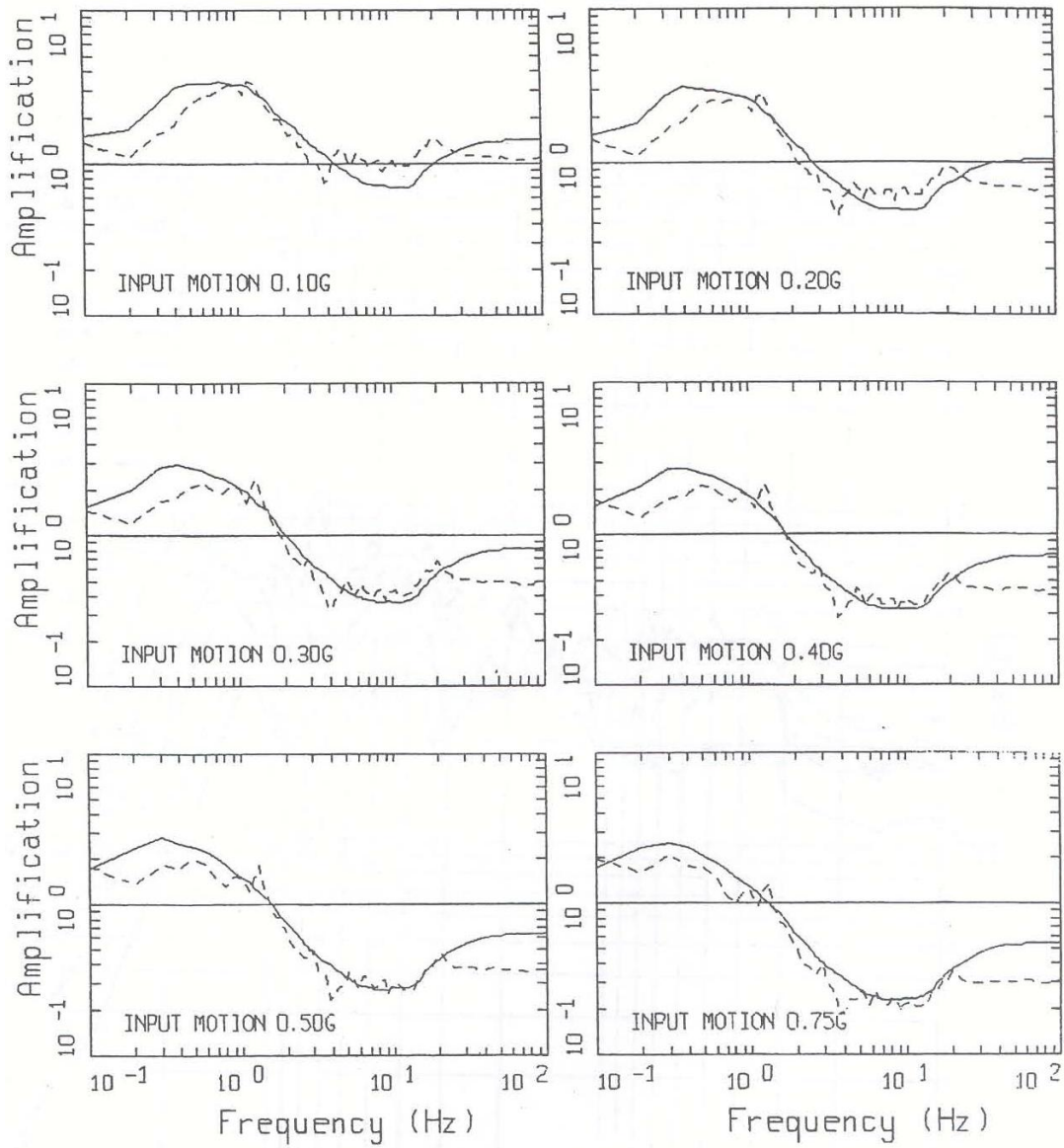
Park *et al.* (2004) evaluated and compared equivalent-linear (EQL) and nonlinear (NL) site response models using the algorithms incorporated in *DeepSoil*. Their reference site was the deep Mississippi embayment soil profile. The authors utilized two sets of dynamic properties and three stochastically simulated input motions of different intensities and relative frequency content (*PGA* ranging from 0.1 g to 0.65 g). In the case of low shaking level ($PGA = 0.1 \text{ g}$, *FIGURE 3.3a*), Park *et al.* (2004) observed similar predictive results between the EQL and fully nonlinear models. On the other hand, at large input intensities ($PGA = 0.65 \text{ g}$, *FIGURE 3.3b*), the researchers observed an evident difference between the EQL and NL analyses. The EQL method clearly showed lower response at short periods, resulting from the spurious filtering and thus underestimation of high frequency amplification.



NEHRP AMPLIFICATION, CATEGORY C, WUS, PENINSULAR RANGE CURVES

LEGEND
 ——— MEDIAN, EQUIVALENT-LINEAR
 - - - MEDIAN, NONLINEAR

Figure 3.1: Amplification factors predicted by equivalent-linear and nonlinear models, for NEHRP category C (from Silva *et al.*, 2000)



NEHRP AMPLIFICATION, CATEGORY E, WUS

LEGEND
 ——— MEDIAN, EQUIVALENT-LINEAR
 - - - - MEDIAN, NONLINEAR

Figure 3.2: Amplification factors predicted by equivalent-linear and nonlinear models, for NEHRP category E (from Silva *et al.*, 2000)

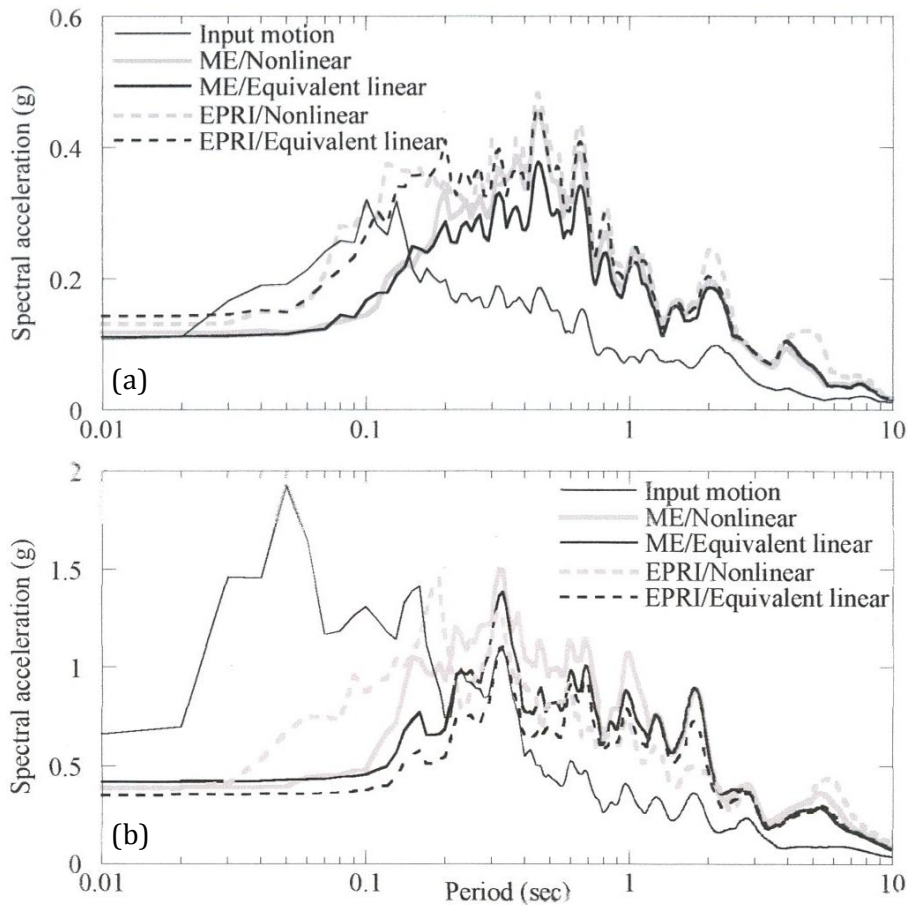


Figure 3.3: Comparison of surface response spectra: (a) $PGA = 0.1 g$, and (b) $PGA = 0.65 g$ (from Park *et al.*, 2004)

3.2.3. Stewart *et al.*, 2008

In their comprehensive study, Stewart *et al.* (2008) performed linear-elastic time domain analyses with alternative specifications of viscous damping (full Rayleigh formulation vs simplified Rayleigh formulation) and target damping ratios (0.5 % or 5 %). The results were compared to an exact solution from linear-elastic frequency domain analyses (LE) with a target damping ratio of 5 %. Stewart *et al.* (2008) used a variety of different NL numerical codes (*DeepSoil*, *D-MOD_2*, *OpenSees*, *SUMDES* and *TESS*), and compared the results with those from the frequency-

domain analysis using *SHAKE2004*. Analyses were performed using a broadband synthetic acceleration history calculated for an outcropping rock site condition, and three different sites: (i) a shallow stiff (Simi Valley Knolls School), (ii) a soft clay with medium depth (Treasure island), and (iii) a deep stiff site (La Cienega).

The results from Stewart *et al.* (2008) provided insight into the differences between the various NL codes. Some NL codes showed greater sensitivity to the value of the target damping ratio. Additionally, the authors concluded that, where available, the viscous damping should be estimated based on the full Rayleigh damping formulation.

3.2.4. Kwak *et al.*, 2008

Kwak *et al.* (2008) presented a verification study on the accuracy of frequency-dependent algorithms. Towards this goal, they performed analyses using the equivalent-linear (EQL) method, the fully nonlinear (NL) method and the equivalent-linear with frequency-dependent soil properties (EQL-FD) method. Both EQL-FD numerical algorithms (Yoshida *et al.*, 2002 and Assimaki and Kausel, 2002) were evaluated. A theoretical 34 m deep soil profile was used as a reference site, at the base of which two time histories, one synthetic and one recorded in a Parkfield earthquake event ($M = 6.0$), were input. The synthetic motion, rich in high frequency content, was utilized to examine the frequency dependence of the performance of the various models. The authors concluded that EQL-FD method shows a larger response at high frequencies compared to both EQL and NL models (*FIGURE 3.4*). The EQL-FD response is particularly large (and unrealistic) when an input motion rich in high frequencies is used (*FIGURE 3.4a*).

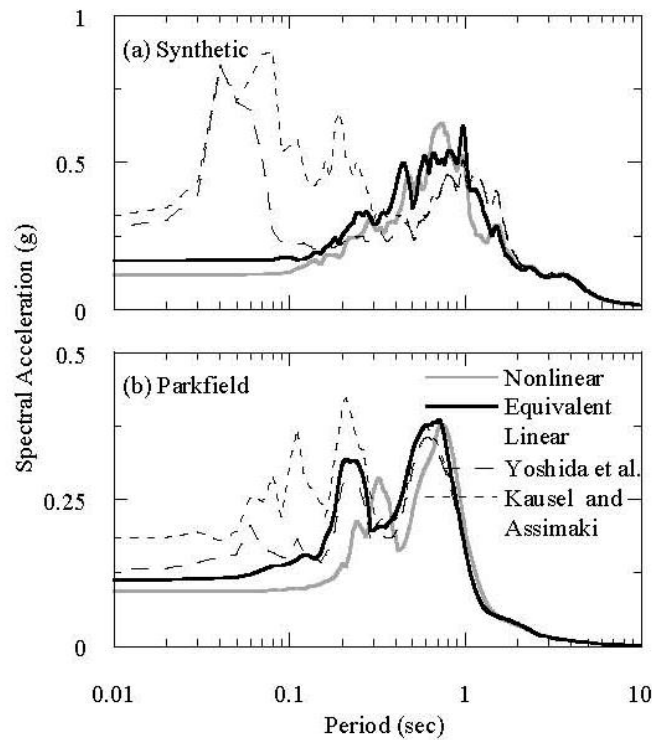


Figure 3.4: Comparison of surface acceleration response spectra produced by different models (from Kwak *et al.* 2008)

3.2.5. Kottke, 2010

Kottke (2010) compared EQL and NL site response methodologies using non-instrumented reference sites and the computer programs *Strata* and *DeepSoil*, respectively. The relative comparison between the theoretical predictions was based on the results of three reference sites: (i) Turkey Flat, (ii) Sylmar County Hospital, and (iii) Calvert Cliffs.

Kottke (2010) concluded that great relative differences between EQL and NL models can be seen at large input intensities. Moreover, NL analysis utilizing frequency-independent Rayleigh damping formulation was proven to be more effective.

3.3. Studies using Borehole Arrays

A list of several major studies associated with the verification of site response models against recordings from instrumented vertical arrays is tabulated in *TABLE 3.2*. The specifications and findings of some of the studies tabulated in *TABLE 3.2* are briefly presented in the following paragraphs.

Table 3.2: Verification studies of site response methodologies against recordings

Reference	Verification of	Sites - Soil Conditions - Recording Locations	Utilized Computer codes
Andrade and Borja, 2000	NL / traditional EQL	LSST site	SHAKE - SPECTRA
Lee et al., 2006	NL / traditional EQL	LSST site	SHAKE - NONLI3
Stewart et al., 2008	NL / traditional EQL	Turkey Flat, La Cienega, KGWH02, Lotung	SHAKE04 - D-MOD_2, DEEPSOIL, TESS, SUMDES
Kottke, 2010	NL / traditional EQL / RVT-based EQL	KSRH10, La Cienega, Lotung	Strata - DEEPSOIL
Kaklamanos et al., 2013	Linear Elastic / traditional EQL	100 Kik-Net vertical arrays	SH1D - SHAKE

3.3.1. Borja *et al.*, 1999

Borja *et al.* (1999) compared the EQL formulation with a fully nonlinear (NL) model. The equivalent-linear analyses were performed using the code *SHAKE* while the nonlinear analyses were conducted using the computer code *SPECTRA*. Recorded motions from three major motions at the Large Scale Seismic Test Site (LSST) at Lotung, Taiwan, were utilized. The back-calculated, reported $G/G_{max} - \log \gamma$ and $D - \log \gamma$ material curves from Zeghal *et al.* (1995) were implemented. Based on the results, a general good agreement between the predicted and recorded motions in terms of the spectral acceleration spectra, for all input motions, were observed (*FIGURE 3.5*). Nevertheless, a systematic underprediction of the response at low periods (or high frequencies) is reported.

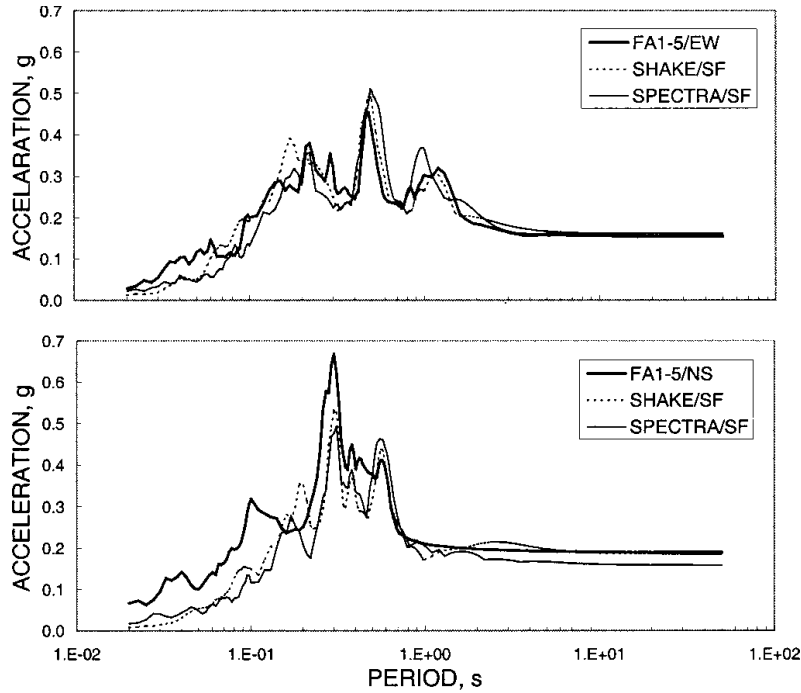


Figure 3.5: Acceleration response spectra at 5% damping: Lotung LSST12 case study (Borja *et al.*, 1999)

3.3.2. Lee *et al.*, 2006

Lee *et al.* (2006) evaluated the equivalent-linear (EQL) and the fully nonlinear (NL) site response approaches, by performing analyses based on the Lotung vertical array in Taiwan. The results were compared with the observed response as recorded by the instrumentation. They used both low ($PGA_{base} < 0.04 g$) and higher ($PGA_{base} > 0.04 g$) intensity ground motions. The authors quantified the difference between observed and calculated response in terms of the bias in the surficial spectral acceleration values, as:

$$Bias = \ln(S_a^{obs}/S_a^{calc}) \quad (3.1)$$

where S_a^{obs} and S_a^{calc} are the observed and computed spectral accelerations, respectively. The results from Lee *et al.* (2006) are shown in *FIGURE 3.6*.

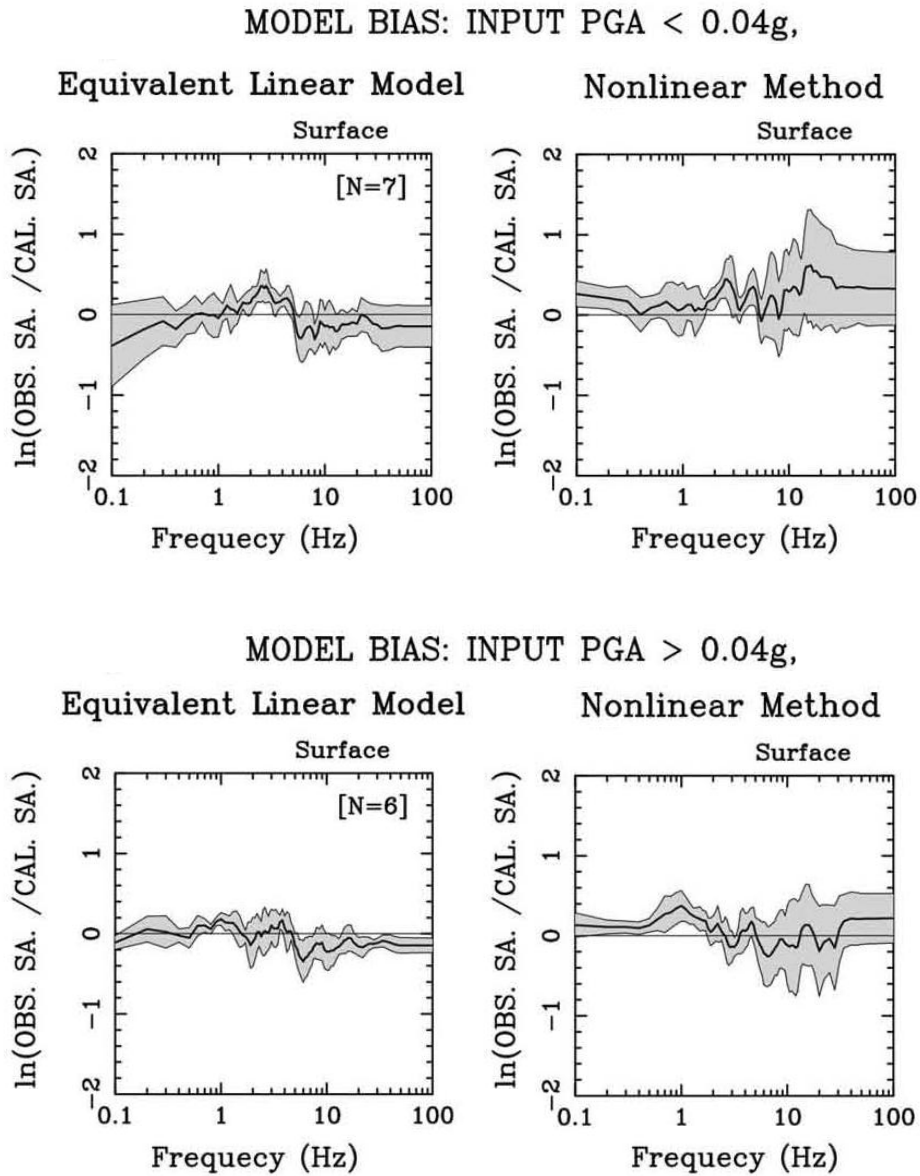


Figure 3.6: Bias in the response as obtained by Lee *et al.* (2006). Positive bias corresponds to underprediction; negative to overprediction

Based on the findings from Lee *et al.* (2006), it can be stated that EQL performed relatively well for both low and high intensity input motions, while NL method shows some underprediction of high frequency components when low

intensity shaking is input to the model. The latter remark is most probably due to the utilization of frequency-dependent formulation of Rayleigh damping.

3.3.3. Stewart *et al.*, 2008

In their comprehensive study, Stewart *et al.* (2008) evaluated nonlinear and equivalent-linear analyses against empirical data from vertical arrays. Stewart *et al.* (2008) performed NL analyses using a variety of different numerical codes (*DeepSoil*, *D-MOD_2*, *OpenSees*, *SUMDES* and *TESS*), while the EQL analyses used *SHAKE2004*. The comparisons against the vertical array data were based on recordings from: (i) La Cienega ($M_w = 4.2$ and $R = 2.7$ km event), (ii) KGW02 Kik-Net ($M_w = 6.4$ and $R = 93$ km event), and (iii) Lotung arrays ($M_w = 6.5$ and $R = 66$ km event). Similar to the Lee *et al.* (2006) study, the researchers defined the residual ($Re(T)$) between the observed and computed surface responses as:

$$Re(T) = \ln S_a^{obs}(T) - \ln S_a^{calc}(T) \quad (3.2)$$

where $S_a^{obs}(T)$ and $S_a^{calc}(T)$ are the observed and computed spectral acceleration, respectively.

The evaluation of the predictive results against observed responses from vertical arrays showed that both EQL and NL models lead to similar responses (FIGURE 3.7). A somehow systematic underprediction of the surficial spectral accelerations at low periods (high frequencies) was observed. More specifically, Stewart *et al.* (2008) showed that, for the La Cienega array, *DeepSoil* and *D-MOD_2* underpredicted the response at periods between 0.07 s and 0.12 s. Similarly, for the KWH02 site, all codes underpredicted the observations at $T < 0.3$ s, while for the Lotung array the underprediction was seen at periods less than 0.7 s.

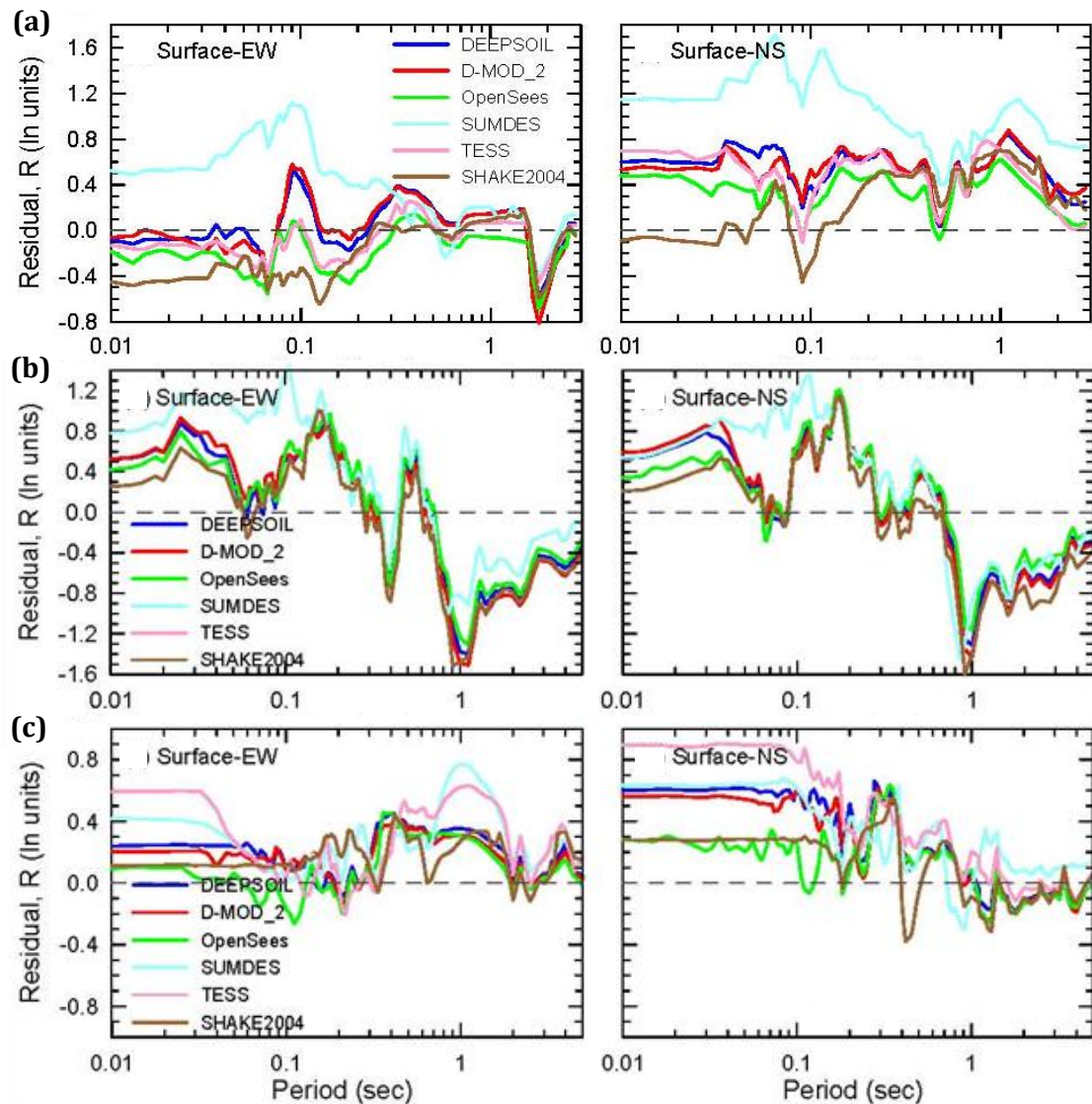


Figure 3.7: Acceleration response spectra for data and simulation results compared through prediction residuals: (a) La Cienega, (b) KGWH02, and (c) Lotung. Positive residual corresponds to underprediction; negative to overprediction (from Stewart *et al.*, 2008)

3.3.4. Kottke, 2010

Kottke (2010) evaluated one-dimensional site response methodologies using instrumented borehole array sites. Equivalent linear (EQL) and nonlinear (NL) analyses were performed, utilizing the computer programs *Strata* and *DeepSoil*, respectively. Evaluation of EQL and NL methods was based on observations from: (i) Lotung, (ii) La Cienaga, and (iii) KSRH10 Kik-Net arrays. Proper modeling of the response at vertical array sites involved the identification of the most representative borehole wavefield. Kottke (2010) concluded that all simulations provided similar results (*FIGURE 3.8*), and their performance greatly depended on the individual site characteristics and the suitability of the one-dimensional wave propagation assumption.

3.3.5. Kaklamanos *et al.*, 2013

Kaklamanos *et al.* (2013) utilized recordings at 100 Kik-Net arrays to assess the accuracy and precision of linear (LE) and equivalent-linear (EQL) one-dimensional site response analysis. The researchers performed analyses using 3720 ground motions with varying input intensities. The main goal of their study was the investigation of the parameters that can serve as the best indicators of the point where the site response methodologies fail to accurately predict the response. Kaklamanos *et al.* (2013) concluded that the level of induced shear strain, as quantified by the value of the maximum shear strain, γ_{max} , serves as the most appropriate measure to evaluate the period dependence of the performance of the theoretical models. Based on their results, the authors provided recommendations regarding the point where the site response models start to break down (*FIGURE 3.9*). Both EQL and LE analyses can efficiently predict the response at spectral periods

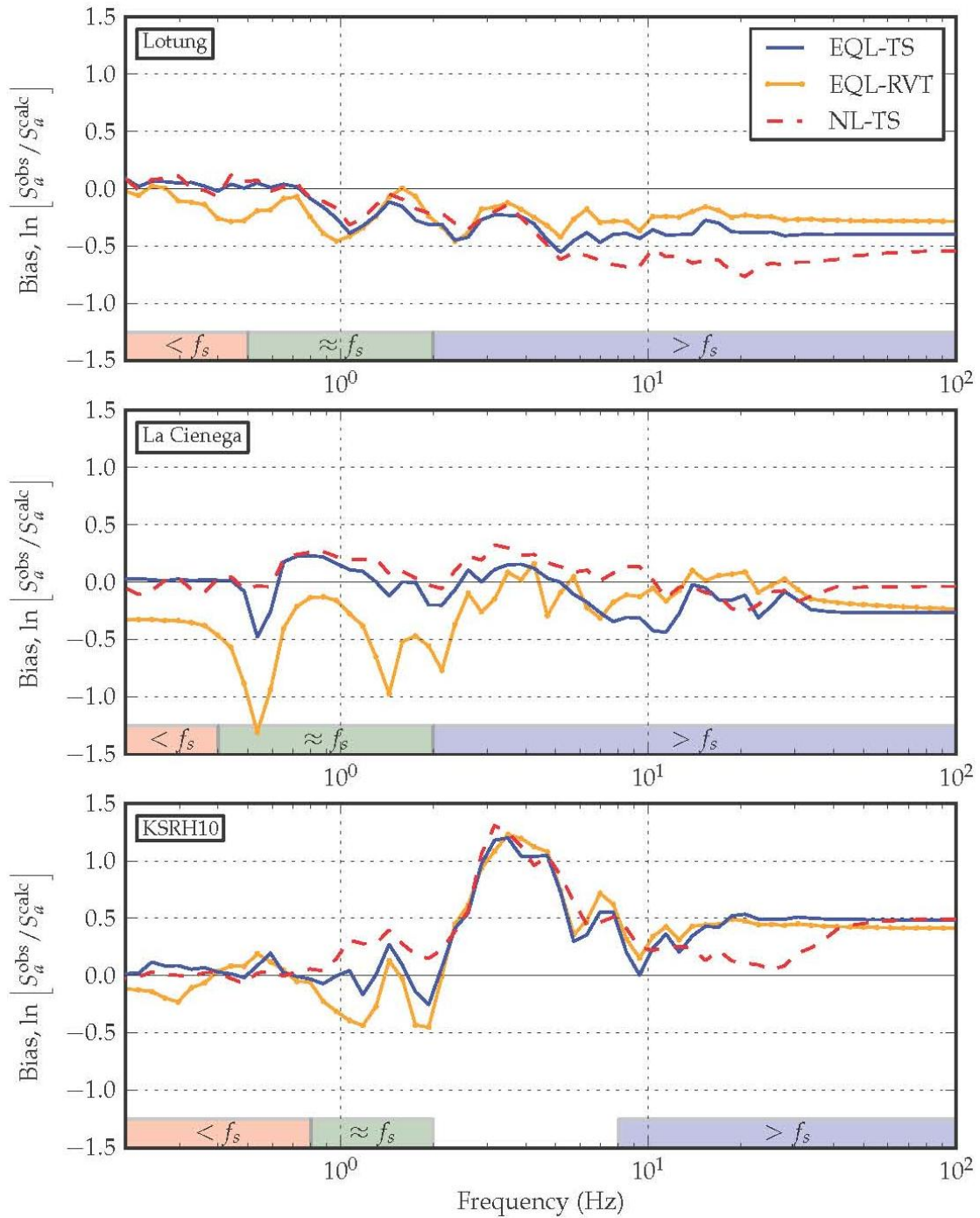


Figure 3.8: Prediction residuals for different site response methodologies. Positive residual shows underprediction; negative residual corresponds to overprediction (from Kottke, 2010)

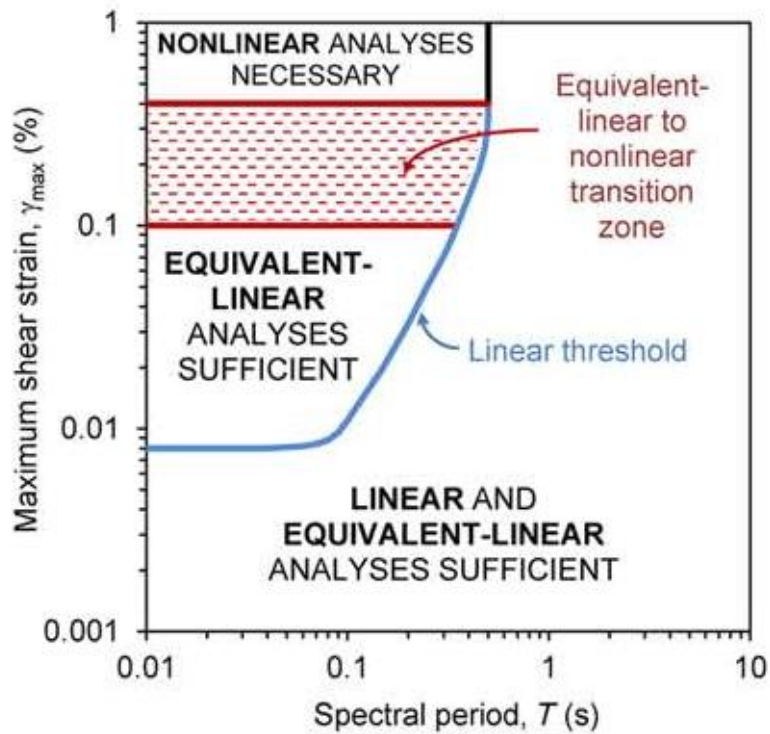


Figure 3.9: Illustration of the period dependence of the accuracy of LE and EQL analysis with respect to the maximum calculated shear strain, γ_{max} (from Kaklamanos *et al.*, 2013)

greater than about 0.5 s, independent of the level of the shaking. However, at periods less than 0.5 s, linear-elastic analysis overpredicts the response at strains beyond 0.01 %, while EQL strongly underpredicts the observations at strains greater than approximately 0.4 % (FIGURE 3.9). Nonlinear analyses were not performed by Kaklamanos *et al.* (2013) and therefore they assumed that nonlinear analysis would be necessary when the EQL approach becomes inaccurate.

3.4. Summary of Observations

Collectively presented, some of the major observations arising from the verification studies listed in TABLES 3.1 and 3.2 can be summarized as:

- At high loading levels ($PGA > 0.4 g$), high frequency amplification ($> 10 Hz$) is larger using NL analysis than using EQL analysis (Silva *et al.*, 2000).
- For soft soils, nonlinear codes give smaller amplification factors than EQL, for high levels of shaking (Silva *et al.*, 2000).
- For soft sites (low site frequency, f_s), a frequency independent formulation of the Rayleigh damping in fully nonlinear analyses is more effective (Kottke, 2010).
- At low intensity motions, NL models overdamp the high frequencies due to numerical errors associated with the time stepping method (Kottke, 2010).
- At moderate to high intensity motions, NL models give greater high frequency amplification factors than EQL due to instantaneous changes in stiffness upon reversal, as well as due to the overdamping of high frequencies in EQL analyses at large strains (Kottke, 2010).
- For linear elastic (LE) conditions or at low intensity motions, the full Rayleigh damping formulation is more effective (Stewart *et al.*, 2008).
- All existing NL codes seem to underpredict the response at high frequencies (Stewart *et al.*, 2008).
- Variability arising from different simulation NL codes (Kwok *et al.*, 2006)
- Model (associated with different NL codes) variability significant at low periods (high frequencies), where the differences in Rayleigh damping formulation play an important role (Kwok *et al.*, 2006).
- Differences in the predictions by different users of a single code (Kwok *et al.*, 2006).

- Equivalent-linear method with frequency dependent material properties (EQL-FD) shows higher response at high frequencies compared to both EQL and NL models (Kwak *et al.*, 2008).

3.5. Summary

Evaluation of one-dimensional site response methods requires the understanding of the modeling and algorithmic details encapsulated within their framework and the manner by which these details affect the performance of the theoretical models. In the past, several researchers have dealt with either the examination of the relative response characteristics of site response methodologies, or with the direct evaluation of the suitability and performance of these theoretical models against recordings from instrumented borehole arrays. A list of several such verification research efforts is illustrated in *TABLES 3.1* and *3.2*. The observations arising from these studies offer valuable contribution in providing explanations and evaluating the consistency of the predictive results of the present study.

Comparative studies between the conventional EQL algorithm and various different fully nonlinear numerical models showed that, in general, they yield similar responses, with the exception of great input intensities where EQL seems to produce lower response at low periods. Evaluation studies of EQL and NL numerical procedures against recorded responses from vertical arrays showed that a, somehow, systematic underprediction of the amplification at high frequencies from both theoretical models is observed. Moreover, EQL-FD algorithms, when compared with the responses from both the conventional equivalent-linear formulation and the fully nonlinear approach, provided higher response at high frequencies.

Chapter 4

Borehole Strong-Motion Arrays

4.1. Introduction

Geotechnical borehole arrays consist of vertically distributed, strong-motion accelerometers within the ground. These arrays have been installed in numerous locations around the globe. Borehole arrays provide critical information for a better understanding of the seismic response of soil and rock media under earthquake shaking. The continuously increasing number of strong-motion recordings from these arrays has become the driving force for more rigorous studies on the assumptions and accuracies of the numerical models commonly used to compute site response (e.g., Stewart *et al.*, 2008; Kottke, 2010; Kaklamanos *et al.*, 2013). Some of these studies were briefly discussed in [Chapter 3](#).

In this chapter, some of the existing instrumented vertical arrays are introduced and the selection of the borehole arrays and corresponding ground motions for the purposes of this study are discussed. Accordingly, the selected instrumented vertical arrays are described and, finally, the signal processing method applied to the recordings is presented.

4.2. Available Geotechnical Borehole Arrays

Over the past decades, the installation and monitoring of geotechnical borehole arrays has been constantly growing. Solely within the United States, Archuleta and Steidl (1998) and Elgamal *et al.* (2001) report more than 40 existing

downhole arrays. A more recent summary of existing borehole arrays within the United States and the world can be found in de Alba *et al.* (2006). The existing geotechnical arrays are divided into three categories (Steidl, 2006): (i) “Extensive”, (ii) “Moderate”, and (iii) “Surface Borehole Pairs”. “Extensive” arrays include at least four downhole sensors in addition to the surface accelerometer. “Moderate” vertical arrays refer to sites where two or three downhole sensors are installed, while “Surface Borehole Pair” arrays involve only two recording accelerometers. A list of instrumented sites in the U.S.A that fall into each one of these categories is shown in *TABLE 4.1*. In addition to the 40 + borehole arrays in the U.S.A., several other countries (e.g. Japan, Taiwan, Greece) have installed and operate borehole arrays. The large number of borehole arrays around the world provides important site response data for a variety of soil conditions and over a large range of input intensities. *TABLE 4.2* presents five of the most comprehensive databases of borehole strong-motion array data. The level of detail in the site characterization strongly differs between arrays, ranging from simple boring logs with lithology and V_S and V_P measurements (e.g. NIED Kik-Net network, Japan), to more detailed geotechnical boring logs and measurements of site conditions (EUROSEISTEST database, Greece).

4.3. Site and Ground-Motion Selection

For the purposes of the present study, the NIED Kik-Net database in Japan was considered as the major resource for vertical array data. The Kiban-Kyoshin (NIED Kik-Net) network is one of the largest sources of strong motion recordings from borehole arrays. It consists of more than 650 sites where surface-borehole pairs of sensors are available. For each site, shear and compression wave velocity profiles are provided along with basic soil and rock descriptions. Despite the fact

Table 4.1: Categorization of geotechnical strong-motion arrays in the U.S.A (information from Steidl, 2006)

Extensive Arrays (4+ borehole sensors)			Moderate Arrays (2-3 borehole sensors)			Surface Borehole Pair (1 borehole sensor)		
Array	Location	Agency	Array	Location	Agency	Array	Location	Agency
Bessie Charmichael School	Bay Area, Northern California	USGS	Carquinez Bridge	Northern California	CGS/CSMIP/Caltrans	Central Fire Station	San Bernardino, South California	USGS/UCSB
Borrego Valley	Southern California	UCSB	Corona Array	Southern California	CGS/CSMIP/Caltrans	Cerritos College	Southern California	USBS
Delaney Park	Anchorage, AK	ANSS/USGS/UAF	Foster City	San Matteo Bridge, Northern California	CGS/CSMIP/Caltrans	Pacific Park Plaza	Emeryville, Northern California	USGS
Embarcadero Plaza	Bay Area, Northern California	USGS	Half Moon Bay	Tunitas, Northern California	CGS/CSMIP/Caltrans	Griffith Park	Southern California	UCSB/SCEC
Eureka Array	Northern California	CGS/CSMIP/Caltrans	La Cienega Array	Los Angeles, Southern California	CGS/CSMIP/Caltrans	Jensen Filtration Plant	Southern California	UCSB/SCEC/USGS
Garner Valley	Southern California	UCSB/NEES	Long Beach Water District	Southern California	UCSB/SCEC	Kentucky Bend	KY, Central US	University of Kentucky
Hayward	San Matteo Bridge, Northern California	CGS/CSMIP/Caltrans	Northeastern University	Boston, Eastern US	Northeastern University	Mira Catalina School	Southern California	UCSB/SCEC
Hollister Observatory	Northern California	UCSB	Olmstead Locks and Dam	IL, Central US	University of Kentucky/ACOE	Obregon Park	Los Angeles, Southern California	CGS/CSMIP/UCSB
Levi Plaza	Northern California	USGS	Paducah	Turkey Flat, Central California	CGS/CSMIP/Caltrans	Ridgely	TN, Central US	University of Kentucky
Meloland Array/El Centro	Southern California	CGS/CSMIP/Caltrans	Rohnert Park	Northern California	CGS/CSMIP/Caltrans	Rinaldi Substation	Southern California	UCSB/SCEC
San Diego Coronado Bridge	Southern California	CGS/CSMIP/Caltrans	San Francisco Bay Bridge	Northern California	CGS/CSMIP/Caltrans	Stone Canyon	Southern California	UCSB/SCEC
Treasure Island NGES site	Northern California	CGS/CSMIP/Caltrans	Sassafras Ridge	KY, Central US	University of Kentucky			
Vincent Thomas Array	Southern California	CGS/CSMIP/Caltrans	University of California	Riverside, Southern California	UC/SCEC			
Wildlife Liquefaction Array	Southern California	UCSB/NEES	Winfield Scott School	Bay Area, Northern California	USGS			

Table 4.2: Borehole array databases

Database	Location	Number of Stations	Agency	Reference
EUROSEISTEST	Mygdonian basin, Northern Greece	19	Aristotle University of Thessaloniki	http://euroseisdb.civil.auth.gr/
NIED Kiban- Kyoshin	Japan	650+	National Research Institute for Earth Science and Disaster Prevention	http://www.kik.bosai.go.jp/
NEES @ UCSB	California/Alaska	8	University of California Santa Barbara	http://nees.ucsb.edu/data/
Center for Engineering Strong- Motion Data	California	36	USGS/CGS/ANSS	http://strongmotioncenter.org/
Strong Motion and Mobil Seismic Networks	Taiwan	131	Institute of Earth Sciences, Academia Sinica	http://www.earth.sinica.edu.tw/~smdmc

that the site characterization is not extensive, the breadth and number of strong motion recordings is large and diverse, something that makes the database suitable for the evaluation of site response methodologies. In addition to the sites selected from the Kik-Net database, recordings from two additional vertical arrays (i.e., La Cienega and Lotung arrays) are also included in this study to supplement the observations at relatively softer sites.

The selection of borehole arrays was based on the shear wave velocity characteristics and the availability of ground motions at each site. Towards this effort, site characterization information and strong motion data obtained through the KiK-Net database were processed and classified. For each site in the database, information was compiled regarding: (1) the time-averaged shear wave velocity over the top 30 m (V_{s30}) of the array, (2) the number of recorded motions, (3) the

peak acceleration of each motion recorded at the base sensor (PGA_{base}), and (4) the depth to the downhole sensor. The distribution of these parameters with respect to the V_{s30} for each site is illustrated in *FIGURE 4.1*. Considering these data, the majority of the Kik-Net database falls between V_{s30} of 200 m/s and 800 m/s and most of these sites have depths to downhole sensor of about 100 m to 200 m . Moreover, most of the sites include fewer than 100 recorded motions, the latter being typically characterized by PGA_{base} less than 0.1 g . *FIGURE 4.2* shows the distribution of sites relative to their NEHRP site classification and the distribution of recordings relative to their PGA_{base} . These data show that the majority of sites are Site Class C ($V_{s30} = 360 - 750 m/s$) and, again, the majority of the recordings have $PGA_{base} < 0.1 g$.

Specific factors for site selection were considered in order to isolate appropriate Kik-Net sites for further investigation. These factors included:

- The stiffness of the site based on the available in-situ shear wave velocity measurements
- The number of recorded motions
- The range of PGA_{base} values
- The availability of high intensity motions as recorded at the downhole sensor

Sites characterized by low V_{s30} were preferred due to the fact that these sites typically exhibit strong nonlinearity during intense ground shaking. Thus, only sites with V_{s30} less than 400 m/s were considered. Sites with such a characteristic along with the availability of high intensity recordings represent the ideal combination. Therefore, the low velocity sites were then subjected to the criterion of having at least one recorded motion at their base sensor with PGA_{base} greater than 0.15 g .

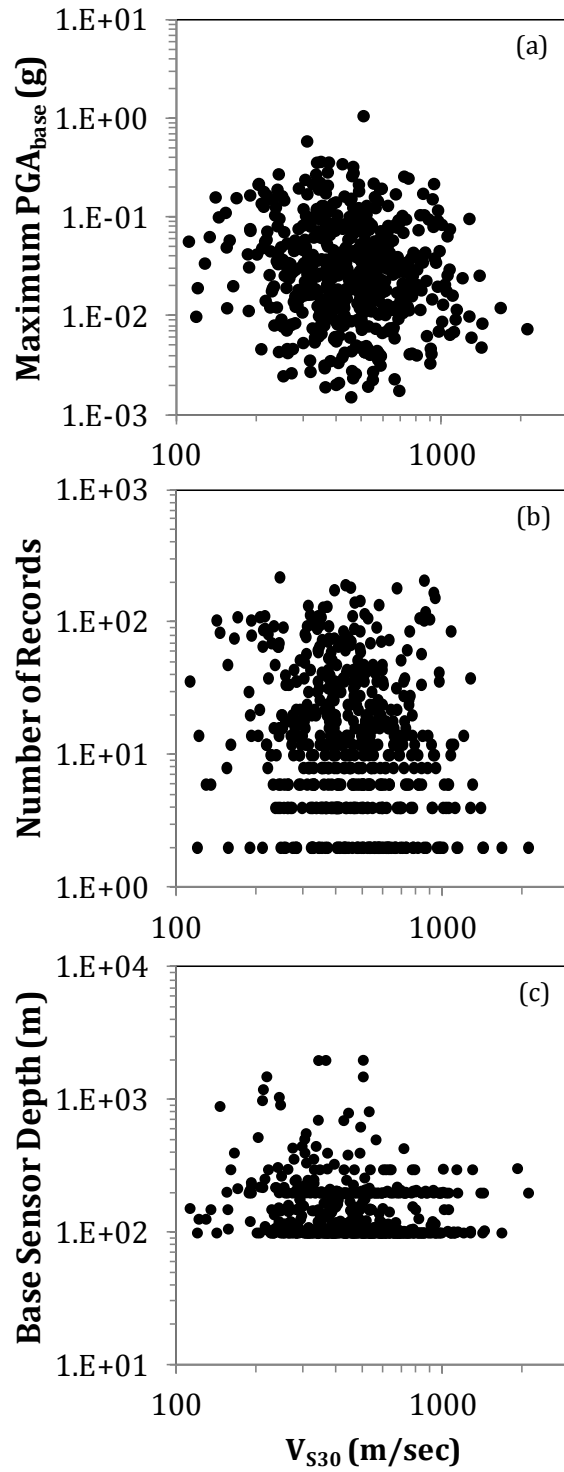


Figure 4.1: Distribution of (a) maximum PGA_{base} , (b) number of records, and (c) depth to downhole sensor with respect to V_{s30} , for the Kik-Net vertical arrays

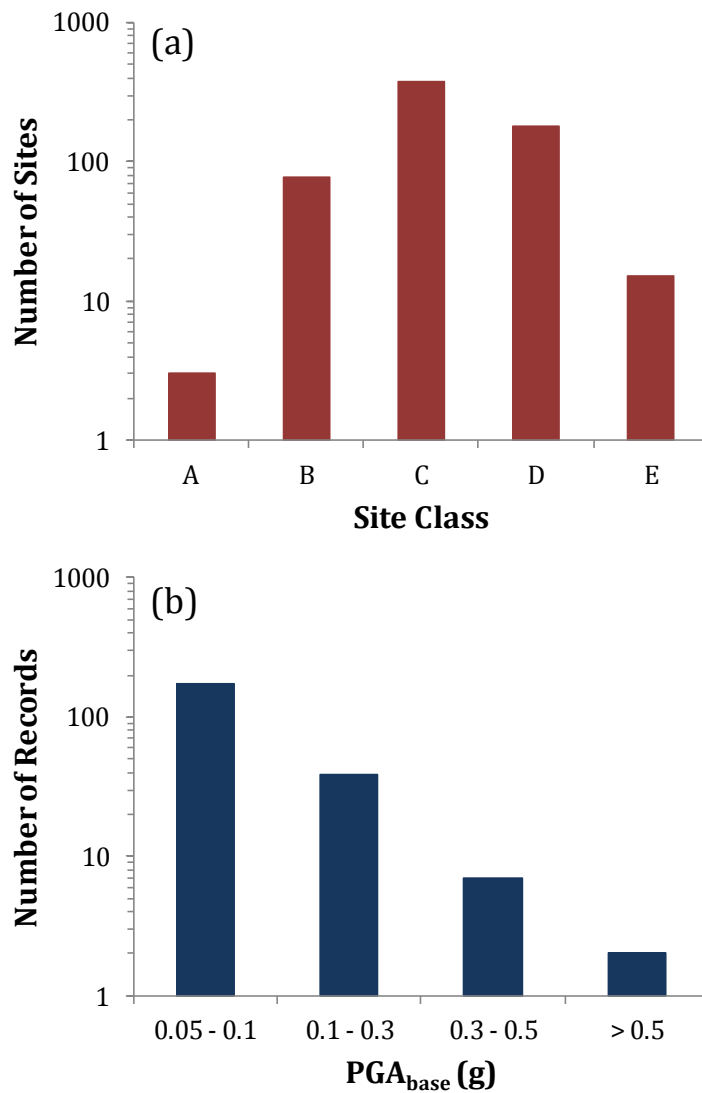


Figure 4.2: (a) Number of sites per NEHRP site classification, and (b) number of records per PGA_{base} range

Using these criteria, eleven KiK-Net sites were identified to be most suitable for this study. The selected sites are presented in TABLES 4.3 through 4.5, in terms of the general site information such as site name, latitude/longitude, altitude, and geomorphic characteristics as determined through *Google Earth 7.1.2.2041* (Google Inc., 2013) (TABLE 4.3); specific characteristics of the site conditions such as V_{s30} , the

minimum shear wave velocity in the profile ($V_{s,min}$), the shear wave velocity at the base sensor ($V_{s,base}$) and the downhole sensor depth (TABLE 4.4); and the number of the recorded motions for each PGA_{base} range (TABLE 4.5). As it can be seen in TABLE 4.3, the selected Kik-Net sites are located in various prefectures of Japan and many are installed in relatively long and wide valleys. This geomorphic characteristic may lead to the avoidance of topographic or basin wave propagation effects, making the one-dimensional assumption more theoretically valid. Nonetheless, the FKSH19 site and, particularly, the TTRH02 site are located at a relatively higher altitude ($> 400\text{ m}$) on inclined, sloping ground. For these sites, it should be noted that topographic effects may influence the results. IBRH13 site is also located at high altitude (505 m), but the ground inclination seems to be minimal.

To supplement this study in terms of softer sites with smaller $V_{s,30}$, we also made use of two additional vertical borehole arrays, namely the La Cienega and Lotung arrays. Relevant information on these arrays can also be found in TABLES 4.4 and 4.5. The La Cienega array is located in Los Angeles, California and was constructed as part of the Resolution Site Response Issues from the Northridge Earthquake (ROSRINE) project. It consists of instrumentation at depths of 0, 18, 100, and 252 m. The shear wave velocity profile at the site indicates a $V_{s,30}$ value of 250 m/s. As part of the site characterization effort, soil samples were taken every 6 m of depth and laboratory tests were conducted on selected samples to measure the variation in shear-modulus and damping with shear strain. The site has recorded one motion with PGA_{base} between 0.05 g and 0.2 g, and one motion with $PGA_{base} > 0.2\text{ g}$. The Lotung array was installed in Taiwan with the contribution of the Electric Power Research Institute (EPRI) and the Taiwan Power Company (TPC). It is instrumented with accelerometers at depths of 0, 6, 11, 17 and 47 m. Measure-

Table 4.3: Site location, surface altitude, approximate valley length and width for the selected sites from Kik-Net database

Site code	Site Name	Latitude	Longitude	Prefecture	Surface Altitude (m)	Approx. Valley Length (km)	Approx. Valley Width (km)
<i>FKSH19**</i>	MIYAKOJI	37.4672	140.7261	FUKUSHIMA	510	N/A	N/A
<i>FKSH20</i>	NAMIE	37.4881	140.9906	FUKUSHIMA	12	10.5	3.7
<i>IBRH11</i>	IWASE	36.3669	140.1434	IBARAKI	67	7.1	7.5
<i>IBRH13</i>	TAKAHAGI	36.7924	140.5784	IBARAKI	505	N/A	N/A
51	<i>IWTH26</i>	38.9661	141.0047	IWATE	125	7.8	1.5
	<i>KSRH06</i>	43.2175	144.4325	HOKKAIDO	30	6.1	2.4
	<i>KSRH07</i>	43.1333	144.3314	HOKKAIDO	38	-	-
	<i>KSRH10</i>	43.2058	145.1208	HOKKAIDO	31	-	-
	<i>MYGH05</i>	38.5764	140.7839	MIYAGI	59	15	6.9
	<i>MYGH10</i>	37.9381	140.8958	MIYAGI	18	1.4	0.6
	<i>TTRH02**</i>	35.2281	133.3936	TOTTORI	410	N/A	N/A

Notes: **Probable topographic effects

Table 4.4: Site characteristics and downhole sensor depth for the selected borehole arrays

Site	Downhole Sensor Depth (m)	V_{S30} (m/s)	$V_{S,min}$ (m/s)	$V_{S,"base"}$ (m/s)	z_{1000} (m)	T_{site} (sec)
FKSH19	100	338	170	3060	> 40	0.32
FKSH20	109	350	350	610	> 60	0.72
IBRH11	103	242	130	2100	30	0.37
IBRH13	100	335	170	3000	34	0.34
IWTH26	108	371	130	680	> 36	0.47
KSRH06	237	326	90	660	> 170	1.55
KSRH07	222	204	100	510	> 82	1.51
KSRH10	255	212	190	1700	36	0.63
MYGH05	337	305	120	1080	260	1.79
MYGH10	205	348	110	770	> 114	1.06
TTRH02	100	310	210	790	> 42	0.20
La Cienega	265	250	140	644	> 249	1.86
Lotung	50	184	114	256	> 50	0.80

ments of V_S and modulus reduction and damping curves are reported in EPRI (1993). The $V_{S,30}$ of the site is 184 m/s and it has recorded 6 motions with PGA_{base} between 0.05 g and 0.2 g, and no motions with $PGA_{base} > 0.2 g$.

In *FIGURE 4.3*, the V_S profiles of the 13 selected sites are presented, as reported by the Kik-Net database and by Kottke (2010) for the La Cienega and Lotung sites. The sites are separated into three groups in *FIGURE 4.5* based on the depth of the borehole sensor and the presence of an impedance contrast within the profile. Specifically, the three groups considered are:

Table 4.5: Number of recordings per PGA_{base} range

Site	< 0.05 g	0.05 g - 0.20 g	> 0.20 g
FKSH19	132	1	1
FKSH20	41	10	1
IBRH11	202	1	1
IBRH13	54	16	2
IWTH26	22	6	2
KSRH06	40	6	-
KSRH07	36	-	2
KSRH10	30	4	-
MYGH05	13	13	1
MYGH10	83	20	1
TTRH02	13	1	2
La Cienega	6	1	1
Lotung	10	6	-

- Group 1: Borehole sensor at depth ≤ 100 m, with no significant impedance contrast within the profile
- Group 2: Significant impedance contrast present within the profile
- Group 3: Borehole sensor at depth > 200 m, with no significant impedance contrast within the profile

The $V_{S,30}$ for the 13 sites ranges from 184 m/s to 371 m/s (TABLE 4.4). The V_S profiles for the Kik-Net sites were derived from surface-source downhole-receiver logging (Thompson *et al.*, 2012), and the reported profiles from NIED were proces-

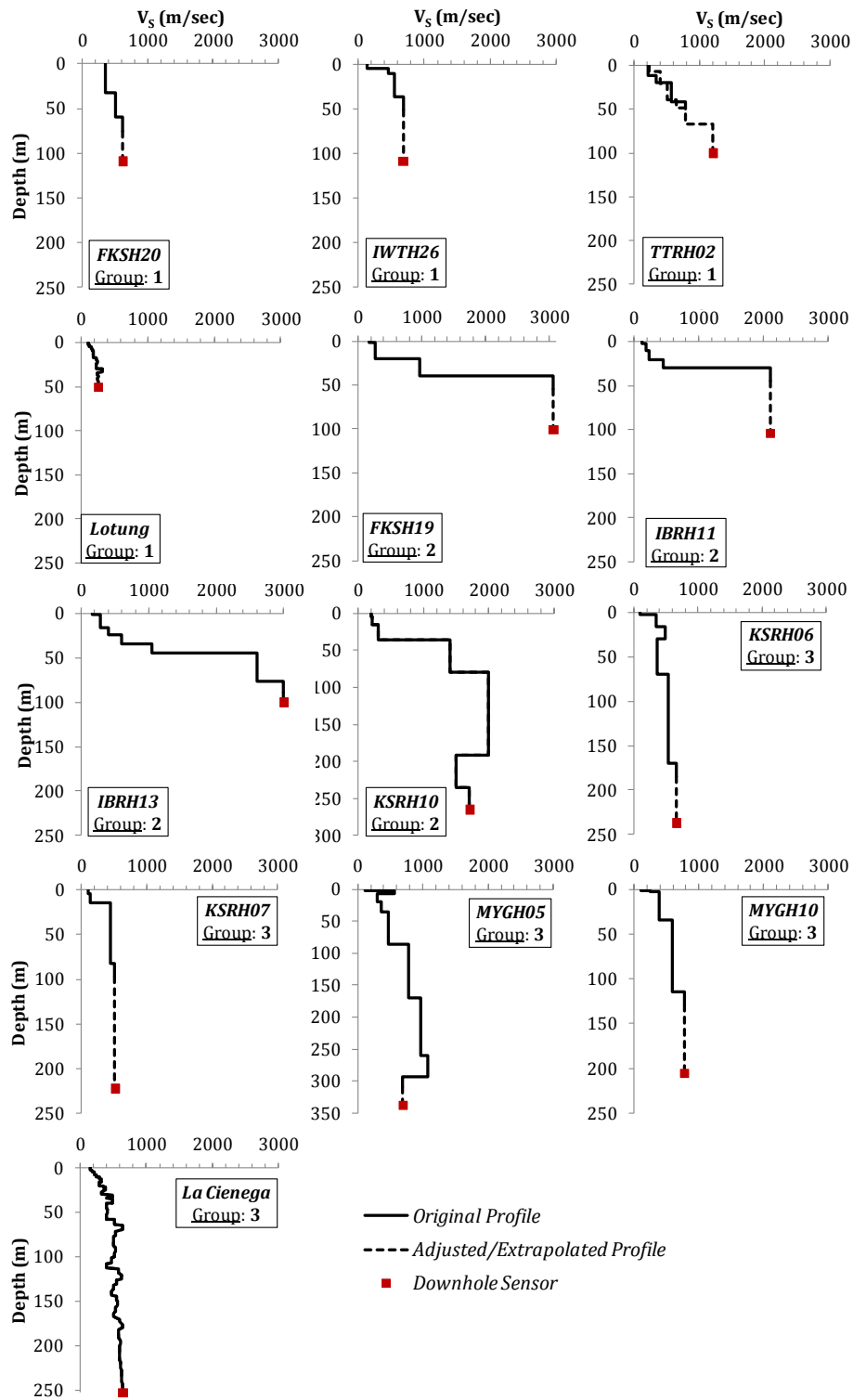


Figure 4.3: Shear wave (V_s) profiles of the considered borehole arrays

sed to represent layered media. Because the V_S profiles reported in the NIED Kik-Net data files often do not extend to the depth where the downhole sensor is located, extrapolation of the measured V_S profile was required.

4.4. Material Property Characterization of the Selected Sites

Modeling of the selected borehole arrays for the performance of one-dimensional site response analysis requires the assignment of specific material properties to each one of the soil layers comprising the sites. In addition, the shear wave velocity profile, the material properties consist of the unit weight (γ_t), and the nonlinear material curves such as the variation of shear modulus (G/G_{max}) and damping (D) with shear strain. It should be mentioned that for most of the sites, and especially the sites retrieved from Kik-Net database, the available information on site-specific material characteristics is limited. Therefore, informed assumptions had to be made concerning several characteristics.

The assigned unit weight (γ_t) distributions with depth for all selected sites are presented in *FIGURE 4.4*. Apart from the La Cienega and Lotung sites, the information depicted in *FIGURE 4.4* is largely a product of assumptions, since the Kik-Net database does not provide any information on unit weight. Nevertheless, the unit weight value assigned to each soil layer was estimated based on the corresponding value of the shear wave velocity (V_S) and the depth of the associated layer. That is, materials closer to the ground surface characterized by low shear wave velocity values were given low unit weight values. Similarly, soil layers at greater depths having larger V_S values were given greater values of γ_t . Given the fact that the results of site response analysis are not very sensitive to the value of γ_t , it is believed that the estimations regarding the assigned unit weight distributions with

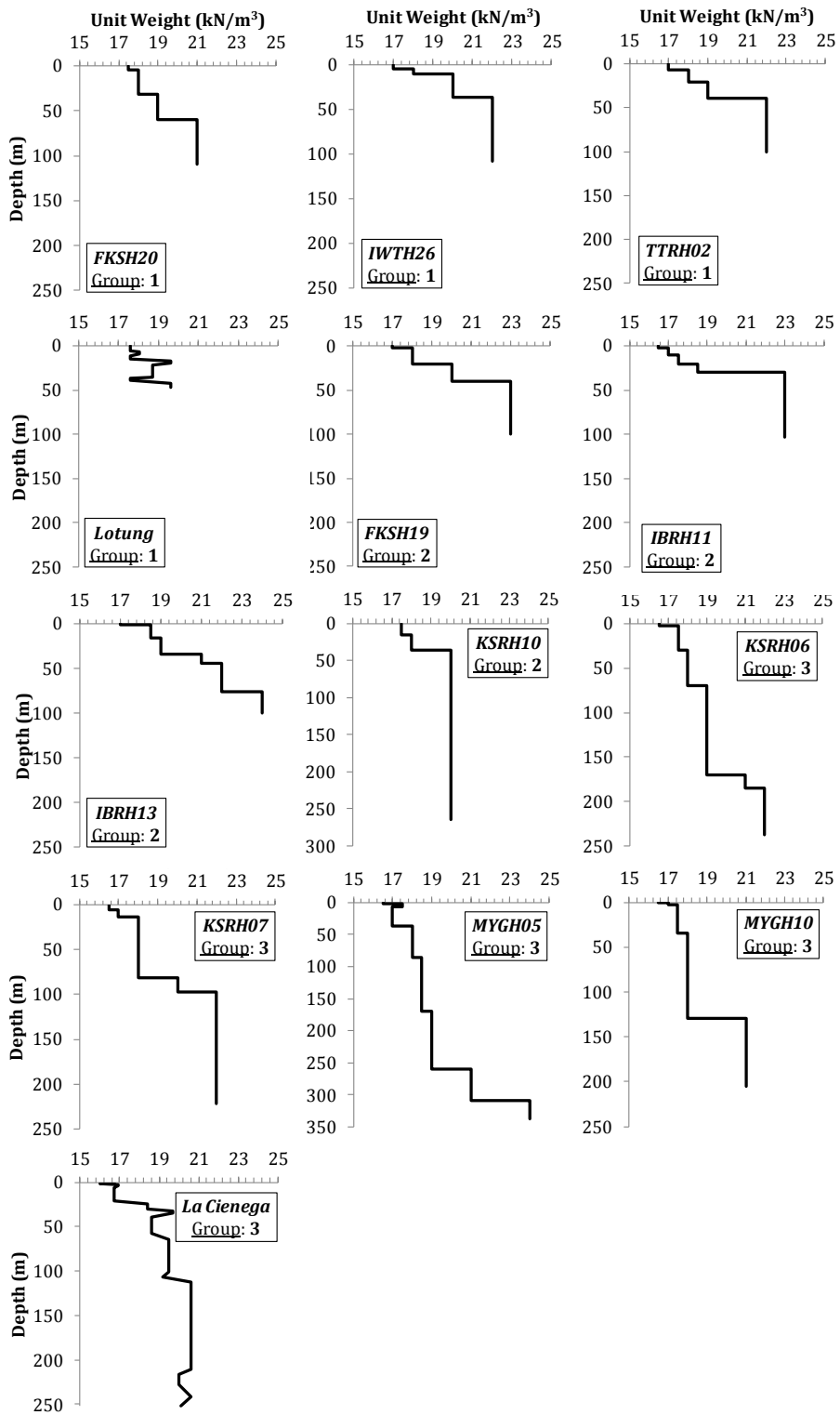


Figure 4.4: Unit Weight (γ_t) profiles of the considered borehole arrays

depth have a minor effect on our observations. For the La Cienega and Lotung arrays, the rigorously attained information on the unit weight distribution with depth is provided by ROSRINE (<http://gees.usc.edu/ROSRINE/>) and EPRI (1993), respectively.

With the exception of the Lotung array, which will be examined separately, the development of nonlinear material curves (i.e. $G/G_{max} - \log \gamma$ and $D - \log \gamma$ curves) at each site, was based on the Darendeli (2001) model. The generation of nonlinear curves based on Darendeli (2001) model requires the specification of several parameters characterizing each soil layer, such as the mean confining pressure (σ'_m) at the center of the layer, the plasticity index (PI), and the overconsolidation ratio (OCR). For the La Cienega array, the Darendeli (2001) model parameters developed by Kottke (2010) were utilized in the present study. Kottke (2010) developed Darendeli (2001) model parameters for the La Cienega site based on the laboratory-measured curves reported by ROSRINE (<http://gees.usc.edu/ROSRINE/>). FIGURES 4.5 and 4.6 illustrate the comparison between the laboratory test data and the nonlinear curves developed by Kottke (2010). TABLE 4.6 summarizes the utilized Darendeli (2001) model parameters developed based on the associated laboratory tests.

In the case of the Kik-Net arrays, the Darendeli (2001) model parameters had to be estimated based on information inferred from the provided simplified boring logs and the in-situ velocity measurements. For the calculation of the distribution of mean confining pressure (σ'_m) with depth, the identification of the level of the ground water table (GWT) was essential. The ground water table (GWT) levels were estimated based on information from the compression wave velocity (V_p) measurements provided in Kik-Net database. It was assumed that the GWT level at

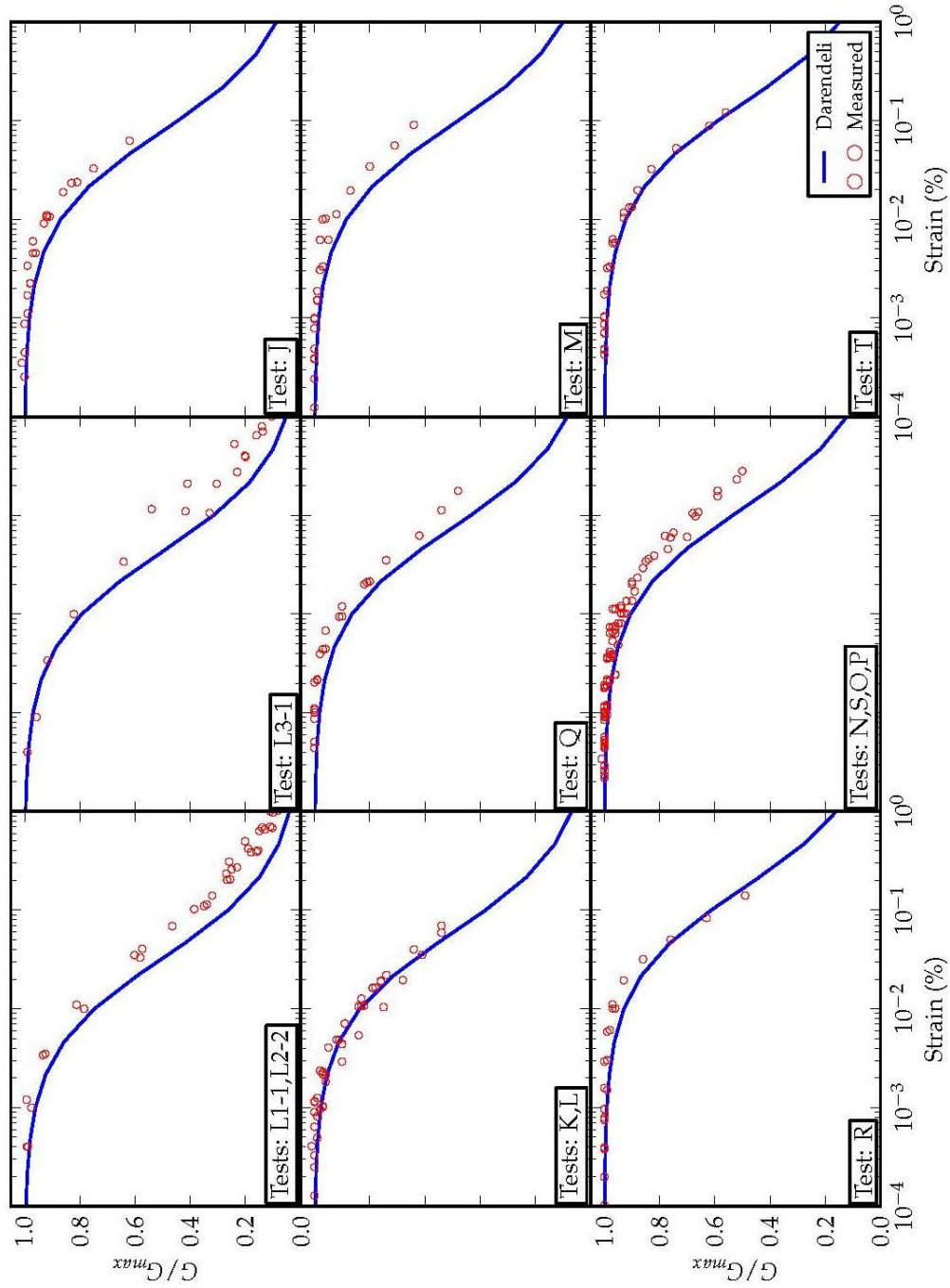


Figure 4.5: Comparison between the selected Darendeli (2001) shear-modulus reduction curves with data from laboratory testing (from Kottke, 2010)

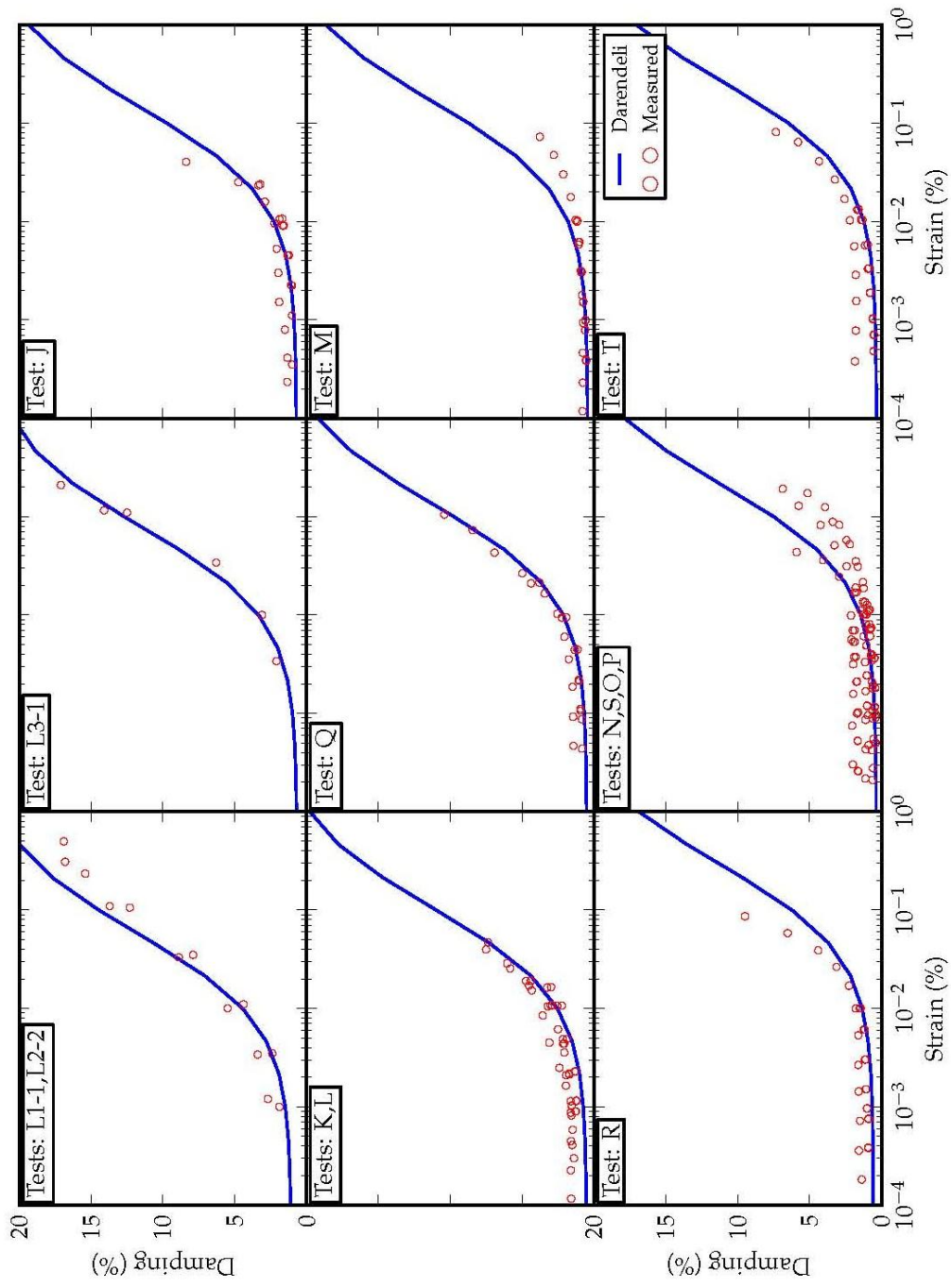


Figure 4.6: Comparison between the selected Darendeli (2001) damping curves with data from laboratory testing (from Kottke, 2010)

Table 4.6: Darendeli (2001) parameters for the La Cienega array (after Kottke, 2010)

Soil Type	Test ID (ROSRINE)	Unit Weight (kN/m ³)	Darendeli (2001) Parameters		
			σ'_m	PI	OCR
Fat Clay A		16.0	0.50	26	1.5
Silty Clay A	L-1-1;L2-1;L2-2	16.9	0.50	6	1
Silt A	L3-1	16.7	1.79	NP	1
Clay A	J	18.4	3.41	16	1
Silt B	K;L	19.7	4.34	NP	1
Silt C	Q	18.6	6.27	4	1
Silty Sand A	M	19.5	10.50	5	1
High Plasticity Silt	R	19.2	13.62	31	1
Silty Sand B	N;S;O;P	20.6	21.03	5	1
Clay B	T	20.0	29.66	10	1

each site was located at the depth where V_p reached approximately a threshold value of 1500 m/s . The latter represents the velocity at which P -waves propagate through water. FIGURE 4.7 presents the compression wave velocity (V_p) distribution with depth for all the selected boreholes, based on which the locations of the GWT levels were identified (TABLE 4.7). Based on the inference from the compression wave velocity values, it is observed that the estimated GWT levels range from 0 m (FKSH20 array) to 20 m (FKSH19 array).

Having established the unit weight distribution with depth and the level of the ground water table for all the Kik-Net sites, the mean confining pressure (σ'_m) at the center of each soil layer was computed assuming an earth pressure coefficient of $K_o = 0.5$. The resulting distributions of σ'_m with depth are shown in FIGURE 4.8. It should be noted that the σ'_m distribution shown for the La Cienega array in FIGURE 4.8 corresponds to the values reported by Kottke (2010).

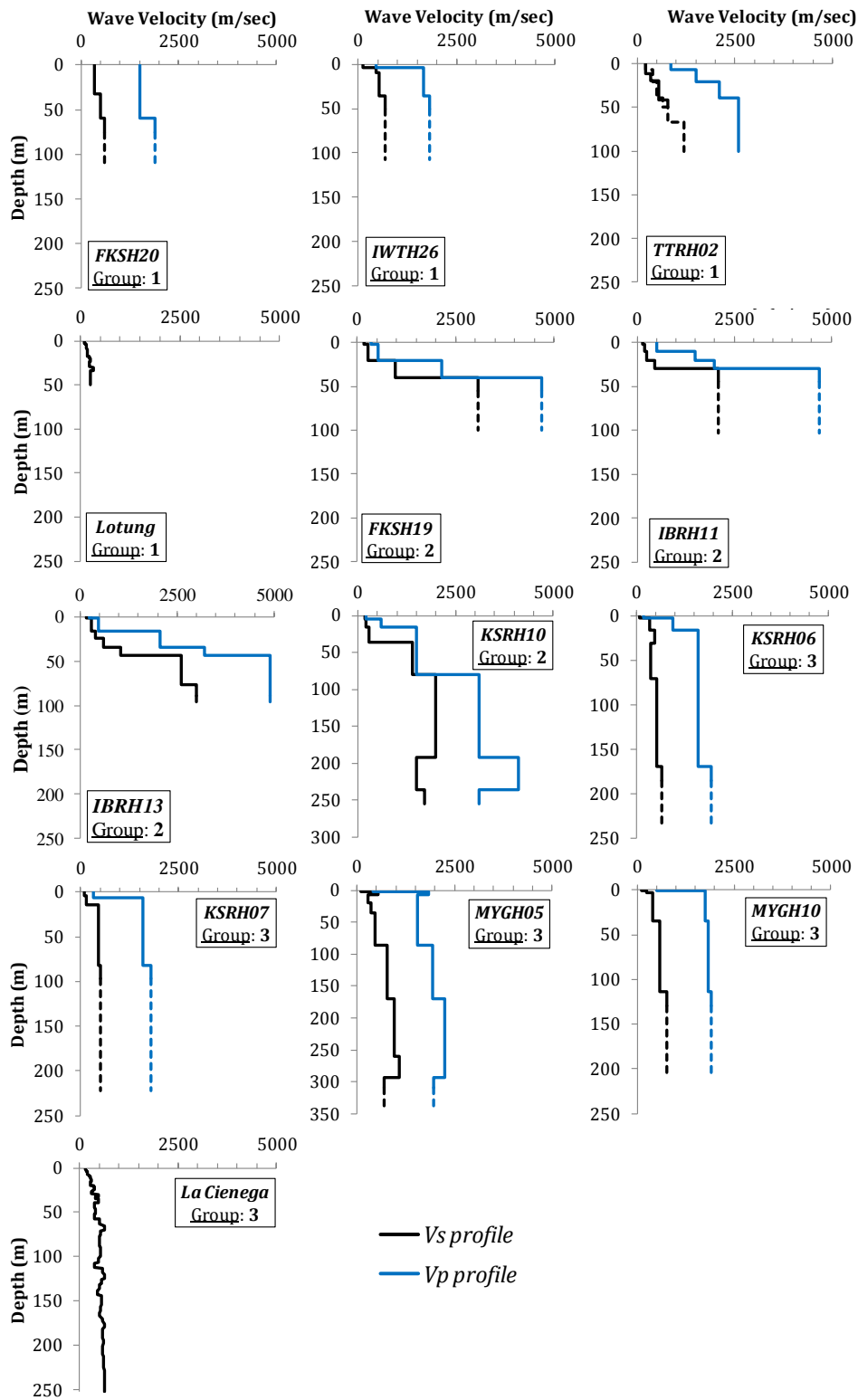


Figure 4.7: Shear (V_s) and Compression (V_p) wave velocity profiles

Table 4.7: Locations of ground water table (GWT)

Site	Location of GWT (m)	Site	Location of GWT (m)
FKSH19	20	KSRH07	6
FKSH20	0	KSRH10	16
IBRH11	10	MYGH05	2
IBRH13	16	MYGH10	1
IWTH26	4	TTRH02	6.5
KSRH06	16		

Plasticity index (PI) values were also assigned to each soil layer comprising each site. The site investigation performed at Kik-Net sites is insufficient to provide a solid basis for the estimation of the PI of the soil materials. Therefore, it was decided that, within the framework of the present study, PI would be assumed to be small and, in most cases, zero. A small value of PI , on the order of 5 – 10, was assigned only to surficial soil materials with relatively low shear wave velocity ($V_S < 200$ m/s). For rock layers at deeper strata characterized by V_S greater than 1000 m/s, more linear modulus reduction and damping curves were assigned using a reference strain (γ_r – shear strain where $G/G_{max} = 0.5$) equal to about 0.1 %. Finally, the last parameter required for the development of the $G/G_{max} - \log \gamma$ and $D - \log \gamma$ curves was the overconsolidation ratio (OCR). Due to the lack of any relevant information, OCR was set to unity for all soil layers and all sites.

As mentioned, an exception to the procedure described above for the determination of nonlinear material properties was the Lotung array. EPRI (1993) reported measurements on modulus reduction and damping curves (FIGURE 4.9) for the Lotung array. These curves, despite the alleged heterogeneity of the soil profile,

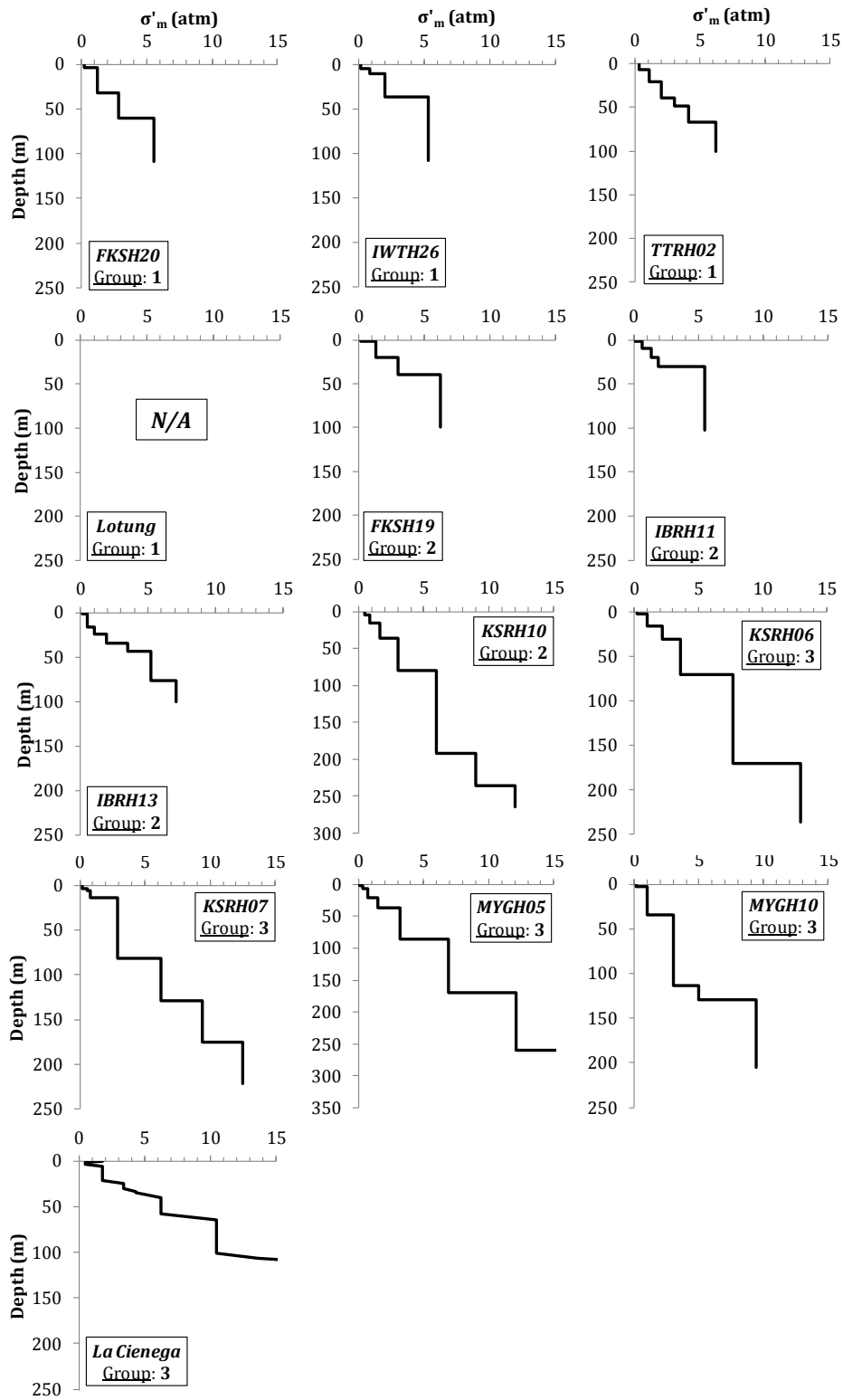


Figure 4.8: Mean confining pressure (σ'_m) variation with depth

show small differences between different materials. Consequently, only one set of nonlinear material properties is reported in the study by EPRI (1993). These curves are tabulated in *TABLE 4.8*, and are also used in the present study.

Table 4.8: Shear modulus reduction and damping ratio curves for the Lotung array (EPRI, 1993)

Shear Strain (%)	G/G_{\max}	Damping (%)
1.00E-04	1.00	1.00
3.14E-04	1.00	1.00
1.00E-03	1.00	1.10
3.16E-03	0.97	1.50
1.00E-02	0.87	2.80
3.16E-02	0.69	5.30
1.00E-01	0.42	10.50
3.16E-01	0.21	16.80
1.00E+00	0.09	22.10

4.5. Signal Processing of Recorded Motions

After the borehole arrays were selected, the corresponding horizontal (East-West and North-South) components of the recorded motions, both at the downhole sensor and the ground surface, were processed in a unified manner. For documentation purposes, information (e.g., date/time of recording, epicentral distance, magnitude) regarding the recorded ground motions that were considered within the framework of the present study can be found in [Appendix A.2](#).

The signal processing applied on the considered ground motions involved the application of a fifth-order Butterworth, time-domain, acausal filter with a low-pass frequency of 30 *Hz*, and a high-pass frequency of 0.15 *Hz*. The corresponding

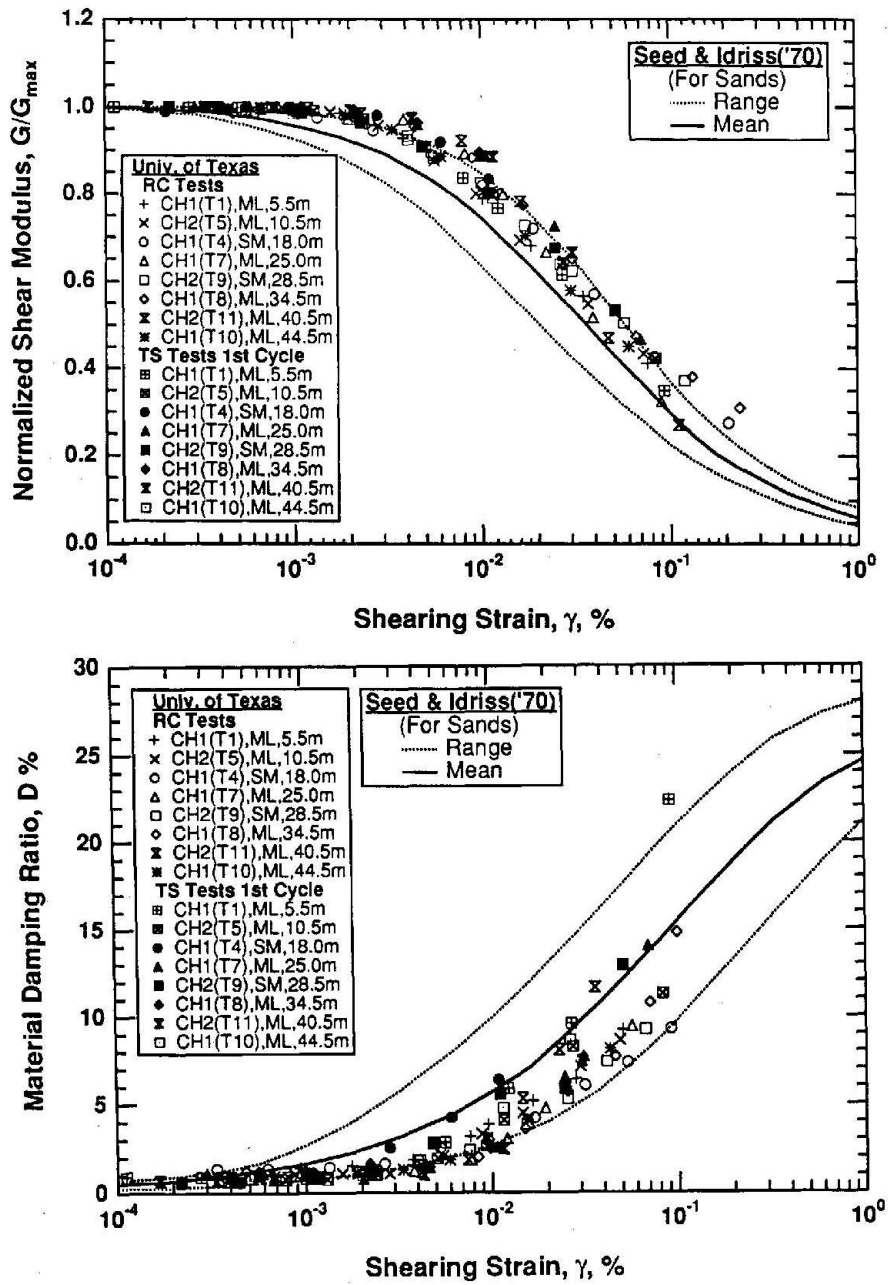


Figure 4.9: Nonlinear soil properties at Lotung site established through laboratory testing (from EPRI, 1993)

transfer function of the applied band-pass Butterworth filter is shown in *FIGURE 4.10*. Subsequently, the recordings were baseline corrected and post-processed, i.e. response and Fourier amplitude spectra were calculated. The obtained empirical transfer functions, i.e. the ratios of surface to “base” Fourier amplitude spectra, were smoothed using a logarithmic triangular window with a width equal to one-fifth of a decade.

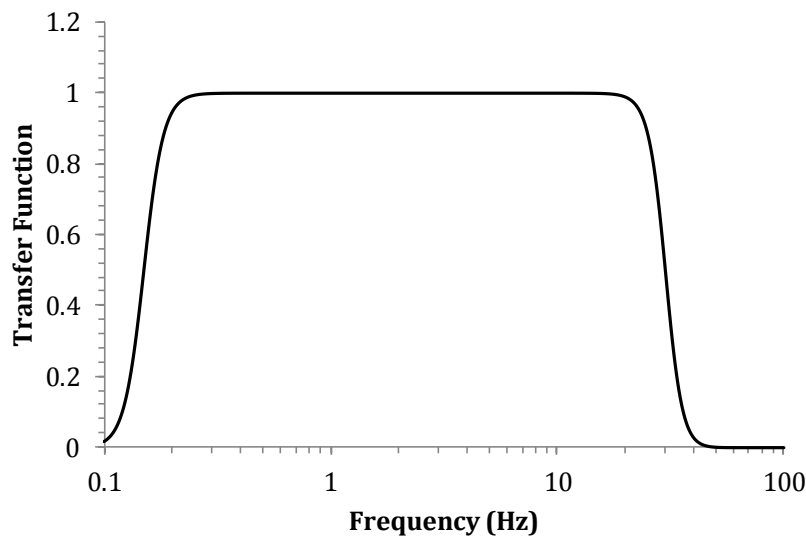


Figure 4.10: Transfer function of 5th order Butterworth filter applied to all recorded time histories

4.6. Summary

In this chapter, geotechnical strong-motion borehole arrays were introduced. Various available sources of vertical array data, both within the U.S.A and abroad, are presented. The NIED Kik-Net database in Japan was selected as the main source of borehole array data for this study because the database consists of more than 650 instrumented sites and a vast number of relevant recordings. Towards selecting appropriate Kik-Net borehole arrays for investigation, several factors were

considered: (i) the stiffness of the site, (ii) the number of the recorded motions, (iii) the range of PGA_{base} values, and (iv) the availability of high intensity motions. In addition to the identified Kik-Net sites, the La Cienega and Lotung vertical arrays also were included in this study because these sites have smaller $V_{S,30}$.

A total of thirteen borehole arrays (11 Kik-Net plus La Cienega and Lotung arrays) fulfilled the established criteria. The selected sites were presented through their site characteristics such as their $V_{S,30}$ and the depth to the downhole sensor. The $V_{S,30}$ for the 13 arrays ranges from 184 m/s to 371 m/s , while the depth to the downhole sensor varies from “shallow” ($\leq 100 m$) to “deep” ($> 200 m$). Some of the sites (FKSH19, IBRH11, IBRH13 and KSRH10), also, exhibit a strong impedance contrast within the top 50 m of the profile.

Finally, the signal processing applied to each record was described. The recorded motions from all sites are processed using a fifth-order Butterworth, time-domain, acausal filter with a low-pass frequency of 30 Hz , and a high-pass frequency of 0.15 Hz . The Fourier amplitude spectra of the recorded motions are used to compute an empirical transfer functions, i.e. the ratio of surface to base Fourier amplitude spectra. These transfer functions are smoothed using a logarithmic triangular window with a width equal to one-fifth of a decade.

Chapter 5

Assessment of Common Assumptions of One-Dimensional Site Response Analysis

5.1. Introduction

A proper evaluation of one-dimensional site response analysis using borehole arrays requires the validity of several common assumptions associated with the theoretical models. One-dimensional site response analysis, by default, involves simplifications regarding: (1) the actual wave propagation conditions at the base of the array, (2) the various small strain attenuation mechanisms encountered in the field, and (3) the directional effects of the passing seismic waves. Any erroneous assumptions regarding the modeling simplifications will inevitably result in exacerbated and inconsequential predictive results. Indeed, modeling errors may mask any potential numerical, algorithmical or theoretical inconsistencies and deficiencies of the site response model. Therefore, an assessment of the modeling assumptions should be performed before evaluating the model's performance when borehole-surface recordings are used as a benchmark.

The present chapter is focused on identifying: *i)* the wavefield assumption best simulating the base sensor boundary conditions at the 13 vertical arrays presented, *ii)* the small-strain damping values that should be used to account for additional in-situ small strain attenuation mechanisms, and *iii)* the validity of the assumed one-dimensionality of each one of the 13 borehole arrays.

5.2. Uncertainty in the Borehole Wavefield

In a one-dimensional layered model, the wave propagation pattern consists of an up-going (A) and a down-going (B) seismic wave (Kramer, 1996), as shown in *FIGURE 5.1*. These waves differ from each other within each layer, except for the free surface layer. At the surface, the zero-stress boundary condition results in perfect reflection of the up-going wave (A) and, thus, the two considered waves have equal amplitudes ($A = B$). Nonetheless, a certain degree of uncertainty exists in the actual wave propagation field (i.e., boundary condition) present at the depth of base recording within a borehole array. That is, the down-going (B) wave may or may not be present at the base of the borehole, a remark that leads to two potential assumptions regarding the motion recorded at depth. One possible assumption is that the downhole response includes both up-going and down-going waves ($A + B$). This assumption is often referred to as a “*within*” motion. The alternative assumption, namely an “*incoming only*” motion, refers to wavefields where only the up-going (A) wave is present. The assumption that best simulates the actual wave propagation conditions at a site of a borehole array is not known a priori. Therefore, a separate set of analyses must be conducted for each borehole array to evaluate the wavefield that best models the observed responses. Previous studies dealing with the identification of the appropriate borehole wavefield assumption provide valuable conceptual and comparative tools on which we based our undertaking.

5.2.1. Previous Studies on the Identification of Borehole Wavefields

Bonilla *et al.* (2002) compared theoretical and empirical results using recordings from the Garner Valley borehole array in California. The particular array

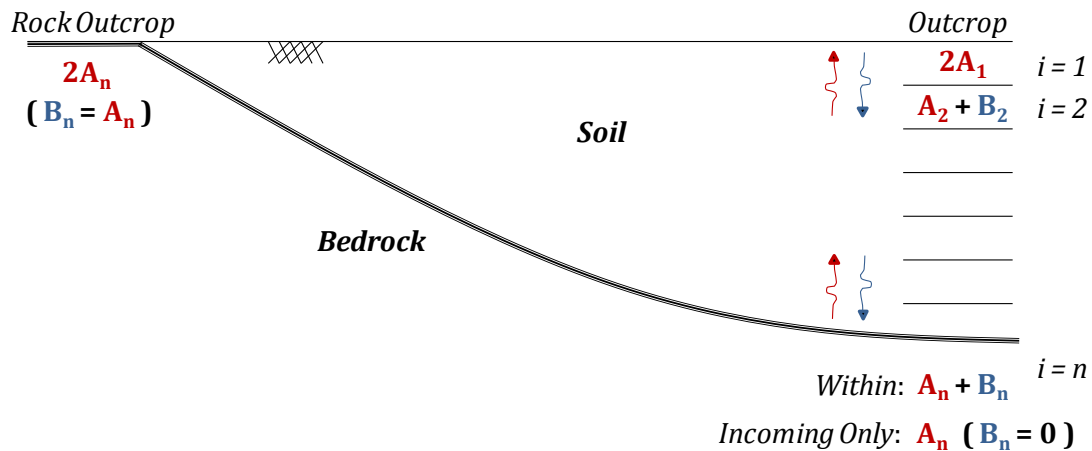


Figure 5.1: Common assumptions regarding wavefield pattern throughout a 1-D layered system (after Kottke, 2010)

involves seven vertically distributed three-dimensional sensors located at depths of 0, 6, 15, 22, 50, 220 and 550 *m*. Using data from these different depths, the authors computed empirical and theoretical transfer functions in order to investigate the wavefield pattern characterizing the response at different locations of the array. To compute the theoretical transfer functions, Bonilla *et al.* (2002) considered two assumptions regarding the seismic waves at depth. The first assumption included both down-going and up-going waves ($A + B$) (“within” assumption – “Borehole Response” in Bonilla *et al.*, 2002), while the second assumption incorporated only the up-going wave (A). The latter assumption was referred to as “outcrop” by the authors, even though it did not account for the perfect reflection of the up-going wave ($A = B$). Thus, to be consistent with the nomenclature used in this study, this case will be referred to as “incoming only” wavefield. The results from Bonilla *et al.* (2002) are shown in *FIGURE 5.2*, for the cases of “within” and “incoming only” wavefields, respectively. The “within” transfer functions seem to better match the observed response for depths less than 50 *m*. At these depths, the transfer functions

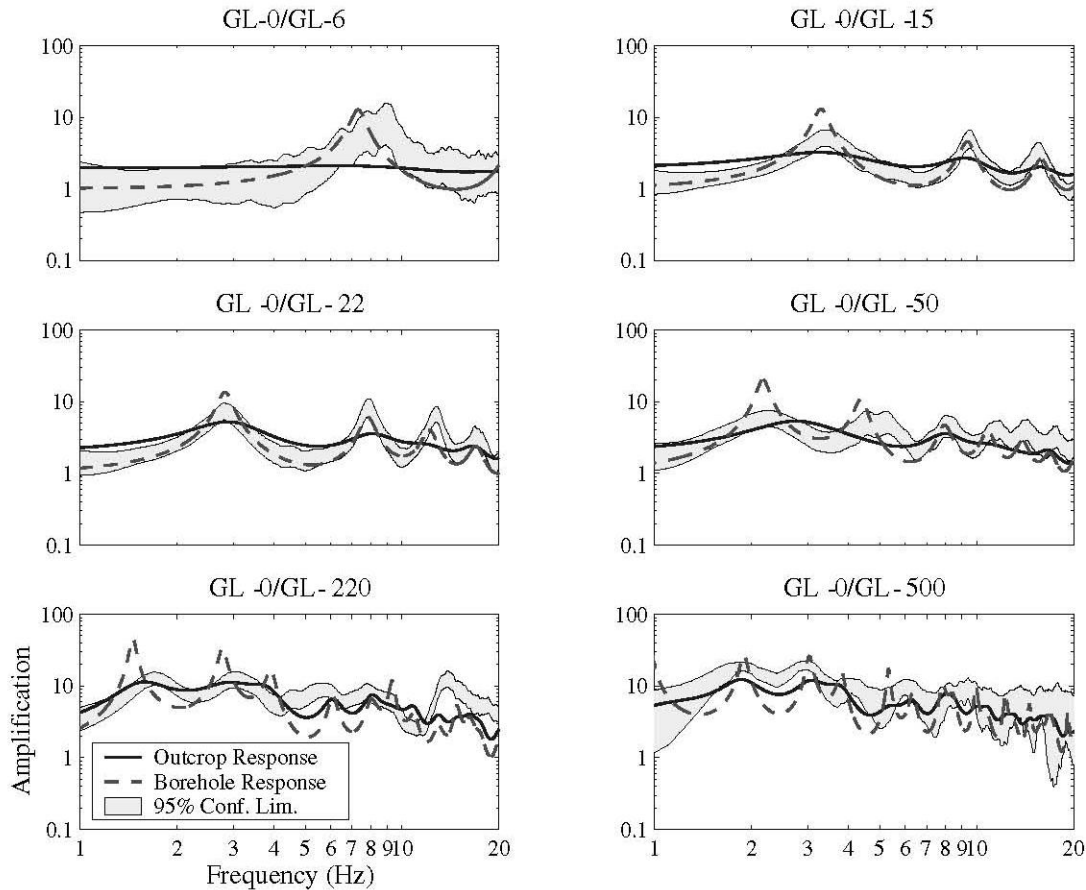


Figure 5.2: Comparison of empirical (shaded area) and theoretical transfer functions evaluated at different depths of Garber Valley borehole array (CA). “Outcrop Response” refers to the “incoming only” wavefield and “Borehole Response” corresponds to a “within” wavefield assumption. (from Bonilla *et al.*, 2002)

are characterized by pronounced peaks due to the destructive interference of the down-going and up-going waves. The latter phenomenon reduces the wave amplitudes at depth and consequently pseudo-resonance is observed. When evaluated at depths greater than 50 m (i.e. at 220 and 550 m in *FIGURE 5.2*), the observed transfer functions indicate a much flatter response, which is better simulated by the “incoming only” assumption. Such a remark is reasonable due to the expected gradual attenuation and/or scattering of the down-going seismic wave

at deeper strata of a profile. Therefore, according to Bonilla *et al.* (2002), the appropriateness of a specific borehole wavefield assumption is directly related to the recording depth.

In another research effort, Thompson *et al.* (2009) utilized data recorded at 13 Kik-Net vertical arrays in Japan to evaluate the appropriateness of the assumed wavefield. Towards this goal, empirical and theoretical linear-elastic transfer functions were obtained for the “within” and “incoming only” wavefields. The results from the Thompson *et al.* (2009) study are shown in *FIGURES 5.3* and *5.4*. Based on their findings, the authors concluded that the actual wave propagation conditions are best simulated by a “within” wavefield for some of the sites (SMNH01, TTRH02, NARH01, KGWH02, and HYGH10 – *FIGURE 5.3*), while an “incoming only” assumption is more representative for other sites (SMNH02, WKYH03, WKYH01, OSKH03, HRSH01, OKYH07, and HYGH07 – *FIGURE 5.4*). For the latter stations, the observed response was substantially flatter with no strong, pseudo-resonance peaks associated with the destructive interference of the up-going and down-going waves. Thompson *et al.* (2009) also investigated whether inaccurate or uncertain shear wave velocities influenced the findings. They utilized two shear wave velocity profiles for the development of the theoretical transfer functions, i.e. one profile with V_S values as reported by Kik-Net database (“borehole”) and another profile incorporating V_S values measured by the Spectral Analysis of Surface Waves (SASW) in-situ method as part of their research. The resulting transfer functions based on both these V_S profiles showed small differences. Consequently, the researchers concluded that, in most cases, the assumptions regarding the computational theoretical framework play a more significant role than the uncertainties associated with the material properties. Fi-

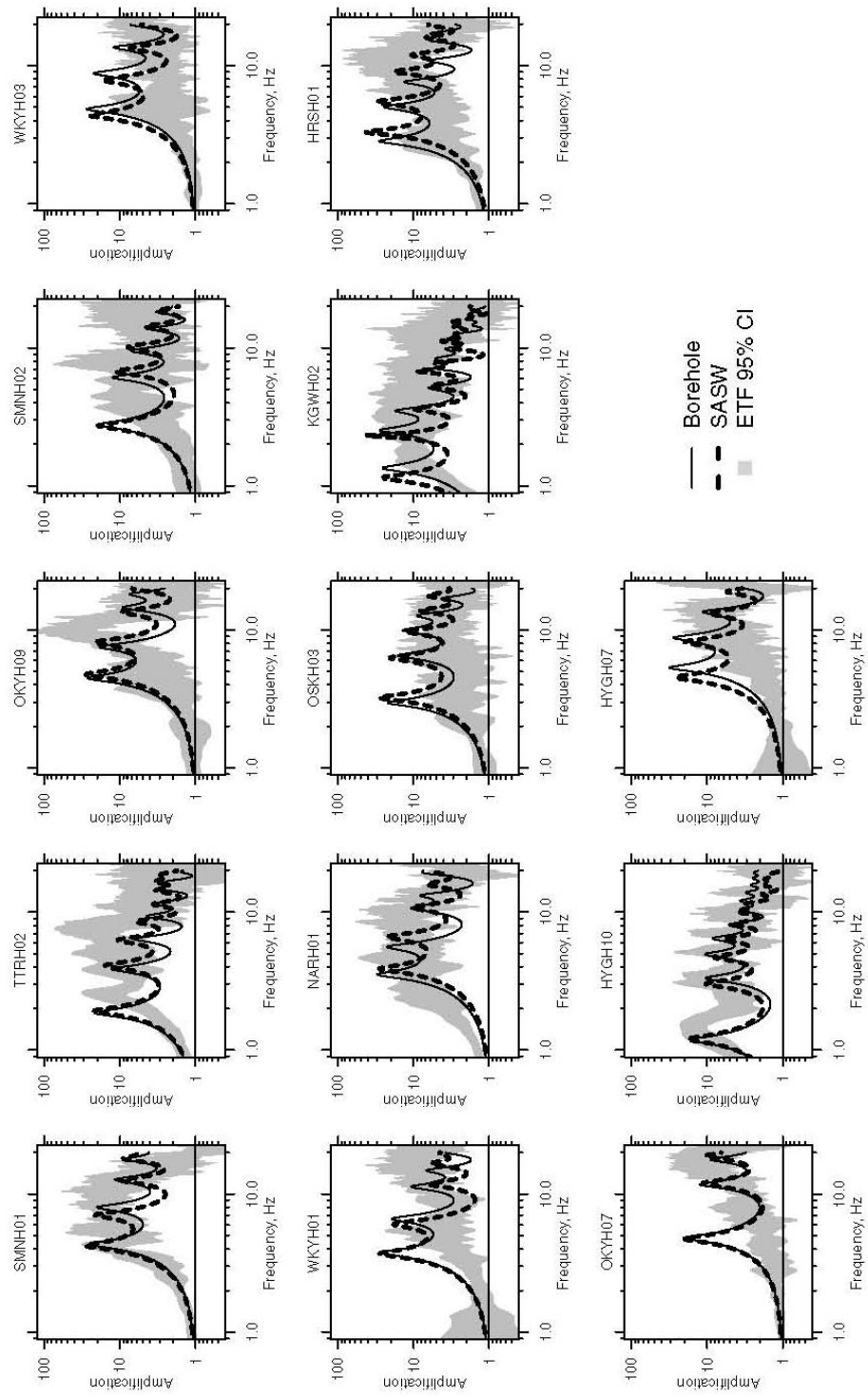


Figure 5.3: Observed and computed transfer functions assuming a “within” wavefield (from Thompson et al., 2009)

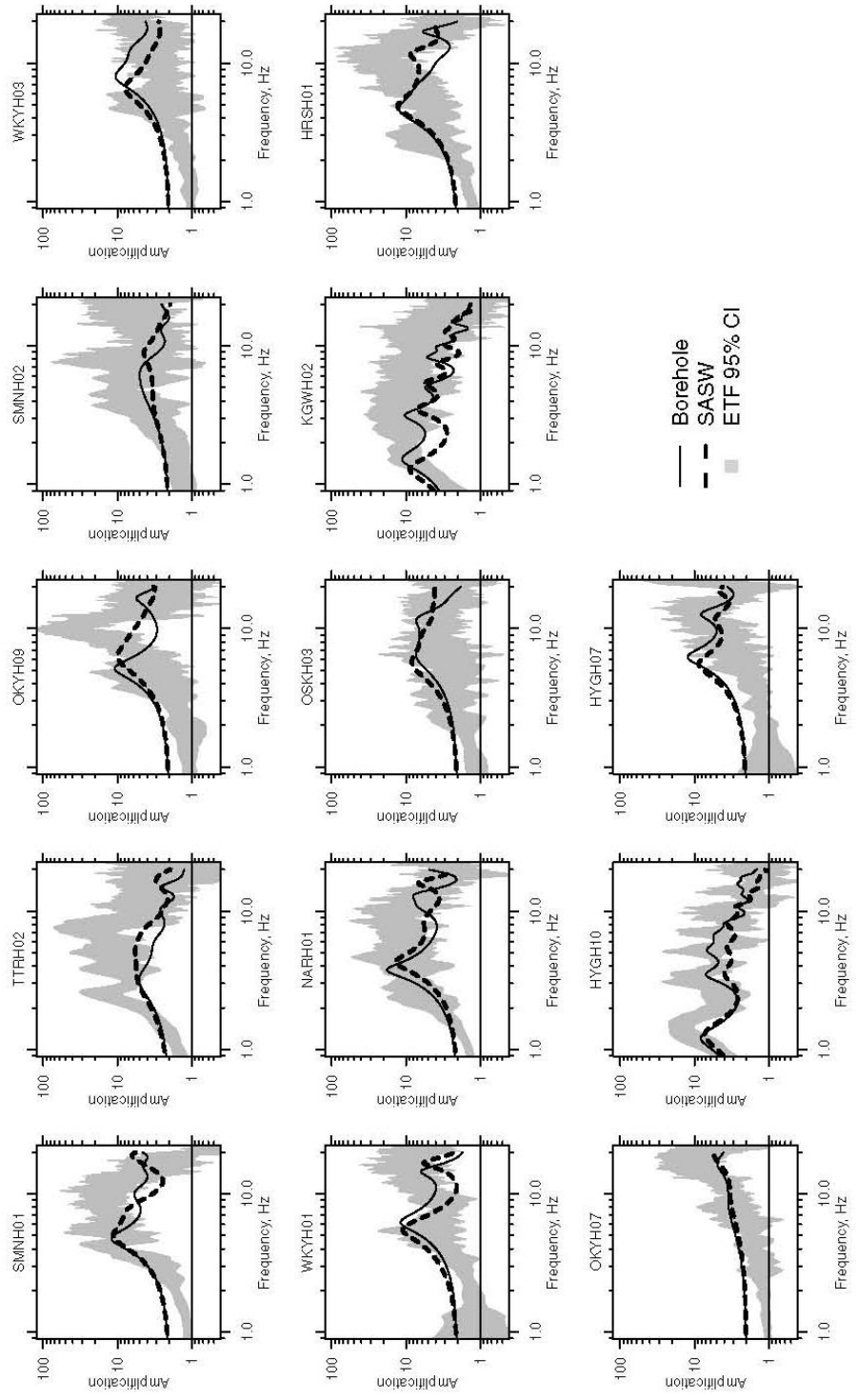


Figure 5.4: Observed and computed transfer functions assuming a “within” wavefield (from Thompson et al., 2009)

nally, Thompson *et al.* (2009) found that for arrays where the theoretical one-dimensional model poorly represents the observed response, a more elaborate modeling of the complete three-dimensional wavefield and spatial heterogeneity is necessary. They concluded that these analyses performed better because the 3-D spatial heterogeneity incorporated into the analyses produced seismic scattering that reduced the down-going wave effect.

5.2.2. Linear-Elastic Transfer Functions

Based on the ideas arising from the studies by Bonilla *et al.* (2002) and Thompson *et al.* (2009), we made an effort to identify the most suitable borehole wavefields under the assumption of 1-D wave propagation for the 13 selected strong motion arrays described in [Chapter 4](#). This is achieved by comparing the observed frequency-domain transfer functions with the theoretical transfer functions computed based on the velocity profile and the different wavefield assumptions. The assumption yielding results most similar to the observations can be considered to be most representative.

More specifically, 1-D linear-elastic analyses (LE) were performed assuming both “within” and “incoming only” wavefields at the base of the 13 arrays. The observed transfer functions were compared with the theoretical transfer functions obtained from the LE analyses. To be consistent with a linear-elastic response, only recorded motions at the base of the arrays with PGA_{base} less than $0.05 g$ were used. The soil layers comprising the sites were modeled as linear-elastic materials, and constant damping values were assigned to them.

Even at low levels of shear deformation, soil materials experience energy dissipation when loaded cyclically. The viscous nature of energy attenuation at low

levels of straining makes the exact conceptual and physical explanation of the phenomenon a laborious task. In most seismic engineering studies, small strain damping is incorporated into the various models (e.g. Darendeli, 2001) through a measure of viscous damping (D_{min}). The damping values from most of these models are based on laboratory testing, and thus they only account for material damping. Therefore, it is essential to note that the commonly utilized values of D_{min} do not account for other mechanisms of energy dissipation in the field such as wave scattering, a phenomenon which will be discussed further in [Section 5.3](#).

Within the framework of selecting the most suitable borehole wavefiled assumption (“within” vs “incoming only”) for the 13 arrays of this study, damping values were assigned at each site using the minimum damping (D_{min}) values obtained from the Darendeli (2001) model ([FIGURE 5.5](#)). The Darendeli (2001) model provides damping values that are confining stress-dependent, with larger damping values (generally $\sim 1.0 \div 2.0$ %) close to the ground surface and smaller values ($\sim 0.3 \div 0.6$ %) at depth, assuming the same PI throughout. For the Lotung array, laboratory measurements yielded similar material properties for all the soil layers comprising the site (see [Chapter 4](#)) and thus a constant value of damping was assigned. The variation in the minimum damping (D_{min}) profile with depth results in the fact that frequencies which sample different depths of the soil profile, attenuate differently. This behavior occurs irrespective of the high frequency filtering typically encountered when seismic waves propagate through soil deposits.

Incorporating the aforementioned damping profiles, linear-elastic analyses assuming both wavefields were performed. In [FIGURE 5.6](#), theoretical transfer functions computed based on both the “within” and “incoming only” assumptions

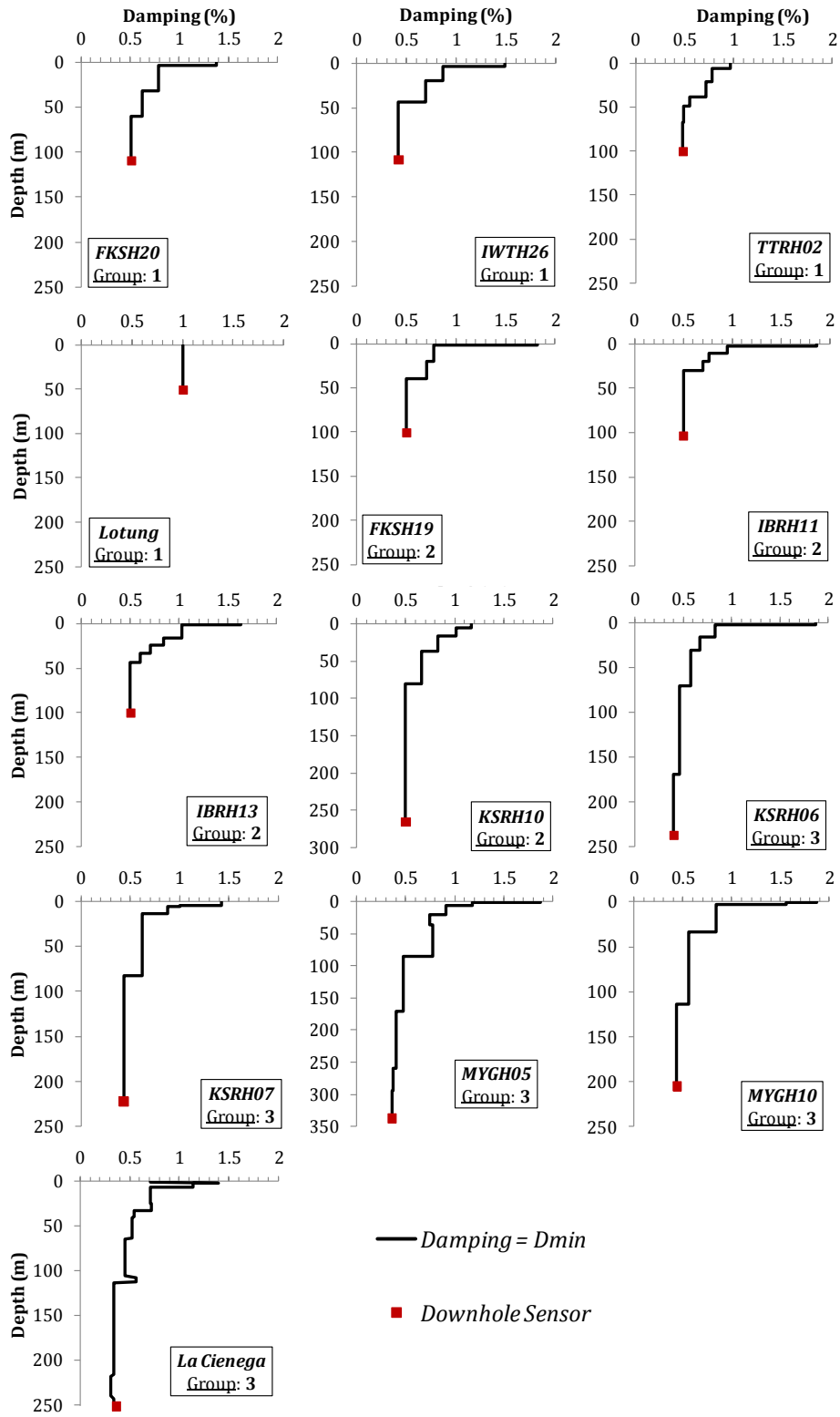


Figure 5.5: Minimum damping (D_{min}) profiles considered

are compared with the observed *median* transfer functions for motions with $PGA_{base} < 0.05 g$. In general, the “within” wavefield produces very tall peaks in the transfer functions due to the destructive interference between the up-going (A) and down-going (B) waves at the modal frequencies of a velocity profile. This phenomenon is more profound at lower frequencies, which are related to the response of deeper layers of the soil profile. The “incoming only” transfer functions are much smoother than the “within” transfer functions because the down-going wave (B) is ignored. Assuming that the down-going wave (B) is not present, also, leads to the “incoming only” transfer function approaching a value equal to 2 at low frequencies, while both the “within” and the observed transfer functions approach unity. It is also clear from *FIGURE 5.6* that the observed transfer functions also indicate either very peaked (FKSH20, IWTH26, TTRH02, FKSH19, IBRH11, IBRH13, and KSRH10 arrays) or relatively flat (KSRH06, KSRH07, MYGH05, MYGH10, and La Cienega arrays) responses. The Lotung array yielded responses which cannot be described as either very peaked (even though slight peaks are present) or as smooth enough to be included in either category.

By comparing the theoretical and observed transfer functions, it can be stated that some sites are better modeled by the “within” assumption while others are better modeled by the “incoming only” wavefield. Nonetheless, it is evident at all sites that the theoretical transfer functions are not able to fully capture the observed transfer functions at all frequencies. The discrepancies are most likely attributed to simplifications associated with one-dimensional wave propagation, as well as to potential bias in the utilized material properties. For example, the MYGH10 site displays strong amplification at frequencies between 5 Hz and 13 Hz, something that is not captured by the theoretical response. Such difference between the obser-

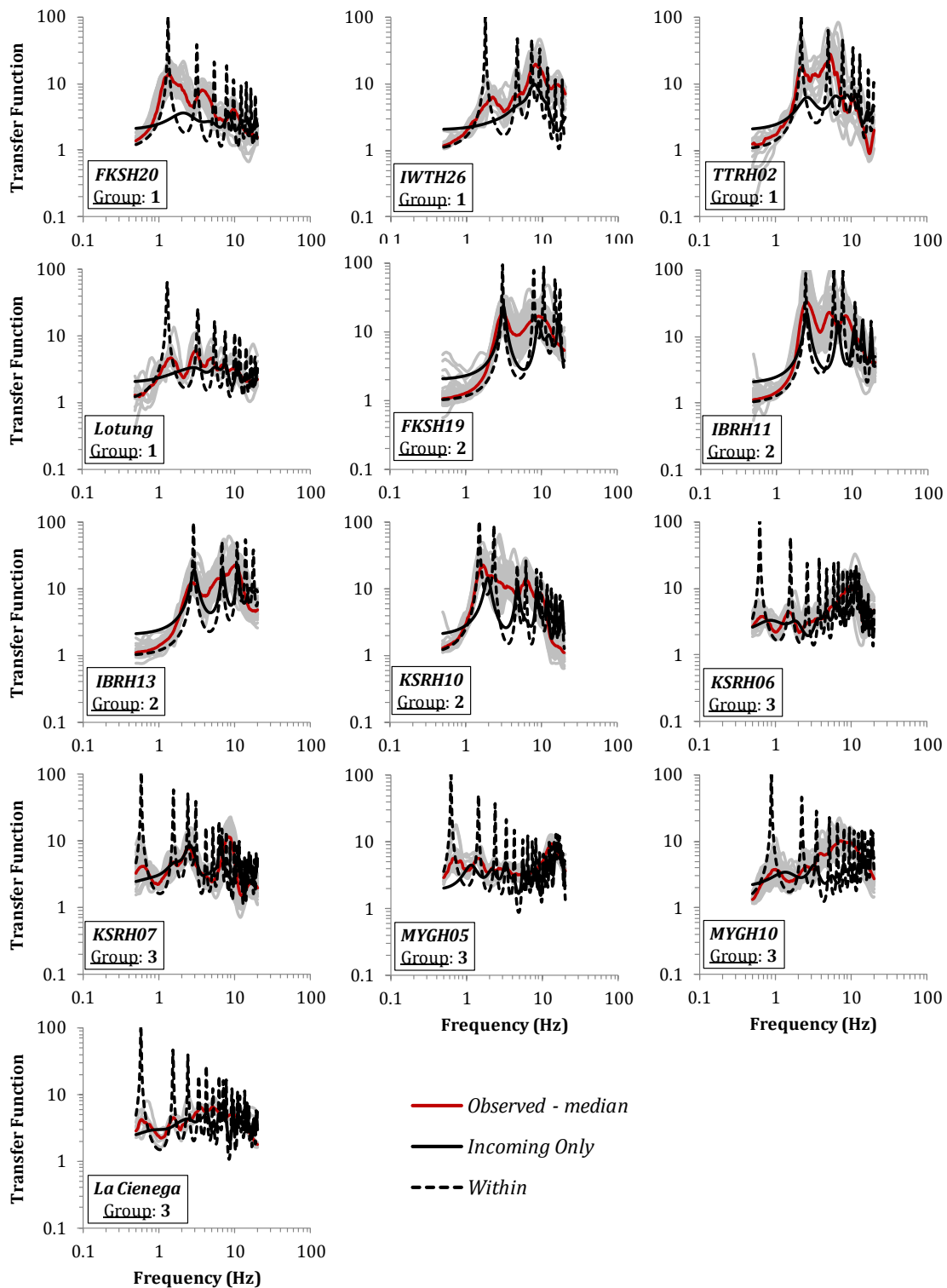


Figure 5.6: Comparison of theoretical linear-elastic transfer functions and observed transfer functions for low intensity motions ($PGA_{base} < 0.05 g$).

ved and computed transfer functions is typically caused by the incorporation of erroneous values of shear wave velocities at the layers of the profile associated with these frequencies.

5.2.3. Selection of Appropriate Wavefield

In accordance with the above observations, the 13 borehole arrays can be subdivided into three groups based on the wavefield deemed most suitable as well as the physical justification for this wavefield (*TABLE 5.1*). The key parameters influencing the selection of the appropriate wavefield are: *i*) the depth to the downhole sensor, and *ii*) the existence of any strong velocity contrasts within the profiles.

The first group (*Group 1*) consists of sites where the downhole sensor is positioned at depths of equal to or less than about 100 *m* (FKSH20, IWTH26, TTRH02, and Lotung arrays). These sites seem to be better characterized by the “within” wavefield assumption. Understandably, the relatively shallow depth of the downhole sensor seems to be related with the presence of both up-going and down-going seismic waves ($A + B$) at the base of the corresponding arrays. It was decided that Lotung array should be included in *Group 1*, primarily due to its shallow downhole sensor depth as well as due to the complete lack of peaks in the “incoming only” transfer function. It is noted though that, in the case of the Lotung and IWTH26 arrays, the “within” transfer functions show substantially higher peaks than the observed peaks at the first two modal frequencies. This inconsistency can be most probably explained by the inability of the one-dimensional theoretical model to capture the actual response at these particular sites. For example, a small vertical and/or lateral variability in the material properties and/or the layer thick-

Table 5.1: Grouping of arrays based on site characteristics and appropriate wavefield boundary condition

Site	Downhole Sensor depth (m)	Selected Wavefield	Location of impedance contrast (m)	Group*
<i>FKSH20</i>	109	Within	N/A	1
<i>IWTH26</i>	108	Within	N/A	1
<i>TTRH02</i>	100	Within	N/A	1
<i>Lotung</i>	50	Within	N/A	1
<i>FKSH19</i>	100	Within/Incoming	40	2
<i>IBRH11</i>	103	Within/Incoming	30	2
<i>IBRH13</i>	100	Within/Incoming	44	2
<i>KSRH10</i>	255	Within/Incoming	36	2
<i>KSRH06</i>	237	Incoming Only	N/A	3
<i>KSRH07</i>	222	Incoming Only	N/A	3
<i>MYGH05</i>	337	Incoming Only	N/A	3
<i>MYGH10</i>	205	Incoming Only	N/A	3
<i>La Cienega</i>	265	Incoming Only	N/A	3

*Group	Characteristics / Description
1	Downhole Sensor Depth: approx. < 100 m
2	Strong impedance contrast within the profile
3	Downhole Sensor Depth: approx. > 200 m

ness at the deeper strata of the profile may cause additional scattering of the seismic waves, and therefore an “apparent” overdamping of the low frequency response. Since the “within” transfer function does not include these additional attenuation mechanisms, it inevitably overpredicts the response.

A second group (*Group 2*) includes sites which, irrespectively of the depth to the downhole sensor, are characterized by a strong shear wave velocity contrast within the first 50 *m* of the profile (FKSH19, IBRH11, IBRH13, and KSRH10 arrays). At these sites, both the “within” and “incoming only” wavefield generate numerical results similar to the observations. It can be claimed that the similarity in the computed transfer functions is caused by the strong velocity contrast which traps the downgoing wave (B), through multiple reflections, in the softer layers near the surface. Therefore, the amplitude of the down-going wave (B_n) near the base of the profile approaches zero and, thus, the “within” wavefield converge to an “incoming only” wave propagation assumption (except at the lowest frequencies). Moreover, the existence of the strong impedance contrast produces relatively higher peaks in the theoretical transfer functions even when the effect of the down-going wave (B) is ignored (“incoming only” assumption).

Finally, the last group (*Group 3*) included sites with a downhole sensor depth greater than approximately 200 *m* (KSRH06, KSRH07, MYGH05, MYGH10, and La Cienega arrays). *Group 3* sites are best simulated by the “incoming only” wavefield. This wavefield provides the best fit because the borehole sensor is relatively deep (i.e. ≥ 200 *m*), such that the down-going wave is not present at the borehole sensor due to the cumulative effect of attenuation/damping in the upper layers. In the field, each propagating seismic wave (up-going or down-going) is distinctively affected by attenuation through wave scattering. By ignoring the down-going wave (“incoming only” wavefield), the effect of these additional in-situ attenuation mechanisms is implicitly introduced into the analysis. Moreover, the fact that the depth to the downhole sensor appears to be the major contributing factor for the ability of a

wavefield to yield results in agreement with the observations, further supports the depth-dependence of the rate of attenuation of the down-going wave (B).

Most site response analyses are aimed at producing acceleration response spectra rather than Fourier amplitude spectra. Therefore, it is worthwhile to illustrate the comparison between the theoretical responses and the observations in terms of spectral amplification factors (AF), which are defined as:

$$AF(T) = \frac{S_a^{surface}(T)}{S_a^{base}(T)} \quad (5.1)$$

where $S_a^{surface}$ and S_a^{base} are the spectral accelerations at the ground surface and base sensor recording, respectively, and T is the spectral period. The amplification factor (AF) displays a smoother response across frequencies because the single-degree-of-freedom transfer function used to compute the response spectra samples a bandwidth of frequencies and acts as a frequency filter.

The observed and computed linear-elastic amplification factors for all 13 borehole arrays are shown in *FIGURE 5.7*. “Within” and “incoming only” amplification factors are depicted. Similar to the observations from the transfer functions, the amplification factors also demonstrate that the “within” wavefield seems to be more suitable for *Group 1* sites (downhole sensor depth ≤ 100 m), while the “incoming only” assumption is more suitable for sites categorized in *Group 3* (downhole sensor depth ≥ 200 m). For *Group 2* sites (strong velocity contrast within the profile), both wavefields produce similar responses. The “within” amplification factors show a response with higher peaks and lower troughs due to the down-going wave effect. As in the case of transfer functions, this phenomenon is mainly seen at higher periods (lower frequencies), i.e. close to the first few modes of vibration of the soil

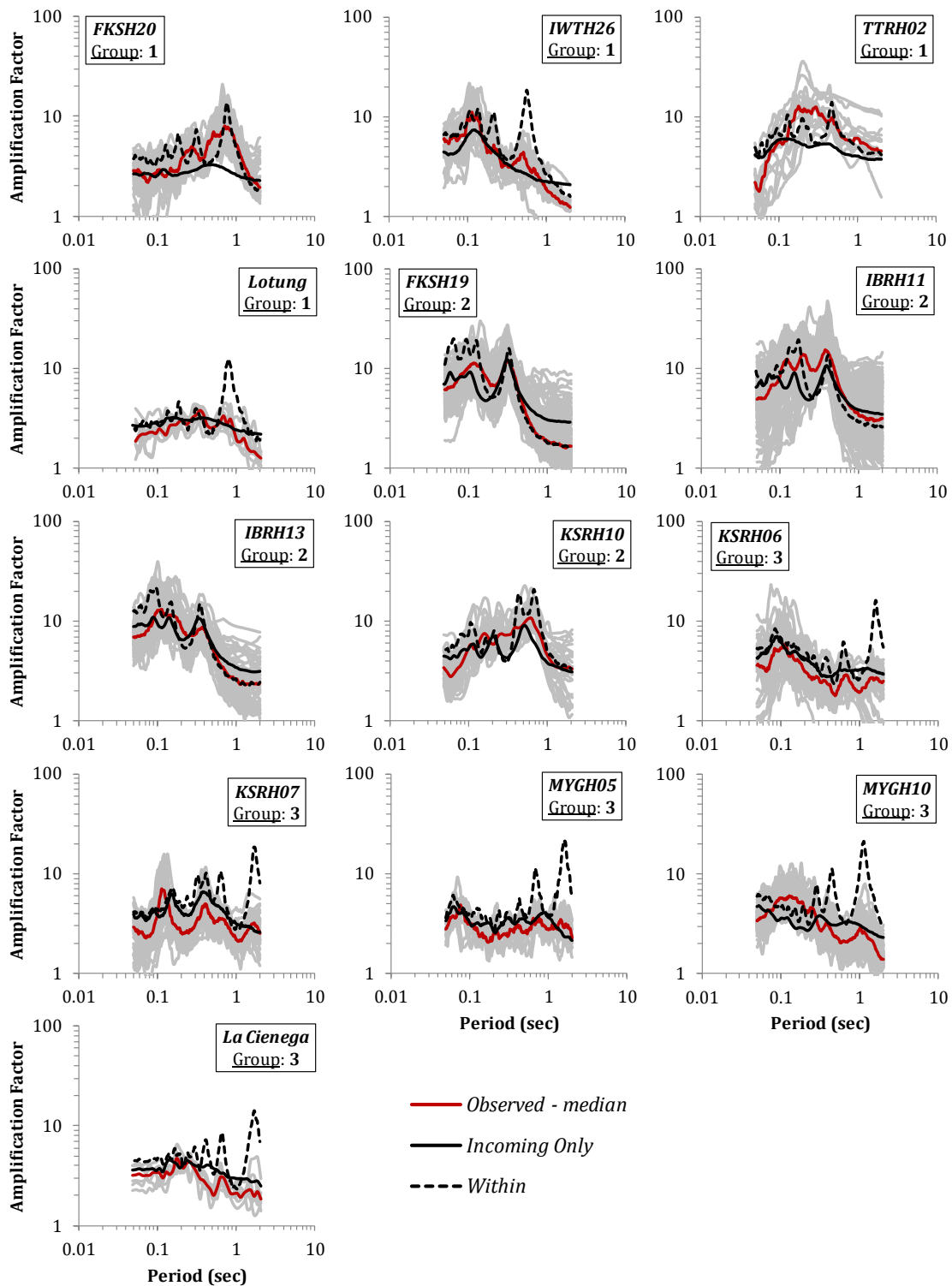


Figure 5.7: Comparison of *median* linear-elastic amplification factors and observed amplification factors for low intensity motions ($PGA_{base} < 0.05 g$).

profile. The “within” wavefield more realistically represents amplification at high frequencies.

It should be noted once again that the theoretical model is not able to fully capture the field observations as depicted in the observed amplification factors. The discrepancies are most probably caused by the inability of the theoretical 1-D model to accurately simulate the wave propagation pattern (including wave scattering due to lateral inhomogeneity), although it is also possible that it is caused by the use of erroneous material properties (i.e. V_S and damping). For example, by examining *FIGURE 5.7*, it can be stated that, for TTRH02 and MYGH10 arrays, the theoretical predictions significantly deviate from observations. As mentioned in *Chapter 4*, TTRH02 site is located at a relatively high altitude on inclined, sloping ground, something contradictory to the assumed one-dimensional wave propagation in a horizontally layered medium. Moreover, theoretical predictions for MYGH10 site seem not able to capture either the location or the magnitude of the peaks in the observed amplification factors. The latter remark possibly indicates that the theoretical model has incorporated wrong values of material properties. Considering the uncertainty associated with in-situ shear wave measurements in combination with the limited breadth of the soil characterization in Kik-Net arrays, the reported shear wave velocity values for MYGH10 array may have resulted in erroneous predictions.

5.3. Uncertainty in the Small-Strain Damping

The preceding analysis regarding the different borehole wavefield assumptions is useful in understanding the general wave propagation pattern within the vertical arrays considered in this study, but it does not take into account

the fact that the “incoming only” wavefield is rarely, if ever, utilized in engineering practice. A “within” assumption is the standard of practice when a ground motion recorded at depth is used as input. Thus, it was decided that the “within” wavefield (e.g. *FIGURE 5.6*) would be assumed for all subsequent analyses of the vertical arrays in this study. Nonetheless, a certain degree of uncertainty exists concerning the appropriate value of D_{min} . As already discussed, the Darendeli (2001) model incorporates only the intrinsic, material damping and does not take into account additional in-situ attenuation mechanisms, inherently present when vertical arrays are involved. These in-situ attenuation mechanisms include several elastic processes, such as wave scattering, geometrical spreading and multipathing (i.e., focusing and defocusing of seismic waves caused by lateral variations in the velocity structure) (Stein and Wyession, 2003). The attenuation through these mechanisms is “apparent”, that is, the propagating wave energy is actually conserved and not lost. The energy loss is perceived through the redistribution of the wave energy.

In contrast with phenomena such as geometrical spreading and multipathing that can be approximated only by two or three dimensional modeling techniques, the observed loss of wave propagation energy through seismic wave scattering can be, at least partly, incorporated in an assumed one-dimensional model. Seismic wave scattering essentially represents the modification of the passing seismic waves by heterogeneities within the soil profile (Thompson *et al.*, 2009). Whether the effect of these heterogeneities can be considered as wave scattering depends on the relative size of the heterogeneity with respect to the wavelength and the distance travelled by the wave through the heterogeneous region (Stein and Wyession, 2003). When the velocity heterogeneity is large enough (i.e., a distinctive velocity layer with sufficient thickness), the wave follows a distinct ray path that is distorted

by multipathing. In contrast, when the velocity heterogeneity is similar in size to the wavelength, the seismic energy is considered to be scattered, and thus an “apparent” energy loss is observed. Therefore, wave scattering should be considered as a frequency-dependent phenomenon, with high-frequency/low-wavelength waves being more profoundly affected by it.

In the past, several researchers have recognized the importance of wave scattering attenuation mechanisms (Assimaki and Steidl, 2007; Thompson *et al.*, 2012). More specifically, Assimaki and Steidl (2007) applied an inversion technique using data recorded at 5 NIED KiK-Net vertical arrays. The ultimate goal of the researchers was to back-calculate the velocity and damping structures of the considered arrays based on the borehole-surface recordings. Based on their results, Assimaki and Steidl (2007) observed that attenuation values close to the surface of the arrays were substantially higher than the ones estimated based on empirical correlations (*FIGURE 5.8*). More specifically, maximum D_{min} values between 5 % and 13 % are reported for the soil layers at the upper 20 m of the considered vertical arrays. Given the expected higher variability/heterogeneity of the materials at the shallower parts of any soil profile, Assimaki and Steidl (2007) attributed the phenomenon on the scattering redistribution of the high-frequency wave energy.

Based on *FIGURE 5.8*, it can be stated that the frequency-dependence of wave scattering is also translated into a depth-dependence of the small-strain damping values, i.e. with higher values of D_{min} close to the surface and lower values at depth. Since the high frequency components sample shallower/thinner strata of the velocity profile, the scattering associated with them is incorporated into the shallow depths of the attenuation profile. Nonetheless, it should be noted that the “apparent” depth-dependence of the small-strain value is an outcome of the fact that the best-fit

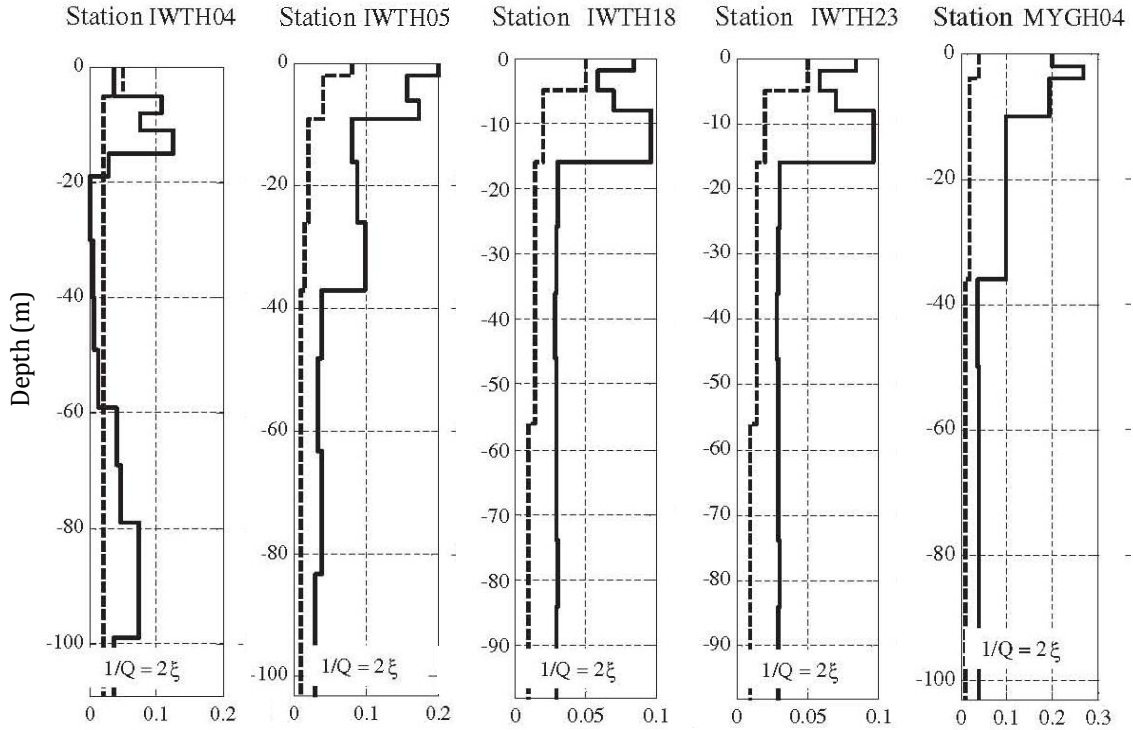


Figure 5.8: Damping structures of 5 KiK-Net arrays obtained from empirical correlations (dashed lines), and from the Assimaki and Steidl (2007) inversion technique (solid line) (Note: $\xi = D_{min}$) (from Assimaki and Steidl, 2007)

attenuation structures developed by Assimaki and Steidl (2007) are based on a frequency-independent D_{min} at each depth. Ideally, attenuation through scattering should be treated as a simultaneously frequency and depth dependent mechanism. The investigation of such a complex relationship is beyond the scope of the present study. Instead, as in Assimaki and Steidl (2007), the present study assumes that the effects of wave scattering are only depth-dependent.

5.3.1. Selection of Best-Fit Small-Strain Damping Profiles

To identify the appropriate amount of additional, depth-dependent, small-strain damping due to scattering, a grid search procedure was adopted. For each

array, multiple linear-elastic analyses were performed and the associated amplification factors computed using the Darendeli (2001) D_{min} profiles (*FIGURE 5.5*) multiplied by a factor ranging from 1 to 10 with a step of 0.25. For each site, the computed *median* linear-elastic amplification factor was compared with the corresponding *median* observed amplification factor for motions with $PGA_{base} \leq 0.05 g$. The comparison between the computed and observed amplification factors was quantified by evaluating the *root-mean-square error* (RMSE) between the computed and observed amplification factors over the period range of 0.05 s (20 Hz) to 2 s (0.5 Hz) for 512 logarithmically spaced periods. The best-fit damping profile was selected as the one having the lowest RMSE value. The results of the procedure described above are tabulated in *TABLE 5.2*, while in *FIGURE 5.9* the factor corresponding to the best-fit damping profile for each vertical array has been plotted against the depth of the downhole sensor of the array. From *FIGURE 5.9* it can be seen that the factor applied to D_{min} varies primarily between 2.25 and 3.5 across most of the arrays. The deeper arrays, particularly the ones in *Group 3*, are fit best with larger factors and more damping. The latter results from the fact that the “within” amplification factors strongly over-predict the response at the first modal periods of the arrays (*FIGURE 5.7*) due to the destructive interference between the up-going (*A*) and down-going waves (*B*). Therefore, for the RMSE to be minimized, the applied factor on the D_{min} profile needs to be higher than it would be in the absence of these pseudo-resonances.

The best-fit damping profiles as well as the initial profiles based on the Darendeli (2001) D_{min} values are depicted in *FIGURE 5.10*. The best-fit damping profiles preserve and amplify the initial depth-dependence of the small-strain damping (*FIGURE 5.5*). The highest values of damping are assigned to the shallow,

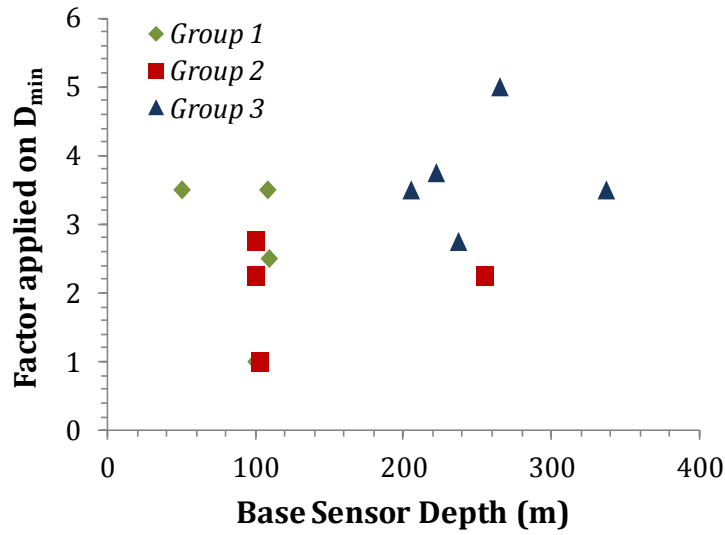


Figure 5.9: Factor applied on D_{min} for the best-fit damping profile vs base sensor depth of each array

Table 5.2: Tabulated factors applied on D_{min} for the best-fit damping profile for each array

Site	Base Sensor Depth (m)	V_{S30} (m/s)	RMSE - Initial	RMSE - Best-Fit	Factor applied on D_{min}	Group
<i>FKSH20</i>	109	350	0.36	0.27	2.50	1
<i>IWTH26</i>	108	371	0.52	0.41	3.50	1
<i>TTRH02</i>	100	310	0.46	0.46	1.00	1
<i>Lotung</i>	50	184	0.45	0.34	3.50	1
<i>FKSH19</i>	100	338	0.36	0.28	2.75	2
<i>IBRH11</i>	103	242	0.35	0.35	1.00	2
<i>IBRH13</i>	100	335	0.31	0.26	2.25	2
<i>KSRH10</i>	255	212	0.37	0.31	2.25	2
<i>KSRH06</i>	237	326	0.52	0.41	2.75	3
<i>KSRH07</i>	222	204	0.68	0.45	3.75	3
<i>MYGH05</i>	337	305	0.68	0.50	3.50	3
<i>MYGH10</i>	205	348	0.78	0.67	3.50	3
<i>La Cienega</i>	265	250	0.62	0.44	5.00	3

thin layers which are typically characterized by more heterogeneity. The developed best-fit damping profiles in *FIGURE 5.10* are considered comparable with the damping structures from Assimaki and Steidl (2007) (*FIGURE 5.8*) which were defined by a more sophisticated inversion technique.

5.3.2. Best-Fit Amplification Factors

Using the best-fit damping profiles, the best-fit *median* linear-elastic amplification factors are presented in *FIGURE 5.11*. The *median* linear-elastic amplification factors calculated with the initial D_{min} profiles are also depicted for reference. The incorporation of increased values of small-strain damping primarily affects the high frequency (low period) response. At sites where no strong first mode over-amplification of the response is observed (FKSH20, TTRH02, FKSH19, IBRH11, IBRH13, KSRH10), the best-fit damping profiles provide amplification factors that better predict the observed high frequency response. On the other hand, at sites where the initial theoretical models yield a high first mode response (IWTH26, Lotung, KSRH06, KSRH07, MYGH05, MYGH10, La Cienega), the updated damping profiles seem to slightly alleviate the initial model's over-amplification, but at the expense of an under-prediction of the high frequency response (*FIGURE 5.11*). Overall, the adopted grid search process of determining the best-fit damping profile provides responses that are, in general, closer to the observations. Nevertheless, it should be strongly stated that the procedure described above assumes that the initial theoretical model (i.e., D_{min} profile, V_S profile, boundary conditions) is a sufficiently accurate starting point.

In order to supplement our observations and to be able to compare the results shown in *FIGURE 5.11* across sites and quantify the accuracy and the uncer-

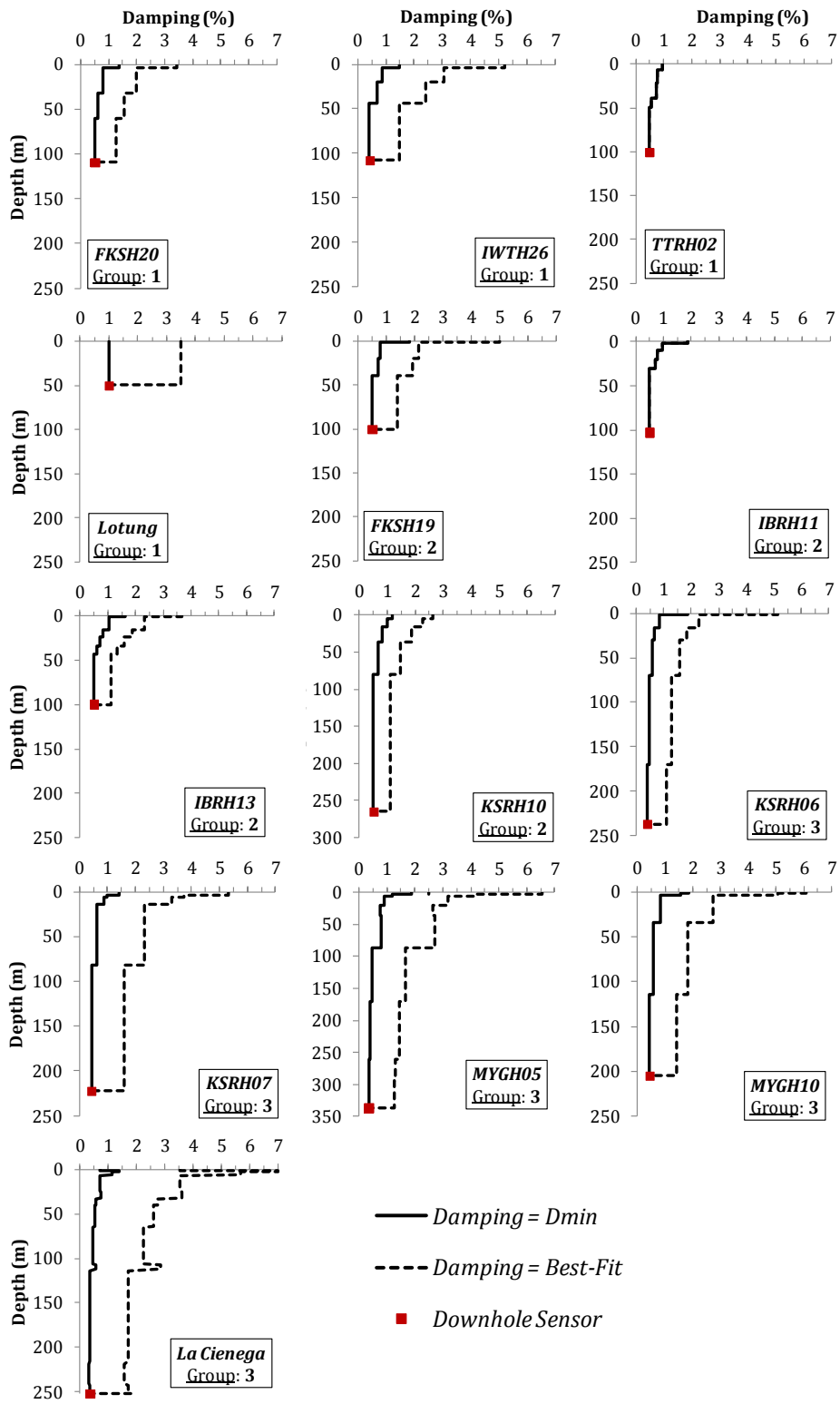


Figure 5.10: Damping profiles based on D_{min} and on the best-fit damping profile

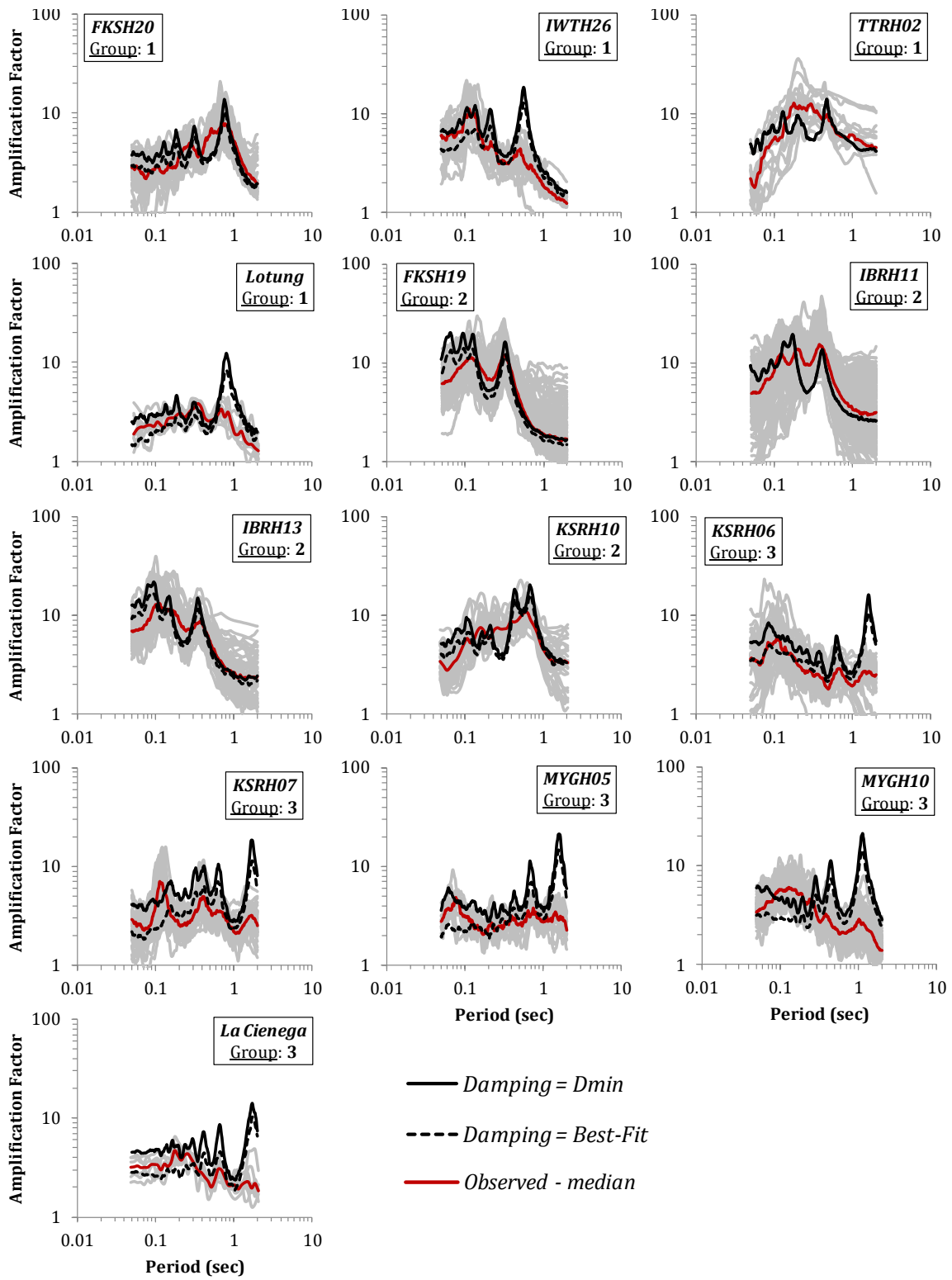


Figure 5.11: Amplification Factors based on D_{min} and on the best-fit damping profile

tainty of the theoretical models, a single unifying measure is introduced. We use a slight alternation of the Abrahamson *et al.* (1990) model for the quantification of the goodness-of-fit between seismological observations and numerical results. Abrahamson *et al.* (1990) identified the residual and the uncertainty of seismological strong-ground-motion simulations by quantifying the misfit between numerically simulated and recorded strong ground motions, in terms of response spectral values. Abrahamson *et al.* (1990) defined that, for the i^{th} record, the observed ($S_{a,i}^{obs}$) and computed ($S_{a,i}^{calc}$) spectral accelerations are related as:

$$\ln S_{a,i}^{obs}(f) = \ln S_{a,i}^{calc}(f) + \mu(f) + \varepsilon_i(f) \quad (5.2)$$

where f is frequency, $\mu(f)$ is the mean residual and $\varepsilon_i(f)$ is the error estimate. The latter provides variability estimates for the residual in the predictions and is assumed to be a normally distributed variable with zero mean and a standard deviation (σ_ε). The same definition of the residual was used in studies by Lee *et al.* (2006), Stewart *et al.* (2008) and Kottke (2010).

In the present study, we identified the misfit (or residual) as the difference between observations and numerical results, in terms of amplification factor (AF) values. This modification is solely semantic because the calculated residual is the same in either case. Therefore, for the i^{th} site and j^{th} recording, the residual (y) between the observed amplification factor (AF^{obs}) and the theoretically calculated amplification factor (AF^{calc}) is given by:

$$y_{i,j}(T) = \ln AF_{i,j}^{obs}(T) - \ln AF_{i,j}^{calc}(T) \quad (5.3)$$

where T is the spectral period. A positive residual represents under-prediction, while a negative residual represents over-prediction of the response. For example,

residuals with values of 1.0, 0.5, -0.5 and -1.0 correspond to ratios of AF^{obs}/AF^{calc} equal to 2.71, 1.65, 0.61 and 0.36, respectively.

The computed *mean* linear-elastic residuals for all 13 borehole arrays are shown in *FIGURE 5.12* based on analyses using the best-fit damping profiles (*FIGURE 5.10*). *FIGURE 5.12* is the direct equivalent of the results shown in *FIGURE 5.11*, for the best-fit damping profile (dashed lines). Again, the high over-prediction of the response by the “within” wavefield at the first few modal periods for relatively deep sites (*Group 3*) is evident. At lower periods (higher frequencies), i.e. at periods less than 0.4 s, the calculated responses are relatively closer to the observations, for all sites.

In addition to the evaluation of the accuracy of the theoretical linear-elastic predictions, an assessment of the associated variability is necessary. *FIGURE 5.13* illustrates the standard deviations of the residual in the predictions (*FIGURE 5.12*). Based on *FIGURE 5.14*, it can be seen that the variability ranges from 0.2 – 0.4 at some sites (FKSH20, IWTH26, Lotung, IBRH11, and KSRH10 arrays) to 0.4 – 0.6 (TTRH02, FKSH19, and IBRH13 arrays). At sites in *Group 3* (downhole sensor depth ≥ 200 m), larger values of standard deviations (up to 0.6) are observed near the first few modal periods, due to the “within” wavefield assumption. Based on *FIGURE 5.14*, there is not a clear conclusion regarding any potential frequency-dependence of the variability.

5.4. Uncertainty in the One-Dimensional Assumption

The proper evaluation of the accuracy of one-dimensional site response analysis (*Chapter 2*) using recordings from geotechnical strong motion arrays inherently assumes that the vertical arrays under investigation can be sufficiently

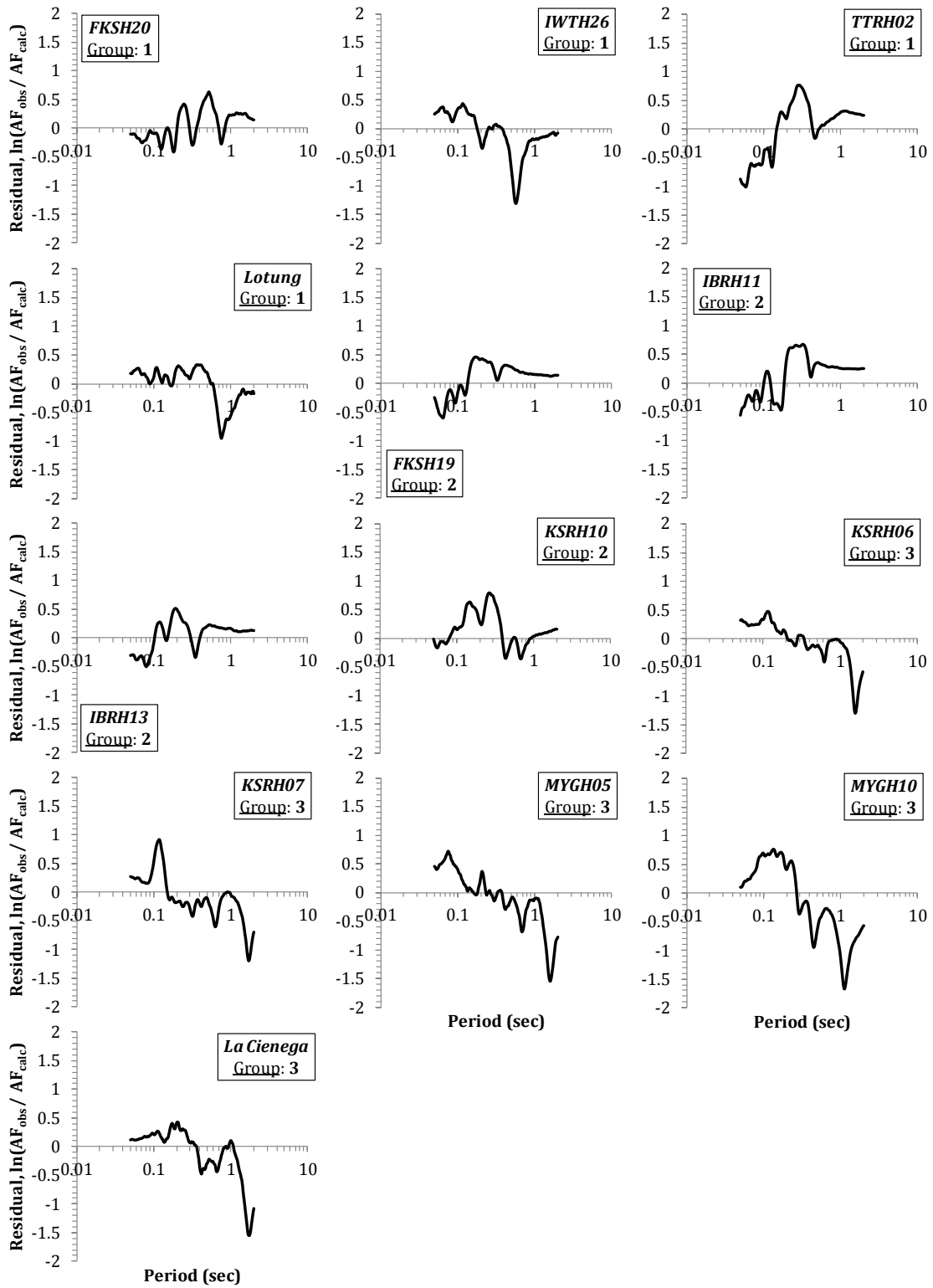


Figure 5.12: Calculated *mean* residuals for all sites based on the best-fit damping profile

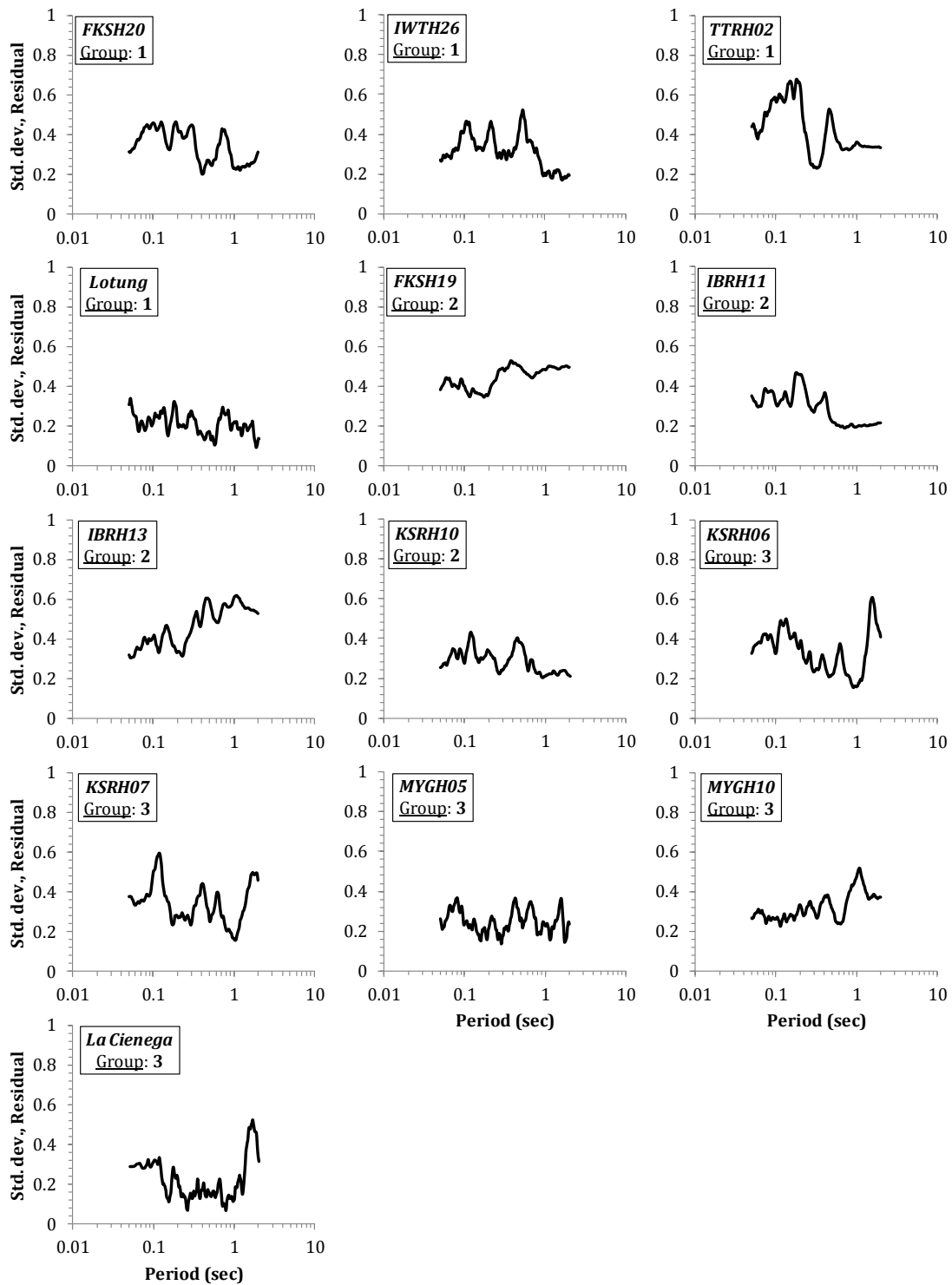


Figure 5.13: Variability associated with the residual in the predictions based on the best-fit damping profile

well represented by a one-dimensional, horizontally layered and infinitely extending medium. Non-vertical, incidence of the seismic waves as well as any lateral variations in the material properties is ignored. Moreover, the presence of more complex phenomena such as surface waves (i.e., Rayleigh and Love waves) in the surficial recordings cannot be investigated using a one-dimensional model. More sophisticated three-dimensional analysis is required to identify and study these phenomena. Therefore, we must acknowledge that there are limitations and errors associated with the modeling of the vertical arrays selected within the framework of the present study. Nevertheless, in engineering practice one-dimensional site response analysis is performed without a prior knowledge of the applicability of its assumptions to the wave propagation conditions at any given site. Therefore, this study applies an assessment of the applicability of the one-dimensional modeling approach to vertical arrays under investigation, but does not exclude any arrays based on a poor fit to the one-dimensional assumption.

Thompson *et al.* (2012) developed taxonomic rules to be applied to vertical arrays for the identification of different sources of error. The researchers studied 100 Kik-Net stations by using motions which produced peak ground accelerations at the surface less than $0.1 g$ to ensure that nonlinear effects were minimized in the analysis. The arrays were modeled as one-dimensional systems, similarly to the present study. Theoretical linear-elastic transfer functions were computed by utilizing a best-fit small strain damping value. The theoretical transfer functions were then evaluated against the empirical transfer functions obtained from the borehole-surface recordings. Finally, the inter-event variability depicted in the empirical transfer functions was quantified.

Thompson *et al.* (2012) defined two criteria for the taxonomy of vertical arrays. First, they acknowledged that high inter-event variability in the observed transfer functions (σ_{ln}) may arise from possible three-dimensional source and path effects that are different from event to event. They suggested that when high inter-event variability is seen in the empirical transfer functions, a more elaborate three-dimensional model may be warranted. To quantitatively define this taxonomic criterion, they calculated the *median* values of σ_{ln} between the first and the fourth peak of the observed transfer functions for each array. They set a threshold value of σ_{ln} at 0.35, with high variability (*H*) indicated when $\sigma_{ln} > 0.35$, and low variability (*L*) indicated when $\sigma_{ln} < 0.35$. FIGURES 5.14a and 5.14b illustrate arrays characterized by “high variability” (*H*), and “low variability” (*L*), respectively.

The second criterion set by Thompson *et al.* (2012) was related with the misfit between the one-dimensional linear-elastic transfer function and the empirical transfer function. As previously discussed, any discrepancies between the theoretical and the observed transfer functions can be attributed to: 1) erroneous values of the material properties, and/or 2) two or three dimensional effects such as lateral heterogeneity. Rather than computing the RMSE between the observations and the predictions, Thompson *et al.* (2012) chose to use a goodness-of-fit measure related to the alignment of the resonant peaks. They selected the Pearson’s sample correlation coefficient (r) as the most appropriate measure.

In general, the Pearson’s sample correlation coefficient (r) between two data series X and Y of the same length (N) can be obtained as:

$$r = \frac{\sum_{i=1}^N [(X_i - \bar{X}) \cdot (Y_i - \bar{Y})]}{\sqrt{\sum_{i=1}^N (X_i - \bar{X})^2} \cdot \sqrt{\sum_{i=1}^N (Y_i - \bar{Y})^2}} \quad (5.4)$$

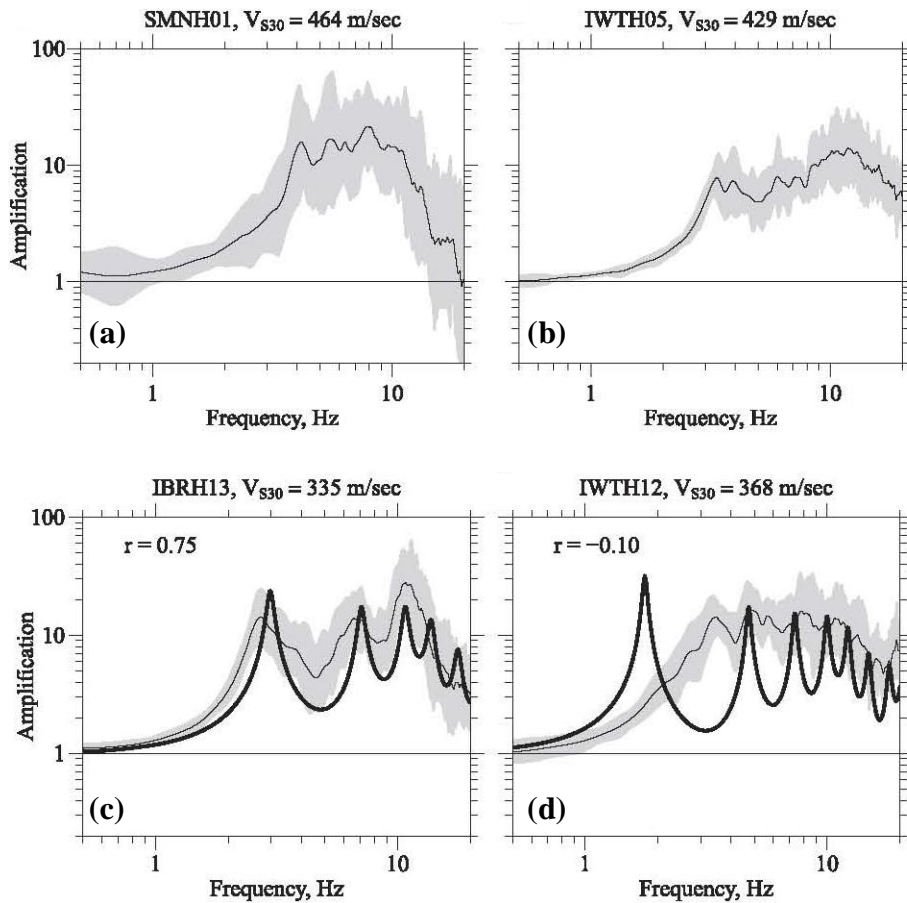


Figure 5.14: Illustration of: (a) a high σ_{ln} array, (b) a low σ_{ln} array, (c) an array with a good fit between the theoretical and the observed transfer functions, and (d) an array with a poor fit between the theoretical and the empirical transfer functions (from Thompson *et al.*, 2012)

where \bar{X} and \bar{Y} are the mean values of X and Y , respectively. The correlation coefficient, r , takes on values between -1 and 1 , and it can be thought of as the dot (inner product) between two vectors in N -dimensional space, where each data series is an N vector of unit length (Wilson, 2011).

Thompson *et al.* (2012) calculated values of r for 200 logarithmically spaced frequencies between the first and the fourth peak of the transfer functions. The researchers classified sites as having a “good fit” (G) when $r > 0.6$, while sites with

$r < 0.6$ were classified as having a “poor fit” (P). FIGURES 5.14c and 5.14d show examples of sites characterized by a “good fit” (G), and “poor fit” (P), respectively.

Thompson *et al.* (2012) used a two letter classification scheme based on the above criteria to define four categories of vertical arrays:

1. *LG arrays* have “low variability” (L), and “good fit” (G). According to Thompson *et al.* (2012), LG arrays are ideal for the assessment and improvement of one-dimensional models.
2. *LP arrays* have “low variability” (L), and “poor fit” (P). Even though these sites may be used to improve one-dimensional analysis, special effort should be made for the identification of specific sources of error (i.e., spatial heterogeneity, erroneous material properties).
3. *HP arrays* have “high variability” (H), and “poor fit” (P). At these arrays, three dimensional effects are most probably influencing the recordings, and thus one-dimensional modeling may not be appropriate.
4. *HG arrays* have “high variability” (H), and “good fit” (G). For Thompson *et al.* (2012), the exact directional effects of the passing seismic waves at these sites are difficult to interpret.

Following a similar procedure as the one developed by Thompson *et al.* (2012), we assessed the possible sources of error associated with the modeling of the particular 13 arrays considered in this study. The only alternation between the adopted procedure and the one described above, is that the taxonomic criteria were applied on the amplification factors rather than on the transfer functions. Moreover, only recorded motions with $PGA_{base} \leq 0.05 g$ were used. The *median* inter-event variability in the observed amplification factors, between the first and the fourth

peak, was obtained. Additionally, the goodness-of-fit, in terms of the alignment of the resonances, between the *median* linear-elastic amplification factor (AF_{calc}) and the *median* observed amplification factor (AF_{obs}), at each vertical array, was evaluated. The Pearson's sample correlation coefficient, r , was computed for 512 logarithmically spaced periods between the first and the fourth peak. The range of the considered frequencies, and the computed *median* σ_{ln} , and correlation coefficients, r , for the 13 sites are tabulated in *TABLE 5.3*. The corresponding two-letter classification based on the scheme proposed by Thompson *et al.* (2012) is also shown.

Based on the results shown in *TABLE 5.3*, it can be observed that there are: 1) 4 sites classified as *LG* (FKSH20, FKSH19, IBRH13 and KSRH10), 2) 7 sites classified as *LP* (IWTH26, Lotung, KSRH06, KSRH07, MYGH05, MYGH10, and La Cienega), and 3) 2 sites classified as *HP* (IBRH11, and TTRH02). Therefore, if the taxonomic criteria (Thompson *et al.*, 2012) are strictly met, the 4 *LG* sites should be considered as ideal for the assessment of the performance of the different one-dimensional site response models, while the 7 *LP* sites could be used only after the identification and minimization of specific sources of error (i.e., shear wave velocity calibration). Contrary, one-dimensional modeling of the 2 *HP* sites should be avoided.

The limited number of vertical arrays under investigation in this study allows for the visual evaluation of the taxonomic criteria, which was not possible for the 100 sites analyzed by Thompson *et al.* (2012). *FIGURES 5.15* through *5.17* separately present the inter-event variability in the observed amplification factors, as well as the comparison between the *median* theoretical and observed amplification factors, for the three groups of arrays (i.e., *Group 1*, *Group 2*, and *Group 3*) defined in *Chapter 4*. Based on visual examination, the *Group 1* sites (*FIGURE 5.15*) generally show low

Table 5.3: Frequency range, *median* σ_{ln} and correlation coefficient, r , for each array

Site	Group	Frequency range (Hz)	Median $\sigma_{ln} - AF_{obs}$	Correlation Coefficient, r	Category
<i>FKSH20</i>	1	0.5 - 20	0.29	0.76	LG
<i>IWTH26</i>	1	1.1 - 20	0.33	0.40	LP
<i>TTRH02</i>	1	1.0 - 20	0.46	0.34	HP
<i>Lotung</i>	1	0.5 - 20	0.2	0.43	LP
<i>FKSH19</i>	2	1.4 - 20	0.29	0.71	LG
<i>IBRH11</i>	2	1.25 - 20	0.38	0.48	HP
<i>IBRH13</i>	2	1.4 - 20	0.31	0.66	LG
<i>KSRH10</i>	2	1.0 - 20	0.28	0.67	LG
<i>KSRH06</i>	3	0.5 - 5	0.24	0.50	LP
<i>KSRH07</i>	3	0.5 - 5	0.25	0.45	LP
<i>MYGH05</i>	3	0.5 - 5	0.23	0.48	LP
<i>MYGH10</i>	3	0.5 - 5	0.23	-0.04	LP
<i>La Cienega</i>	3	0.5 - 5	0.21	-0.06	LP

variability and good fit between the computed and the observed *median* amplification factors, even for sites with an r value lower than 0.6 (*IWTH26* and *Lotung*). For *IWTH26* and *Lotung* arrays, the resonances are well aligned, yet the correlation coefficient is small because it overemphasizes the large overprediction of the response near the first modal period of the site due to the “within” wavefield assumption. The *TTRH02* array is the sole *Group 1* site that is not fit adequately by the model. This particular site is characterized by high σ_{ln} and severe discrepancies between the predicted and the observed amplification factors. As mentioned previously, the *TTRH02* site is located at a relatively high altitude on sloping ground, which violates the assumed one-dimensional wave propagation in a horizontally

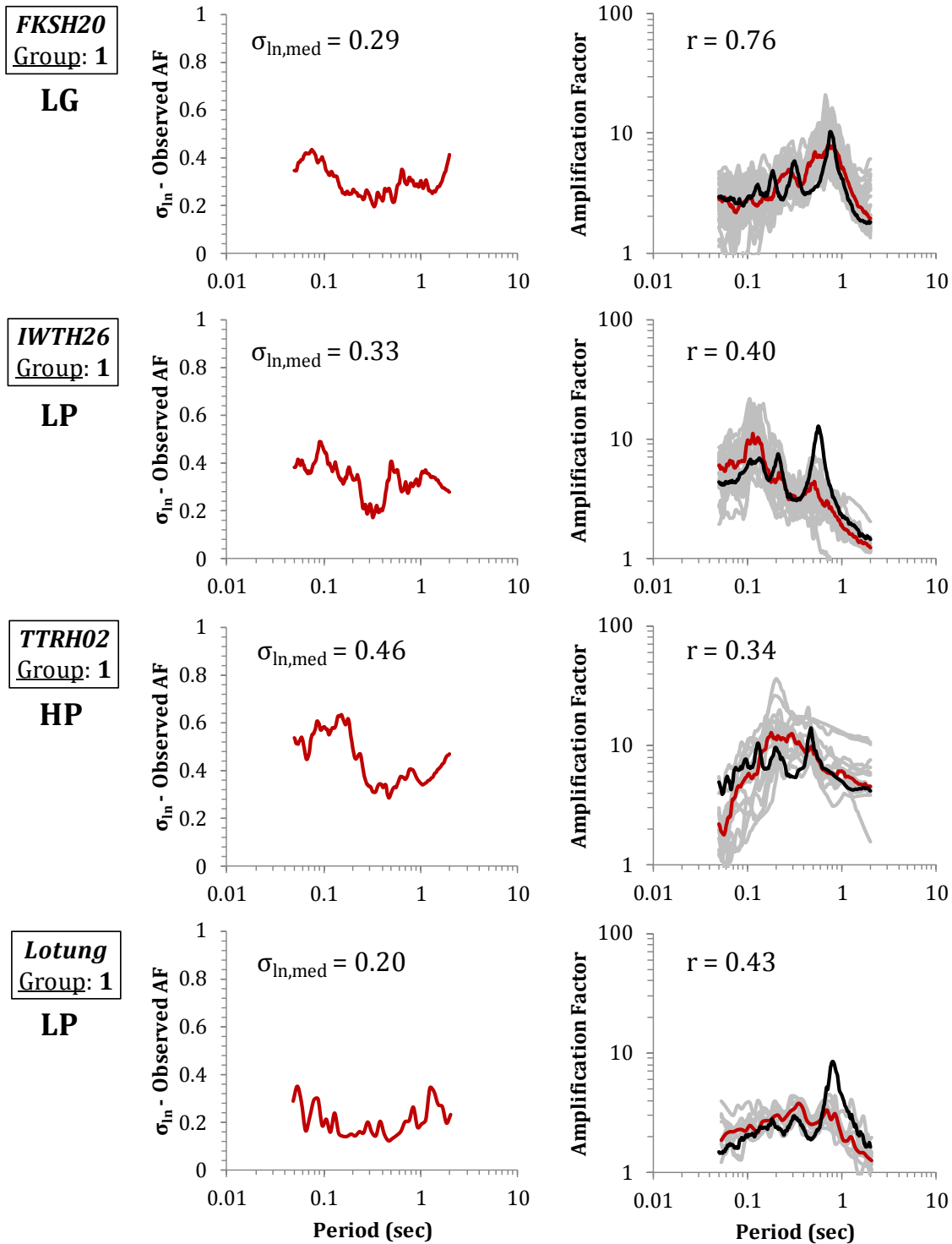


Figure 5.15: Inter-event variability (σ_{ln}) and comparison between the observed and computed amplification factor, for *Group 1* sites.

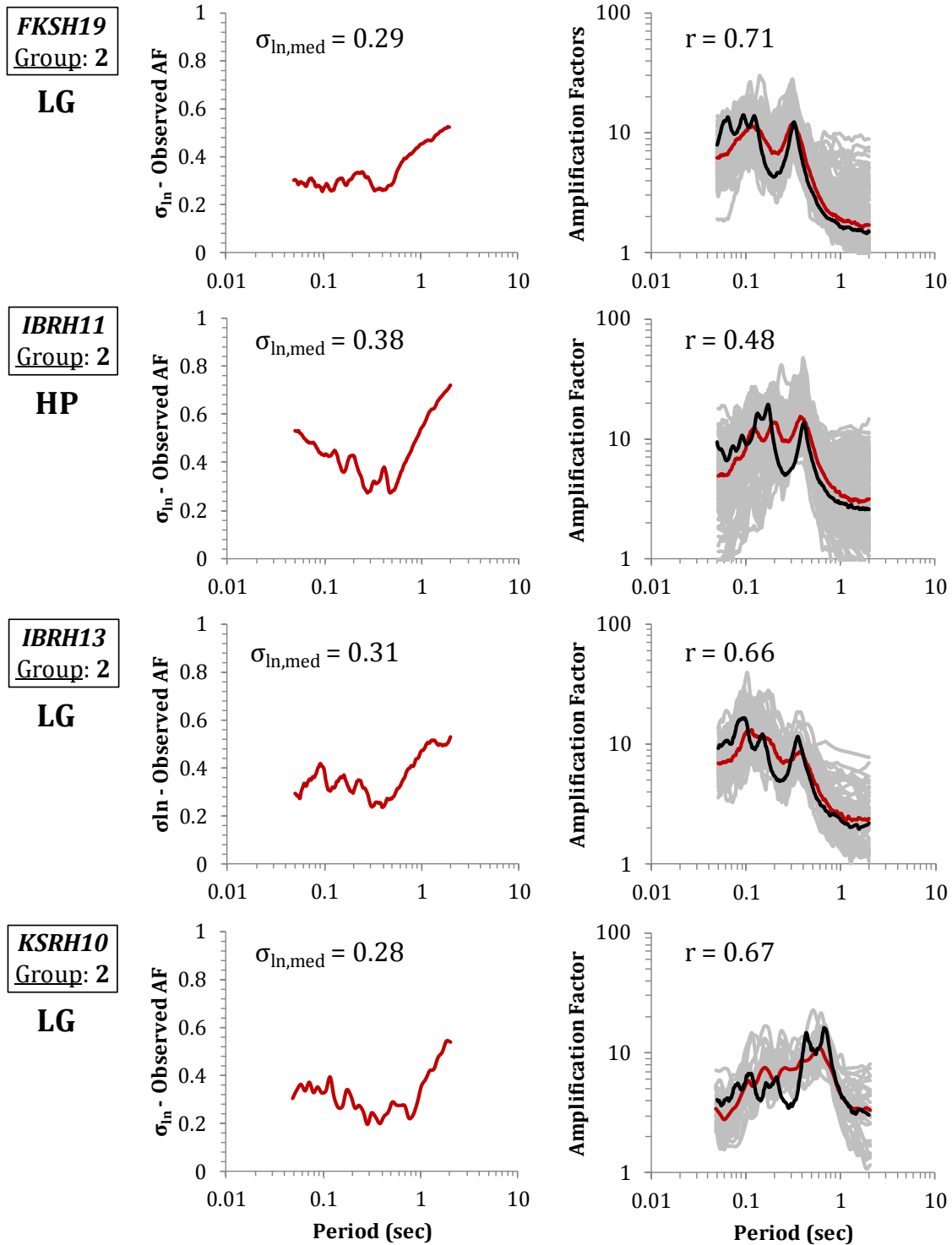


Figure 5.16: Inter-event variability (σ_{ln}) and comparison between the observed and computed amplification factor, for Group 2 sites.

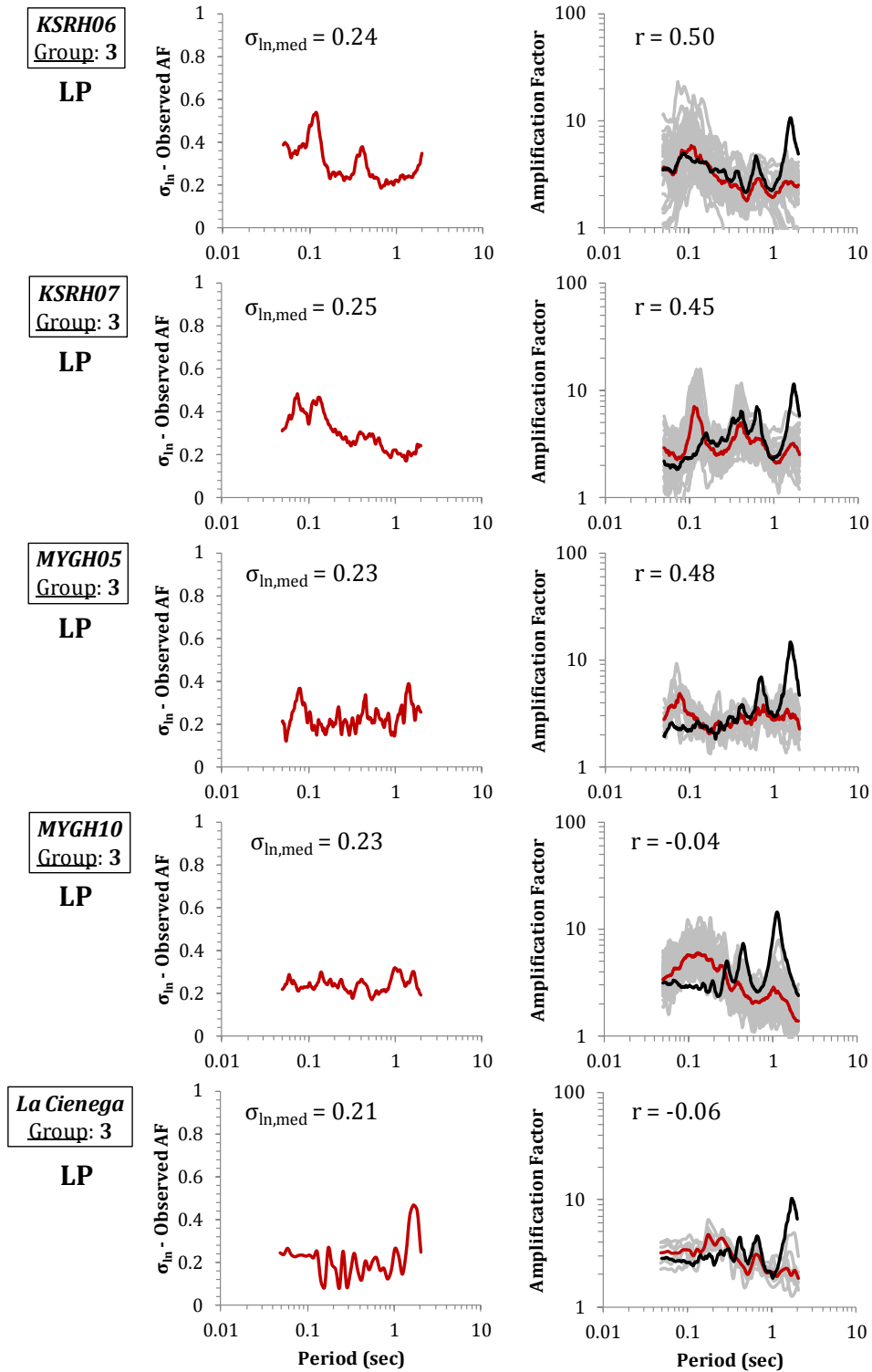


Figure 5.17: Inter-event variability (σ_{ln}) and comparison between the observed and computed amplification factor, for Group 3 sites.

layered medium. A more elaborate three-dimensional modeling of the response at the particular site may yield results closer to the observations.

Based on visual examination, all *Group 2* sites show very good agreement between the observed and theoretical amplification factors (*FIGURE 5.16*). Nevertheless, all of these arrays also display substantial variability at high periods ($T > 0.6 - 0.8$ s). Given the fact that a strong velocity contrast within the first 50 m of the profile is a common characteristic of these arrays, it can be inferred that the recordings may be influenced by other phenomena, such as trapped surface waves (i.e., Love waves). Despite this observation, due to the high goodness-of-fit, we think that *Group 2* sites are suitable for one-dimensional modeling, with the remark that special care should be taken when the high period response is evaluated.

Finally, *Group 3* arrays are characterized by low variability (*FIGURE 5.17*), indicating an applicability of the one-dimensional assumption. Moreover, from *FIGURE 5.17* it can be seen that the peaks of the computed and observed amplification factors are very well aligned for the KSRH06, and MYGH05 sites. In contrast, for the KSRH07, MYGH10 and La Cienega arrays the peaks are well aligned only at the first two site periods. At lower periods (higher frequencies), different degrees of misfit are observed. For example, a clear disagreement between the predictions and the observations is seen at $T \sim 0.12$ s, for both KSRH07 and MYGH10. Particularly for MYGH10, the difference is seen across a wide range of periods. This observation is probably due to the incorporation of erroneous shear wave velocity values of the strata at shallow depths. A shear wave velocity calibration may alleviate these discrepancies.

5.5. Summary

In this chapter, common assumptions regarding one-dimensional site response analysis were evaluated. Accordingly, we identified: *i)* the wavefield assumption best simulating the boundary conditions at the 13 vertical arrays presented in [Chapter 4](#), *ii)* the small-strain damping values that should be used to account for additional in-situ small strain attenuation mechanisms, and *iii)* the validity of the assumed one-dimensionality of each one of the 13 borehole arrays.

First, by comparing the theoretical linear-elastic and observed transfer functions, it was illustrated that some sites are better modeled by the “within” assumption while others are better modeled by the “incoming only” wavefield. The key parameters influencing the selection of the appropriate wavefield were: *i)* the depth to the downhole sensor, and *ii)* the existence of any strong velocity contrasts within the profiles. The first group (*Group 1*) of sites consisted of sites where the downhole sensor is positioned at depths of, approximately, equal to or less than 100 *m* (FKSH20, IWTH26, TTRH02, and Lotung arrays). These sites seemed to be better characterized by a “within” wavefield assumption. A second group (*Group 2*) included the sites which are characterized by a strong shear wave velocity contrast within the first 50 *m* of the profile (FKSH19, IBRH11, IBRH13, and KSRH10 arrays). At these sites, both “within” and “incoming only” type of motions can be input at their base with the corresponding numerical results being similarly close to the observations. Finally, the last group (*Group 3*) included sites with a downhole sensor depth greater than approximately 200 *m* (KSRH06, KSRH07, MYGH05, MYGH10, and La Cienega arrays). *Group 3* sites were best simulated by the “incoming only” wavefield.

Assuming a “within” wavefield assumption for all 13 vertical arrays considered, we identified the best-fit small-strain damping profiles that could incorporate the attenuation through wave scattering. For each considered array, multiple linear-elastic amplification factors were computed using motions with $PGA_{base} \leq 0.05 g$ and the D_{min} profiles multiplied by a ranging factor. The best-fit value of the latter was obtained by minimizing the RMSE between the computed and observed responses. The deeper arrays, particularly the ones categorized in *Group 3*, are related with relatively larger factors applied on D_{min} . The best-fit damping profiles preserve and exacerbate the initial depth-dependence of the small-strain damping. The highest values of damping are assigned to the shallow, thin layers which are typically associated with higher heterogeneity and thus greater attenuation through wave scattering.

Finally, the taxonomic rules developed by Thompson *et al.* (2012) were applied to the 13 selected vertical arrays to assess the different sources of error associated with the one-dimensional modeling. Moreover, the limited number of vertical arrays under investigation allowed for the visual evaluation of the taxonomic criteria. Most vertical arrays showed a low inter-event variability in the observed amplifications factors, and a relatively good agreement between the predictions and the observations. Exceptions to this remark were the TTRH02 and MYGH10 arrays. TTRH02 site is located at a relatively high altitude on sloping ground, something that violates the assumed one-dimensional wave propagation in a horizontally layered medium. Calibration of the shear wave velocity of the shallow strata of the MYGH10 profile seems to be required in order to capture the high frequency peaks in the observed amplification factors.

Chapter 6

Assessment of Performance of One-Dimensional Site Response Methodologies

6.1. Introduction

As discussed in [Chapter 5](#) the performance of one-dimensional site response is affected by several factors, such as: 1) simplifications associated with the one-dimensional wave propagation assumption, 2) biases in the utilized material properties, or 3) deficiencies of certain aspects of the theoretical models and/or numerical algorithms. After the assessment of the errors associated with the one-dimensional modeling of the specific 13 vertical arrays for linear elastic conditions at small strains ([Chapter 5](#)), deficiencies associated with the various 1-D models that incorporate soil nonlinearity (EQL, EQL-FD and NL, see [Chapter 2](#)) can be isolated and identified by evaluating the theoretical results against the recordings.

This chapter describes an assessment of the various theoretical models. The assessment is first made on a site-by-site basis. In this case, the performance of the EQL, EQL-FD and NL site response methodologies is assessed, at each one of the 13 sites. Then, an overall assessment of the different models is quantified by combining the results from all 13 arrays. Physical explanations regarding any discrepancies between the predictive results and the observations are provided. Specifically, the effect of the intensity of shaking is investigated. Finally, we compare our results with the results of Kaklamanos *et al.* (2013), as presented in [Chapter 3](#).

6.2. General Framework – Example of Site Response Validation

The assessment of the performance of the 1-D site response methodologies (EQL, EQL-FD and NL) includes the comparison of site response results with recordings from the selected borehole arrays. The equivalent-linear analyses (EQL, EQL-FD) were performed using the “within” wavefield assumption for all 13 sites, as described in [Chapter 5](#), while nonlinear analyses were conducted assuming a perfectly rigid base (which is the equivalent of the “within” wavefield assumption). The latter assumption was based on the findings by Stewart *et al.* (2008) and Kottke (2010), who indicated that a perfectly rigid base represents the boundary conditions typically encountered at the base of vertical arrays. Moreover, modulus reduction and damping curves, based on the Darendeli (2001) model, were assigned to all soil materials, as discussed in [Chapter 4](#).

The results from the analyses initially, were classified according to their corresponding level of shaking, as depicted by the peak acceleration of the input motions (PGA_{base}). Since the recorded peak ground acceleration at the base sensor ranges from low (less than 0.05 g) to high (greater than 0.3 g), the effect of input intensity on the accuracy of the predictions is investigated. Five different ranges of PGA_{base} were considered; $PGA_{base} \leq 0.05 g$, $0.05 g < PGA_{base} \leq 0.10 g$, $0.10 g < PGA_{base} \leq 0.20 g$, $0.20 g < PGA_{base} \leq 0.30 g$, and $PGA_{base} > 0.30 g$. [TABLE 6.1](#) tabulates the number of motions within each PGA_{base} range, for each borehole array. As expected, most of the recorded motions at the base of the arrays are characterized by $PGA_{base} \leq 0.05 g$, with the number of motions across the 13 sites and the five PGA_{base} bins not being evenly distributed. For example, IBRH11 has a large number of motions with $PGA_{base} \leq 0.05 g$ (202 motions), while the TTRH02 array has a relatively small number of motions with $PGA_{base} \leq 0.05 g$ (10

Table 6.1: Number of motions per PGA_{base} range for all vertical arrays

Site	$< 0.05 g$	$0.05 g - 0.1 g$	$0.1 g - 0.2 g$	$0.2 g - 0.3 g$	$> 0.3 g$
<i>FKSH20</i>	41	9	1	-	1
<i>IWTH26</i>	22	4	2	2	-
<i>TTRH02</i>	13	1	-	-	2
<i>Lotung</i>	10	3	3	-	-
<i>FKSH19</i>	132	-	1	-	1
<i>IBRH11</i>	202	-	1	1	-
<i>IBRH13</i>	54	9	7	2	-
<i>KSRH10</i>	30	4	-	-	-
<i>KSRH06</i>	40	-	6	-	-
<i>KSRH07</i>	36	-	-	2	-
<i>MYGH05</i>	13	7	5	1	-
<i>MYGH10</i>	83	17	3	1	-
<i>La Cienega</i>	6	-	1	1	-

motions). In general, it should be noted that the number of sites and number of input motions with PGA_{base} values within each of the PGA_{base} ranges varies substantially. For example, 682 motions from 13 sites are included in the $PGA_{base} \leq 0.05 g$ range, 30 motions from 10 sites are included in the $0.10 g < PGA_{base} \leq 0.20 g$ range, and 4 motions from 3 sites are included in the $PGA_{base} > 0.30 g$ range.

The evaluation of the site response approaches is conducted by specifically comparing the observed and theoretically computed amplification factors, i.e. the ratios of surface to base response spectra. To compare the results across sites and at different levels of input intensity, the residuals (misfit) in the predictions (i.e. $y = \ln(AF^{obs}/AF^{calc})$) at each site are computed. Positive residuals indicate that the observed amplification is under-predicted by the calculations, while negative

residuals indicate that the observed amplification is over-predicted. To demonstrate the approach used to compare observations and computations, we initially focus on the results from one site. We select the borehole array whose predictive response is less affected by inaccurate material properties (i.e. layering, V_S profile, modulus reduction and damping curves) or the actual wave propagation pattern (i.e. boundary conditions, topographic effects). Based on our engineering judgment, the IBRH13 vertical array is selected to serve as the example site. The following discussion may involve only one out of the thirteen sites analyzed, but many of the observations are valid for the other borehole arrays.

FIGURE 6.1 illustrates the comparison between observed and computed *median* amplification factors for borehole array IBRH13 at different input level intensities. Results are shown for four ranges of PGA_{base} , with *median* values of $0.01 g$, $0.06 g$, $0.11 g$, and $0.20 g$, respectively. As seen in *FIGURE 6.1*, the performance of the EQL, EQL-FD, and NL models strongly depends on the level of shaking, and thus implicitly on the magnitude of the induced shear strains. At low intensity levels, namely for PGA_{base} less than $0.05 g$, there is strong agreement between the observations and theoretical results at all frequencies. A slight over-prediction occurs at periods less than $0.1 s$ and a slight under-prediction at a period of about $0.25 s$, but still the agreement is quite good. As input intensity increases, the computed amplifications factors from the site response methods deviate from each other, as well as from the observations, at periods less than about $0.3 s$ to $0.4 s$. In general, the EQL and NL models strongly under-predict the amplification at shorter periods. EQL-FD analysis seems to agree better with the observations at periods between $0.1 s$ and $0.3 s$, with the exception of the highest input intensities ($PGA_{base} \sim 0.20 g$). Here, some under-prediction is observed. However, at periods

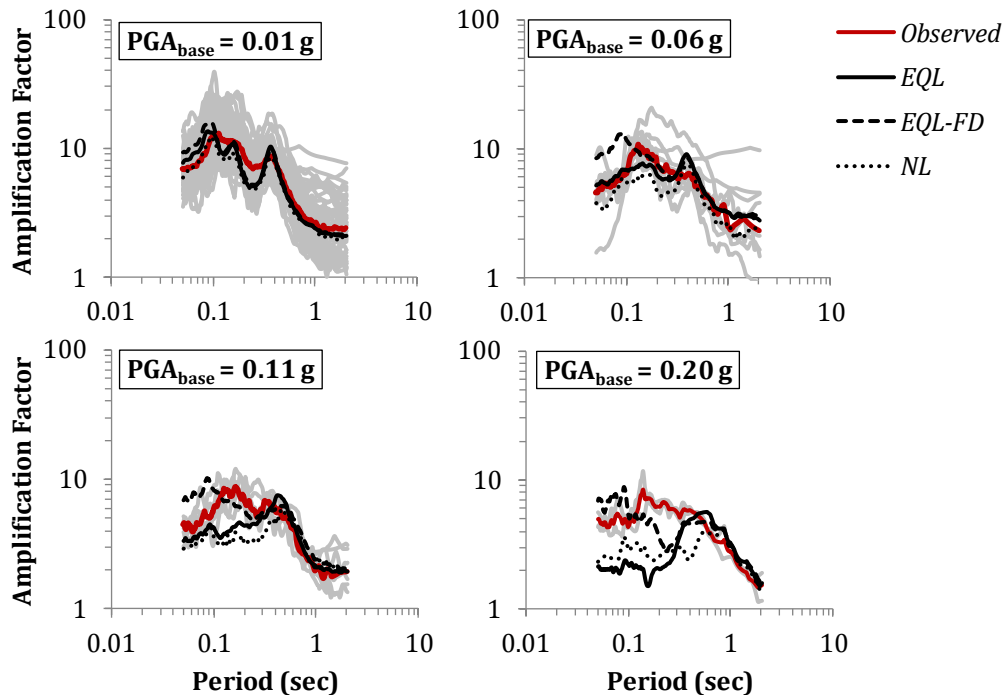


Figure 6.1: Observed and computed Amplification Factors, for the IBRH13 borehole array

below 0.1 s, the EQL-FD approach systematically over-predicts the site amplification. *FIGURE 6.2* presents the corresponding residuals for the results for the IBRH13 site. The results in *FIGURE 6.2* are the direct equivalent of the results in *FIGURE 6.1*, with the EQL and NL approaches producing large positive residuals (i.e., under-prediction) at high frequencies and large input intensities and the EQL-FD approach producing negative residuals (i.e., over-prediction) at high frequencies and large input intensities.

The aforementioned observations regarding the performance of the different site response methods are confirmed by comparing the observed and computed acceleration time series obtained at the surface of the IBRH13 site. For example, *FIGURE 6.3* presents the observed and computed acceleration time series for a motion with $PGA_{base} = 0.01 g$ which was recorded at IBRH13 site on 08/04/03, 20: 57.

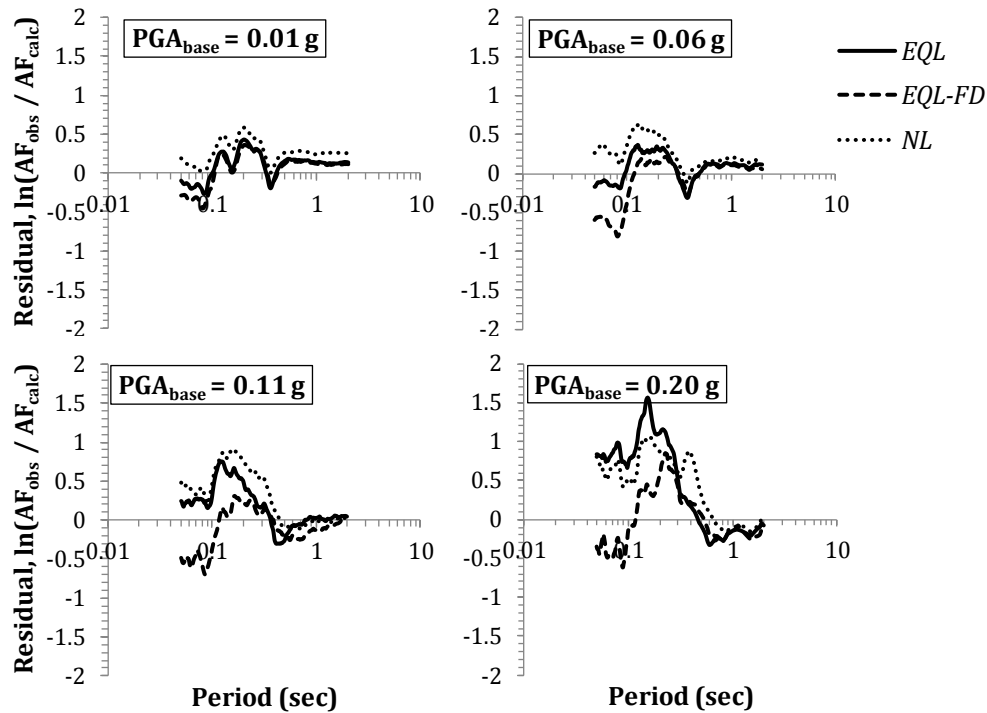


Figure 6.2: Calculated Residuals for all site response methods, for IBRH13 borehole array

Based on *FIGURE 6.3*, it can be seen that the computed responses from the three site response methods are similar to each other and to the observed acceleration time series. On the other hand, the computed acceleration time series at the surface of the IBRH13 site using an input motion with $PGA_{base} = 0.18 g$ recorded on 03/11/11, 14:54, show substantial deviations from the observed response (*FIGURE 6.4*). More specifically, the EQL and NL site response analyses are associated with an under-prediction of the peak ground acceleration and a lack of several high frequency motion components that are present in the observed time series. EQL-FD analysis provides a better prediction of the peak ground acceleration while enhancing the acceleration time history with high frequency motion components.

While the PGA_{base} provides an indication of the induced soil nonlinearity and it is independent of any computations, to fully understand the numerical results

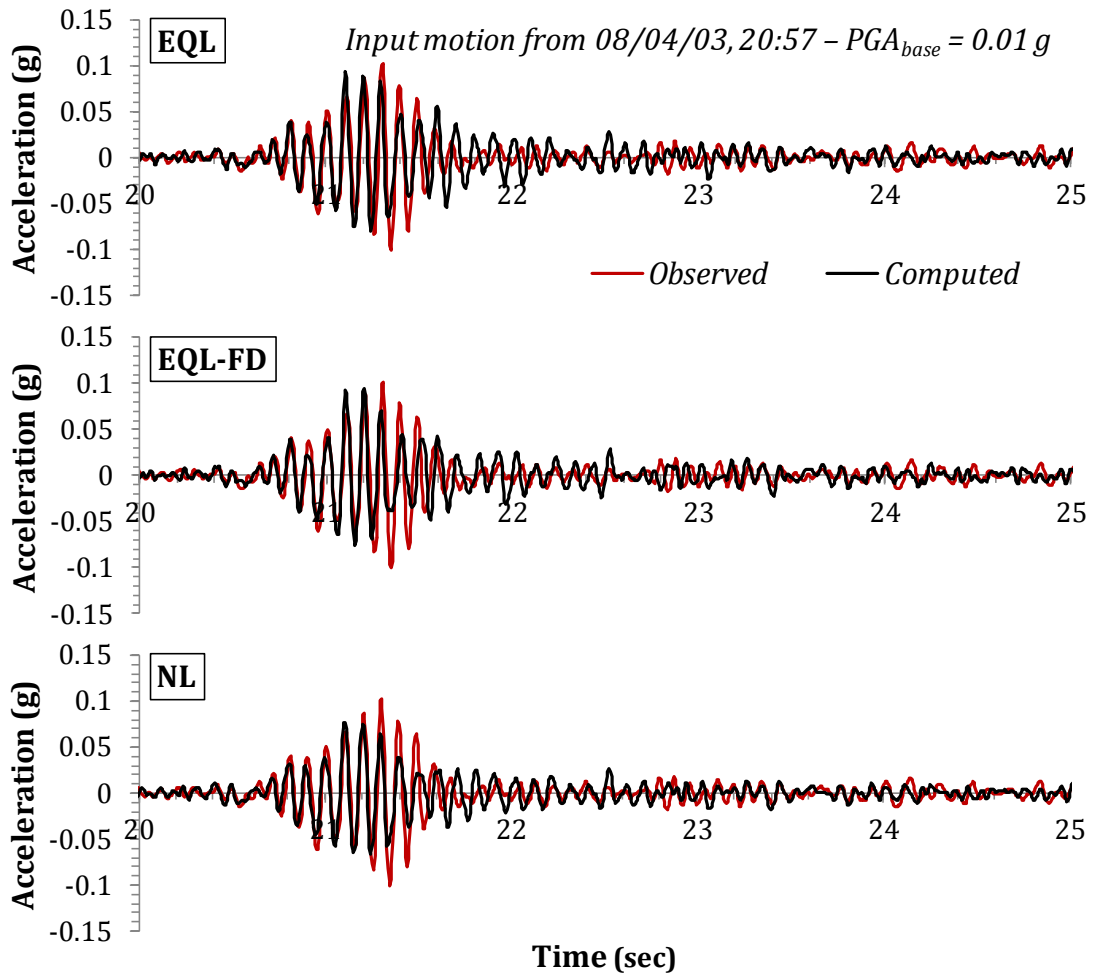


Figure 6.3: Observed and compute acceleration time series at the surface of the IBRG13 site using an input motion recorded on 08/04/03, 20: 57

across all of the vertical arrays, the calculated maximum shear strains, γ_{max} , is used. The magnitude of the induced shear strains is the parameter mostly influencing the accuracy of the predictive results because it directly influences the G/G_{max} and damping values used in site response computations. *FIGURE 6.5* plots the computed γ_{max} , as a function of input motion intensity (PGA_{base}) for each site, and for the different site response methods. As expected, the maximum calculated shear strain increases proportionally with PGA_{base} . The calculated maximum strain varies from 0.001 % at low levels of input intensity to almost 6 % at high PGA_{base} values and so-

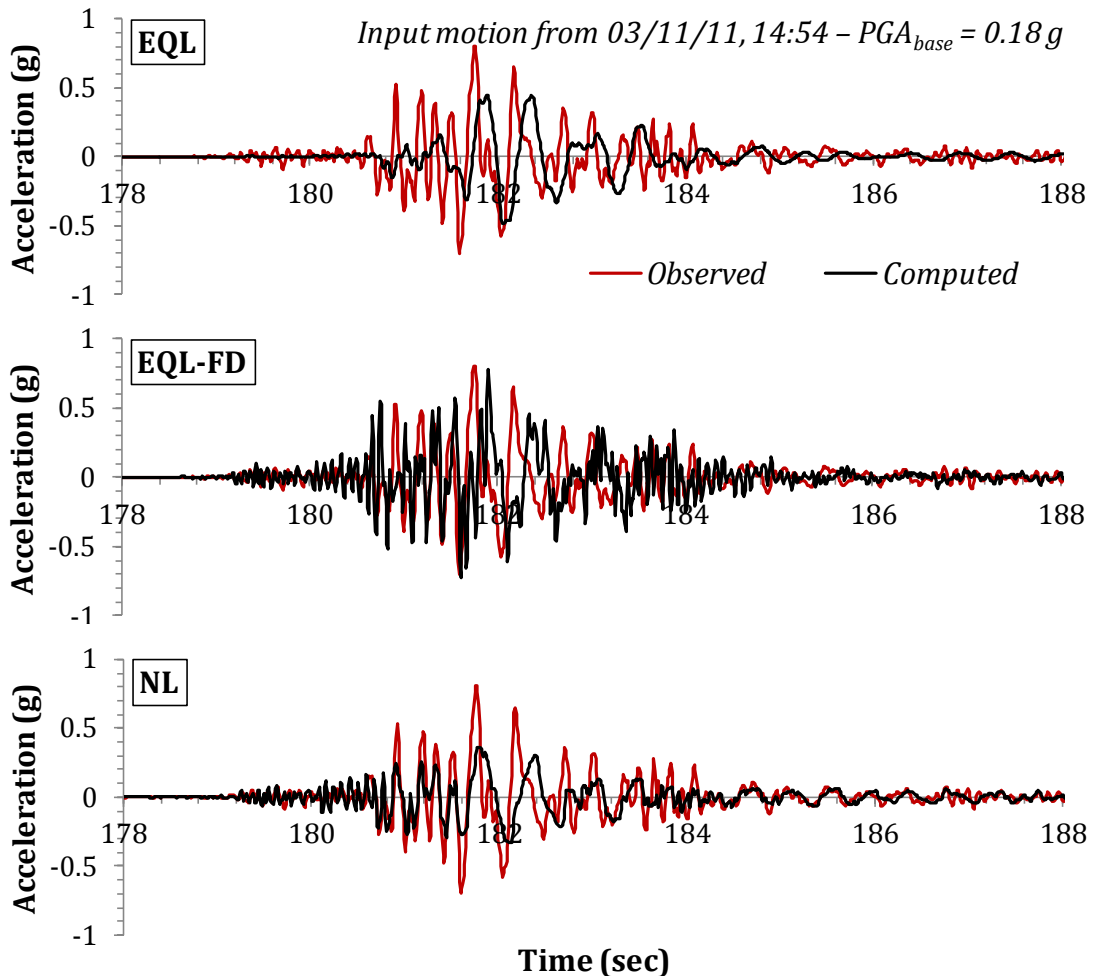


Figure 6.4: Observed and compute acceleration time series at the surface of the IBRG13 site using an input motion recorded on 03/11/11, 14: 54

fter sites (i.e., IWTH26 array). Given the differences in the shear wave velocity profiles and/or the material types at these sites, different sites experience different strain levels at the same input intensity. Nonetheless, the EQL, EQL-FD and NL approaches generally produce the same level of shear strain with only minor differences at higher PGA_{base} values. Thus, any observed differences in the calculated responses are solely due to the theoretical scheme used to develop the numerical models and not the level of induced shear strain.

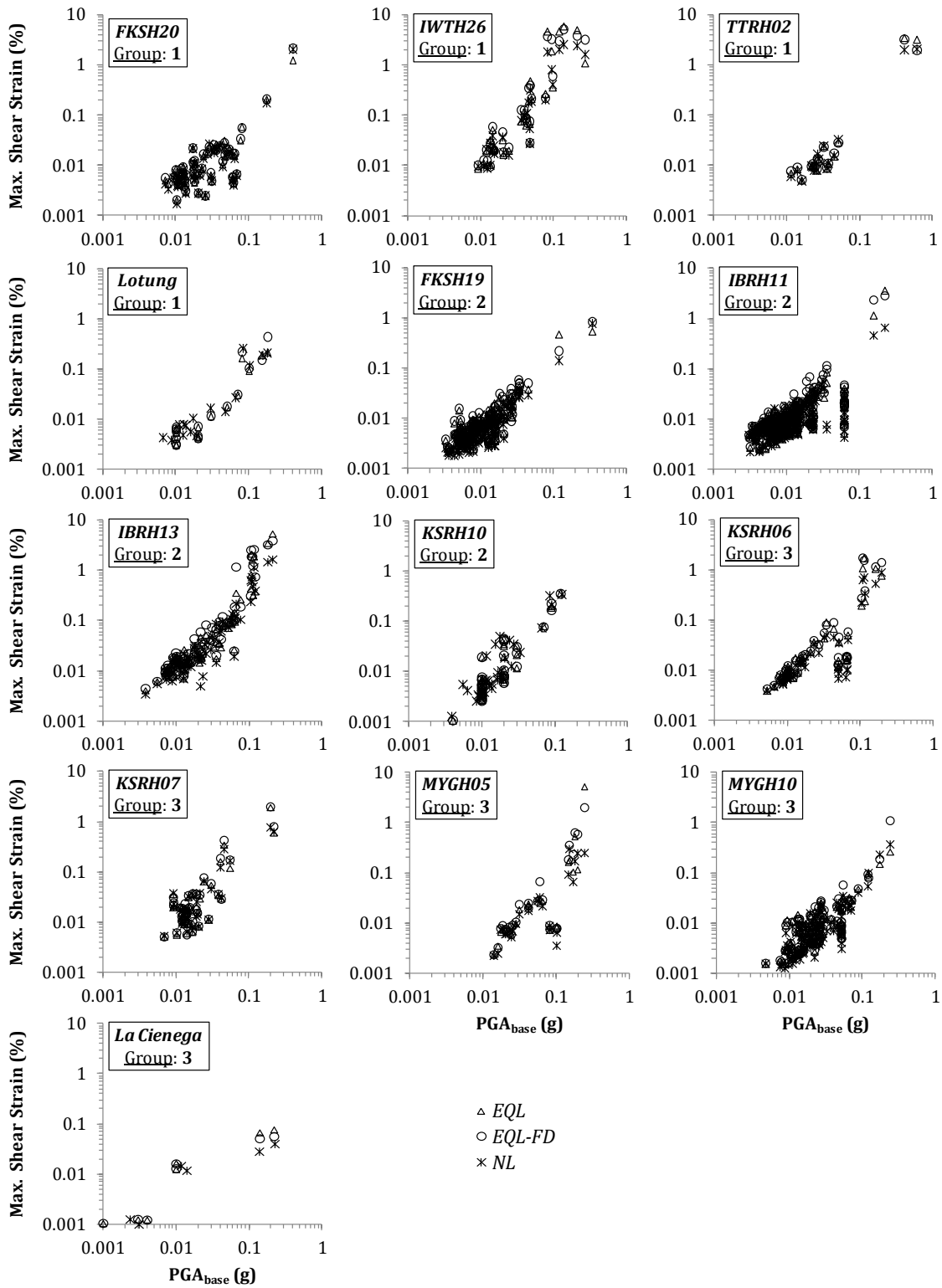


Figure 6.5: Calculated maximum shear strain (γ_{max}) for all sites and input intensities

It should be noted that γ_{max} is computed as part of the analysis and thus is not an independent measure that can be predicted a priori. Nonetheless, the computed γ_{max} should be proportional to the actual induced strains in the soil deposit. Several studies (e.g. Trifunac and Lee, 1996) have indicated that the calculated γ_{max} can be approximated by the ratio of the recorded peak ground velocity at the surface (PGV_{surf}) to a measure of the shear wave velocity at the upper parts of a soil profile (e.g. $V_{S,30}$ or the minimum shear wave velocity, $V_{S,min}$). In the case of instrumented vertical arrays where surface recordings are available, the peak strain ($PGV_{surf}/V_{S,30}$ or $PGV_{surf}/V_{S,min}$) can be obtained before any site response analysis is performed.

FIGURE 6.6 plots the calculated maximum shear strains (γ_{max}) versus the peak strain estimates ($PGV_{surf}/V_{S,min}$) for all sites, input motions and site response models considered. The site response models provide γ_{max} values which are proportional to $PGV_{surf}/V_{S,min}$. The computed γ_{max} is slightly smaller than $PGV_{surf}/V_{S,min}$ at strains less than about 0.03 % and substantially larger at strains greater than 0.1 %. At larger strains, ($PGV_{surf}/V_{S,min}$) tends to be less than γ_{max} because it uses the small-strain shear wave velocity. Nonetheless, despite the discrepancies between the pre-analysis ($PGV_{surf}/V_{S,min}$) and post-analysis (γ_{max}) strain indicators, it can be safely assumed that the latter provides a good predictor of the actual maximum shear deformation induced within the soil deposits.

After the verification of the appropriateness of the categorization of the results based on γ_{max} , the amplification factor residuals (i.e. $y = \ln(AF^{obs} / AF^{calc})$), at specified spectral periods, can be plotted against the corresponding value of γ_{max} . Consequently, the effect of the magnitude of the shear induced deformations on the accuracy of the site response models can be more thoroughly investigated.

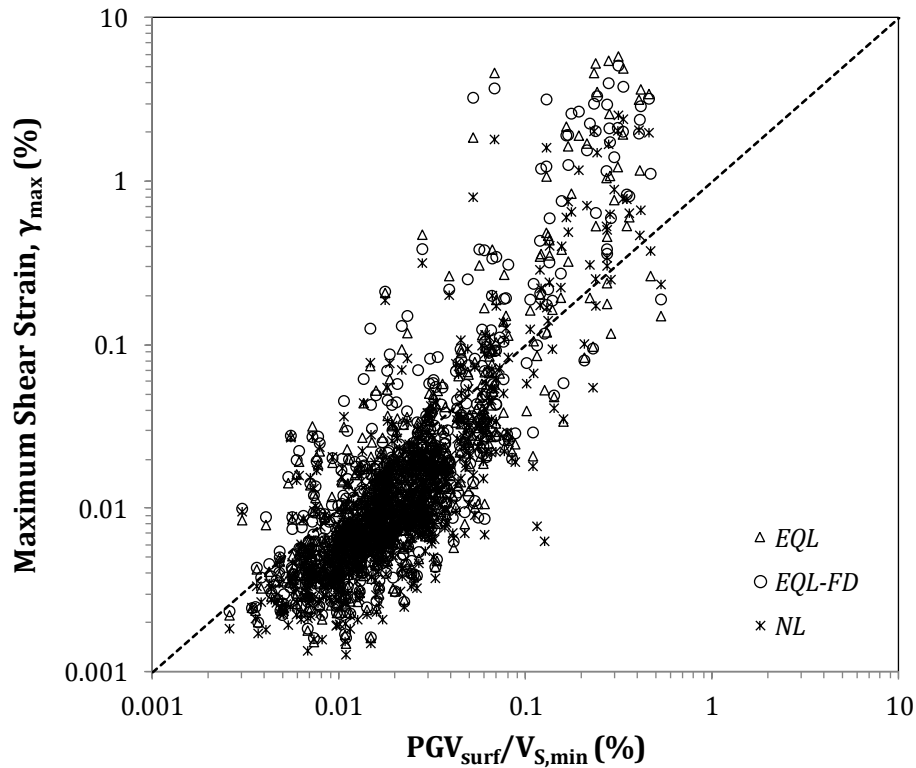


Figure 6.6: Relationship between the calculated maximum shear strains (γ_{max}) and the peak shear strain estimates ($PGV_{surf}/V_{S,min}$) for all sites, input motions and site response models

FIGURE 6.7 illustrates the strain dependence of the amplification residuals from the three site response approaches, for the IBRH13 site. Residuals computed at 6 spectral periods ($T = 0.05$ s, 0.1 s, 0.3 s, 0.5 s, 1.0 s, and 2.0 s) are depicted. At short periods ($T = 0.05$ s and $T = 0.1$ s), the EQL and NL models produce average residuals close to zero at $\gamma_{max} < 0.1$ %, while almost all of the residuals are positive at $\gamma_{max} > 0.1$ %. On the contrary, the EQL-FD residuals at the same spectral periods ($T = 0.05$ s and $T = 0.1$ s), become negative at lower strain values, namely at $\gamma_{max} > 0.01$ %. As the period increases, the differences in the residuals between the three models are gradually reduced. At periods of 0.5 s, 1.0 s, and 2.0 s, the residuals from all three site response models are, for all practical purposes, the same and the

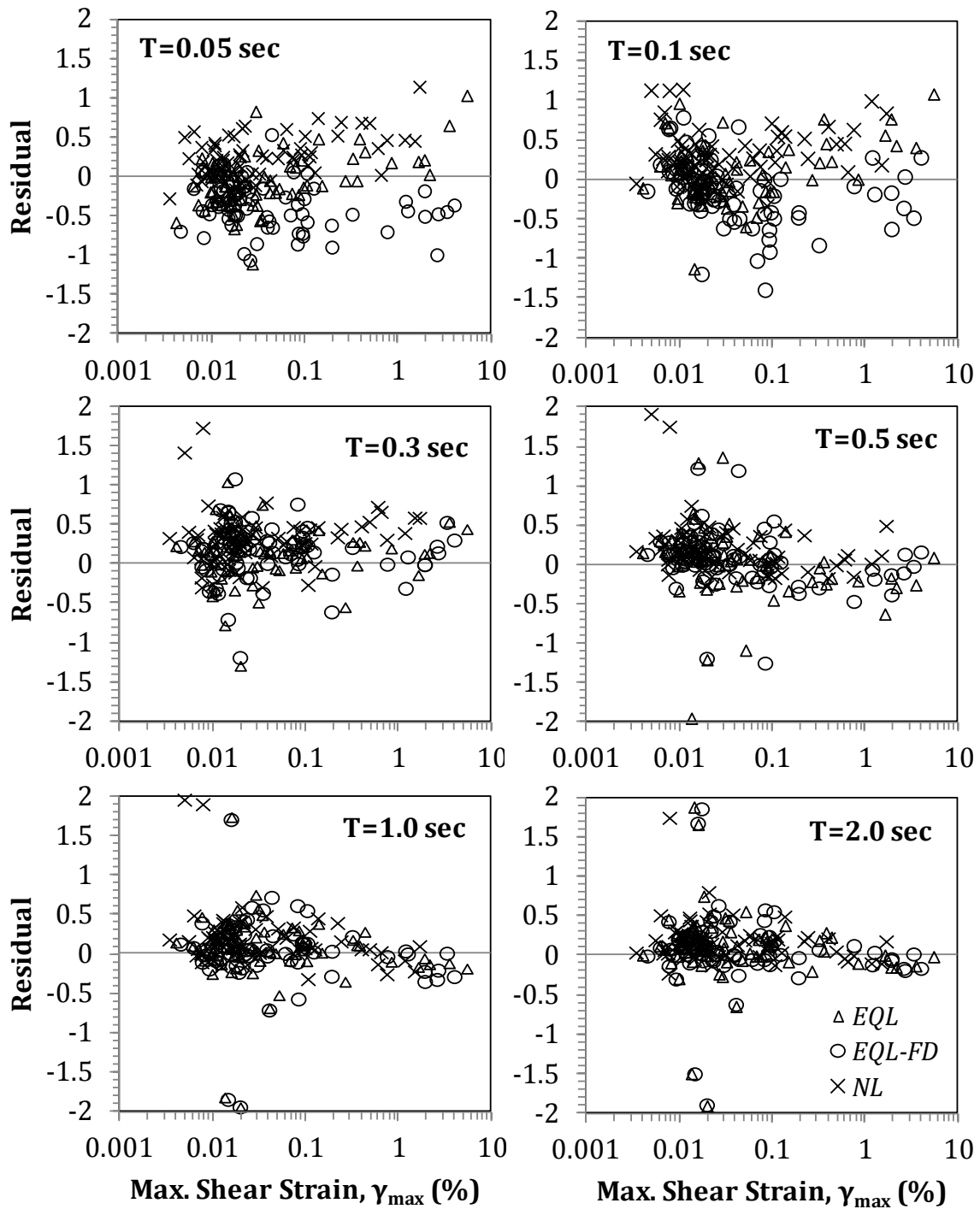


Figure 6.7: Amplification residuals ($y = \ln(AF^{obs} / AF^{calc})$) computed at 6 distinct spectral periods versus calculated maximum shear strain, for IBRH13 site

average residual is very close to zero. This result indicates that at long periods all three models can accurately predict the response. The observations from *FIGURE 6.7* may represent only one out of the thirteen vertical arrays analyzed, but many of these observations are valid for the other sites, as discussed next.

6.3. Results from Analyses on a Site-by-Site Basis

Following the general framework discussed above, the results of our analyses are presented individually for each of the 13 borehole arrays. The evaluation of the performance of the EQL, EQL-FD and NL site response models is made by examining the strain dependence of the amplification residuals (i.e., $y = \ln(AF^{obs} / AF^{calc})$) at 6 spectral periods; $T = 0.05$ s, 0.1 s, 0.3 s, 0.5 s, 1.0 s, and 2.0 s, similar to *FIGURE 6.7* for IBRH13 site. The residuals are first presented and analyzed for periods of $T = 0.05$ s, 0.1 s and 0.3 s and subsequently for periods of $T = 0.5$ s, 1.0 s and 2.0 s.

It is important to keep in mind that the computed amplification residuals may unavoidably reflect the limitations and/or errors in one-dimensional modeling. As discussed in *Chapter 5*, the assumed borehole wavefield as well as potential errors in the material properties (i.e., V_S profile) may lead to inaccurate estimates of the response at specific spectral periods. The periods at which these inaccuracies occur are different for each site. For example, it was shown in *Chapter 5* that the TTRH02 site displayed significant differences between the computed and observed amplification across all spectral periods and these differences most likely are caused by topographic effects. Alternatively, for the KSRH07 and MYGH10 sites the differences between the computed and observed amplification occurred only at spectral periods around 0.1 s, possibly indicating the need for calibration of the

material properties (i.e. shear wave velocity, V_S). Finally, it was observed in [Chapter 5](#) that the “within” wavefield assumption leads to substantially large first mode amplification, particularly at sites where the depth to the downhole sensor exceeds 200 m (*Group 3* sites - KSRH06, LSRH07, MYGH05, MYGH10, and La Cienega).

Keeping in mind the above remarks, *FIGURES 6.8* through *6.10* present the amplification residuals versus maximum calculated strain (γ_{max}) for all sites and the three site response models, at spectral periods of 0.05 s, 0.1 s, and 0.3 s, respectively. From these figures, some trends are obvious across all sites. Particularly, it can be observed that the three site response models provide similar responses at strains smaller than about 0.01 %, irrespectively of the spectral period. For most sites, the average residuals at these strains are close to zero. Because the sites are responding in essentially a linear elastic manner at these strains, the three site response models predict similar responses. Considering that, for most sites, linear elastic analysis (LE) produced responses in good agreement with the observations when input motions with $PGA_{base} < 0.05 g$ were used ([Chapter 5](#)), the relatively low *average* residuals at $\gamma_{max} \leq 0.01 \%$ by the EQL, EQL-FD and NL models is expected.

At larger strain values ($\gamma_{max} > 0.01 \%$), and particularly at $T = 0.05 s$ and $T = 0.1 s$ (*FIGURES 6.8* and *6.9*), the EQL-FD method systematically yields smaller residuals than the EQL and NL methods. That is, the computed short period amplification factors from the EQL-FD model are systematically higher than those computed using the EQL and NL methods. This trend is further magnified with increasing shear straining. At strains greater than about 0.1 %, the EQL-FD residuals are strongly negative for most sites, while the EQL and NL residuals become strongly positive. Therefore, as in the example case of the IBRH13 array (*FIGURE 6.7*),

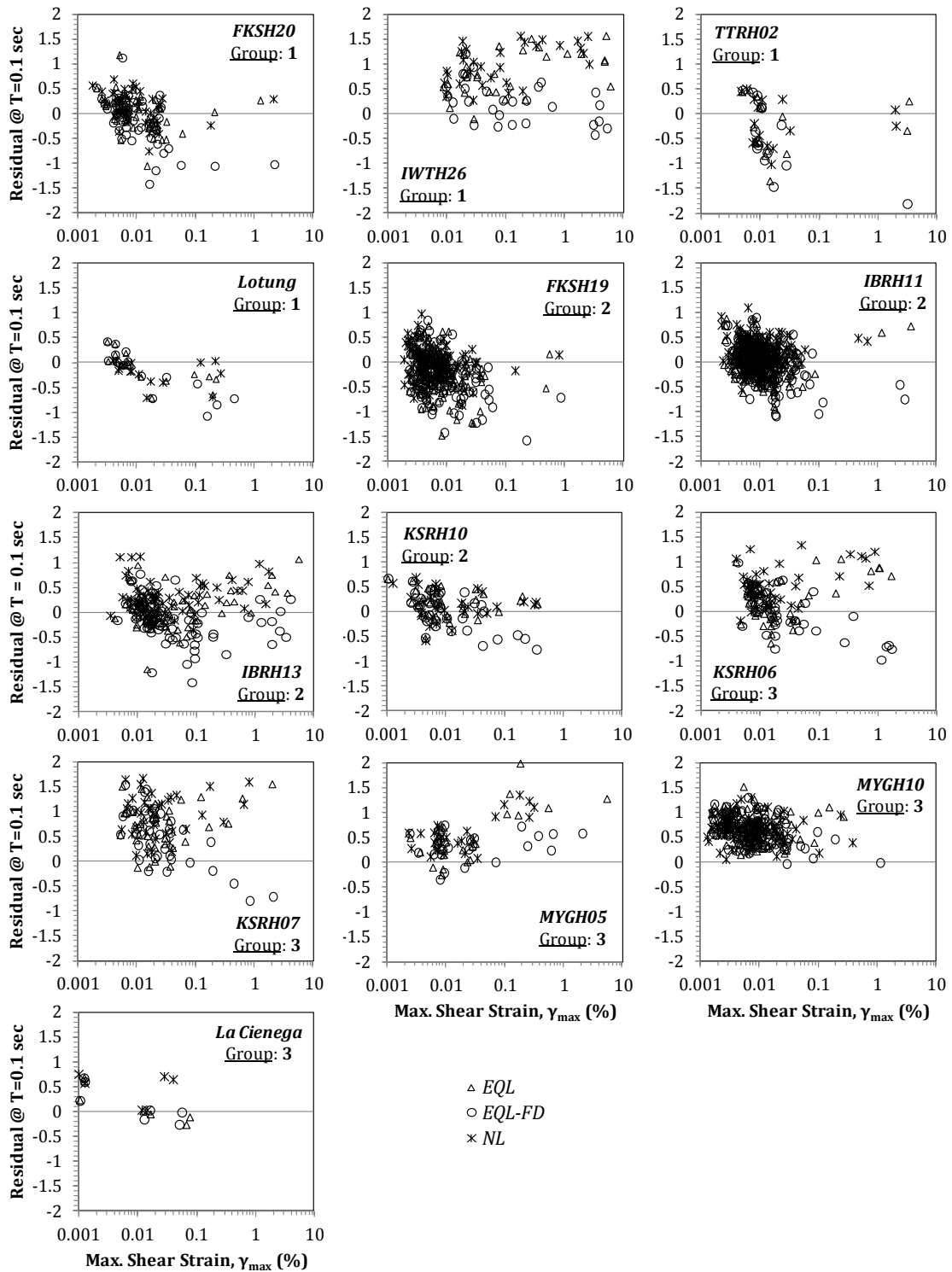


Figure 6.9: Residuals vs maximum calculated shear strains (γ_{max}) for all sites and site response methods - $T = 0.1$ s

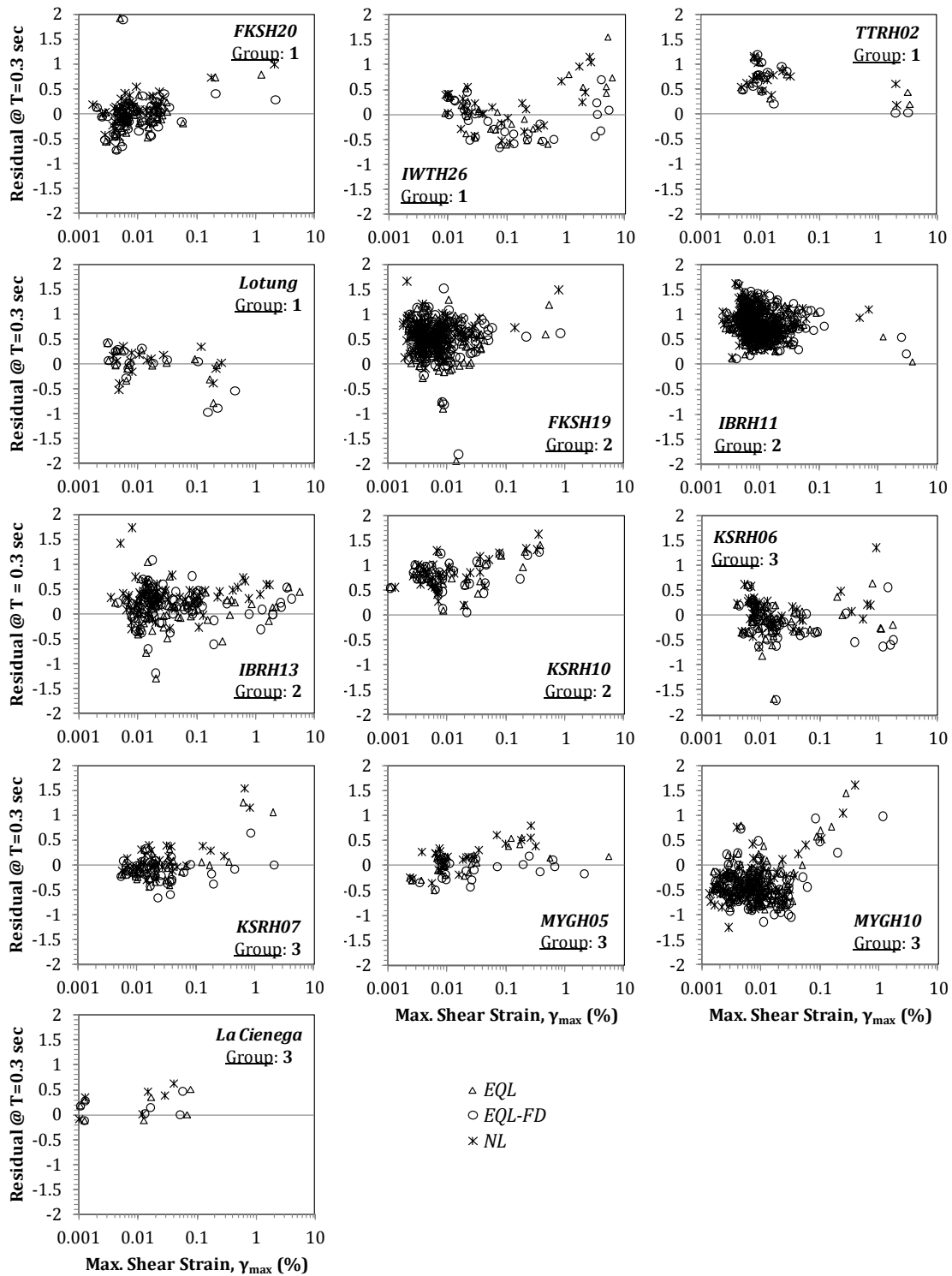


Figure 6.10: Residuals vs maximum calculated shear strains (γ_{max}) for all sites and site response methods - $T = 0.3$ s

we observe an over-prediction of the response by the EQL-FD model and an under-prediction by the EQL and NL methods, at $T = 0.05$ s and $T = 0.1$ s, for most sites. Moreover, the EQL and NL models seem to provide very similar results across all strains and spectral periods (FIGURES 6.8-6.10). The observed differences between the computed amplification factors are substantially smaller, almost negligible, at $T = 0.3$ s (FIGURE 6.10). The accuracy of the site response models at $T = 0.3$ s seems to be predominantly affected by the appropriateness of one-dimensional modeling at each site and not by a particular approach to modeling the nonlinear response.

Summarizing, as seen in FIGURES 6.8 through 6.10, when the earthquake induced strain increases ($\gamma_{max} > 0.01$ %), the EQL-FD model deviates from the EQL and NL models, at low periods ($T = 0.05$ s and $T = 0.1$ s). At strains greater than 0.1 % all three models seem unable to capture the observed behavior at short periods. The EQL and NL models strongly under-predict the amplification, while the EQL-FD approach systematically over-predicts the site amplification. The under-prediction of high frequency amplification by the EQL approach at large strains is well-known; it occurs because only a single value of the effective strain is used in each layer to select the damping for the analysis. This damping is too large and it over-damps the high frequency response relative to the observations. The over-prediction by the EQL-FD method is explained by the fact that the EQL-FD method utilizes damping values which are close or equal to the minimum damping values incorporated in the damping curve. Consequently, the EQL-FD method models a nearly-linear-elastic high frequency response, characterized by amplification that is larger than the observations.

Unexpectedly, the NL model predicts high frequency responses (FIGURES 6.8 and 6.9) that are very similar to those obtained by the EQL model, even at large

strains. The NL method models the entire nonlinear stress-strain relationship of a soil at every point in time during earthquake shaking, and thus, theoretically, it should more accurately predict the response across all frequencies. Nonetheless, the NL site response under-predicts the high frequency response when γ_{max} exceeds 0.1 % (FIGURE 6.8). This finding may be the product of several factors, such as: *i*) the lack of consideration of the shear strength at large strains, *ii*) erroneous values of damping at large strains.

An important issue to be considered in site response analysis is the representation of the shear strength at large strains. This issue is most critical for softer soils and/or larger input intensities, conditions that induce large shear strains that may begin to mobilize shear stresses close to the shear strength. The Darendeli (2001) model for modulus reduction is based solely on laboratory tests that do not apply strains large enough to mobilize the shear strength. Therefore shear strength is not explicitly considered in the analyses shown here. However, the consideration of large strain properties will be discussed in [Chapter 8](#). Similarly, possible errors associated with the utilized damping values at large strains, as obtained from the Darendeli (2001) model, may lead to substantial deviations from the observed high frequency responses. Nonetheless, a modification of damping at large strains without a solid theoretical framework or laboratory measurements supporting it would introduce additional uncertainties and thus it was not considered in this study.

FIGURES 6.11 through 6.13 illustrate the strain dependence of the amplification residuals computed at spectral periods of $T = 0.5$ s, 1.0 s, and 2.0 s, respectively. Based on these three figures, it can be observed that the EQL, EQL-FD and NL site response methods produce very similar large period responses across all strains.

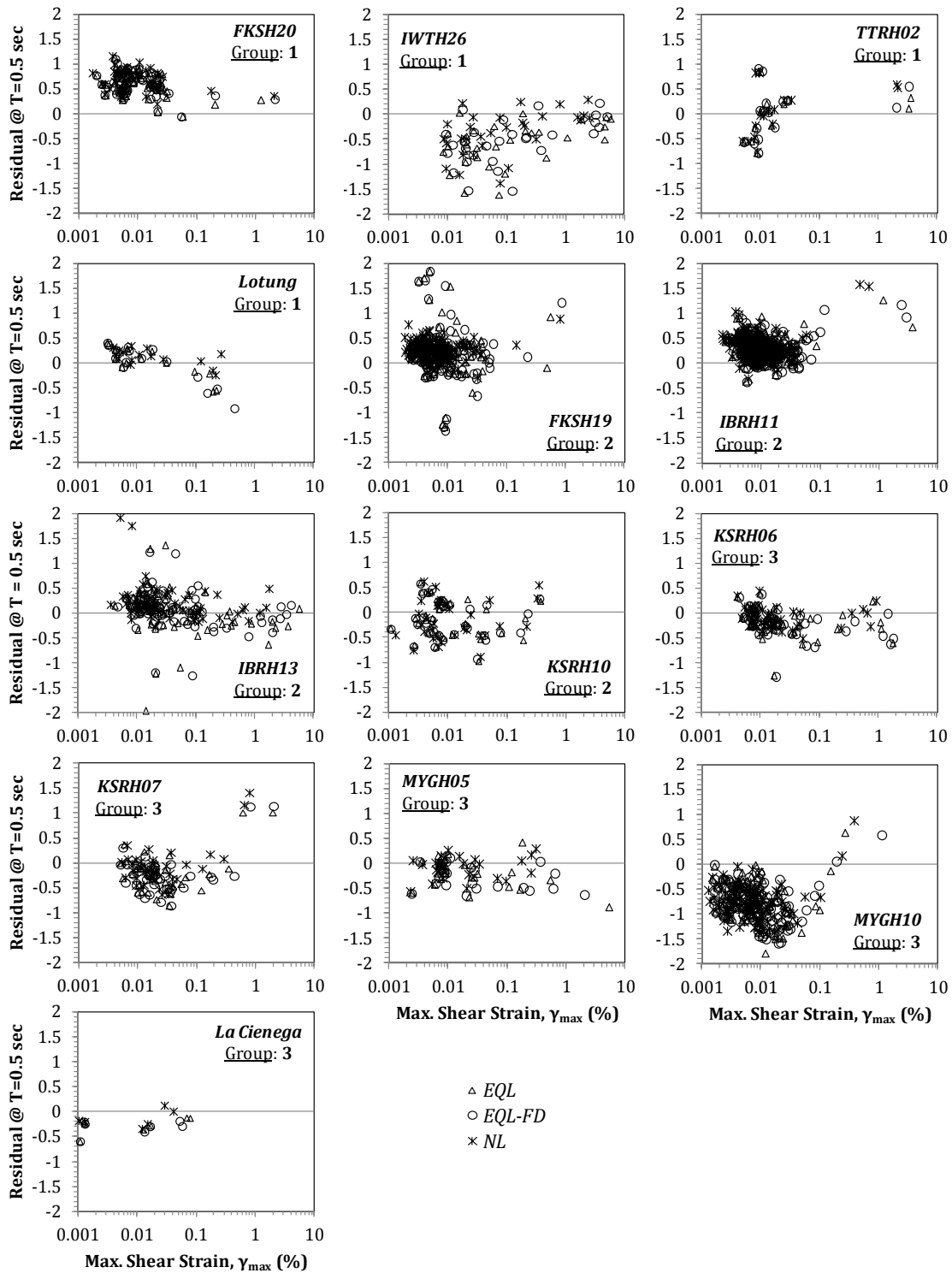


Figure 6.11: Residuals vs maximum calculated shear strains (γ_{max}) for all sites and site response methods - $T = 0.5$ s

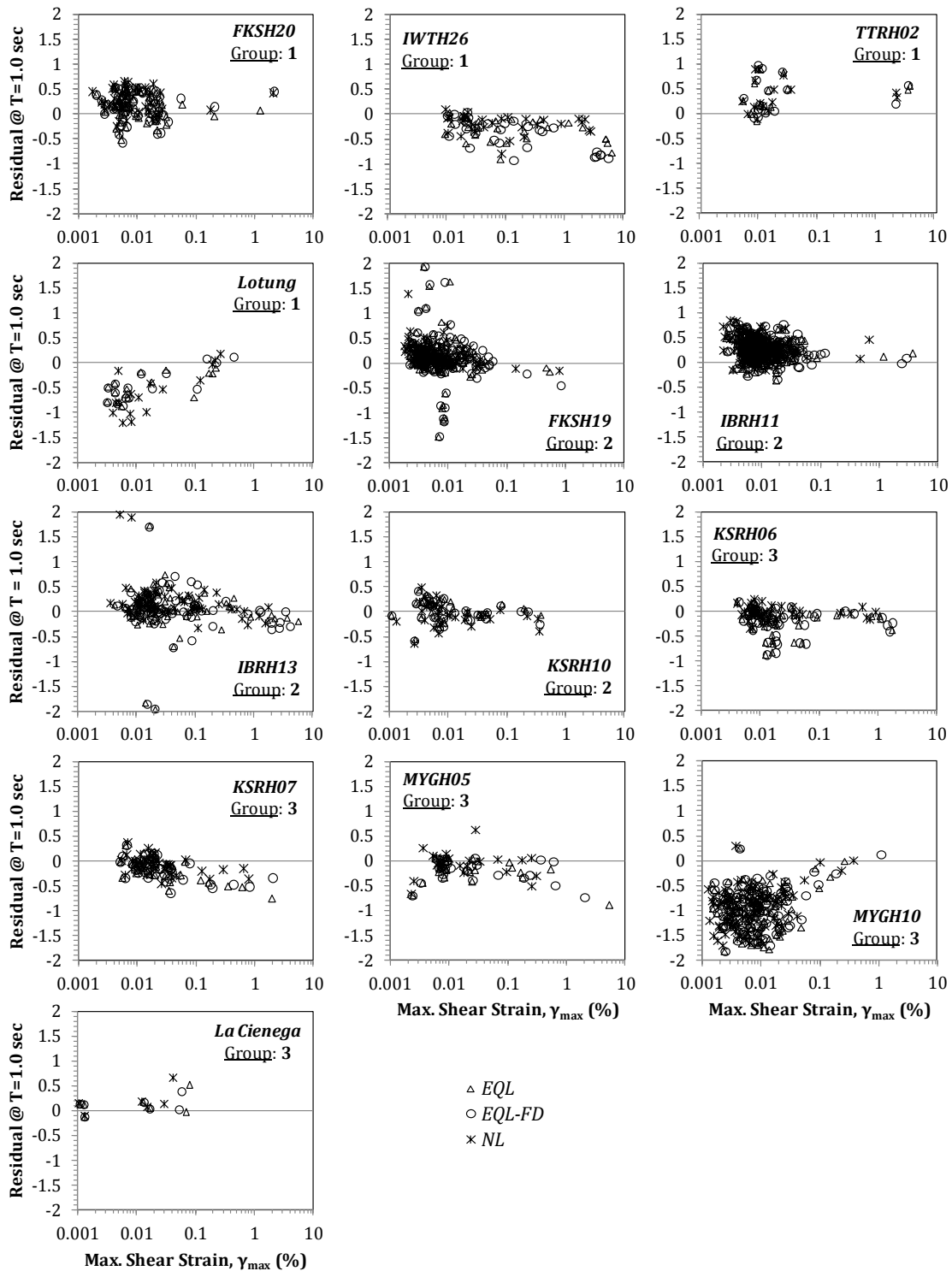


Figure 6.12: Residuals vs maximum calculated shear strains (γ_{max}) for all sites and site response methods - $T = 1.0$ s

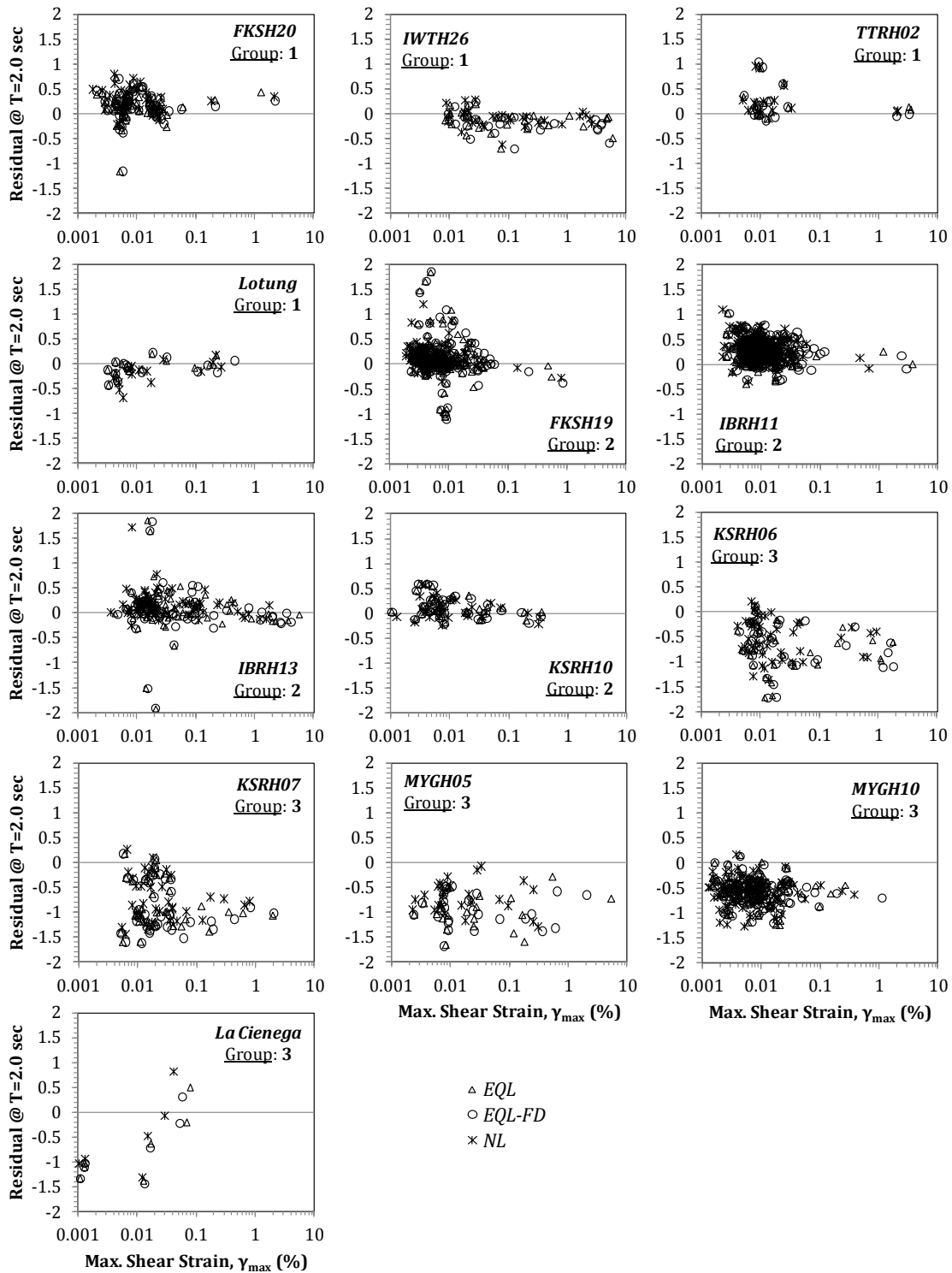


Figure 6.13: Residuals vs maximum calculated shear strains (γ_{max}) for all sites and site response methods - $T = 2.0$ s

This observation is independent of the performance of the theoretical models with respect to the observations, i.e. the magnitude and sign of the corresponding prediction residuals. Therefore, it can be noted that at large periods, differences in the numerical approaches have a minimal effect on the computed site response. The ability of the site response methods to match the recorded motions at these periods depends only on whether the adopted one-dimensional model can accurately represent the actual conditions at each site.

FIGURES 6.11 through *6.13* very effectively illustrate the modeling errors at each site. For example, at $T = 0.5$ s (*FIGURE 6.11*) strong negative residuals of up to -1.5 are seen at IWTH26 and MYGH10 arrays. Such negative residuals correspond to an over-prediction of the amplification by a factor of 4. This over-prediction is more prevalent at strains less than about 0.1 %. As discussed in *Chapter 5*, IWTH26 is one of the sites that exhibit stronger responses than the observations at the first few modes due to the “within” boundary condition (e.g. *Group 3* sites from *Chapter 5*) and in this case the site period is close to 0.5 s ($T_{site} = 0.47$ s). Similarly, the second mode site period for the MYGH10 site is close to 0.5 s and causes the over-prediction. The strong negative residuals gradually decrease with increasing strain ($\gamma_{max} > 0.1$ %), due to the increased nonlinearity and the associated reduction in the calculated peaks in the amplification factor.

Similar observations can also be made for the residuals computed at a spectral period of $T = 1.0$ s (*FIGURE 6.12*). While one-dimensional site response seems to accurately predict the observed response at most vertical arrays (i.e., *average* residuals close to zero), strong negative residuals of about -1.0 and -1.5 are seen at the Lotung and MYGH10 arrays, respectively. Again, the residuals at these sites gradually become smaller with increasing shear straining. The site

periods (T_{site}) at Lotung and MYGH10 sites are 0.80 s and 1.06 s, respectively. Therefore, the discrepancies can be attributed to the strong first mode over-amplification of the response due to the incorporation of a “within” wavefield. Finally, the misfits between the theoretical and recorded responses at a spectral period of 2.0 s are shown in *FIGURE 6.13*. Generally, *Group 1* and *Group 2* sites are characterized by small *average* residuals across all strain levels. On the other hand, all of the *Group 3* arrays show substantial negative residuals. Because the site periods range from 1.06 s (MYGH10 site) to 1.86 s (La Cienega array), once again, it can be concluded that the problematic representation of the boundary conditions at the base is the primary cause for the excessive first-mode over-amplification by the theoretical models.

6.4. Aggregated Results

Evaluating one-dimensional site response against recordings from vertical arrays on a site-by-site basis is influenced by site-specific issues, such as the applicability of the one-dimensional assumption to the site or the appropriateness of the utilized material properties (i.e., V_s profile and/or layer thickness). An alternative approach to evaluating the site response approaches would average the effects of these site-specific limitations across different sites and allow us to draw broader conclusions regarding the accuracy of the site response methods. To achieve this goal, the results from all of the considered arrays are aggregated. It should be noted that the limited number of vertical arrays considered in this study (13) as well as the imbalance in the distribution of the number of recordings from site-to-site, particularly at larger strains, may somewhat affect our observations.

6.4.1. Strain and Period Dependence of Residuals

Accordingly, the amplification residuals from all 13 sites are computed at 270 logarithmically spaced periods between 0.05 s and 2.0 s. To present the aggregate results in an effective and concise manner, the computed residuals are grouped into 10 different, equally spaced, spectral period bins. Therefore, 27 residuals are included within each period bin for each record. The average residual value is computed across each period bin for each motion, and these values are aggregated across all motions and all sites. These residuals are depicted in *FIGURES 6.14* and *6.15* (grey points), for the 10 spectral period bins considered. In these figures, the residuals are plotted against the corresponding maximum calculated shear strain (γ_{max}).

To better visualize the strain dependence of the computed residuals in *FIGURES 6.14* and *6.15*, mean values are calculated within 15 γ_{max} bins. These bins are listed in *TABLE 6.2* along with the corresponding number of motions within that bin. The mean residuals across the different strain bins are presented in *FIGURES 6.14* and *6.15* (black points/black line). The corresponding 90 % confidence intervals are also shown (dotted black line).

FIGURES 6.14 and *6.15* further strengthen the general remarks made during the site-by-site examination of the amplification residuals. At periods less than about 0.32 s (*FIGURE 6.14*), all three models generally match the observations at $\gamma_{max} < 0.1$ % (mean residuals ~ 0). However, some non-zero mean residuals are observed especially at very small strains ($\gamma_{max} < 0.004$ %). The cause of this inconsistency will be further investigated in a subsequent section. The EQL and NL methods seem to strongly under-predict the amplification (mean residuals as large

Table 6.2: Defined γ_{max} ranges and associated number of motions for all site response methods

Bin No	γ_{max} (%) range		Number of Motions		
	$\gamma_{max,min}$ (%)	$\gamma_{max,max}$ (%)	EQL	EQL-FD	NL
1	0.0010	0.0016	6	4	9
2	0.0016	0.0026	23	20	30
3	0.0026	0.0041	72	74	86
4	0.0041	0.0066	143	129	141
5	0.0066	0.0105	179	172	187
6	0.0105	0.0168	114	117	107
7	0.0168	0.0268	93	103	83
8	0.0268	0.0430	55	47	47
9	0.0430	0.0687	18	26	14
10	0.0687	0.1100	17	25	13
11	0.1100	0.2199	18	14	16
12	0.2199	0.4398	10	13	16
13	0.4398	0.8796	8	7	13
14	0.8796	2.0000	10	10	6
15	2.0000	10.0000	11	16	6

as ~ 1.0) at strains greater than approximately 0.1 %. Across the same periods, the EQL-FD method deviates from the observations at strains greater than approximately 0.03 % to 0.1 %; this strain threshold is slightly smaller than for the EQL and NL models. Additionally, the EQL-FD method over-predicts the response at large strains as previously noted.

At spectral periods greater than 0.32 s (*FIGURE 6.15*), all three of the site response methods yield very similar results, with mean residuals very close to zero. An exception to this observation is the NL method within the period range of $T = 0.32 - 0.46$ s. Here large under-prediction of the amplification at $\gamma_{max} > 0.1$ % can still be noted. Therefore, it appears that the over-damping at large strains ext-

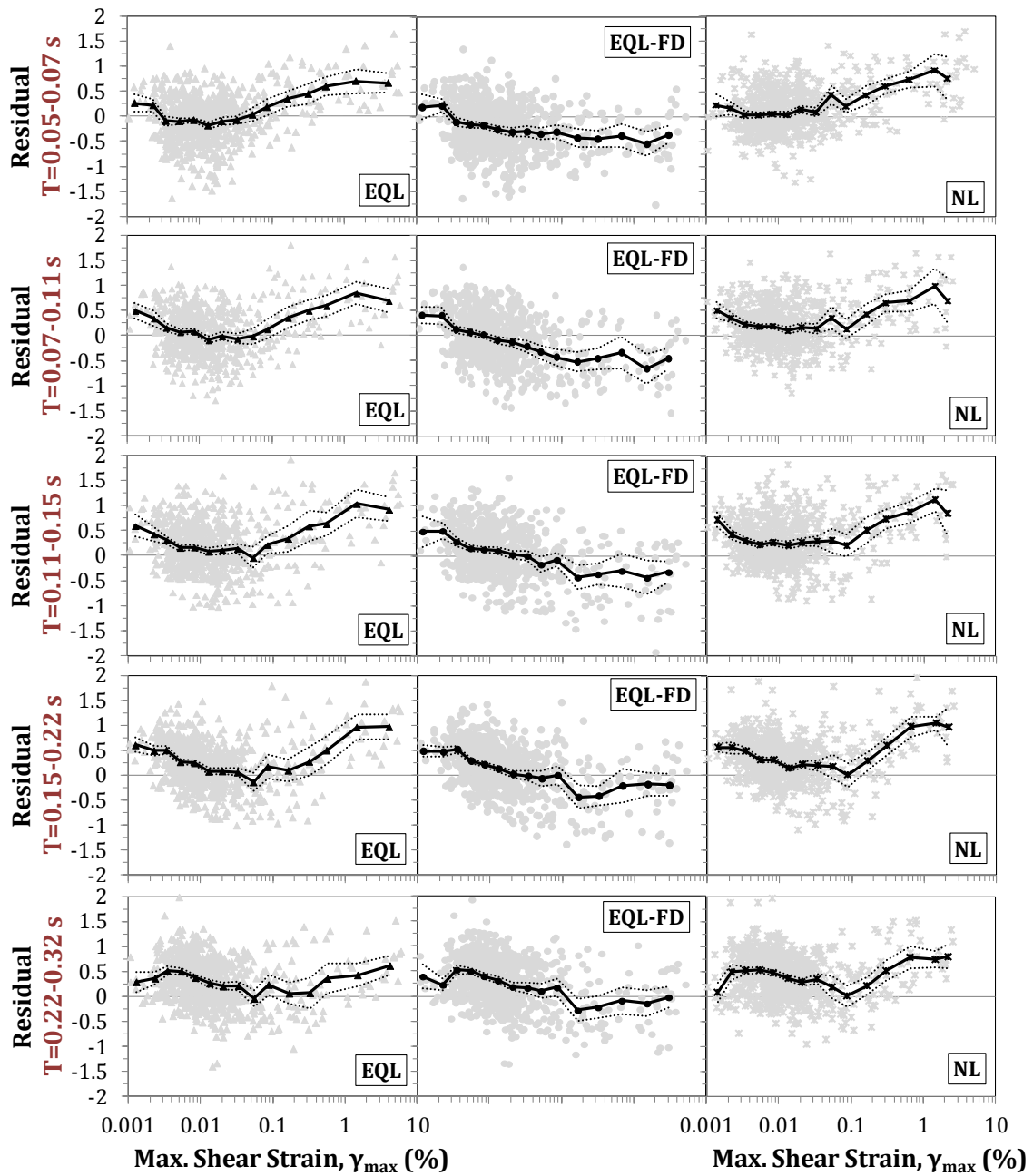


Figure 6.14: Combined *average* prediction residuals vs maximum calculated shear strains (γ_{max}) for all sites and site response methods, within 5 different spectral period bins – $0.05\text{ s} < T < 0.32\text{ s}$ – grey dots represent the average residual from 27 spectral periods included within each of the 5 spectral period bins depicted, *black dot/line* represents the *mean* residual within a narrow γ_{max} range, *black dotted line* represents the corresponding 90 % confidence intervals

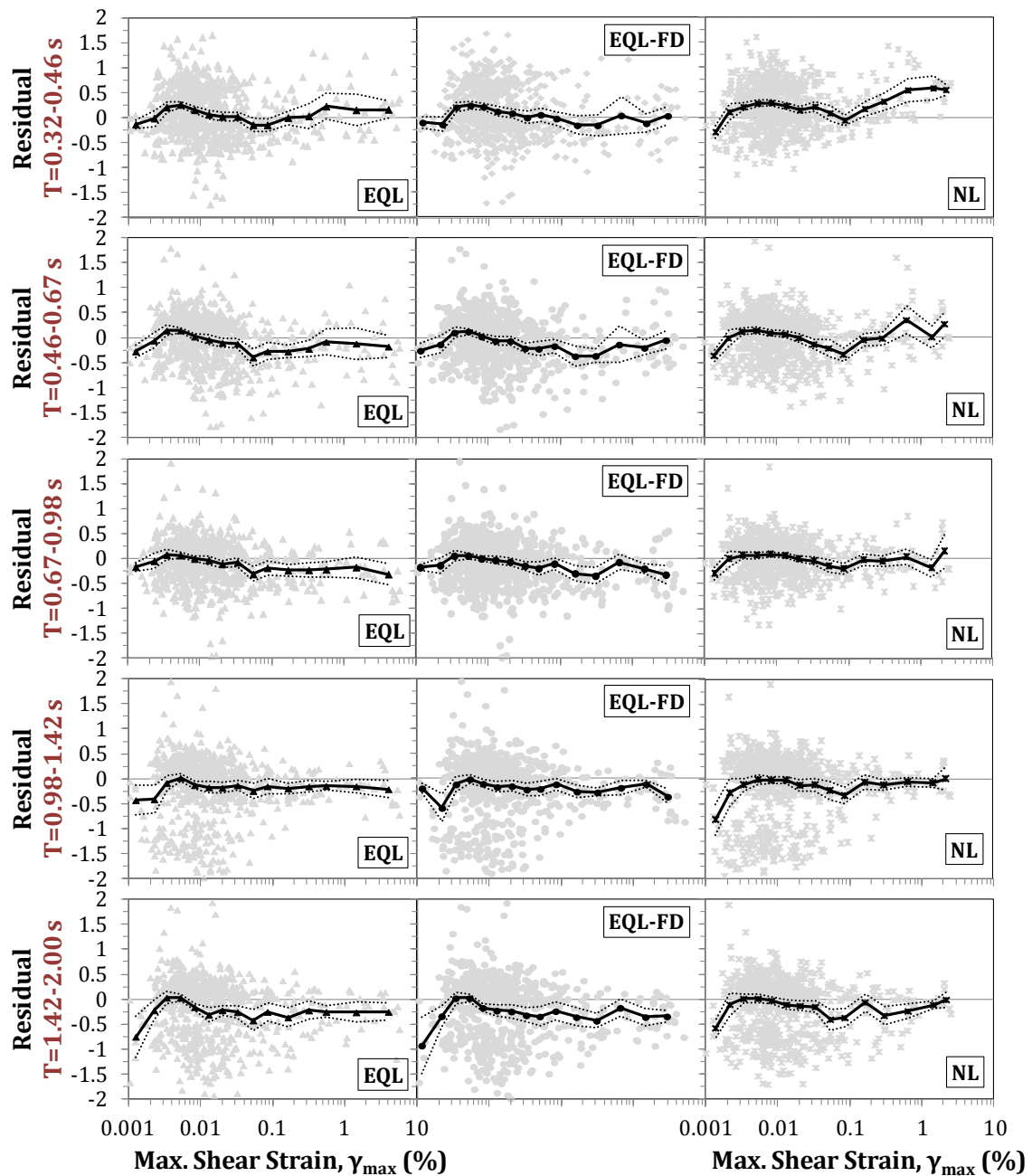


Figure 6.15: Combined *average* prediction residuals vs maximum calculated shear strains (γ_{max}) for all sites and site response methods, within 5 different spectral period bins – $0.32\text{ s} < T < 2.0\text{ s}$ – grey dots represent the average residual from 27 spectral periods included within each of the 5 spectral period bins depicted, *black dot/line* represents the *mean* residual within a narrow γ_{max} range, *black dotted line* represents the corresponding 90 % confidence intervals

ends over a wider range of frequencies for the NL method as compared to the EQL and EQL-FD methods. Moreover, slightly negative residuals (i.e., over-prediction) across all strains are observed at the largest periods, particularly at $T = 1.42 - 2.0$ s. Because 40 % of the sites analyzed are *Group 3* sites that showed large amplification near the first modal period due to the assumed “within” wavefield and because the site periods for sites included in *Group 3* are on the order of 1.0 – 2.0 s, it can be inferred that *Group 3* sites are driving the mean residuals negative at larger spectral periods. Indeed, the highly negative amplification residuals that can be observed at strains less than 0.003 %, and at periods greater than 0.98 s, for all the site response approaches, are a result of the same modeling effect.

To simultaneously and more effectively present the combined effect of the maximum calculated shear strain (γ_{max}) and the spectral period (T) on the performance of the one-dimensional site response methods, contour plots of the computed *mean* residuals have been developed for all three models (*FIGURE 6.16*). Here the *mean* residuals are plotted against the corresponding values of γ_{max} and T . The same γ_{max} ranges defined in *TABLE 6.2* are used. Within each γ_{max} bin, *mean* residuals are calculated at each one of the 270 logarithmically spaced periods between 0.05 s and 2.0 s. In *FIGURE 6.16*, the *mean* prediction residuals have been colored based on their sign. That is, strong positive residuals (i.e., under-prediction) are shown in red, while strong negative residuals (i.e., over-prediction) are shown in blue. A range of “acceptable” prediction residuals is colored in green. We chose to define this “acceptable” range residuals within approximately ± 0.2 , which corresponds to the computed *AF* ($AF_{calculated}$) falling within approximately ± 20 % of the observed *AF* ($AF_{observed}$).

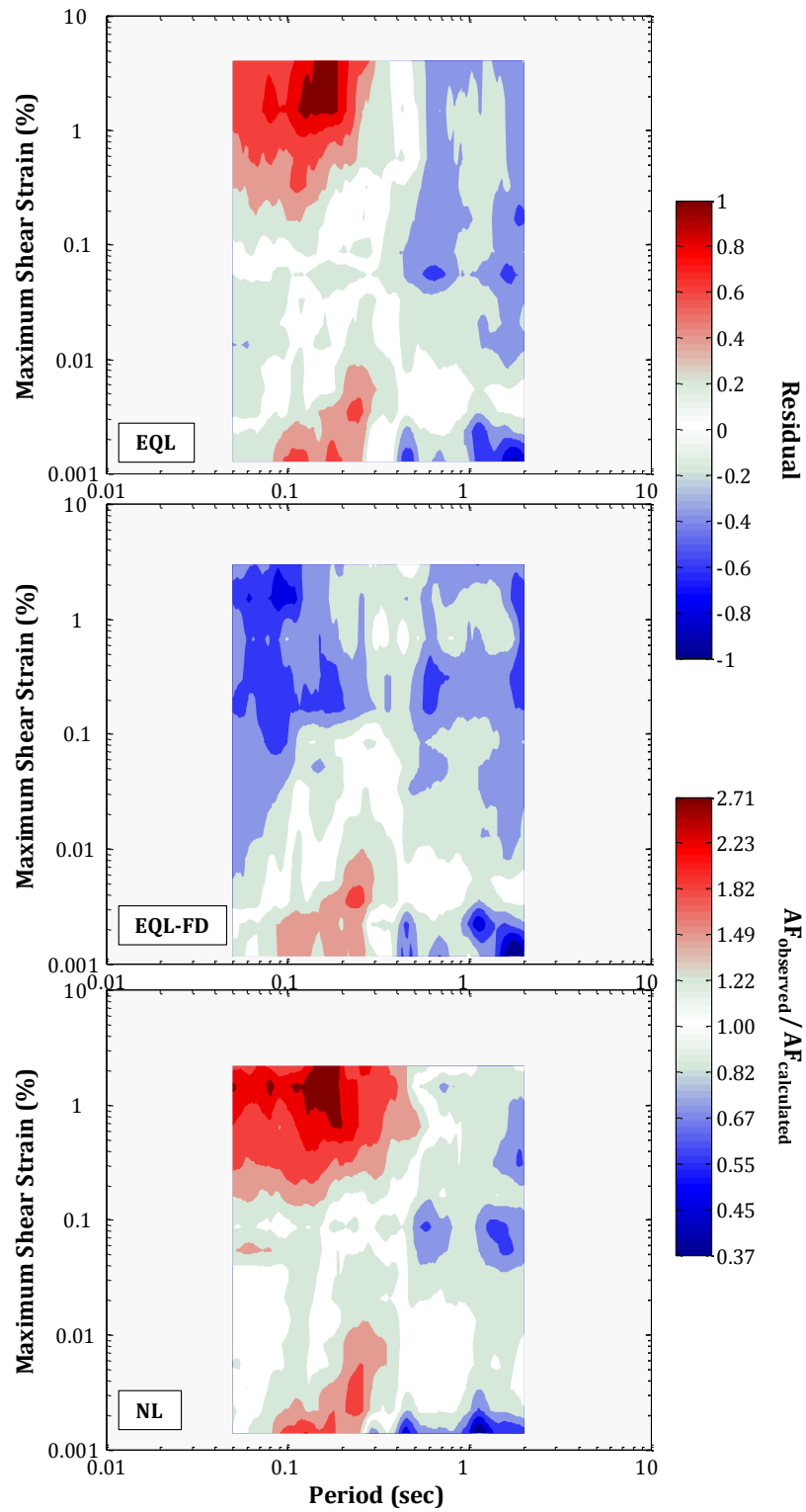


Figure 6.16: Contour plots of *mean* prediction residuals vs maximum calculated shear strains (γ_{max}) vs spectral period (T) for all site response methods

The contributions of each site to the overall *mean* residuals are quantified in *TABLE 6.3*, for each one of the 15 strain bins considered. *TABLE 6.3* presents the percentage contributions to the *mean* residuals only for the EQL method. Nonetheless, the percentage contributions are very similar for the EQL-FD and NL models. For documentation purposes, the percentage contributions for the EQL-FD and NL methods can be found in *Appendix A.3* (*TABLES A.3* and *A.4*). *TABLE 6.3* also highlights the strain bins in which more than 33.3 % of the data come from a single site. This information is useful to investigate the potential for site-specific biases in the overall mean residuals shown in *FIGURE 6.16*.

The results in *FIGURE 6.16* allow for the visualization of the observations previously discussed. Generally, the three models predict very similar responses and small residuals at strains less than 0.1 %. However, there are some discrepancies at these small strains. Specifically, all models yield under-prediction of amplification at strains less than 0.007 % and periods between 0.09 s and 0.25 s, and there is some over-prediction at periods greater than 0.5 s. The systematic under-prediction can be attributed to two factors. First, at strains less than 0.002 % to 0.003 %, the MYGH10 and La Cienega sites contribute most of the data to the overall *mean* response (*TABLE 6.3*). As seen in *Chapter 5*, these two sites show strong under-prediction of the response at periods around 0.1 s due to modeling errors. MYGH10 seems to need a calibration of the upper portion of the V_S profile, while the selection of the best-fit minimum damping (D_{min}) profile at the La Cienega array generated an under-prediction of the high frequency amplification, although this damping profile slightly reduced the excessive first mode amplification.

Second, at strains between 0.003 % and 0.007 %, the overall response seems to be driven by the data from only two sites FKSH19 and IBRH11. Even though, in

Table 6.3: Percentage contribution of each individual array to the overall *mean* residual depicted in *FIGURE 6.16*

γ_{\max} (%)	from	to	Percentage Contribution (%)													Total Number of Motions	
			FKSH20	IWTH26	TTRH02	Lotung	FKSH19	IBRH11	IBRH13	KSRH10	KSRH06	KSRH07	MYGH05	MYGH10	La Cienega		
0.001	0.002	-	-	-	-	-	-	-	16.7	-	-	-	-	-	33.3	50.0	6
0.002	0.003	8.7	-	-	-	34.8	8.7	-	-	-	-	-	4.3	43.5	-	-	23
0.003	0.004	5.6	-	-	2.8	44.4	13.9	-	6.9	1.4	-	-	1.4	23.6	-	-	72
0.004	0.007	11.9	-	0.7	3.5	20.3	37.1	1.4	6.3	3.5	2.8	0.7	11.9	-	-	-	143
0.007	0.011	5.0	1.7	3.9	1.1	17.9	34.1	5.0	3.4	5.6	2.2	6.1	14.0	-	-	-	179
0.011	0.017	5.3	1.8	3.5	0.9	11.4	31.6	13.2	1.8	11.4	7.0	-	10.5	1.8	-	-	114
0.017	0.027	9.7	5.4	1.1	1.1	9.7	26.9	12.9	3.2	4.3	8.6	4.3	12.9	-	-	-	93
0.027	0.043	3.6	5.5	1.8	1.8	10.9	21.8	20.0	5.5	5.5	12.7	3.6	7.3	-	-	-	55
0.043	0.069	5.6	16.7	-	-	5.6	11.1	16.7	5.6	16.7	11.1	-	5.6	5.6	-	-	18
0.069	0.110	-	11.8	-	5.9	-	5.9	41.2	5.9	5.9	-	-	5.9	11.8	5.9	-	17
0.110	0.220	5.6	16.7	-	16.7	-	-	11.1	11.1	5.6	11.1	16.7	5.6	-	-	-	18
0.220	0.440	-	20.0	-	-	-	-	40.0	10.0	10.0	10.0	10.0	10.0	-	10.0	-	10
0.440	0.880	-	12.5	-	-	25.0	-	25.0	-	12.5	12.5	12.5	-	-	-	-	8
0.880	2.000	10.0	20.0	-	-	-	10.0	20.0	-	30.0	10.0	-	-	-	-	-	10
2.000	10.000	-	36.4	18.2	-	-	9.1	27.3	-	-	-	-	9.1	-	-	-	11

general, these sites are well represented by the modeling assumptions (i.e., one-dimensionality, boundary conditions, material properties), they are characterized by a small amplification trough around 0.2 s. This trough is caused by the destructive interference of the up-going and down-going waves at depth. The systematic over-prediction at longer periods at small strains is caused by all models producing negative residuals across almost the entirety of strains at two period ranges, namely 0.5 s – 0.6 s and 1.0 s – 2.0 s. This phenomenon seems to be less pronounced for NL model. As explained in previous discussions, these two period ranges roughly correspond to the first or the second modal periods of the sites. At these periods, the “within” wavefield resulted in excessive first and, in some cases, second mode amplification. Sites categorized in *Group 3* contribute predominantly to this observation.

At strains greater than 0.01 % and periods smaller than 0.3 – 0.4 s, the EQL-FD amplification residuals become negative. Between 0.01 % and 0.1 %, the EQL-FD method over-predicts the response by about 50 – 55 %. The frequency range over which the over-prediction is observed increases with increasing γ_{max} . The over-amplification is exacerbated even further at $\gamma_{max} > 0.1$ % and at periods less than 0.2 – 0.3 s. Over-amplification as large as 130 % can be seen at strains greater than 1.0 % and periods close to 0.1 s. This result is caused by the fact that the EQL-FD method utilizes damping values that are close or equal to the minimum damping (D_{min}) at short periods and this leads to a near-linear-elastic response at short periods.

As seen in *FIGURE 6.16*, the EQL and NL models yield very similar results even under the largest strains within the upper left corner of the $\gamma_{max} - T$ plane. Specifically, both models under-predict the observed response at strains greater

than approximately 0.1 – 0.2 % and periods less than 0.3 – 0.4 s. This remark becomes more prevalent with increasing shear strain. Indeed, the predicted AF may be as small as 0.35 of the observed value at strains close to or greater than 1.0 % and periods between 0.1 s and 0.2 s. Nevertheless, it is worthwhile to mention that the under-prediction of amplification from the NL model is observed over a slightly wider range of spectral periods than for the EQL model. The EQL model over-damps the high frequencies due to the large peak strain used for the selection of strain-compatible soil properties. The under-prediction by the NL model can be possibly attributed to erroneous values of the laboratory based Darendeli (2001) model for the G/G_{max} and damping curves at large strains.

6.4.2. Effect of T_{site}

To specifically examine the performance of the different one-dimensional site response methodologies near their site period, we normalize the spectral period (T) by the T_{site} of each vertical array. T_{site} was estimated based on the first peak of the observed transfer functions for motions with $PGA_{base} \leq 0.05 g$. Therefore, at each site, amplification residuals are calculated at 270 logarithmically spaced values of T/T_{site} ranging from T_{min}/T_{site} to T_{max}/T_{site} ; where $T_{min} = 0.05 s$ and $T_{max} = 2.0 s$, respectively. TABLE 6.4 presents the site periods (T_{site}) and the corresponding ranges in T/T_{site} , for all of the vertical arrays. Based on TABLE 6.4, it is obvious that the range of T/T_{site} varies substantially from site-to-site because T_{site} varies considerably. To compute the corresponding *mean* residuals across all sites, we must first ensure that at each T/T_{site} , data from enough sites are included in the computations. This process is schematically illustrated in FIGURE 6.17. We selected the minimum and maximum values of T/T_{site} by specifying that no less than 7 sites

Table 6.4: Site periods (T_{site}) and corresponding ranges in T/T_{site} for all vertical arrays - $T_{min} = 0.05$ s and $T_{max} = 2.0$ s

No	Site	T_{site}	T_{min}/T_{site}	T_{max}/T_{site}
1	FKSH20	0.72	0.07	2.79
2	IWTH26	0.47	0.11	4.30
3	TTRH02	0.20	0.25	9.81
4	Lotung	0.80	0.06	2.51
5	FKSH19	0.32	0.15	6.19
6	IBRH11	0.37	0.13	5.34
7	IBRH13	0.34	0.15	5.88
8	KSRH10	0.63	0.08	3.18
9	KSRH06	1.55	0.03	1.29
10	KSRH07	1.51	0.03	1.33
11	MYGH05	1.79	0.03	1.12
12	MYGH10	1.06	0.05	1.89
13	La Cienega	1.86	0.03	1.08

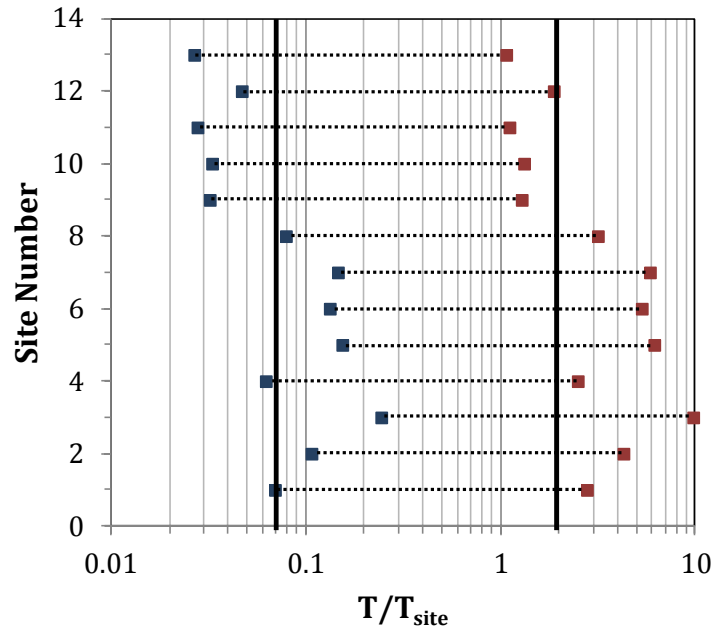


Figure 6.17: Selection of appropriate range of T/T_{site} for the computation of the mean prediction residuals across all sites

should be contributing to the overall mean amplification residuals at any given T/T_{site} value. Therefore, for the computation of the *mean* residuals, a range of T/T_{site} between 0.07 and 2.0 was deemed the most appropriate (FIGURE 6.17).

FIGURE 6.18 shows the contour plots of the mean residuals against the corresponding γ_{max} and T/T_{site} values, for all three site response models. The effect of the over-prediction at the site period due to the within assumption is clearly identified when plotting the data as a function of T/T_{site} . Seven out of the thirteen vertical arrays considered in this study are characterized by over-prediction at the site period, thus rendering the overall *mean* residuals strongly negative. Particularly at low strains ($\gamma_{max} < 0.003\%$), over-amplification of up to 170% can be seen. Lengthening of the site period with increasing strain also can be observed in FIGURE 6.18, as the largest negative residuals occur at $T/T_{site} = 1.0$ at small strains and T/T_{site} greater than 1.0 at large strains. Note that T_{site} used in the normalization is the small strain value.

The period dependence of the performance of the site response models at large strains is, once more, apparent in FIGURE 6.18. The EQL and NL models under-predict the response at small T/T_{site} values, and strains greater than 0.1%. When normalized by T_{site} , it is clear that the range of T/T_{site} over which under-prediction occurs increases with increasing γ_{max} . At strains 0.1% – 0.2%, only T/T_{site} of about 0.1 is affected, while at strains greater than 1.0% the underprediction is observed at T/T_{site} less than about 0.8. For the EQL-FD method, the amplification residuals become negative at strains greater than 0.01% and $T/T_{site} < 0.3$. The range of T/T_{site} which experiences negative residuals is almost independent of the shear strain level.

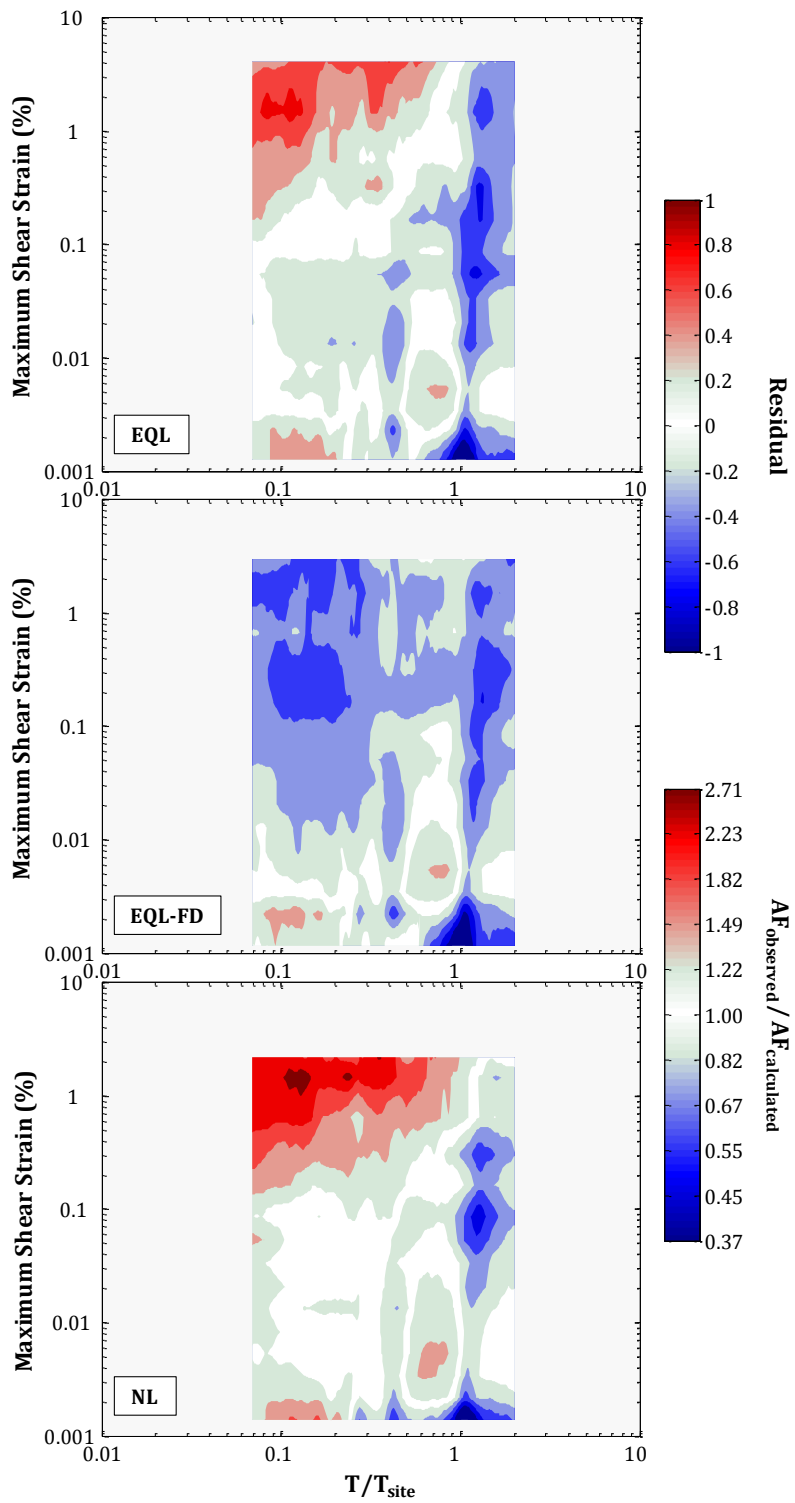


Figure 6.18: Contour plots of *mean* prediction residuals vs maximum calculated shear strains (γ_{max}) vs normalized period (T/T_{site}) for all site response methods

6.4.3. Comparison of Results with Kaklamanos *et al.* (2013)

To further strengthen the conclusions arising from the results presented in this chapter, we perform a comparison of our major observations with results from similar studies retrieved from the literature. In particular, the strain and period dependence of the amplification residuals from the different site response methodologies, as depicted in *FIGURE 6.18*, is compared against the results from Kaklamanos *et al.* (2013).

As discussed in *Chapter 3*, Kaklamanos *et al.* (2013) utilized recordings at 100 Kik-Net arrays to assess the accuracy and the precision of linear-elastic (LE) and equivalent-linear (EQL) one-dimensional site response analysis. Based on their results, the authors provided recommendations regarding the points at which the site response models start to break down. The recommendations state that both EQL and LE analyses can efficiently predict the response at spectral periods greater than about 0.3 s to 0.5 s, independent of the level of the shaking. At periods less than 0.3 s to 0.5 s, they noted that linear-elastic analysis over-predicts the response at strains beyond 0.01 %, while EQL strongly under-predicts the response at strains greater than approximately 0.4 %. At these strain levels, the authors suggest that NL analyses should be performed for the recorded response to be accurately predicted. However, NL analyses were not performed by Kaklamanos *et al.* (2013) and their recommendations to use NL analysis was based solely on the widely held belief that nonlinear analysis is more accurate at large strains.

To compare the recommendations from Kaklamanos *et al.* (2013) with the results from this study, the strain and period thresholds from Kaklamanos *et al.* (2013) regarding the appropriate analysis type are plotted (*FIGURE 6.19*) on top of

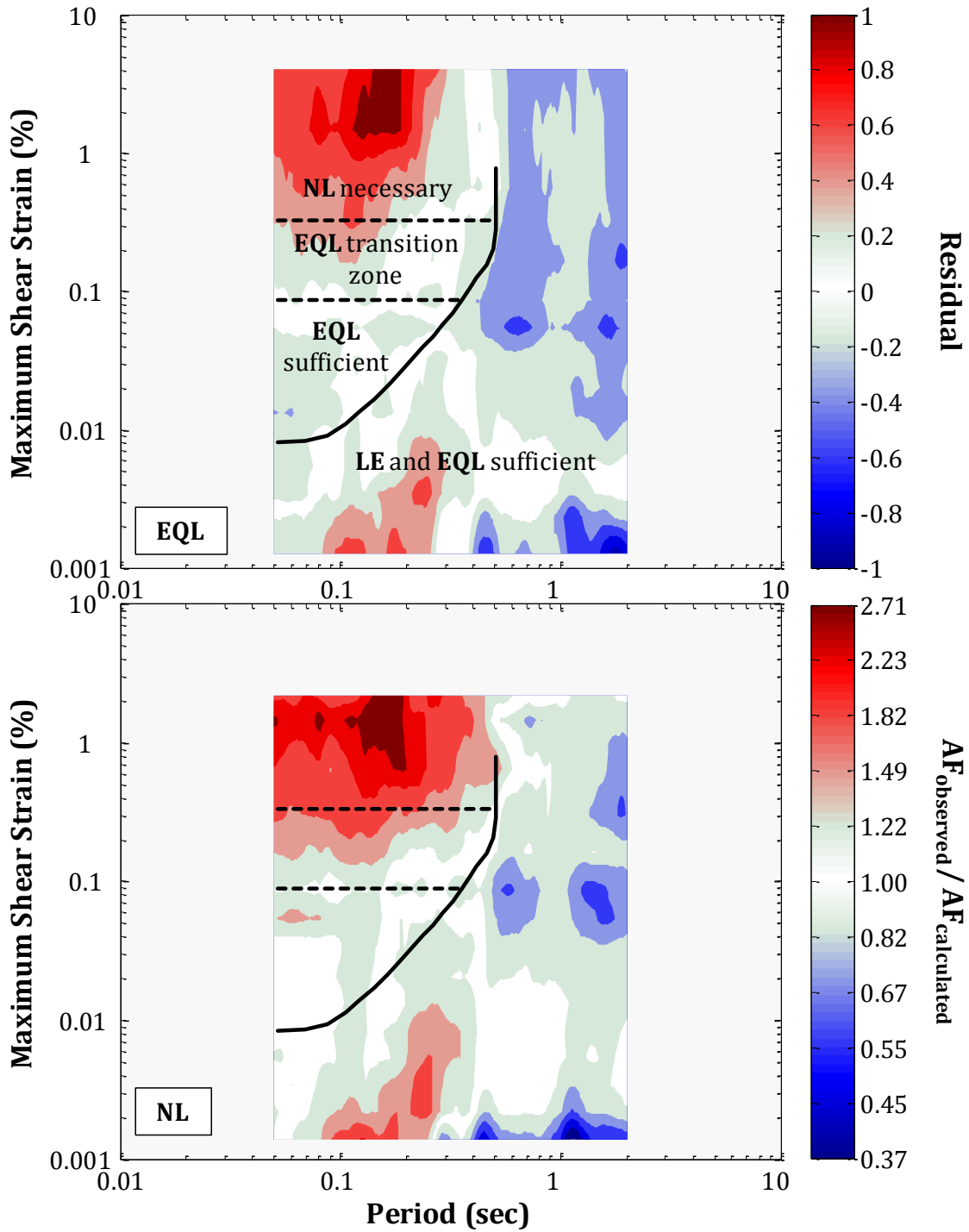


Figure 6.19: Comparison of *mean* prediction residuals vs γ_{max} vs T , for the EQL and NL site response methods, with recommendations from Kaklamanos *et al.* (2013) (black lines)

the amplification residuals from this study. For the EQL method, Kaklamanos et al. (2013) and this study predict similar strain and period ranges over which the method accurately predicts the site amplification. The two studies also predict similar strain and period thresholds at which the EQL method starts to deviate from observations and under-predicts the response. However, it is here where the results from this study provide additional information about the applicability of NL analysis at large strains. Kaklamanos *et al.* (2013) state that NL analysis is necessary at strains larger than 0.4 % and periods less than 0.5 s. However, our results show that the amplification residuals in this period and strain range show strong under-prediction by the NL analysis. Thus, NL analysis does not predict amplification any more accurately than EQL analysis in this period range and at large strains. This under-prediction at large strains indicates a problem with one-dimensional analysis at large strains, rather than a problem with EQL analysis.

6.5. Summary

This chapter involved the assessment of the 1-D site response methodologies (EQL, EQL-FD and NL) at the 13 selected vertical arrays. The evaluation of the site response approaches was conducted by comparing the observed and computed amplification factors (AF). To compare the results across sites, the residuals in the predictions (i.e. $y = \ln(AF^{obs} / AF^{calc})$) at each site were obtained. Since the behavioral characteristics of the various site response models is affected by the level of shear strain, the strain dependence of the prediction residuals was examined.

The evaluation of the performance of the models was made both on a site-by-site basis and in an aggregated manner. First, the results from our analyses were presented for each one of the 13 borehole arrays. Generally, all three site response

models provided a similar response at strains smaller than about 0.01 %, irrespectively of the spectral period. At larger strain values ($\gamma_{max} > 0.01 \%$), and particularly at $T = 0.05 \text{ s}$ and $T = 0.1 \text{ s}$, the EQL-FD method systematically yields smaller residuals (larger amplification) than the EQL and NL methods. Moreover, the EQL and NL models seem to provide very similar results across all strains and spectral periods. The observed differences between the three site response models are substantially smaller, almost minimized, at $T > 0.3 \text{ s}$. At these spectral periods, any discrepancy between the computed and the observed responses are due to errors in the modeling assumptions.

To average the effects across all sites, the results from all considered arrays were aggregated. The relationship between the computed *mean* residuals and shear strain at different periods was investigated for all three models. Based on our results, the three site response models display residual close to zero except from the upper left corner of the $\gamma_{max} - T$ plane; i.e. at larger strains and shorter periods. In this zone, the EQL-FD method over-predicts the response while both the EQL and NL methods under-predict the observed response. The EQL results from this study are consistent with the recommendations by Kaklamanos *et al.* (2013); however, the NL results from this study indicate that modeling the fully nonlinear response of the soil does not improve the prediction of site amplification at larger strains.

Chapter 7

Variability Evaluation

7.1. Introduction

The results presented in [Chapter 6](#) focused on the differences, on average, between the observed and predicted responses at 13 downhole array sites. However, considering all of the recorded data, there is considerable variability between the observations and predictions. Investigating this variability provides additional insights into the performance of site response analysis.

The different components of variability can be evaluated by using methodologies proposed by several researchers in the context of either ground motion prediction equations (e.g., Al Atik *et al.*, 2010; Lin *et al.*, 2011; Rodriguez-Marek *et al.*, 2011) or site response analysis (e.g., Kaklamanos *et al.*, 2013). Herein, the main conceptual framework of Kaklamanos *et al.* (2013) is adopted and used to investigate the influence of different parameters on the variability.

7.2. Identification of Sources of Variability

As presented in [Chapter 3](#), Kaklamanos *et al.* (2013) utilized recordings at 100 Kik-Net arrays to assess the accuracy and the precision of linear (LE) and equivalent-linear (EQL) one-dimensional site response analysis. The researchers performed analyses using 3720 ground motions with varying input intensities. The main goal of their study was the investigation of the parameters that can serve as the best indicators of the point at which the site response methodologies fail to

accurately predict the response. The authors used a mixed effects regression, based on the work of Bradley (2011), to explicitly distinguish and quantify different sources of variability. Assuming that the observation residuals at a specific frequency, ($y_{i,j} = \ln AF_{i,j}^{obs} - \ln AF_{i,j}^{calc}$), represent a normally distributed random variable with mean μ_y and standard deviation σ_y , Kaklamanos *et al.* (2013) separated the residuals into different components, as:

$$y_{i,j} = \alpha + \eta_{s,i} + \varepsilon_{i,j} \quad (7.1)$$

where α is the “fixed effect”, $\eta_{s,i}$ is the inter-site residual, and $\varepsilon_{i,j}$ is the intra-site residual. The “fixed effect”, α , represents the mean residual across all sites and recordings. The inter-site residual, $\eta_{s,i}$, quantifies the “site-specific” average residual and is assumed to be a normally distributed random variable with, *ideally*, a zero mean ($\mu_{\eta_s} = 0$) and standard deviation τ_s . For the i^{th} site, $\eta_{s,i}$ represents the misfit between the mean residual of the site and the “fixed effect”, α . The intra-site residual, $\varepsilon_{i,j}$, expresses the “within-site” variability and is a normally distributed random variable with zero mean ($\mu_\varepsilon = 0$) and standard deviation σ . $\varepsilon_{i,j}$ represents the difference between a single observation, $y_{i,j}$, and the site-corrected mean residual ($\alpha + \eta_{s,i}$). A schematic illustration of the definition of inter-site and intra-site residuals is shown in *FIGURE 7.1*. Note that τ_s refers to the site-to-site variability, while σ quantifies the single-site, motion-to-motion variability.

Considering the linear mixed effects model of Equation 7.1, the mean (μ_y) and standard deviation (σ_y) of the observation residuals can be split into three components, namely: 1) the fixed effect, α ; 2) the inter-site standard deviation, τ_s ; and 3) the intra-site standard deviation, σ . Specifically, the variability measures of $y_{i,j}$ are given by:

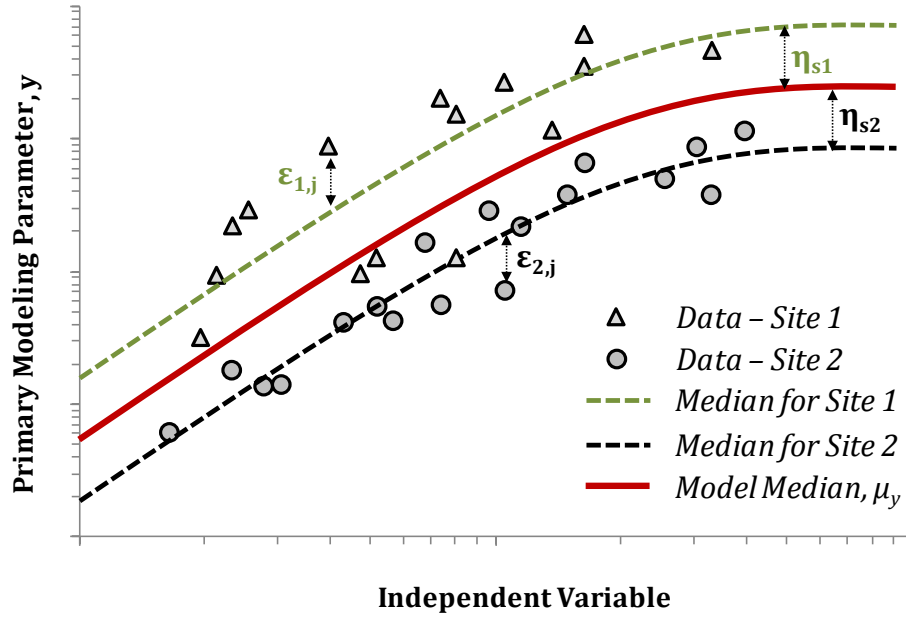


Figure 7.1: Schematic definition of inter and intra-site residuals (reproduced based on Figure 1 in Al Atik *et al.* (2011))

$$\mu_y = \alpha \quad (7.2)$$

$$\sigma_y = \sqrt{\tau_s^2 + \sigma^2} \quad (7.3)$$

Kaklamanos *et al.* (2013) examined the period dependence of the variability estimates using the procedure described above. *FIGURE 7.2* presents their results in terms of: *a*) the fixed effect, α , *b*) the total standard deviation, σ_y , *c*) the intra-site standard deviation, σ , and *d*) the inter-site standard deviation, τ_s . Also shown are 95 % confidence intervals of these parameters. The authors concluded that linear and equivalent-linear site response analyses, generally, under-predict the response, except in the range of 0.5 – 2 s, where a slightly negative residual is observed. At this point, it is worthwhile to note that Kaklamanos *et al.* (2013) did not distinctively study the effect of the level of the input motion intensity on the compu-

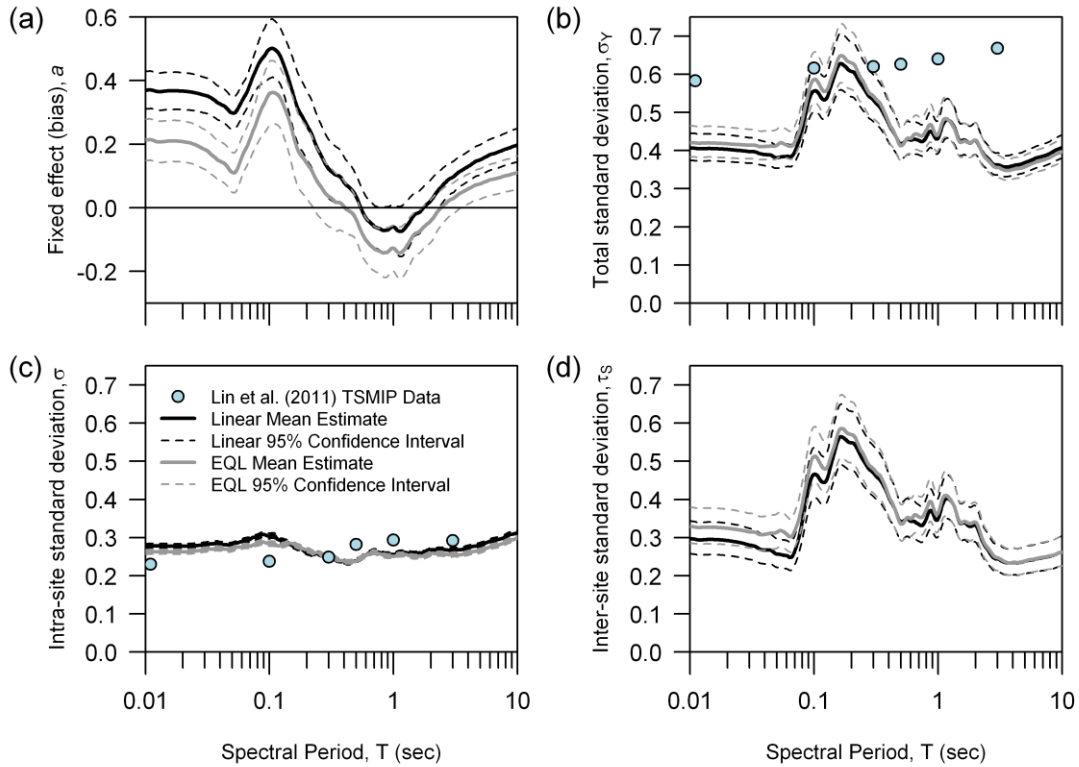


Figure 7.2: Results from Kaklamanos *et al.* (2013) in terms of: (a) fixed effect, α , (b) total standard deviation, σ_y , (c) intra-site standard deviation, σ , and (d) inter-site standard deviation, τ_s . (from Kaklamanos *et al.*, 2013)

ted residual. Thus linear and non-linear systems are not treated separately in the residual representations. Therefore, EQL provides smaller predictive residuals than LE analyses. The phenomenon is more pronounced at high frequencies ($T < 0.08$ s), which are more significantly affected by damping.

Furthermore, Kaklamanos *et al.* (2013) observed that both EQL and LE models are characterized by similar inter-site, intra-site, and total variability. The intra-site standard deviation (σ) was found to be period independent and equal to a value in the range of 0.25 – 0.35. However, the inter-site (τ_s) standard deviation shows a period dependence between about 0.07 s and 0.5 s. Over this period range, an increased level of variability is observed (i.e., 0.5 – 0.6). The researchers

attribute this phenomenon to the frequency content of the input motions and the first mode response of the sites under investigation.

7.3. Quantification of Site Response Variability

In *Chapter 6*, the maximum calculated shear strain (γ_{max}) was used to quantify the level of shaking and induced level of soil nonlinearity. To compute variability, a significant population of data is required and therefore we use fewer strain bins each of which span a larger range of strains. The three different bins of γ_{max} values are established based on the findings presented in *Chapter 6*; $\gamma_{max} \leq 0.01\%$, $0.01\% \leq \gamma_{max} \leq 0.10\%$, and $\gamma_{max} > 0.10\%$. *TABLE 7.1* tabulates the number of input motions at each site that result in γ_{max} values within each of the γ_{max} bins. Because the computed strains are different for each site response model, the motions are tabulated separately for the EQL, EQL-FD and NL approaches. The number of motions generating γ_{max} values within each of the strain bins varied substantially. For example, for the EQL model, 398 motions from 13 sites are included in the $\gamma_{max} \leq 0.01\%$ bin, and 321 motions from 13 sites are included in the $0.01\% \leq \gamma_{max} \leq 0.10\%$ bin, but only 59 motions from 12 sites are included in the $\gamma_{max} > 0.10\%$ bin. A larger number of γ_{max} bins (i.e., 5 instead of 3) could have been used to investigate more fully the strain dependence of the variability, but such categorization would have led to inaccurate estimates of variability due to the lack of enough data at the larger γ_{max} bins.

By combining the observations and numerical results from all borehole arrays using Equation 7.1 and grouping the results based on the computed γ_{max} , we are able to quantify the fixed effect (i.e., α) of the EQL, EQL-FD and NL methods at different strain levels and also quantify the variability associated with the site am-

Table 7.1: Number of input motions per borehole array and γ_{max} range

Site	$\gamma_{max} \leq 0.01\%$			$0.01\% \leq \gamma_{max} < 0.1\%$			$\gamma_{max} > 0.1\%$		
	EQL	EQL-FD	NL	EQL	EQL-FD	NL	EQL	EQL-FD	NL
FKSH19	97	97	107	33	33	23	2	2	2
FKSH20	31	30	34	19	20	16	2	2	2
IBRH11	117	109	127	85	91	75	2	4	2
IBRH13	7	8	13	51	49	43	14	15	16
IWTH26	1	1	3	17	16	15	12	13	12
KSRH06	16	16	20	24	24	20	6	6	6
KSRH07	7	7	9	26	26	24	5	5	5
KSRH10	21	21	21	10	10	10	3	3	3
MYGH05	14	13	14	6	7	8	6	6	4
MYGH10	66	66	77	36	36	24	2	2	3
TTRH02	8	7	8	6	7	6	2	2	2
La Cienega	4	4	4	4	4	4	-	-	-
Lotung	9	9	8	4	3	4	3	4	4
TOTAL	398	388	445	321	326	272	59	64	61

plification predicted by these models. At this point, it should be noted that the fixed effect, or bias, is the same as the average residual discussed in *Chapter 6*. While the observations regarding the fixed effect will be similar to those from *Chapter 6* (except that we use fewer strain bins in this analysis), they are presented for completeness.

FIGURES 7.3 through *7.5* summarize the results for the EQL, EQL-FD and NL methods, respectively. *FIGURES 7.3a*, *7.4a* and *7.5a* illustrate the mean residuals along with the corresponding 90 % confidence intervals, while *FIGURES 7.3b*, *7.4b*, and *7.5b* present the corresponding standard deviations. Results are shown for the three shear strain bins defined above. The mean residuals (μ_y) represent the “fixed effect”

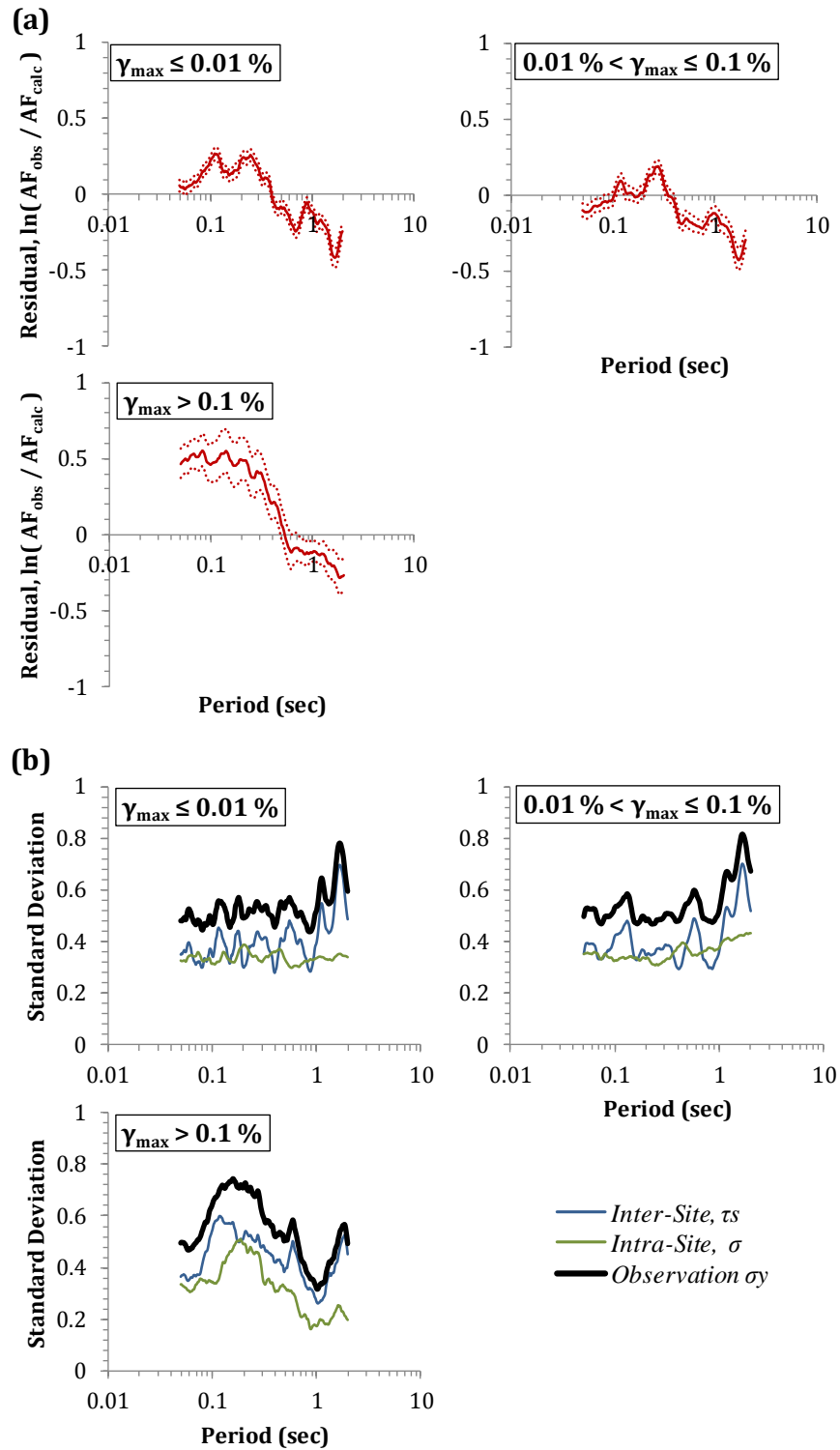


Figure 7.3: (a) Mean residuals, and (b) standard deviations for amplification factors computed by the EQL approach

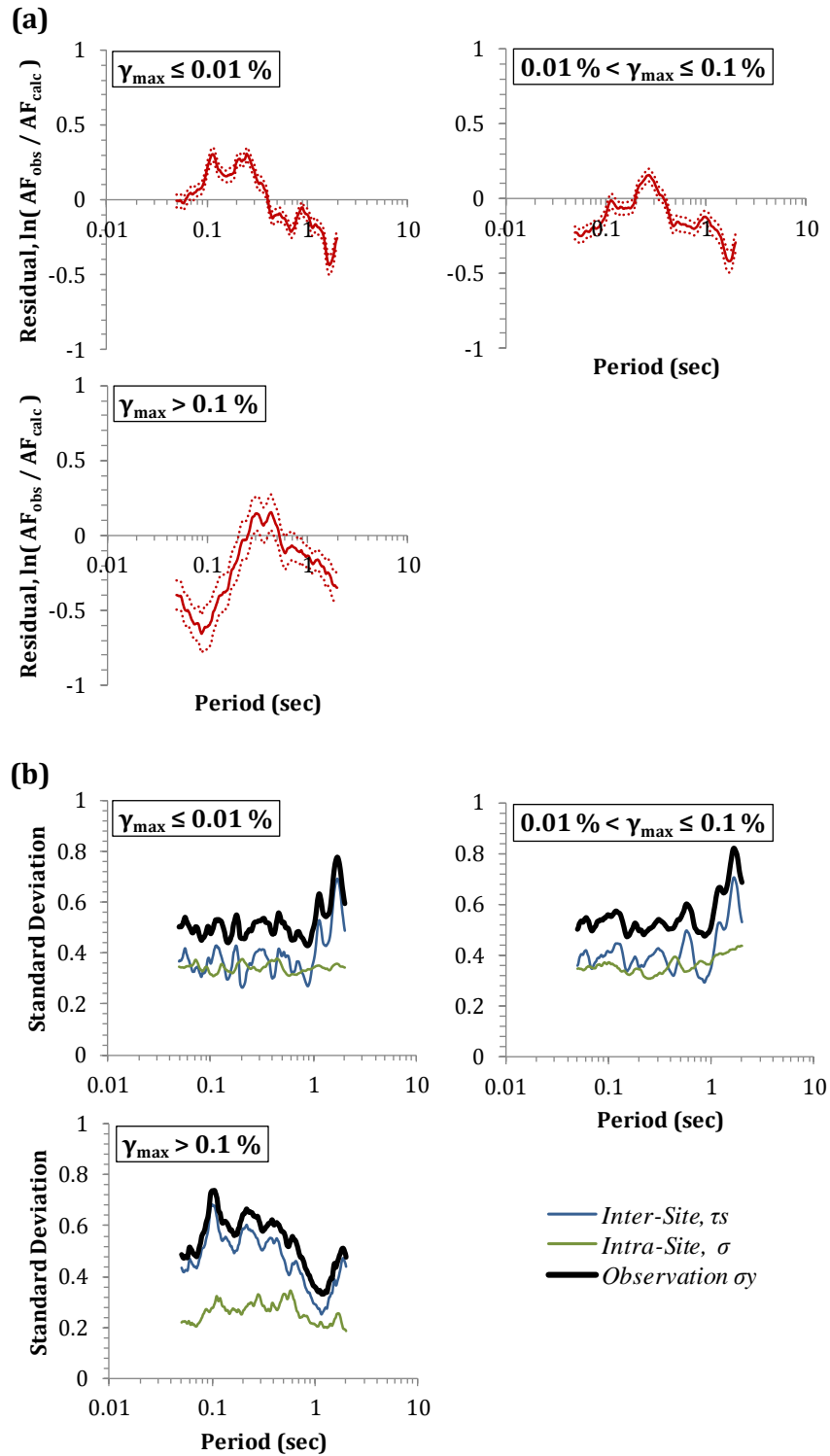


Figure 7.4: (a) Mean residuals, and (b) standard deviations for amplification factors computed by the EQL-FD approach

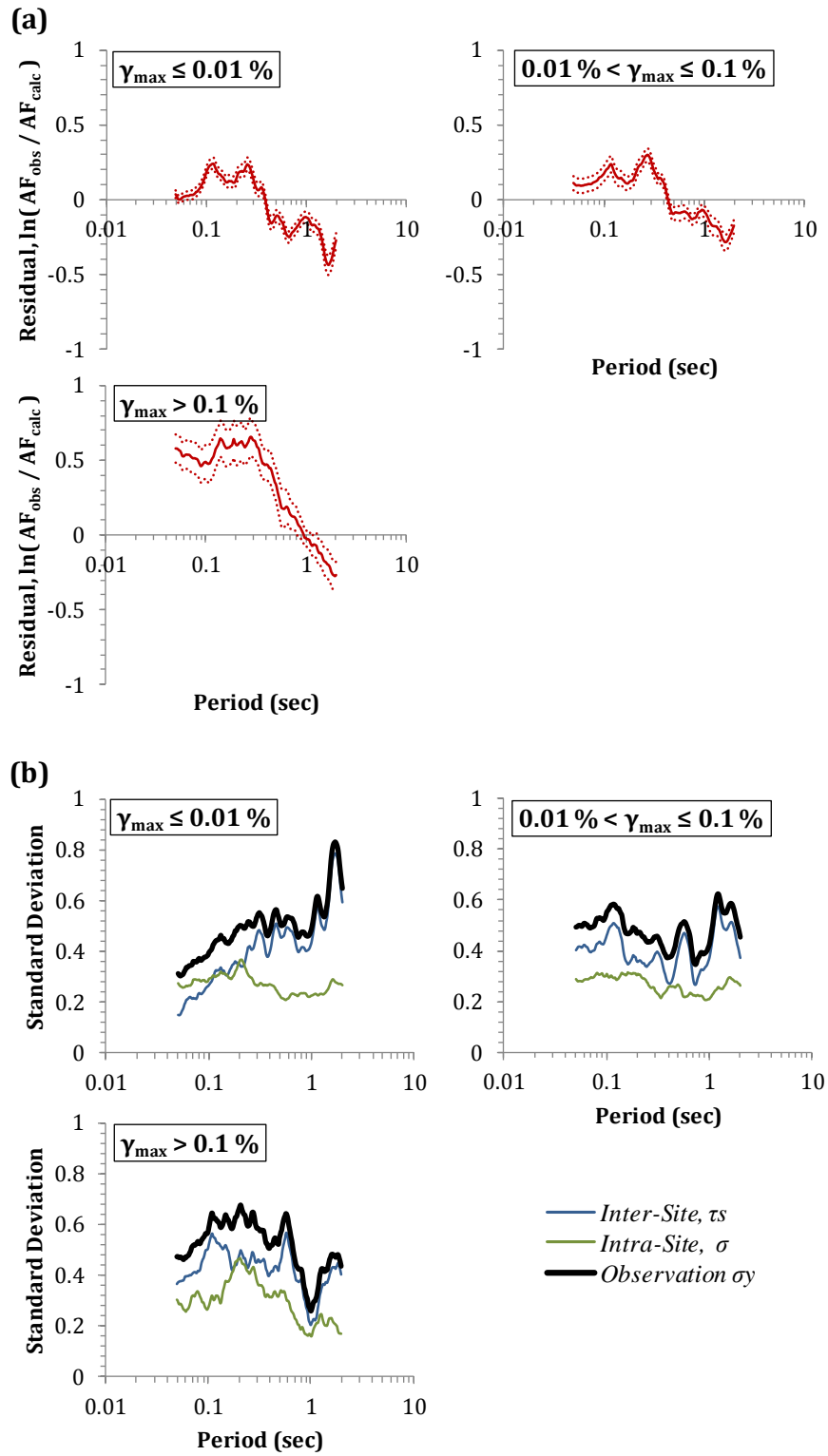


Figure 7.5: (a) Mean residuals, and (b) standard deviations for amplification factors computed by the NL approach

α , while the total standard deviations (σ_y) include inter-site and intra-site standard deviations (τ_s and σ , respectively).

It should be noted that the mean inter-site residual (μ_{η_s}), could have been included in *FIGURES 7.3* through *7.5* to fully represent the model, as developed based on the observations from this study. Although μ_{η_s} is assumed to be zero-valued, this assumption is not fully achieved because of the relatively limited number of borehole arrays considered (13) and because the number of recordings is not evenly distributed among the sites. Nonetheless, even though the computed values of μ_{η_s} are not zero, they are close to zero (~ 0.1), and do not affect the validity of our overall conclusions.

FIGURE 7.4a, demonstrates that the accuracy of the EQL method strongly depends on the level of the induced strains. At smaller strain levels ($\gamma_{max} \leq 0.10\%$), the EQL method yields mean residual values relatively close to zero across almost the entire period range, with the exception of periods close to 1.5 – 2.0 s where an overamplification of the response is observed. This result is caused by the fact that the “within” wavefield results in high first mode amplification particularly at sites with depth to the downhole sensor greater than 200 m (*Group 3* sites). When the induced strain level increases ($\gamma_{max} > 0.10\%$), the responses from the EQL approach deviate from the observations, with the average residual becoming large and positive. At periods smaller than approximately 0.4 – 0.5 s, the EQL approach under-predicts the response by as much as factors of 1.5 to 3.0. Under-prediction of the response can be attributed to the inability of the numerical model to deal with excessive nonlinearities caused by strong shaking, as more thoroughly explained in [Chapter 6](#).

The total observational standard deviation for the EQL method (σ_y , *FIGURE 7.3b*) at smaller strains ($\gamma_{max} \leq 0.10\%$) is approximately 0.45 – 0.5 at periods less than 1.0 s but it increases up to 0.75 at larger periods. The inter-site and intra-site standard deviations contribute almost equally (~ 0.3 to 0.4) to the total standard deviation at periods less than 1.0 s, while at larger periods τ_s is the dominant contributor. The intra-site variability (σ) seems to be period independent at a value of about 0.35, an observation which is in agreement with the values indicated by Kaklamanos *et al.* (2013) and shown in *FIGURE 7.2*. The inter-site standard deviation (τ_s), on the other hand, shows a period dependence, increasing from 0.3 – 0.5 to almost 0.6 – 0.7 at periods greater than 1.0 s. This result, once again, is caused by the fact that the “within” wavefield produces excessive first mode amplification at various sites. Because only some sites display this feature at long periods, the inter-site variability across all sites is increased. At larger strains ($\gamma_{max} > 0.10\%$), the total variability, σ_y , increases to about 0.65 – 0.8 at $0.1\text{ s} < T < 0.4\text{ s}$. Moreover, the peak in σ_y at $T > 1.0\text{ s}$ observed at smaller strains is substantially decreased. At $\gamma_{max} > 0.10\%$, the inter-site component of variability dominates across all spectral periods, with the intra-site standard deviation being smaller. At these levels of shaking the calculated maximum strain, and not input motion characteristics, predominantly influences the performance of the theoretical model, which may explain why the intra-site variability is smaller than the inter-site variability in this case. Moreover, the larger inter-site variability (τ_s) can also be attributed to the fact that analyses resulting in large shear strains include fewer motions per site, making the estimates of the average inter-site residuals ($\eta_{s,i}$) less reliable which increases τ_s .

The EQL-FD results are shown in *FIGURE 7.4*. At small strain levels ($\gamma_{max} \leq 0.01\%$), the residuals and standard deviations from the EQL-FD approach are very similar to those for the EQL approach because at small strains both approaches are essentially the same. As the magnitude of the induced strains increases (i.e. $0.01\% \leq \gamma_{max} \leq 0.10\%$, and $\gamma_{max} > 0.10\%$), the mean residuals for the EQL-FD model gradually become negative at periods less than about $0.2 - 0.3$ s. These residuals indicate an over-prediction of the amplification by factors as large as 1.5 to 2.0, at $\gamma_{max} > 0.10\%$. As previously discussed in *Chapter 6*, the over-amplification of high frequencies is caused by the utilization of low damping values (i.e., close to D_{min}) at high frequencies.

In terms of the variability in the calculated residuals for the EQL-FD approach (*FIGURE 7.4b*), the total standard deviation (σ_y) at all strain levels is similar to that for the EQL method, as expected. As in the case of the EQL method, at larger strains ($\gamma_{max} > 0.10\%$) the inter-site variability (τ_s) is the primary contributing factor to the total standard deviation, with the corresponding intra-site standard deviation (σ) taking relatively small values ($0.2 - 0.3$). However, again, it should be noted that the fewer number of motions per site included in the analyses at large strains makes the computed average residuals ($\eta_{s,i}$) less reliable which increases τ_s .

FIGURE 7.5 illustrates the period dependence of the mean residuals and variability for NL site response analyses. The observations regarding the accuracy of the NL model (*FIGURE 7.5a*) are very similar to those made for the EQL approach. At smaller strains, the average residuals are close to zero and at larger strains the average residuals become positive (i.e., the model under-predicts the response) at short periods. At $\gamma_{max} > 0.10\%$, this under-prediction at short periods by the NL method seems to be more pronounced than in the case of EQL, i.e. μ_y values of up to

0.65 are observed at $T < 0.2 - 0.3$ s, while these values were about 0.5 for EQL. Moreover, strong positive residuals extend to larger spectral periods, (i.e., as large as 1.0 s for NL analysis, but only as large as 0.5 s for EQL analysis). The inability of the NL method to accurately reproduce the recorded response at large strains may be a result of using G/G_{max} curves that do not appropriately constrain the shear strength at large strains.

The different components of variability for the NL analyses are presented in *FIGURE 7.5b*. The total standard deviation (σ_y) at small strain levels is very similar to that for the EQL and EQL-FD methods, further strengthening our conclusion that the overall variability in the predictive estimates is independent of the numerical scheme used to compute the site response. Unlike the EQL and EQL-FD results, the inter-site variability for the NL analysis contributes more to the total standard deviation even at low strains ($\gamma_{max} < 0.10$ %). Intra-event variability seems to be, once again, period independent and close to 0.30, a value slightly lower than the equivalent for the EQL model (*FIGURE 7.3b*). Moreover, for $\gamma_{max} \leq 0.10$ %, the fact that not all of the considered sites are well represented by the “perfectly rigid base” assumption leads to an increase in τ_s at periods greater than 1.0 s. The effect is mitigated with increasing strains. Indeed, for $0.01\% \leq \gamma_{max} \leq 0.10\%$, the distinctive high period ($T > 1.0$ s) peaks in τ_s and σ_y which were observed for both EQL and EQL-FD models are almost non-existent for NL method.

FIGURE 7.6 summarizes the *mean* observation residuals (μ_y) and total standard deviations (σ_y) for the EQL, EQL-FD and NL approaches across the three shear strain bins considered. At $\gamma_{max} \leq 0.01$ %, all site response methodologies yield almost identical *mean* prediction residuals and total standard deviations across all spectral periods. The NL analysis displays a slightly smaller total variability

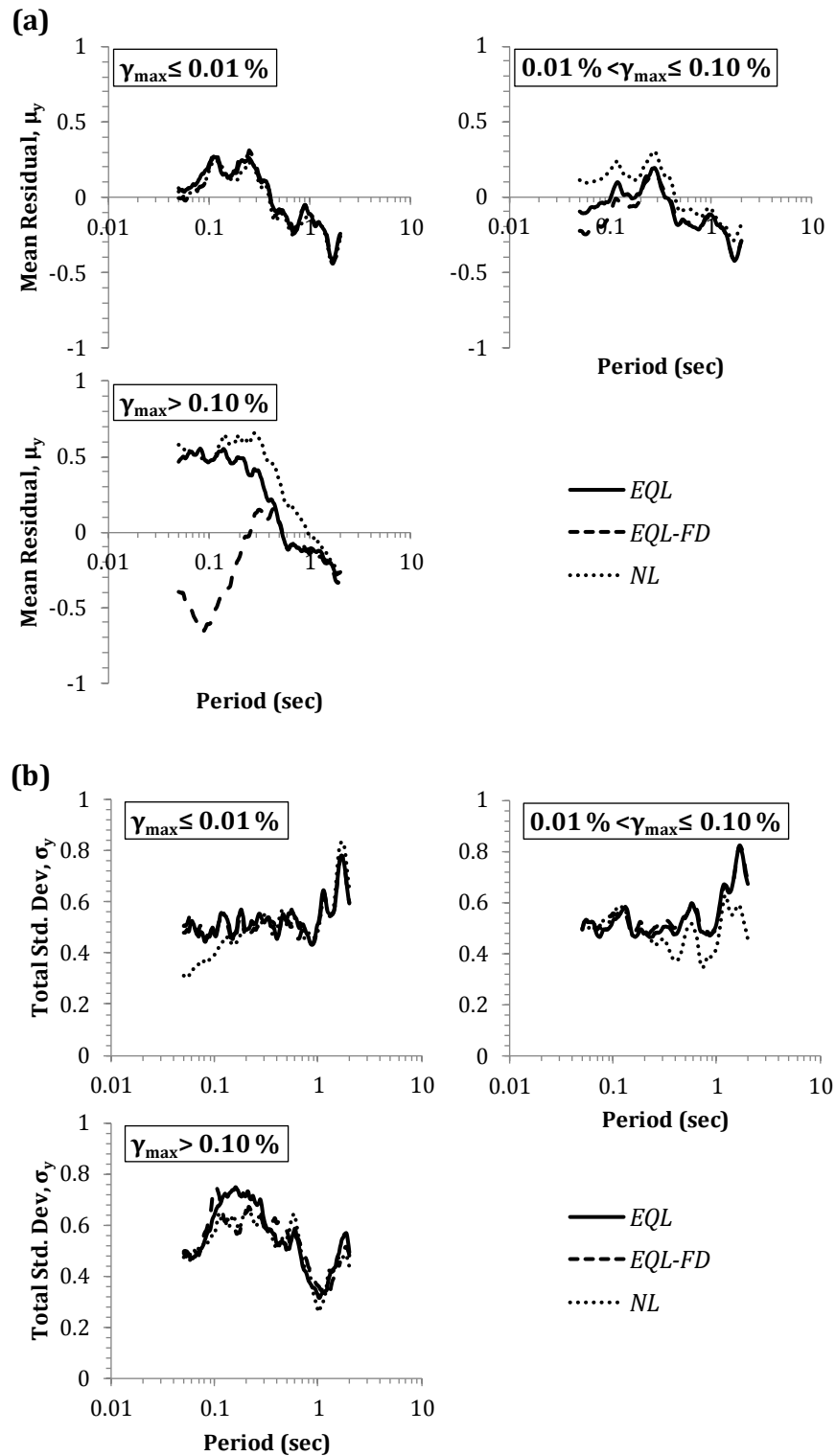


Figure 7.6: (a) Mean residuals, μ_y , and (b) total standard deviations, σ_y , across different induced shear strain levels, for all site response models

lity at periods less than 0.15 s. All models show large mean residuals and total standard deviations at $T = 1.5 - 2.0$ s, due to the utilization of the “within”/“perfectly rigid base” assumptions.

As the calculated shear strains increase, deviations in μ_y between the different models are evident. At $0.01 \% \leq \gamma_{max} \leq 0.10 \%$, the NL method produces the largest residuals (i.e., lower amplification) than the other methods, across all periods. At periods less than about 0.4 s, NL analysis under-predicts the observed response by a factor of up to 1.30. On the other hand, at the same periods, the EQL results are in better agreement with the observations ($\mu_y = +/-0.1$ which represents $+/-10 \%$), while EQL-FD residuals become increasingly negative. The EQL and EQL-FD methods provide almost identical results at $T > 0.4$ s. In terms of the total standard deviation (*FIGURE 7.6b*), the EQL and EQL-FD models provide very similar results, while the NL method seems to be characterized by lower σ_y at $T > 0.2$ s.

The most significant differences in the different site response methodologies can be seen at strains greater than 0.10 %. At strains larger than 0.1 %, the EQL and NL residuals become increasingly positive for periods less about than 0.5 s and indicate an under-prediction in the response. The under-prediction by the NL method is slightly greater and it extends to larger periods than for the EQL model. The EQL-FD approach results in substantial negative residuals (i.e., over-amplification) at periods less than 0.2 s, but this over-prediction appears to be generally less than the under-prediction by the EQL and NL methods. At large strains ($\gamma_{max} > 0.10 \%$), the total variability, σ_y , is larger than at small strains and increases to about 0.65 – 0.8 at $0.1 \text{ s} < T < 0.4 \text{ s}$. Moreover, the total standard deviations are, the same for the three site response approaches.

7.4. Effect of T_{site} and T_m

7.4.1. Effect of T_{site}

To investigate the period dependence of the mean residuals and variability with respect to the first mode response of the vertical arrays, we computed the total standard deviation (σ_y) as a function of the spectral periods (T) divided by the site period (T_{site}). To ensure that enough sites are represented at each T/T_{site} value, a procedure similar to the one described in [Section 6.4.1](#) was followed; we selected the minimum and maximum values of T/T_{site} by setting that no less than 7 sites contribute to the overall variability at any given T/T_{site} . Therefore, the variability is shown only for T/T_{site} between 0.07 and 2.0. The collective results of our analysis, in terms of *mean* observation residuals (μ_y) and total standard deviations (σ_y) for the EQL, EQL-FD and NL models and for the three shear strain ranges considered, are presented in [FIGURE 7.7](#).

The dependence of the mean residuals ([FIGURE 7.7a](#)) on the magnitude of the shear induced strains is, once again, evident. All three site response models show an increasing deviation of the residuals from zero with increasing level of shear strain, at T/T_{site} less than about 1.0 (i.e., periods less than the site period). While the EQL and NL methods still have mean residuals close to zero at strains between 0.01 % and 0.1 %, the EQL-FD method starts to deviate from a zero residual within the same strain range. The largest residuals occur at $T/T_{site} \cong 0.08$ for $\gamma_{max} > 0.10$ %. Here, the EQL and NL approaches display strong positive residuals ($\mu_y \cong 0.55 - 0.65$), while the EQL-FD method displays strong negative residuals ($\mu_y \cong -0.50$). At T/T_{site} close to 1.0 all three models show excessive over-amplification (i.e., negative residuals) due to the within wavefield assumption, although this effect is reduced with increasing shear strain due to larger damping in the soil.

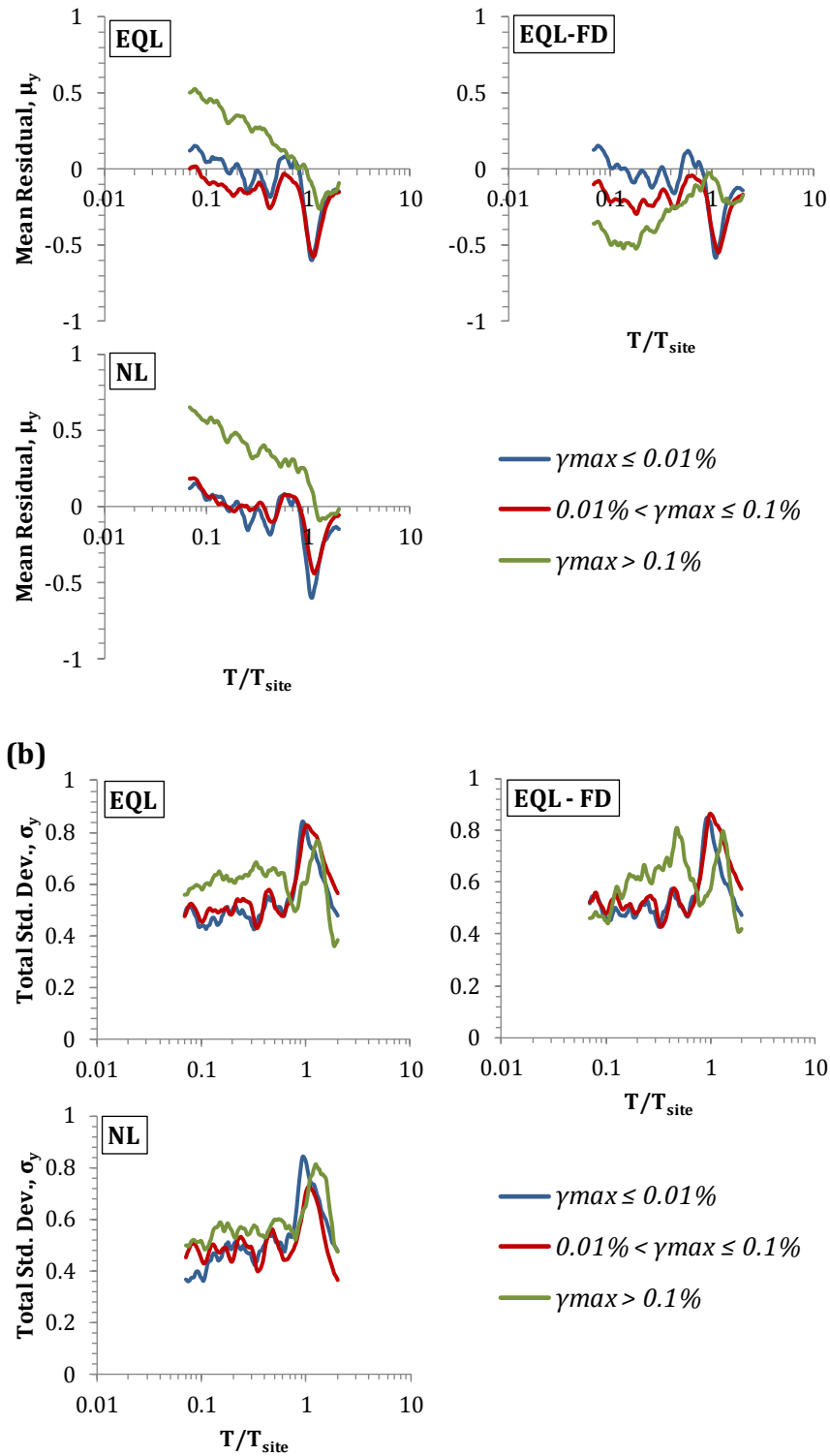


Figure 7.7: (a) Mean residuals, μ_y , and (b) total standard deviations, σ_y , versus normalized period (T/T_{site}) across different induced shear strain levels

The total standard deviations (σ_y) as a function of T/T_{site} for the EQL, EQL-FD and NL models are shown in *FIGURE 7.7b*. At smaller strain levels (i.e. $\gamma_{max} \leq 0.10\%$), the total variability is on the order of 0.4 – 0.5 at $T/T_{site} < 1.0$ and it increases to almost 0.8 at $T/T_{site} \cong 1.0$ for all three methods. The latter observation is, once more, caused by the site-to-site difference in the degree of suitability of the assumed boundary conditions (i.e., within wavefield) at the base. At larger strains the total variability shows a slight increase at $T/T_{site} < 0.8$, for all models.

7.4.2. Effect of T_m

The frequency content of the input motion may influence the results from one-dimensional models, and this effect is investigated here. Rathje *et al.* (1998) indicated that the mean period (T_m) provides a good measure of the frequency content of strong ground motions. T_m is computed from the Fourier Amplitude Spectrum and is defined as:

$$T_m = \frac{\sum_i C_i^2 (1/f_i)}{\sum_i C_i^2} \quad \text{for } 0.25 \text{ Hz} \leq f_i \leq 20 \text{ Hz, with } \Delta f \leq 0.05 \text{ Hz} \quad (7.4)$$

where C_i are the Fourier amplitude coefficients. f_i are the discrete fast Fourier transform (FFT) frequencies between 0.25 Hz and 20 Hz, and Δf is the frequency interval used in the FFT computation. *FIGURE 7.8* presents the calculated T_m values for all the motions and all sites, with respect to their respective PGA_{base} . The vast majority of the utilized input motions are characterized by T_m between 0.1 s and 0.5 s. A slight trend of an increasing T_m with increasing input motion intensity is observed, but this trend is not clearly identified.

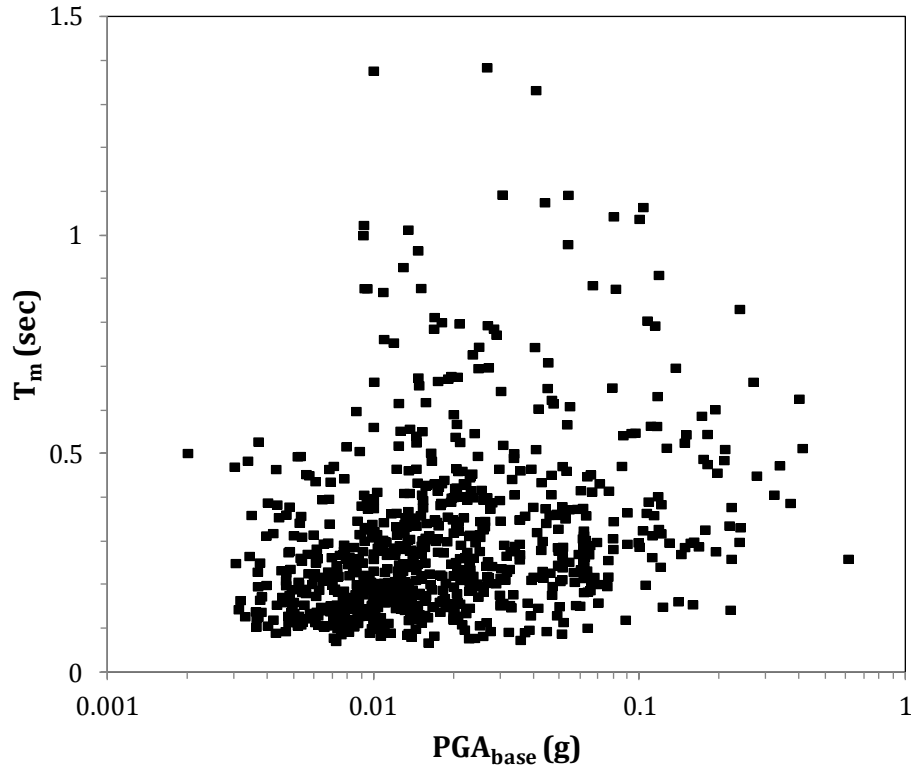


Figure 7.8: Mean period (T_m) of the input motions versus their respective PGA_{base}

The most effective way to investigate the effect of T_m on the accuracy of the different site response methods is by examining the effect of the frequency content on the intra-site residuals ($\varepsilon_{i,j}$). $\varepsilon_{i,j}$ is the most appropriate measure for such an undertaking because it represents the motion-to-motion, “within-site” variability. As mentioned in [Section 7.2](#), $\varepsilon_{i,j}$ is considered to be a normally distributed random variable with zero mean ($\mu_\varepsilon = 0$) and standard deviation σ . $\varepsilon_{i,j}$ represents the difference between a single observation, $y_{i,j}$, and the site-corrected mean residual ($\alpha + \eta_{s,i}$).

Based on data from all sites, *mean* intra-site residuals (μ_ε) have been calculated for recordings with $T_m < 0.33$ s, and $T_m > 0.33$ s. In these analyses, motions with $T_m < 0.33$ s represent “high frequency content”, while motions with

$T_m > 0.33$ s represent “low frequency content”. Moreover, the *mean* intra-site residuals were categorized based on the level of straining, using the same γ_{max} bins defined previously (i.e., $\gamma_{max} \leq 0.01$ %, 0.01 % $\leq \gamma_{max} \leq 0.10$ %, and $\gamma_{max} > 0.10$ %). The results of this analysis are presented in *FIGURE 7.9*, in terms of the period dependence of μ_ε , for the three site response models and γ_{max} bins. Theoretically, the computed μ_ε should be close to zero.

At $\gamma_{max} \leq 0.01$ % and 0.01 % $\leq \gamma_{max} \leq 0.10$ %, the frequency content of the input motion seems to have only minimal impact on the computed *mean* intra-site residuals μ_ε and they are close to zero across all spectral periods. Therefore motion-to-motion variability in the frequency content of the input motion does not affect the accuracy of the theoretical models at these strain levels. On the other hand, *FIGURE 7.9c* illustrates that at $\gamma_{max} > 0.10$ % the mean intra-site residuals deviate significantly from zero. The “high frequency content” motions ($T_m < 0.33$ s) are associated with negative *mean* intra site residuals at low periods, while the “low frequency content” motions ($T_m > 0.33$ s) are associated with positive *mean* intra-site residuals. The values of μ_ε deviate from zero by as much as ± 0.30 for the EQL method, ± 0.15 for the EQL-FD method, and ± 0.20 for the NL method. Despite these non-zero mean intra-site residuals, it should be noted that if we combine the $\varepsilon_{i,j}$ from all motions to obtain the overall μ_ε at $\gamma_{max} > 0.10$ %, the final mean value will be close to zero.

These results indicate that “high frequency content” motions yield higher short period amplification and “low frequency content” motions yield smaller short period amplification than the *mean AF* of the array at which they were recorded. For example, if the mean response from a theoretical model strongly under-predicts the observations (i.e., positive inter-site residual, $\eta_{s,i}$), then a “high frequency con-

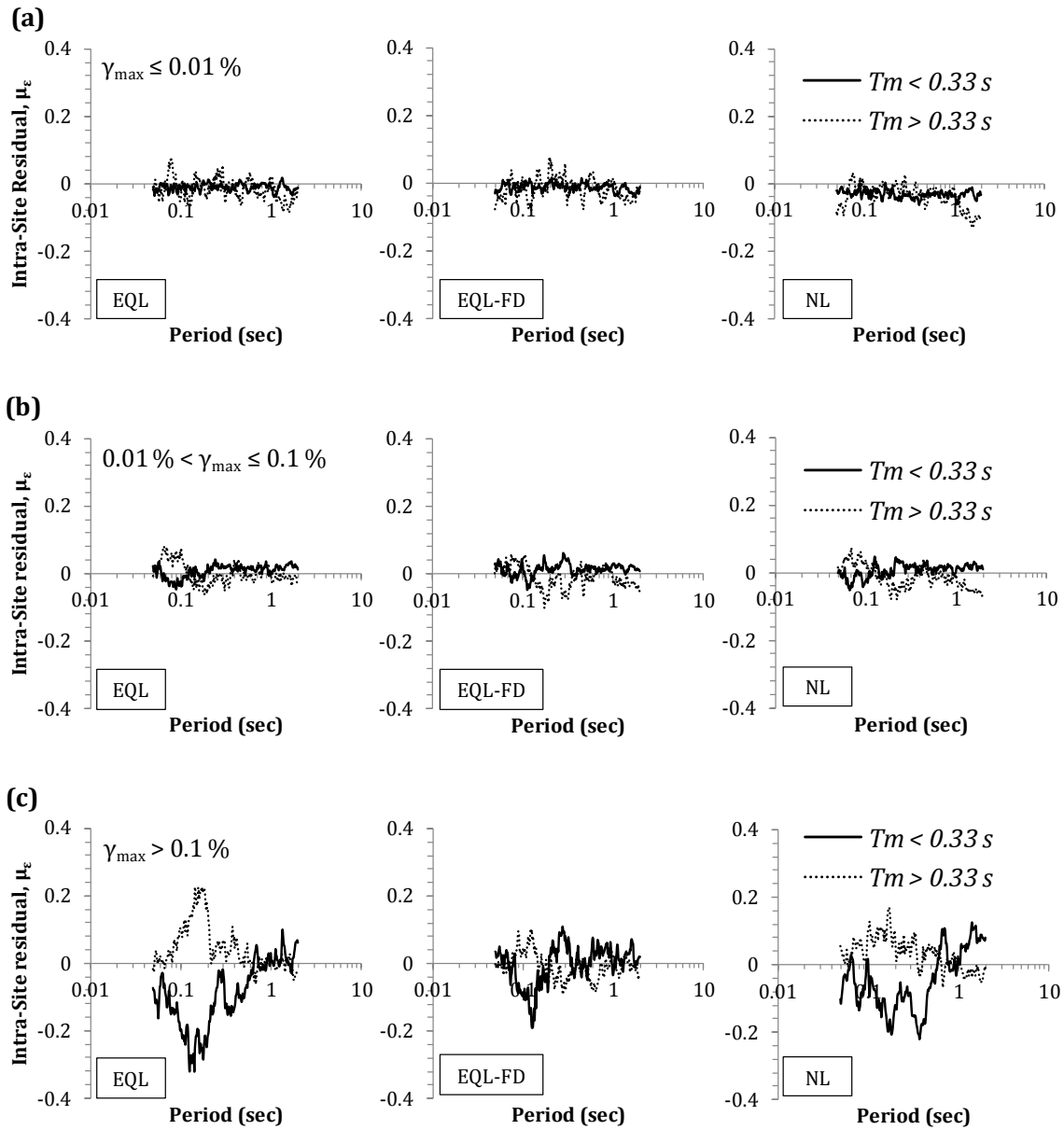


Figure 7.9: Mean intra-site residuals, $\epsilon_{i,j}$, for all site response models computed using motions with $T_m < 0.33\text{ s}$ (solid line) and motions with $T_m > 0.33\text{ s}$ (dashed line), for: (a) $\gamma_{max} < 0.01\%$, (b) $0.01\% < \gamma_{max} < 0.01\%$, and (c) $\gamma_{max} > 0.1\%$

tent” motion at that site would produce less under-prediction and a “low frequency content” motion would produce an even greater under-prediction.

To provide an example regarding this effect, we plot the period dependence of the residuals from two single events at IWTH26 site (*FIGURE 7.10*). The selected events produced similar shear strains ($\gamma_{max} \sim 0.2\%$), but were characterized by different frequency contents. More specifically, one motion was associated with $T_m = 0.28\text{ s}$ (i.e., $T_m < 0.33\text{ s}$ - “high frequency motion”) and one motion was associated with $T_m = 0.65\text{ s}$ (i.e., $T_m > 0.33\text{ s}$ - “low frequency motion”). Again, at low spectral periods, the residual from the “high frequency content” motion ($T_m = 0.28\text{ s}$) is lower than the residual from the “low frequency content” motion ($T_m = 0.65\text{ s}$). Therefore, larger high frequency amplification is predicted by the “high frequency content” motion.

A schematic explanation of this effect is shown in *FIGURE 7.11*. The schematic depicts the idealized shear strain Fourier Amplitude Spectra ($\gamma(f)$) from two input motions that produce very similar γ_{max} values, and thus very similar effective strains (γ_{eff}) to define the strain compatible properties. The difference between the two idealized input motions is their frequency content. One motion is characterized by a low T_m (“high frequency content” motion), while the other motion is characterized by a high T_m (“low frequency content” motion). The red line in *FIGURE 7.11* represents the γ_{eff} value translated into the frequency domain.

As noted previously, the damping assigned in EQL analysis is based on a single effective shear strain (γ_{eff}) and in the case of substantial straining (e.g. $\gamma_{max} > 0.10\%$), a large damping value is assigned. The large damping tends to over-damp high frequencies and lead to an under-prediction in the response at high frequencies. If a “low frequency content” motion is used (high T_m dashed line in

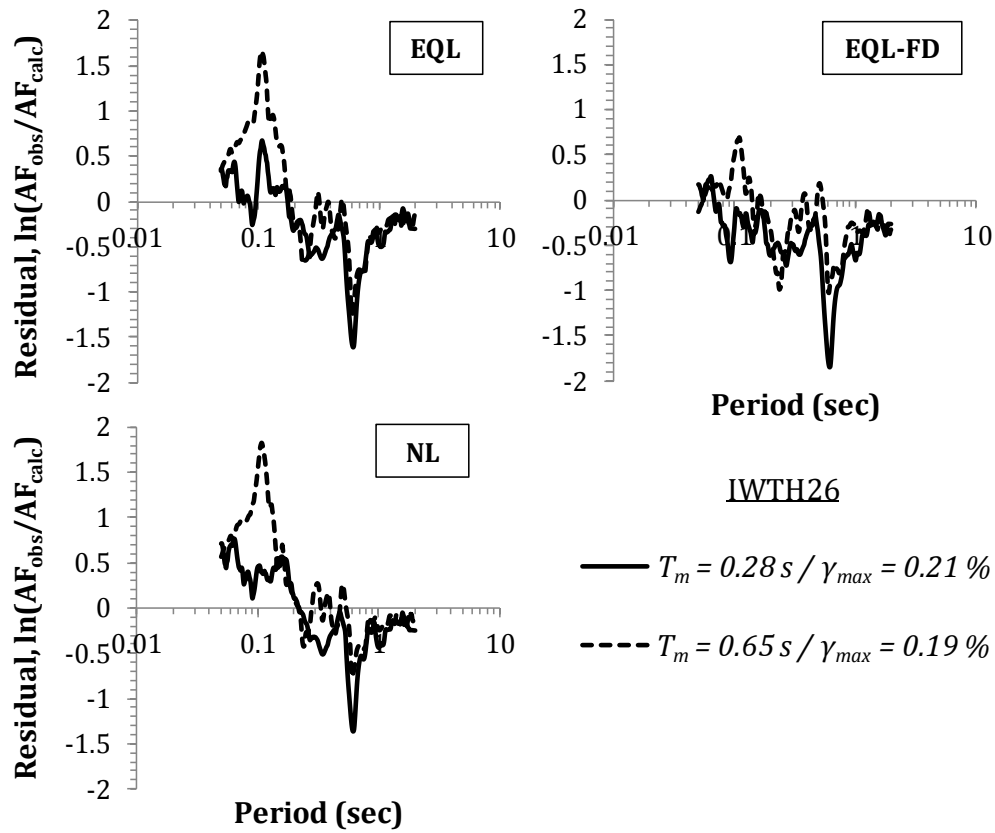


Figure 7.10: Amplification residuals for all site response models computed using two single events recorded at IWTH26 site

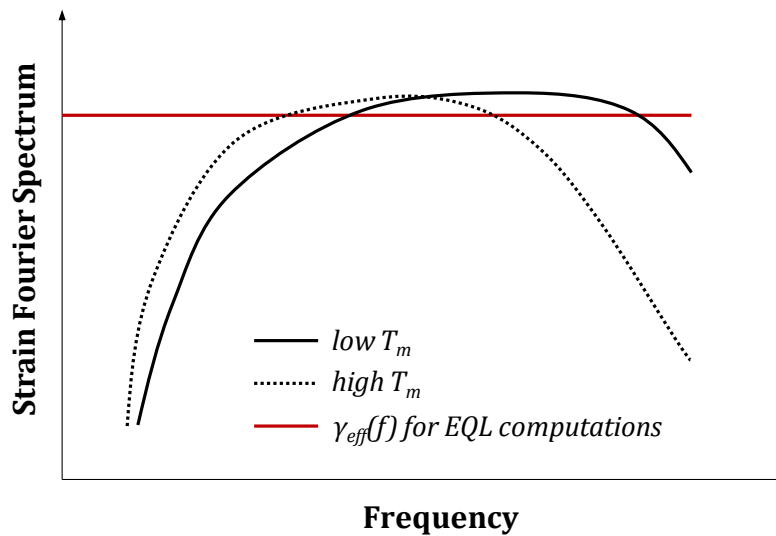


Figure 7.11: Schematic explanation of the dependence of the amplification residuals on the frequency content of the input motion, for EQL method

FIGURE 7.11) then a larger portion of the shear strain Fourier Spectrum ($\gamma(f)$) is misrepresented by the γ_{eff} line at high frequencies. The high frequencies associated with the misrepresented portion of $\gamma(f)$ are therefore further over-damped by EQL analysis for larger T_m motions. In contrast, if a “high frequency content” motion is used (low T_m - solid line in *FIGURE 7.11*) then a smaller portion of the shear strain Fourier Spectrum ($\gamma(f)$) is misrepresented by the γ_{eff} line at high frequencies. Consequently, EQL analysis does not over-damp the high frequencies as severely for low T_m motions. The effect of T_m on the mean intra-site residuals from EQL-FD analysis is small relative to the results from EQL analysis. This result is because EQL-FD analysis uses frequency-dependent properties that minimize the effect shown in *FIGURE 7.11*.

The mean intra-site residuals for NL analysis are also affected by T_m , although an effective strain is not used in NL analysis and cannot explain the effect. However, NL analysis shows the same systematic under-prediction of the high frequency response as EQL analysis. For NL analysis the under-prediction was primarily attributed to the utilization of G/G_{max} values inconsistent with the shear strength, which leads to large strains and excessive damping. It is postulated that when a “high frequency content” motion is used (low T_m), a larger range of frequencies is affected by the smaller G/G_{max} and the larger damping values at large strains.

7.5. Comparison of Variability Estimates with Previous Studies

The bias and variability estimates obtained in this study are compared with with results from Kaklamanos *et al.* (2013). *FIGURE 7.12* illustrates the comparison in terms of mean residuals (μ_y), total standard deviations (σ_y) and inter and intra-site

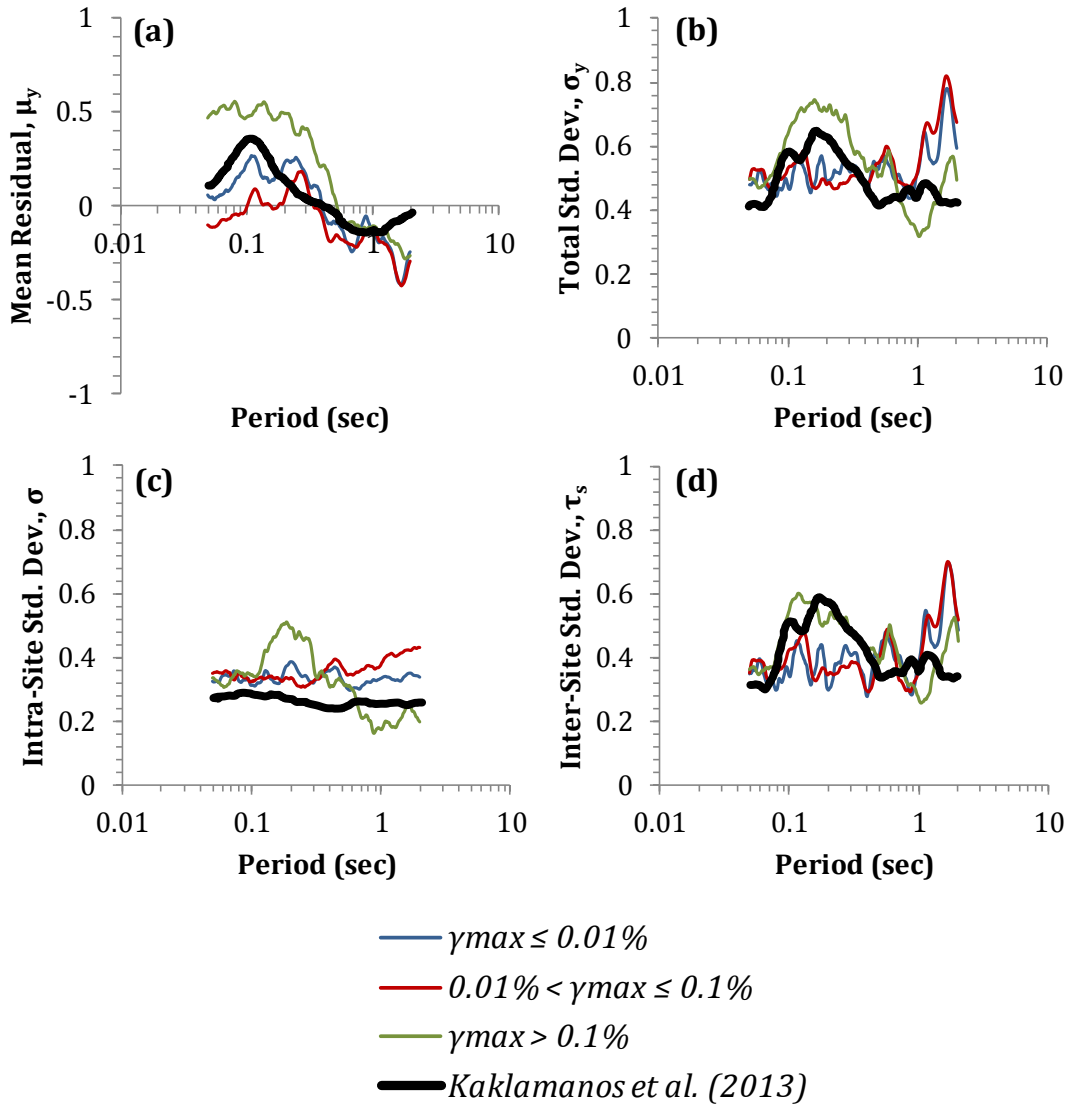


Figure 7.12: Comparison of across-site uncertainty estimated for EQL approach with Kaklamanos *et al.* (2013), in terms of : (a) fixed effect, α , (b) total standard deviation, σ_y , (c) intra-site standard deviation, σ , and (d) inter-site standard deviation, τ_s .

standard deviations (τ_s and σ , respectively). Since Kaklamanos *et al.* (2013) studied the performance of linear-elastic (LE) and equivalent linear (EQL) site response methodologies, the comparison with our results relates only to the EQL method.

Moreover, it is important to note that Kaklamanos *et al.* (2013) did not consider the influence of shaking level or induced strain on the variability estimates.

Nonetheless, good agreement is observed between the two studies (*FIGURE 7.12*). Kaklamanos *et al.* (2013) reports positive mean residuals of as high as $\mu_y \cong 0.40$ at periods less than about $0.3 - 0.4$ s (*FIGURE 7.12a*). Because these values represent the average across different shaking levels, they fall in-between our computed mean residual values for small strain ($\gamma_{max} \leq 0.10$ %) and large strain ($\gamma_{max} > 0.10$ %) levels. At periods greater than $0.3 - 0.4$ s and less than 1.0 s, Kaklamanos *et al.* (2013) report a small negative residual which is in accord with the results of this study irrespectively of the γ_{max} range. The only substantial difference between the two studies is seen at $T = 1.5 - 2.0$ s, where the results of this study indicate a much greater over-prediction of the response. The over-prediction is caused by the fact that 40 % of the sites used in this study were associated with an excessive first mode amplification (*Group 3* sites) due to the utilization of a “within” borehole wavefield, while Kaklamanos *et al.* (2013) performed EQL analyses on 100 Kik-Net arrays and therefore such modeling effects were averaged out.

In terms of total variability (σ_y , *FIGURE 7.12b*), the Kaklamanos *et al.* (2013) results again correspond with the average of our estimates across different γ_{max} levels. As in the case of the mean residuals, the largest inconsistency in the σ_y values between the two studies is found at $T = 1.5 - 2.0$ s and $\gamma_{max} \leq 0.10$ %. Furthermore, intra-site standard deviations (σ , *FIGURE 7.12c*) from Kaklamanos *et al.* (2013) are in the order of 0.3, which is slightly smaller than our results (~ 0.35). Nonetheless, both studies show that the intra-site standard deviation, σ , is period independent, at least at $\gamma_{max} \leq 0.10$ %. The inter-site standard deviation, τ_s , (*FIGURE*

7.12d), is also similar between the two studies, with the exception of $T = 1.5 - 2.0$ s and $\gamma_{max} \leq 0.10$ % where our analyses show substantial variability ($\tau_s \sim 0.75$). Based on the results in *FIGURE 7.12d*, it can be claimed that Kaklamanos *et al.* (2013) provides τ_s estimates that correspond to larger levels of shear strain ($\gamma_{max} > 0.10$ %).

7.6. Summary

The variability in the predicted site amplification from the three site response methods was assessed using the observations from all 13 vertical arrays used in this study. The main conceptual framework as well as the notation utilized by Kaklamanos *et al.* (2013) was adopted. The categorization of the results was based on γ_{max} . Three different ranges of γ_{max} were established; $\gamma_{max} \leq 0.01$ %, 0.01 % $\leq \gamma_{max} \leq 0.10$ %, and $\gamma_{max} > 0.10$ %.

At $\gamma_{max} \leq 0.01$ %, all site response methodologies yielded almost identical *mean* residuals and variability estimates across all spectral periods. For all three models, the total observational standard deviation was approximately 0.45 – 0.5 at periods less than 1.0 s but it increased to up to 0.75 at larger periods. The inter-site and intra-site standard deviations contribute almost equally (~ 0.3 to 0.4) to the total standard deviation at periods less than 1.0 s, while at larger periods τ_s is the dominant contributor. As the shear strain level increased, deviations in the mean residuals between the three models were observed. At these strains greater than 0.10 %, the EQL and NL residuals became increasingly positive (i.e., under-prediction) for periods less than 0.5 s. On the other hand, EQL-FD approach resulted in substantial over-amplification at periods less than 0.2 s. At large strains ($\gamma_{max} > 0.10$ %), the total variability, σ_y , is larger than at small strains and increases

to about 0.65 – 0.8 at $0.1\text{ s} < T < 0.4\text{ s}$. At these strain levels, the inter-site component of variability dominates across all spectral periods, with the intra-site standard deviation being smaller.

The period dependence of the variability estimates with respect to the first mode response of the vertical arrays was investigated by developing across-site variability estimates, as a function of the spectral periods (T) divided by the site period (T_{site}). All three site response models showed an increasing deviation from the observed amplification with increasing level of shaking (i.e., $\gamma_{max} > 0.10\%$), at T/T_{site} values less than 0.7 – 1.0. Moreover, the effect of the frequency content of the input motions was investigated. It was observed that, at $\gamma_{max} > 0.10\%$, “high frequency content” motions (i.e., $T_m < 0.33\text{ s}$) systematically produce higher short period amplification than the *mean AF* of the array at which they were recorded. On the other hand, “low frequency content” motions (i.e., $T_m > 0.33\text{ s}$) resulted in lower short period amplification than the *mean AF* of the site at which they were recorded. Finally, we compared the across-site variability estimates obtained in this study with results from Kaklamanos *et al.* (2013). A very good agreement between the two studies was observed, considering the fact that Kaklamanos *et al.* (2013) did not provide separate variability estimates at different levels of shaking.

Chapter 8

Improvement of Performance of One-Dimensional Site Response Methodologies

8.1. Introduction

Based on the results presented in *Chapters 6* and *7*, it was concluded that the EQL, EQL-FD and NL one-dimensional site response methodologies are all unable to accurately predict the high frequency ($T < 0.2 - 0.4$ s) seismic response of soil deposits, when large shear deformations are experienced. More specifically, the present study indicates that the EQL and NL models strongly under-predict the response at $T < 0.4$ s when $\gamma_{max} > 0.10$ %, while the EQL-FD model strongly over-predicts the observations at approximately $T < 0.2$ s when $\gamma_{max} > 0.01$ %.

Consequently, an effort to improve the performance of the one-dimensional theoretical models is necessary. Towards this goal, two procedures were adopted. First, the influence of accounting for the shear strength of the soil materials at large strains is considered. In this case, the utilized modulus reduction curves ($G/G_{max} - \log \gamma$) are altered to match a target shear strength for each material. Second, further work was focused on the refinement and improvement of the EQL-FD algorithm. Our main goal here was to modify the details in the implementation of the procedure, rather than reexamine its overall theoretical framework.

At this point, it should be stated that for the following analyses, site-specific modeling deficiencies should be avoided. That is, only vertical arrays whose response can be simulated reasonably well by a one-dimensional model should be

considered. Therefore, based on our findings from [Chapter 5](#), we decided to exclude the TTRH02 and MYGH10 arrays from the subsequent analysis. The LE response at these sites showed the largest deviations from the observations ([Chapter 5](#)). The TTRH02 site is located at a relatively high altitude on inclined, sloping ground ([Chapter 4](#)), something contradictory to the assumed one-dimensional system. For the MYGH10 site, the theoretical predictions were not able to capture either the location or the amplitude of the peaks in the observed amplification factors ([Chapter 5](#)), something that indicates that the site response is not captured well by the one-dimensional assumption.

8.2. Strength Correction at Large Strains

In the past, researchers (i.e., Chiu *et al.*, 2008; Stewart and Kwok, 2008; Hashash *et al.*, 2010) have pointed out that site response analysis must incorporate the shear strength of the soils at large strains. This issue is most critical for softer soils and/or larger input intensities, because it is these conditions that induce large shear strains that may begin to mobilize shear stresses close to the shear strength. The Darendeli (2001) model used herein is based on laboratory tests for the development of the modulus curves. Typically, these tests do not apply strains large enough to mobilize the shear strength, and therefore the shear strength is not explicitly considered when using these curves. Nonetheless, a modulus reduction curve may be extrapolated to shear strains as large as 10 % using the hyperbolic equation of the Darendeli (2001) model and, thus, one must evaluate whether the shear strength implied by the modulus reduction curve at large strains is reasonable. In this study, the calculated γ_{max} reached values as large as 6 % for EQL and EQL-FD analysis, and 2.6 % for NL analysis ([Chapter 6](#)), which makes the

utilization of proper G/G_{max} values at large strains a critical factor for these site response computations.

Chiu *et al.* (2008) and Hashash *et al.* (2010) indicated that modifying the backbone hyperbolic stress-strain curve based on shear strength data at large strains leads to a decrease in γ_{max} , and a corresponding increase in the computed response. For the purposes of nonlinear analysis, Hashash *et al.* (2010) developed a procedure in which the modulus reduction curve ($G/G_{max} - \log \gamma$) is modified at large strains to achieve a target shear strength. The proposed procedure involves the following steps:

1. The stress-strain curve represented by a modulus reduction curve is derived from the G/G_{max} values at each strain level and the G_{max} ($G_{max} = \rho \cdot V_S^2$) of a given soil layer. Noting that the moduli in a G/G_{max} curve represent secant moduli, the shear stress (τ) at any given value of shear strain (γ) is computed as:

$$\tau = G_{max} \cdot \left(\frac{G}{G_{max}} \right)_{\gamma} \cdot \gamma \quad (8.1)$$

where $\left(\frac{G}{G_{max}} \right)_{\gamma}$ is the G/G_{max} value at shear strain level γ .

2. The implied shear strength obtained via the $\tau - \gamma$ relationship (Equation 8.1) is compared with a *target shear strength*. The target shear strength is defined either through a friction angle (for granular materials) or through an undrained shear strength (for fine-grained materials). The target shear strength is computed for an effective vertical stress (σ'_v) at the middle of a given soil layer.

3. If the implied shear strength is different than the target shear strength, the modulus reduction curve data points ($G/G_{max} - \log \gamma$) are manually adjusted (increased or decreased) at shear strains greater than 0.1 % to match the target shear strength at large strains.
4. Based on the developed modulus reduction points from the previous step, a new pair of modulus reduction and damping curves is found by using the MRDF curve fitting procedure (Phillips and Hashash, 2009) (see [Chapter 2](#)).
5. The shear strength implied by the new $G/G_{max} - \log \gamma$ relationship at large strains is computed and compared with the target shear strength. Steps 3 – 5 are repeated if necessary.

Note that when incorporating a strength correction to EQL analysis, the target modulus reduction points can be used directly as the modulus reduction curve in the analysis without any change to the damping curve.

FIGURE 8.1 shows an example application of the above procedure for a hypothetical sand layer with a shear wave velocity of 135 m/s and a vertical effective stress (σ'_v) of 100 kPa. *FIGURE 8.1* displays the original Darendeli (2001) modulus reduction and damping curves (*FIGURE 8.1a* and *8.1b*) along with the derived stress-strain curve ($\tau - \gamma$) (*FIGURE 8.1c*). Based on the $\tau - \gamma$ curve, the maximum shear stress (τ_{max}) is predicted as approximately 17 kPa, a value that corresponds to a friction angle of only 10° at large strains. Assuming a more realistic friction angle of 30°, the *target shear strength* for the sand layer at $\sigma'_v = 100$ kPa is 57 kPa. Following the procedure developed by Hashash *et al.* (2010), the original modulus reduction curve is modified at large strains (approximately at $\gamma > 0.03$ %) by manually adjusting the data points to achieve a target shear strength of 57 kPa

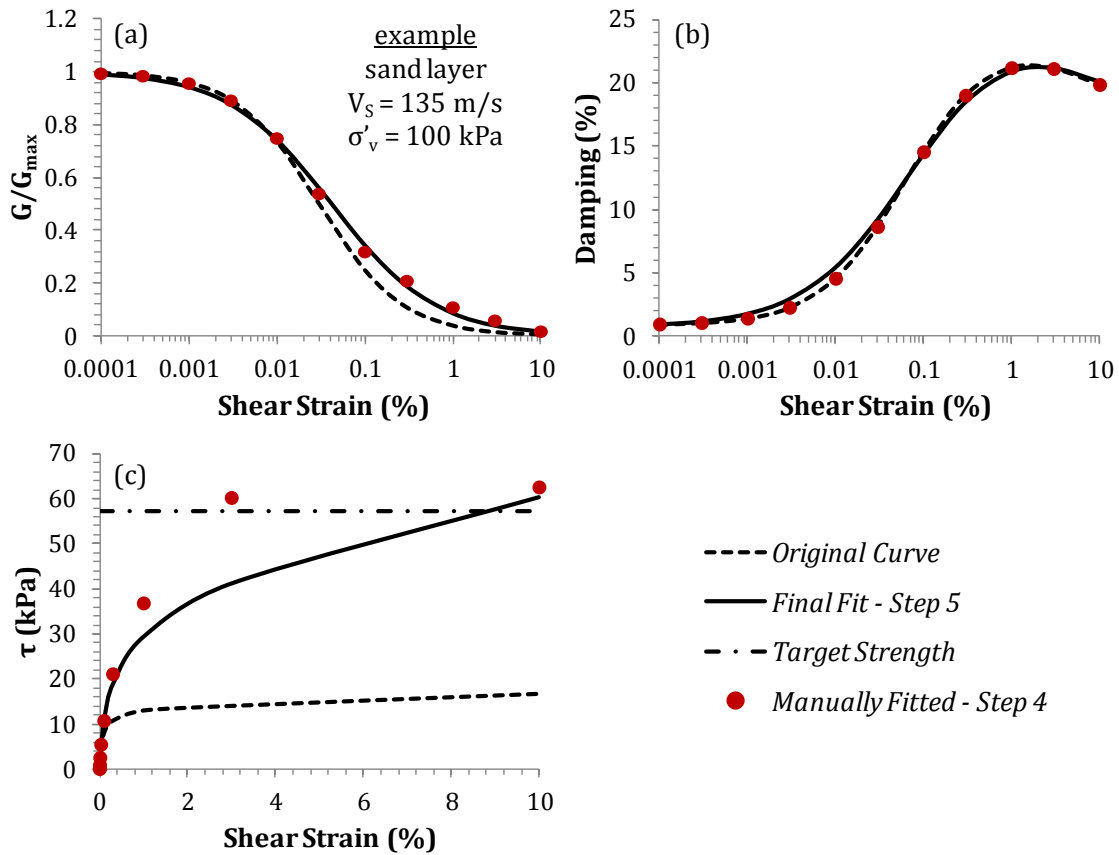


Figure 8.1: Example application of the Hashash *et al.* (2010) procedure for the modification of the G/G_{max} curve to account for the shear strength at large strains

(red dots in *FIGURE 8.1*). These points were selected to mobilize the shear strength at a shear strain of 3 %. Subsequently, the MRDF curve fitting procedure (Phillips and Hashash, 2009) is implemented to find a new pair of modulus reduction and damping curves that fit the target modulus reduction data points. The resulting G/G_{max} and damping curves, and the corresponding $\tau - \gamma$ curve are shown in *FIGURE 8.1* (solid lines). While the hyperbolic fit may not fit the manually selected points at all strain levels, the target shear stress at large strains (i.e., the strength) is achieved. The modified modulus reduction curve (*FIGURE 8.1a*) shows modest deviations from the original curve at strains larger than about 0.01 %, but these changes are

sufficient enough to significantly alter the stress-strain curve such that realistic shear stresses are mobilized at large strains. Moreover, it should be stated that the changes to the damping curve after the MRDF curve fitting are even less significant.

Following the same rationale, the one-dimensional models used for EQL, EQL-FD and NL site response analysis were modified to account for the shear strength at large strains. The Hashash *et al.* (2010) procedure was implemented for the 11 vertical arrays considered in this study. Specifically, the Darendeli (2001) modulus reduction curves were modified to match a reasonable target friction angle (φ). Because changing the nonlinear property curves at one depth may simply shift large strains to another layer, the modulus reduction curves were modified for all materials with a potential of straining to a level of more than 0.1 %. This led to the application of a strength correction to all layers within the upper 50 m of the soil profiles with a shear wave velocity of less than 500 m/s.

Ideally, the *target shear strength* would be determined based on data from a detailed geotechnical site investigation (i.e., data from laboratory and/or in-situ static or dynamic shear strength tests). Due to the lack of extensive geotechnical characterization, particularly at the Kik-Net sites, a layer-specific determination of target shear strengths is not possible. Therefore, a single target friction angle of 29° was assumed for all layers that were strength corrected. Such an assumption surely introduces errors in the modified modulus reduction curves. Nevertheless, the purpose of the present study is to evaluate and document the generic effect of the strength correction procedure on the obtained responses, and therefore a more detailed determination of the target shear strength at each layer goes beyond the scopes of this study.

8.2.1. Example Application of Shear Strength Correction Procedure

To effectively explain the results associated with the adopted strength correction procedure, the IWTH26 array is used as an example site. *FIGURE 8.2* presents the original and modified modulus reduction and damping curves as well as the derived stress-strain relationships for the soil layer that was strength corrected. This layer extends from the ground surface to a depth of 4 m, and has a shear wave velocity of 130 m/s. For the IWTH26 array, only one soil layer met the criteria for strength correction (i.e., $V_S < 500 \text{ m/s}$ and $depth < 50 \text{ m}$). Nonetheless, it should be noted that, for most sites, three or more soil layers were strength corrected. For documentation purposes, the original and modified curves for all vertical arrays and assorted strength corrected soil layers can be found in [Appendix A.4](#).

The strength correction is applied at the depth that experienced γ_{max} in the original analyses. For the IWTH26 site, γ_{max} occurred at a depth of 3.5 m and associated effective vertical stress of 59.5 kPa. *FIGURE 8.2* shows that for $V_S = 130 \text{ m/s}$ and $\sigma'_v = 59.5 \text{ kPa}$, the shear strength at large strains is underestimated by a factor of 3 when using the Darendeli (2001) curve. The target shear strength is achieved by a slight increase in the modulus reduction data points at strains greater than about 0.03 %. The updated damping curve shows only minor deviations from the original Darendeli (2001) model. As in the case of the original analysis, the damping curve has been shifted up at small strains to account for the additional attenuation due to wave scattering, as discussed in [Chapter 5](#). At this point, it is worthwhile to mention that in almost 80 % of the layers that were strength corrected, the target shear strength was larger than the one predicted by

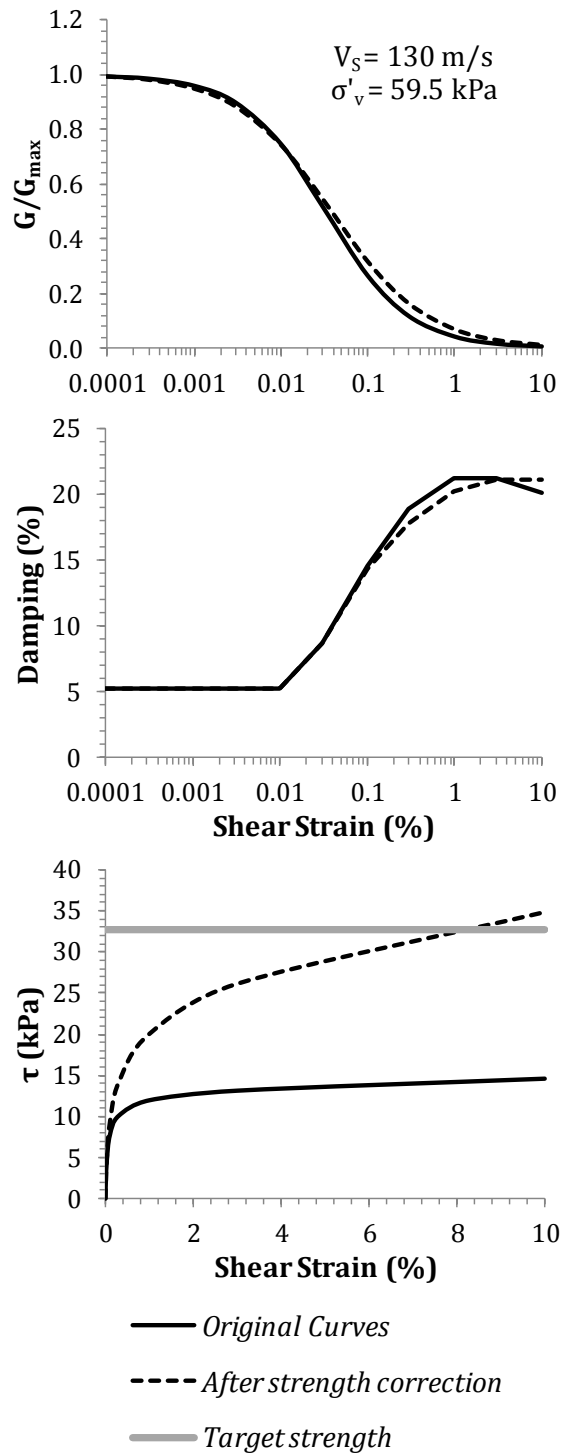


Figure 8.2: Original and modified modulus reduction and damping curves as well as the derived stress strain relationships for the strength corrected layer at IWTH26 array

the corresponding V_S value and the associated modulus reduction curve.

Using the modified modulus reduction and damping curves, EQL, EQL-FD and NL site response analyses were performed. *FIGURE 8.3* presents the relationship between the computed maximum shear strains (γ_{max}) before and after the strength correction for all the motions analyzed for the IWTH26 site. Based on *FIGURE 8.3*, it is evident that due to the incorporation of higher shear strength at large strains, the calculated γ_{max} are reduced for all models. Differences are observed for shear strains greater than about 0.03 %, which corresponds with the shear strain at which the original and strength corrected modulus reduction curves start to deviate. The most pronounced reduction in γ_{max} is experienced by the EQL method. In an extreme case, γ_{max} was reduced from about 5.5 % to approximately 0.25 %. The NL model shows a smaller reduction in γ_{max} due to the fact that the NL analyses were providing smaller γ_{max} values than the EQL and EQL-FD methods when the original modulus reduction curves were utilized.

To illustrate the effect of the reduced γ_{max} , *FIGURE 8.4* presents the computed surface response spectra (*FIGURE 8.4a*) and the corresponding *AF* residuals (*FIGURE 8.4b*) for the IWTH26 site, for an input motion recorded on 06/14/08, 08:43 with $PGA_{base} = 0.21 g$. Only a high intensity event is used because our main goal is to evaluate the effect of the strength correction on the computed response at large strains. Surface response spectra and the prediction residuals before and after the strength correction are depicted, and the corresponding values of calculated γ_{max} before and after the strength correction are listed in *TABLE 8.1*. Note that γ_{max} decreases significantly when the strength correction is included. In *FIGURE 8.4*, the effect of the reduction in γ_{max} is clearly observed as an increase in spectral acceleration and amplification at periods less than about 0.5 s for both the EQL and

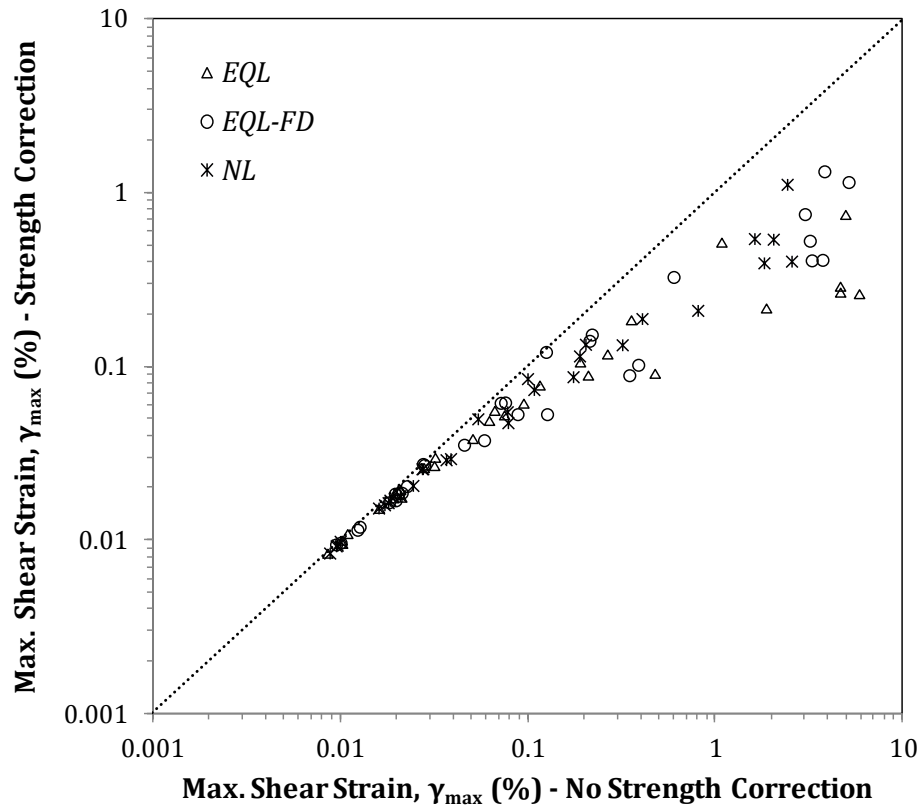


Figure 8.3: Relationship between the computed maximum shear strain (γ_{max}) before and after the strength correction, for all site response models – IWTH26 array

NL approaches, although the increase for the NL analysis is smaller than for the EQL analysis. Nonetheless, the increased responses in both cases still result in spectra that are smaller than the observed. The residuals decrease from 1.7 to almost 1.0 for the EQL analysis and from 1.6 to 1.3 for the NL approach. The smaller effect on the NL analysis is probably due to the fact that, the strength correction resulted in a smaller reduction in γ_{max} (TABLE 8.1) for the NL method. On the other hand, the high frequency response ($T < 0.2$ s) from the EQL-FD approach is almost unaffected by the modification of the modulus reduction curve and the reduction in maximum shear strain. As explained in [Chapters 6](#) and [7](#), the high frequency response by the EQL-FD approach strongly depends on the damping value that is assigned at each

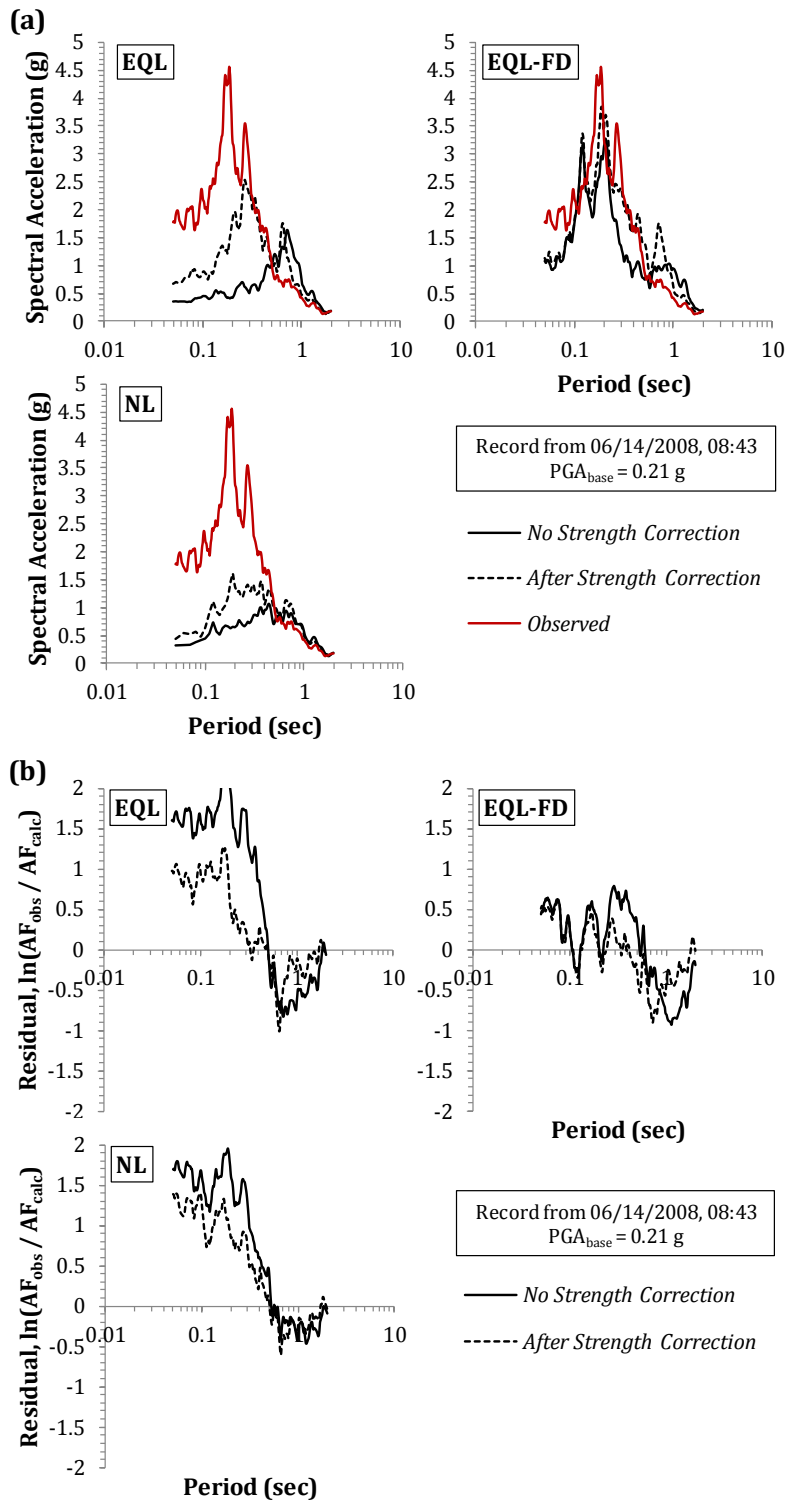
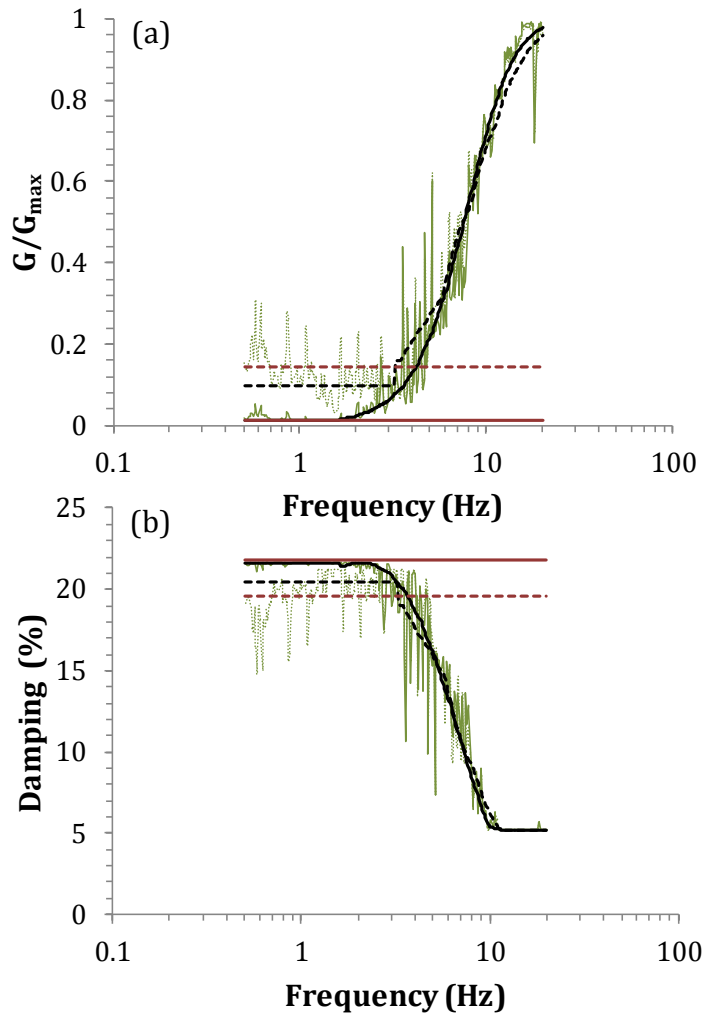


Figure 8.4: (a) Surface response spectra, and (b) amplification factor residuals before and after the strength correction for all site response models, at IWTH26 array

Table 8.1: Maximum shear strains (γ_{max}) in %, computed before and after the strength correction for all site response models, and for a input motion recorded on 06/14/2008, 08:43 at IWTH26 array

Model	γ_{max} - No Strength Correction (%)	γ_{max} - After Strength Correction (%)
<i>EQL</i>	4.96	0.754
<i>EQL-FD</i>	3.83	1.33
<i>NL</i>	2.42	1.12

frequency. Because the strength correction procedure does not significantly alter the utilized damping curve and the strains associated with high frequencies remain small, the EQL-FD high frequency response remains almost the same. *FIGURE 8.5* illustrate the frequency-dependence of the utilized modulus reduction and damping for the EQL and EQL-FD analyses presented in *FIGURE 8.4*. At frequencies greater than about 5 Hz (i.e., $T < 0.2$ s), the EQL-FD analyses before and after the strength correction use similar G/G_{max} and damping values and thus result in similar responses. On the other hand, based on *FIGURE 8.4*, it can be seen that the longer period response ($T > 0.2$ s) from the EQL-FD model is affected by the modification of the G/G_{max} curve at large strains. The computed spectral accelerations are increased due to the fact that, after the strength correction, the EQL-FD analysis incorporates substantially larger G/G_{max} values at these periods (*FIGURE 8.5a*). Moreover, *FIGURE 8.5* also helps explain why the strength correction does not reduce γ_{max} for the EQL-FD analysis as much as it does for the EQL and NL analyses (*TABLE 8.1*). The EQL-FD method utilizes a smoothed shear strain spectrum (Assimaki and Kausel, 2002), which results in material properties that are averaged and constant at frequencies below 3.1 Hz (*FIGURE 8.5*). Understandably, at several frequencies below 3.1 Hz, the average G/G_{max} value is substantially smaller than the one infer-



Record from 06/14/2008, 08:43
 $PGA_{base} = 0.21 \text{ g}$

- EQL-FD / complete spectrum / No strength correction
- ⋯ EQL-FD / complete spectrum / After strength correction
- EQL-FD / smooth spectrum / No strength correction
- - - EQL-FD / smooth spectrum / After strength correction
- EQL / No strength correction
- - - EQL / After strength correction

Figure 8.5: Frequency-dependence of: (a) modulus reduction, and (b) damping for EQL and EQL-FD, for an input motion recorded on 06/14/08, 08:43 with $PGA_{base} = 0.21 \text{ g}$

red by the updated modulus reduction curve (green lines in *FIGURE 8.5*). Therefore, the computed γ_{max} value is smaller than the one that would have been obtained if the complete shear strain spectrum was used. This inconsistency of the EQL-FD method will be addressed in *Section 8.3*.

8.2.2. Overall Results

Similar to the example case for the IWTH26 array, the strength correction procedure was applied to the remaining vertical array sites of this study (except for the MYGH02 and TTRH02 sites, as discussed earlier). EQL, EQL-FD and NL site response analyses were performed using the updated modulus reduction and damping curves at large strains. *FIGURE 8.6* presents the comparison between the γ_{max} values computed before and after the application of the strength correction, for all sites and site response models. Similar to *FIGURE 8.3*, the reduction in shear strain after the shear strength correction is evident, although in a few cases the shear strain was increased. The EQL and EQL-FD methods show the most significant reduction in γ_{max} , while the updated γ_{max} values from the NL approach are decreased to a lesser extent.

Based on the results from the new analyses, prediction residuals for the computed amplification factors ($y = \ln(AF^{obs}/AF^{calc})$) were obtained. The residuals were evaluated at different spectral periods (T) and maximum calculated shear strains (γ_{max}). The evaluation was made using the same concepts and procedures as discussed in *Chapter 6*. The *mean* values of the residuals were calculated within 15 γ_{max} ranges (see *TABLE 6.2*) and across all spectral periods. Then, the *mean* residuals were plotted against the corresponding values of γ_{max} and T (*FIGURES 8.7 to 8.9*), for all models. In *FIGURES 8.7 to 8.9*, the prediction residuals are

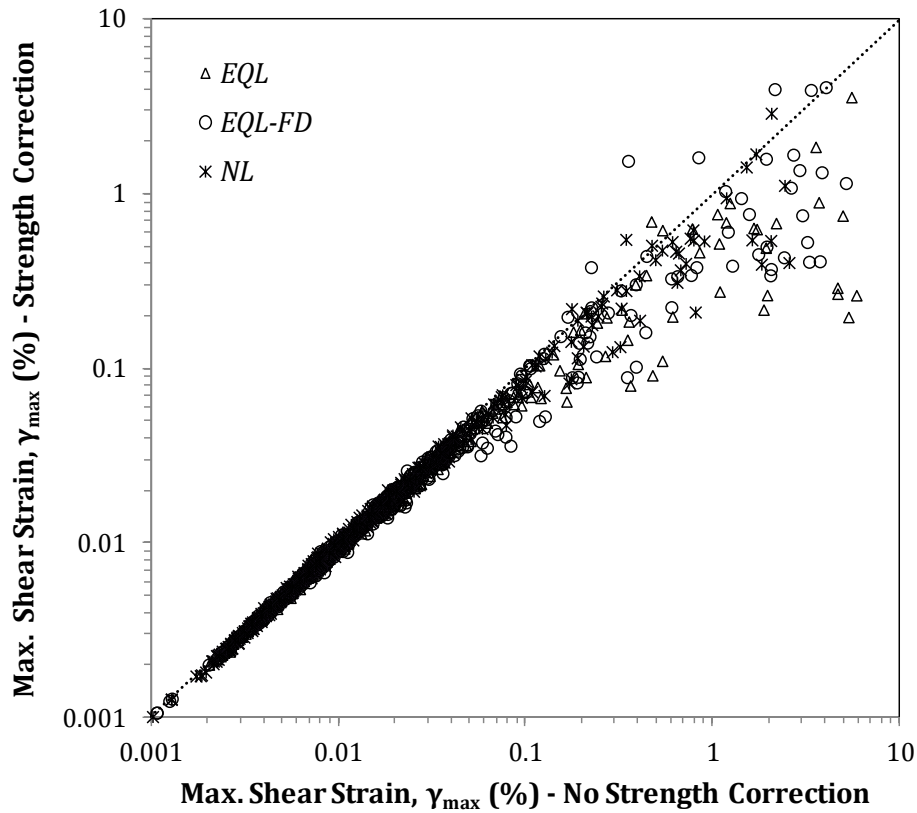


Figure 8.6: Relationship between the computed maximum shear strain (γ_{max}) before and after the strength correction, for all site response models

shown before and after the incorporation of the updated strength at large strains. To ensure that our main observations are based solely on statistically meaningful measures, *mean* residuals are depicted only for γ_{max} bins that contain at least 4 observations. Furthermore, to more carefully examine the effect of the strength correction procedure on the performance of the theoretical models at high frequencies and large strains, the response at $T < 0.4 s$ and $\gamma_{max} > 0.1 \%$ is highlighted. To illustrate the reduction in γ_{max} , this region is highlighted only up to the largest γ_{max} from the analysis after the strength correction. The peak *mean* residual (y_{max} for EQL and NL; y_{min} for EQL-FD) and the magnitude of the average *mean* residual (y_{avg}) within the highlighted $T - \gamma_{max}$ spaces are also depicted.

FIGURE 8.7 presents the results for the EQL method. The strength correction procedure leads to a notable improvement in the performance of the model with the zone of significant under-prediction (i.e., red areas) drastically reduced. The incorporation of the shear strength at large strains has a dual effect on the computed amplification. First, as noted previously, the calculated shear strains are significantly reduced. For the EQL analyses performed, the largest computed γ_{max} decreased from about 4.5 % to 0.6 % (note the extent of data on the strain axis in FIGURE 8.7). Therefore, while the EQL approach may still be unable to accurately capture the site response at high frequencies when $\gamma_{max} > 1.0$ %, this effect is not observed in the overall *mean* residuals shown in FIGURE 8.7, because these strain levels were not induced by the input motions used in this study. The second effect of the strength correction on the computed *AF* can be seen by examining the prediction residuals at $0.1\% < \gamma_{max} < 0.6\%$ (FIGURE 8.7). At these strain levels, which are present in both the original and strength corrected results, there is a slight reduction in the high frequency under-prediction by the EQL approach. For example, the average *mean* prediction residual (y_{avg}) at $T < 0.4$ s and $0.1\% < \gamma_{max} < 0.6\%$ is reduced from 0.35 to about 0.32 and the maximum mean prediction residual (y_{max}) is reduced from 0.80 to 0.75. This result can be explained by the fact that the strength correction increases the stiffness at strains greater than about 0.1 %, which allows for larger motions to propagate through the layer.

The period and shear strain dependence of the *mean* prediction residuals for the EQL-FD approach, is shown in FIGURE 8.8, for the original and strength corrected modulus reduction curves. These data show that the change in the computed response after the shear strengths are corrected is even less pronounced than in the case of the EQL model. The maximum computed γ_{max} is reduced from approximate-

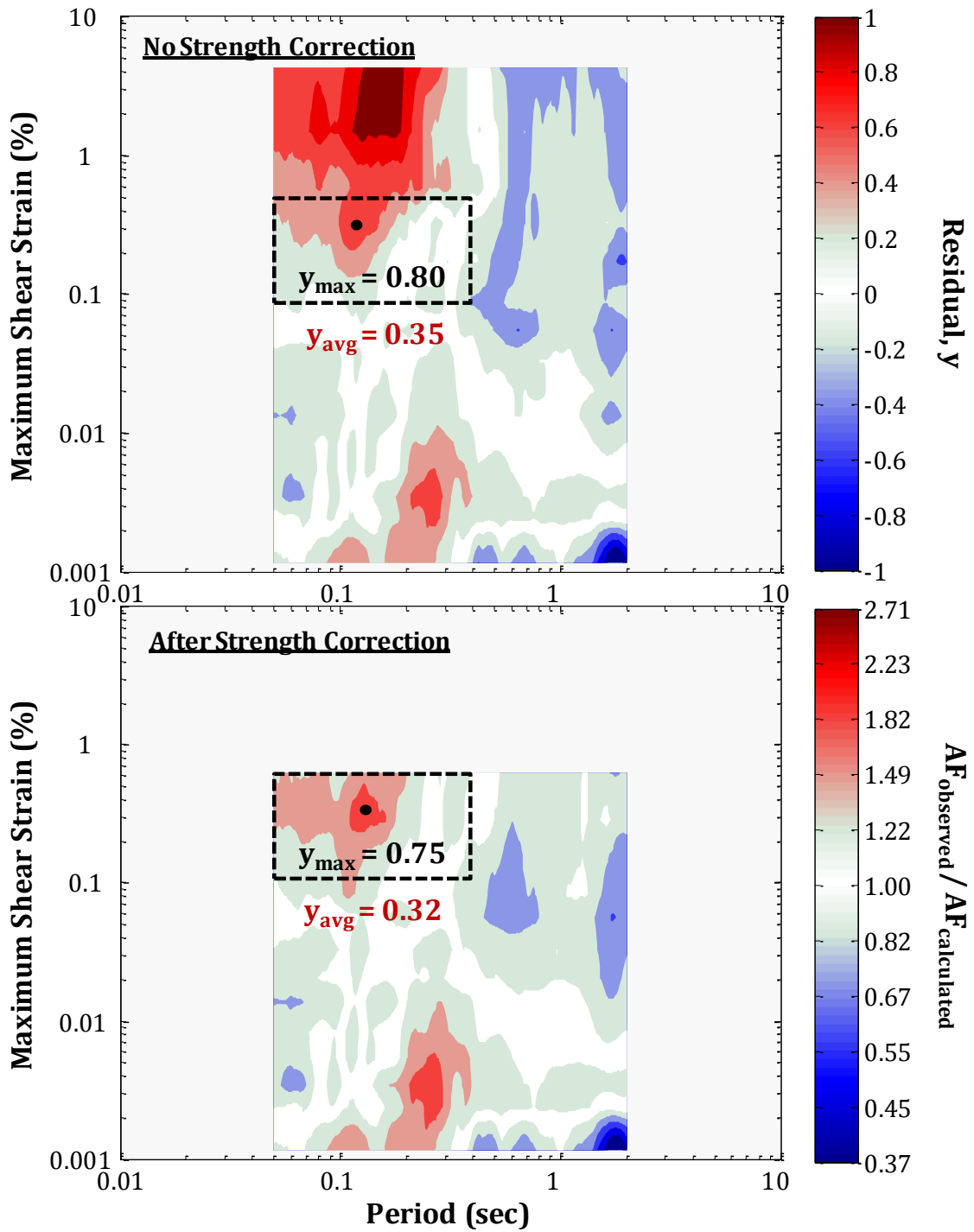


Figure 8.7: Contour plots of *mean* prediction residuals vs maximum calculated shear strains (y_{max}) vs spectral period (T) obtained before and after the strength correction procedure – EQL method

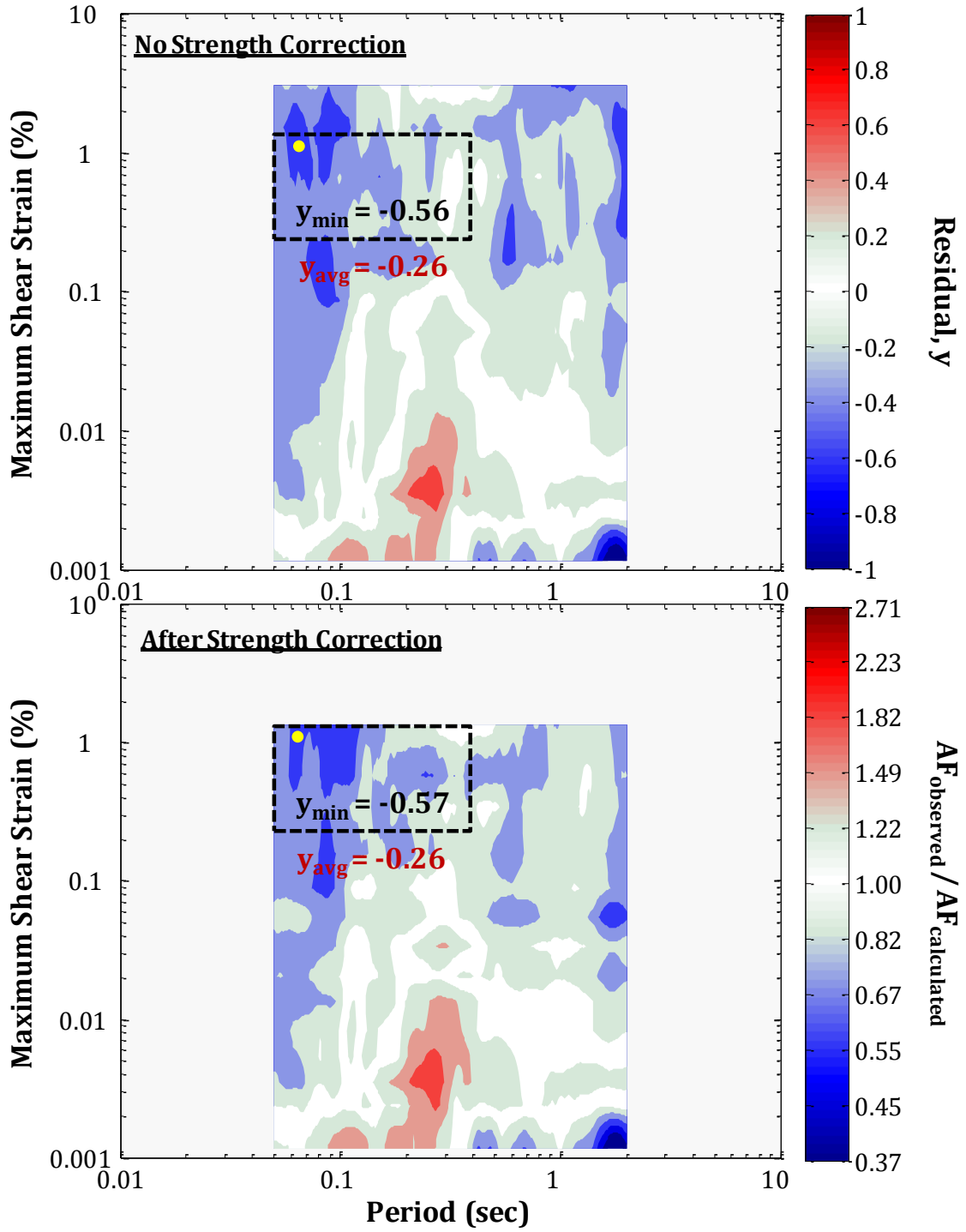


Figure 8.8: Contour plots of *mean* prediction residuals vs maximum calculated shear strains (γ_{max}) vs spectral period (T) obtained before and after the strength correction procedure – EQL-FD method

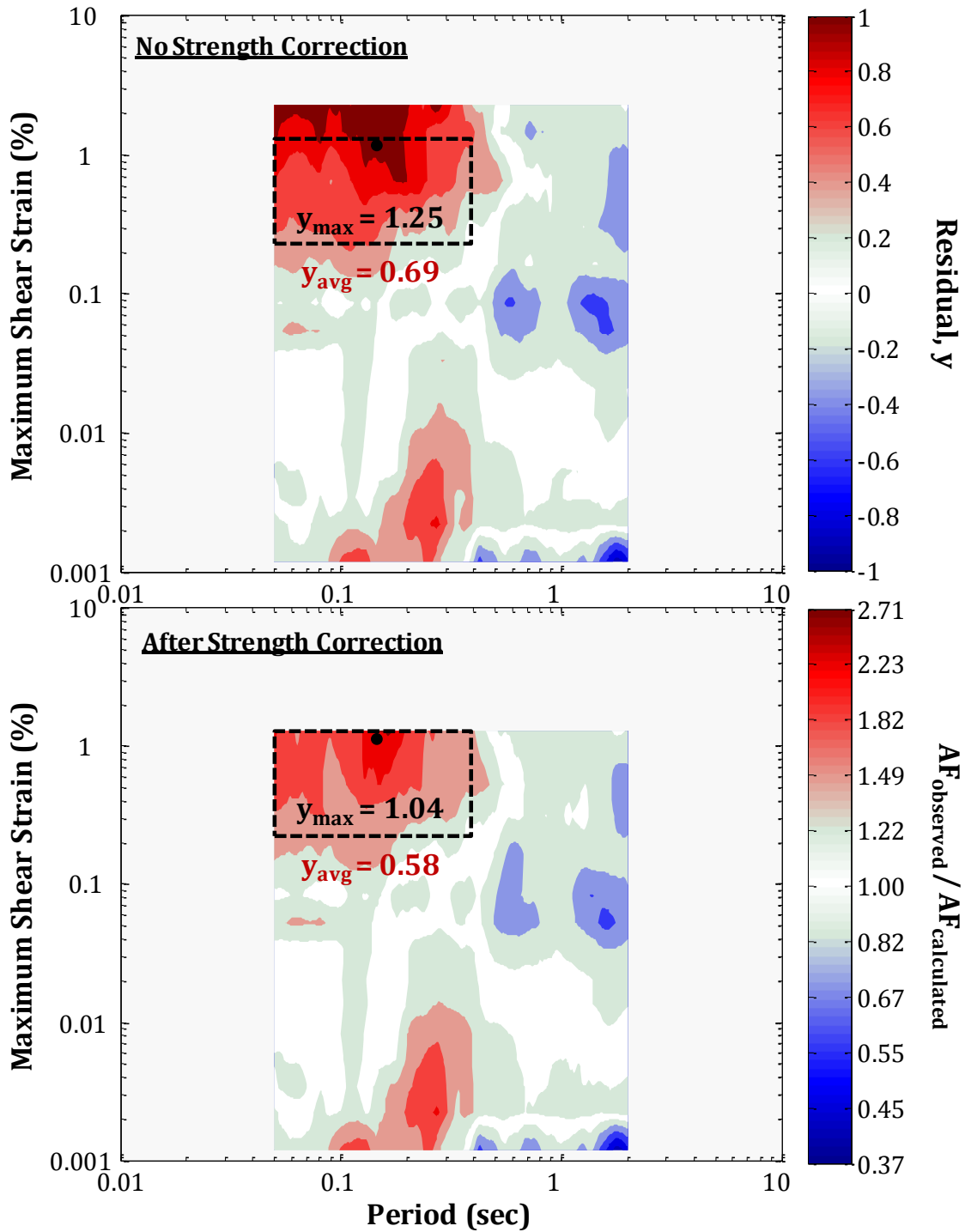


Figure 8.9: Contour plots of *mean* prediction residuals vs maximum calculated shear strains (γ_{max}) vs spectral period (T) obtained before and after the strength correction procedure – NL method

ly 3.5 % to 1.3 %, but this reduction in strain is not as significant as the one observed for the EQL method. This is due to the fact that the EQL-FD analysis incorporates an average G/G_{max} value over a wide range of frequencies that is smaller than the value used by the EQL analysis (*FIGURE 8.5*). The fact that the computed EQL-FD response, particularly at high frequencies ($T < 0.2$ s), is not affected significantly by the updating of the G/G_{max} curves at large strains is explained by the fact that the EQL-FD response primarily depends on the utilized damping values at high frequencies. Although the strains are reduced by the strength correction, the strains at high frequencies are basically the same before and after the strength correction (*FIGURE 8.5*). Because the strength correction procedure causes only minor alterations to the damping curves, the over-amplification (i.e., negative residuals) at high frequencies does not change when the strength correction is included. As a result, *FIGURE 8.8* shows that the average mean residual computed at $T < 0.4$ s basically does not change.

Finally, *FIGURE 8.9* shows the *mean* prediction residuals across different spectral periods and shear strains for the NL site response analyses with the original and strength corrected modulus reduction curves. Similar to the observations made for the EQL method (*FIGURE 8.6*), the incorporation of more reasonable values of shear strength at large strains improves the performance of NL site response analysis at high frequencies ($T < 0.4$ s) and large strains ($\gamma_{max} > 0.1$ %). First, the calculated maximum γ_{max} values are decreased from about 2.2 % to 1.2 %, although this observed reduction in γ_{max} is the smallest among the three site response methods considered. Nonetheless, over the strain levels present in both the original and strength corrected results (i.e., 0.1 % to 1.0 %), the improvement of the performance of the NL method at periods less than 0.4 s is more

significant than for the other methods. For example, the average mean prediction residual (y_{avg}) at $T < 0.4$ s decreases from approximately 0.69 to 0.58 (FIGURE 8.9), which translates into a reduction in the under-prediction from a factor of 2.0 to a factor of 1.8 and the maximum prediction residual (y_{max}) decreases from 1.25 to 1.04. Nonetheless, even after the application of the strength correction procedure, the NL method significantly under-predicts the high frequency response at large strains and the under-prediction is even more significant than for EQL analysis.

FIGURES 8.10 to 8.12, show the mean prediction residuals as a function of the spectral period (T) divided by the site period (T_{site}) of each vertical array. Because each site has a different value of T_{site} , the residuals from each site are translated to different values of T/T_{site} . To develop the $T/T_{site} - \gamma_{max}$ contour plots, we followed the same concepts and procedures described in Chapter 6. FIGURES 8.10 to 8.12 show the resulting contour plots of the *mean* residuals computed before and after the application of the strength correction procedure for all three site response models. These figures emphasize the influence of the strength correction on the response at large strains (i.e., $\gamma_{max} > 0.1$ %) and $T/T_{site} < 0.5$. In $T/T_{site} - \gamma_{max}$ space, the responses computed after the strength correction are characterized by smaller *mean* residuals (i.e., higher amplification) for all site response models.

Overall, the results presented herein indicate that the application of a strength correction to the modulus reduction curve improves the performance of EQL and NL one-dimensional site response analyses at large strains. The improvement predominantly comes from reducing the computed shear strains for the given input motions. On the other hand, the performance of the EQL-FD approach is almost unaffected by the strength correction. Nonetheless, it should be noted that in applying the strength correction to the sites investigated in this study,

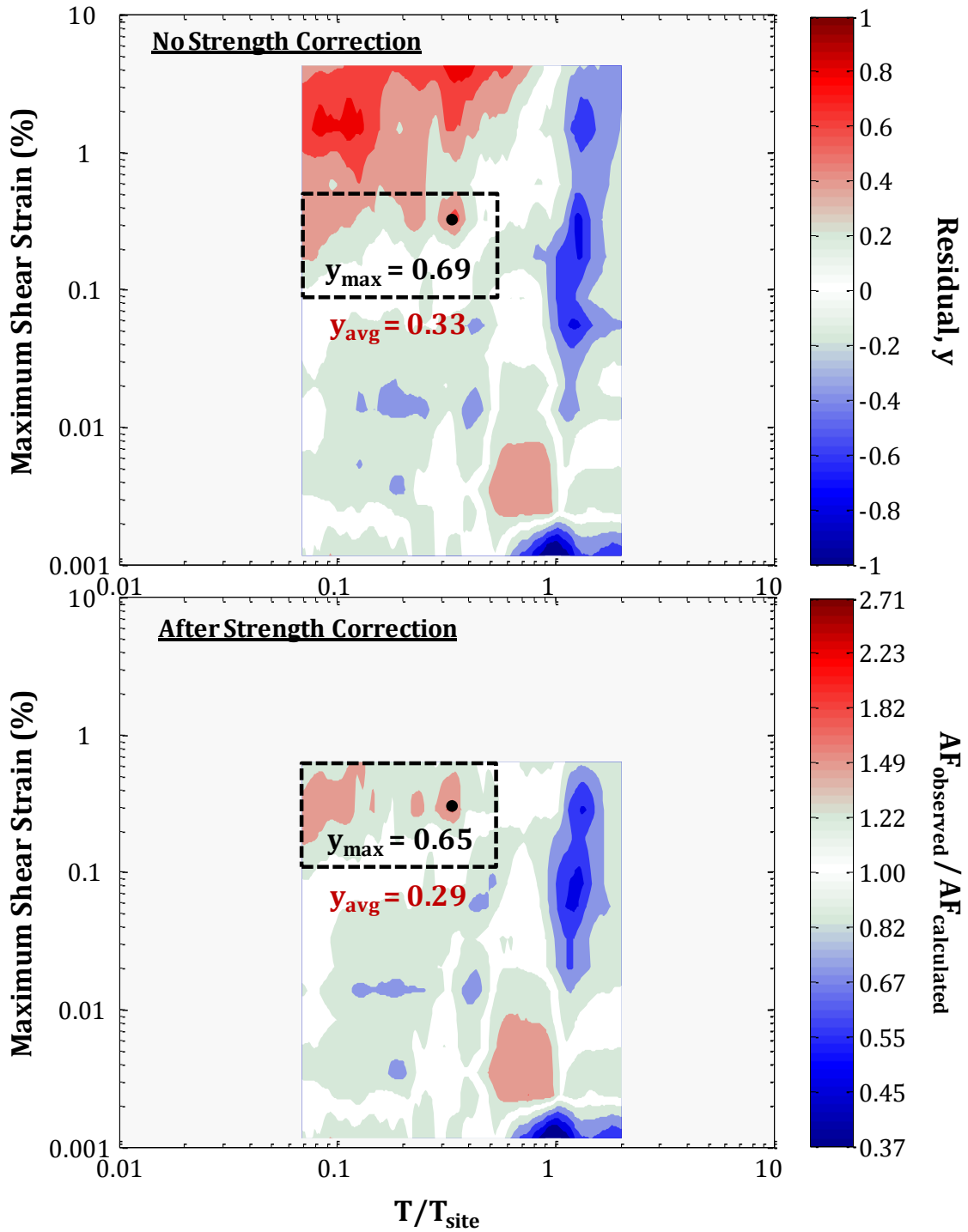


Figure 8.10: Contour plots of *mean* prediction residuals vs maximum calculated shear strains (y_{max}) vs T/T_{site} obtained before and after the strength correction procedure – EQL method

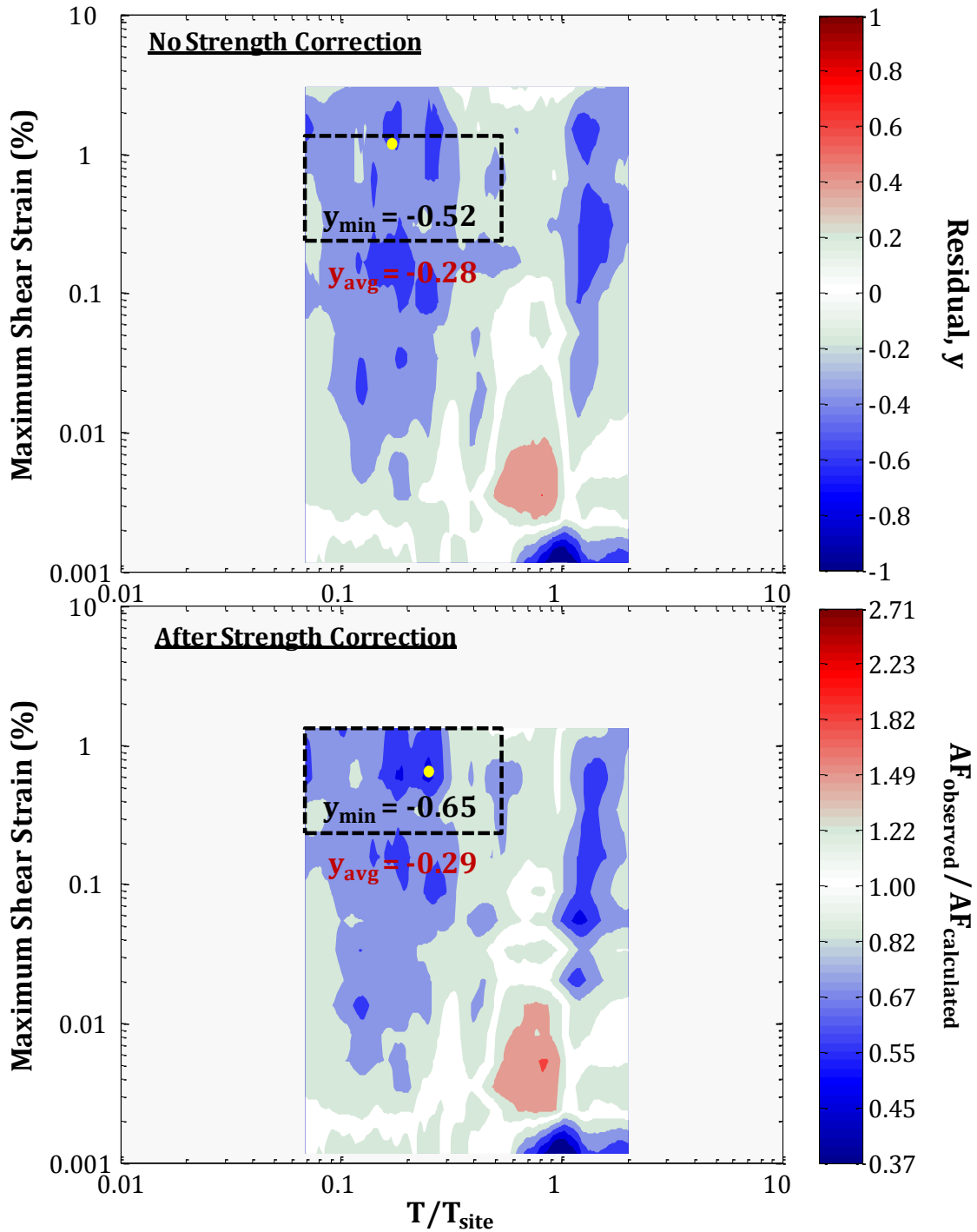


Figure 8.11: Contour plots of *mean* prediction residuals vs maximum calculated shear strains (γ_{max}) vs T/T_{site} obtained before and after the strength correction procedure – EQL-FD method

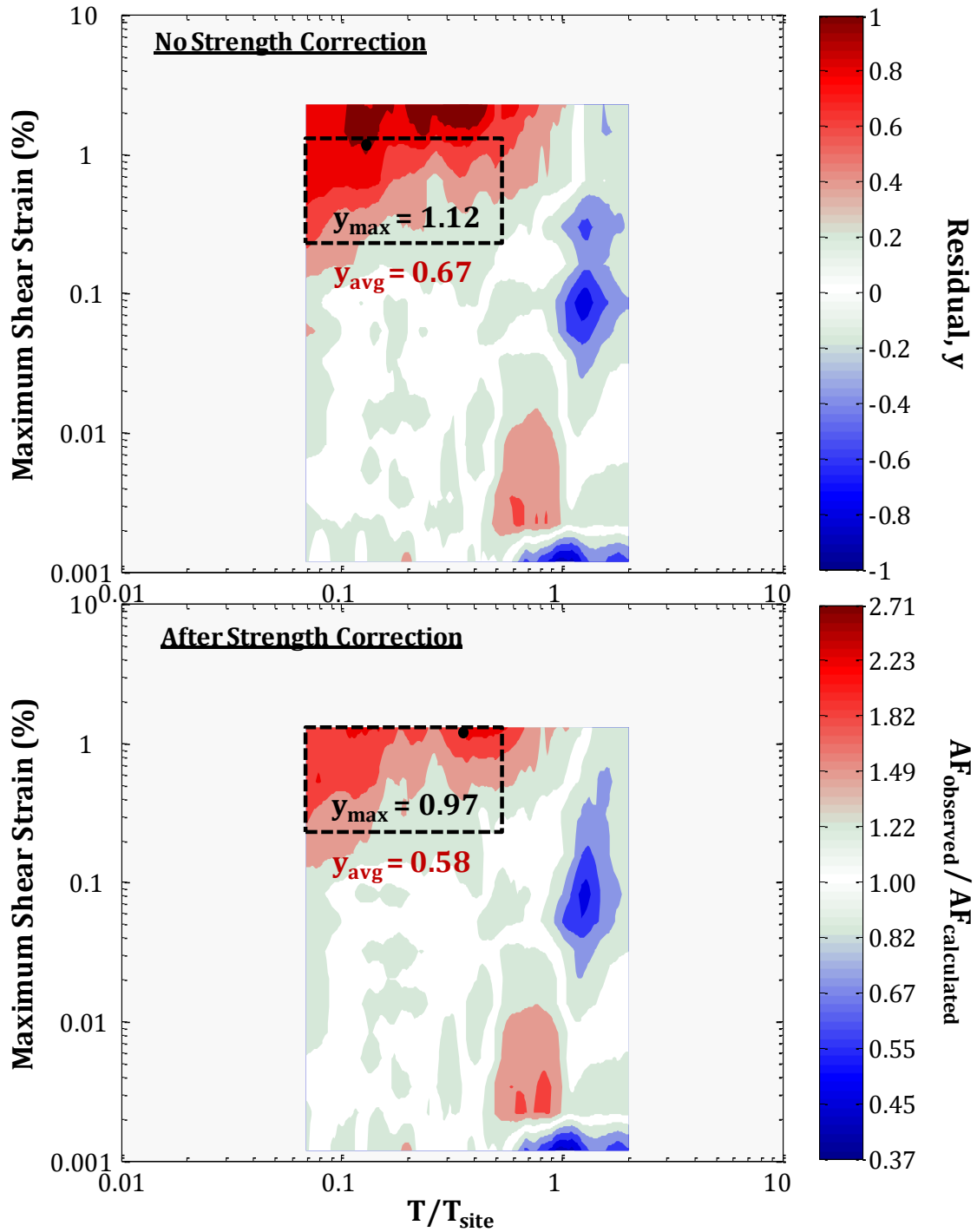


Figure 8.12: Contour plots of *mean* prediction residuals vs maximum calculated shear strains (y_{max}) vs T/T_{site} obtained before and after the strength correction procedure – NL method

an arbitrary but reasonable target friction angle of 29° was selected for all layers and sites. A more thorough site investigation focused on shear strength characterization could yield further improvement to the site response analyses. Additionally, the modification to the modulus reduction curve was somewhat arbitrary in nature in terms of its shape and the strain at which the strength was mobilized. A more rigorous approach that takes into account stress strain data might further improve the results. Finally, the shear strength correction involves primarily the alteration of the $G/G_{max} - \log \gamma$ curve at large strains, with the damping curve remaining, for all practical purposes, unaffected. The main justification for the strength correction is based on the extrapolation of the laboratory measurements of G/G_{max} to large strains without considering the shear strength. Since the same issue may be relevant regarding the extrapolation of laboratory measurements of damping, one could logically argue that the $D - \log \gamma$ curve needs to be modified at large strains as well. A simultaneous alteration of the modulus reduction and damping curves would certainly affect the computed responses and potentially improve the predictions.

8.3. Proposed Modifications to EQL-FD Algorithm

The previous discussion focused on improving site response predictions through the modification of the modeling parameters (i.e., $G/G_{max} - \log \gamma$ curves), without any consideration to changing the details of the numerical algorithm associated with each model. Because 1-D EQL and NL formulations are well-established and generally accepted theoretical models, further modification of these methods are not investigated. However, refinement of the EQL-FD method is examined since this method has not received as much attention in the literature.

Towards improving the EQL-FD procedure, two alterations are proposed. First, we propose that the frequency-dependent material properties (G/G_{max} and damping, D) are incorporated in the analysis after the completion of the initial EQL iterations and thus the convergence to a value of effective shear strain. Second, we modify the numerical procedure by selecting the frequency dependent material properties based on the complete and scaled shear strain Fourier Amplitude Spectrum ($\gamma(f)$) rather than the smoothed spectrum, as originally proposed by Assimaki and Kausel (2002). The effect of the two modifications on the EQL-FD method is investigated by performing analyses using the same vertical arrays and conceptual framework as in [Section 8.2](#).

8.3.1. Performing EQL-FD Computations After EQL Iterations

As discussed in [Chapter 2](#), the most widely used EQL-FD algorithms (Yoshida *et al.*, 2002; Assimaki and Kausel, 2002) incorporate a smoothed shear strain frequency spectrum to perform site response calculations. Kausel and Assimaki (2002) indicated that the utilization of the smoothed shear strain spectrum was necessary in order to avoid numerical instabilities. These instabilities are most possibly related with the inability of convergence of the model when the highly irregular, complete shear strain spectrum is used. Therefore, any modification of the EQL-FD approach that avoids these numerical instabilities allows for the incorporation of the complete shear strain spectrum. The point at which the frequency-dependent properties are incorporated into the EQL-FD method is one such modification that is investigated here.

Accordingly, we propose that the frequency-dependent properties be incorporated after the initial EQL iterations have been completed, followed by shear

strain iterations using the frequency-dependent properties. This modification can lead to: 1) easier convergence of the EQL-FD model when the complete shear strain frequency spectrum is used, and 2) reduced computational time. A benefit of incorporating the frequency-dependent properties after the EQL model has converged, is that the number of required iterations for the EQL-FD method is significantly reduced. Indeed, one could argue that after the EQL model has already converged towards a certain strain level, any further EQL-FD iterations are not required. Nonetheless, even if additional EQL-FD iterations are incorporated, only 2 – 3 iterations commonly are sufficient for convergence. By reducing the number of required EQL-FD iterations, we minimize the possibility to encounter numerical instabilities when utilizing the complete shear strain frequency spectrum for site response computations. Furthermore, each iteration of the EQL-FD approach requires more computing time than the traditional EQL approach because of the need to loop through frequency to specify the frequency-dependent properties. Therefore, a reduction in the number of EQL-FD iterations leads to a reduction in computing time. Such reduction in the processing time is desirable for the site response analysis of deep sites under a large number of long duration input time histories. Indeed, for some deep vertical arrays used in the present study (e.g. KSRH06, KSRH07, MYGH05), the proposed modification led to a reduction of the processing time by 40 – 50 %.

The change in the EQL-FD approach to iterations only changes modestly the computed maximum shear strain. For example, *FIGURE 8.13* presents the comparison between the maximum shear strains (γ_{max}) computed using both iteration schemes (i.e., all iterations with frequency dependent properties vs EQL iterations followed by iterations using frequency dependent properties) and a smooth shear strain spe-

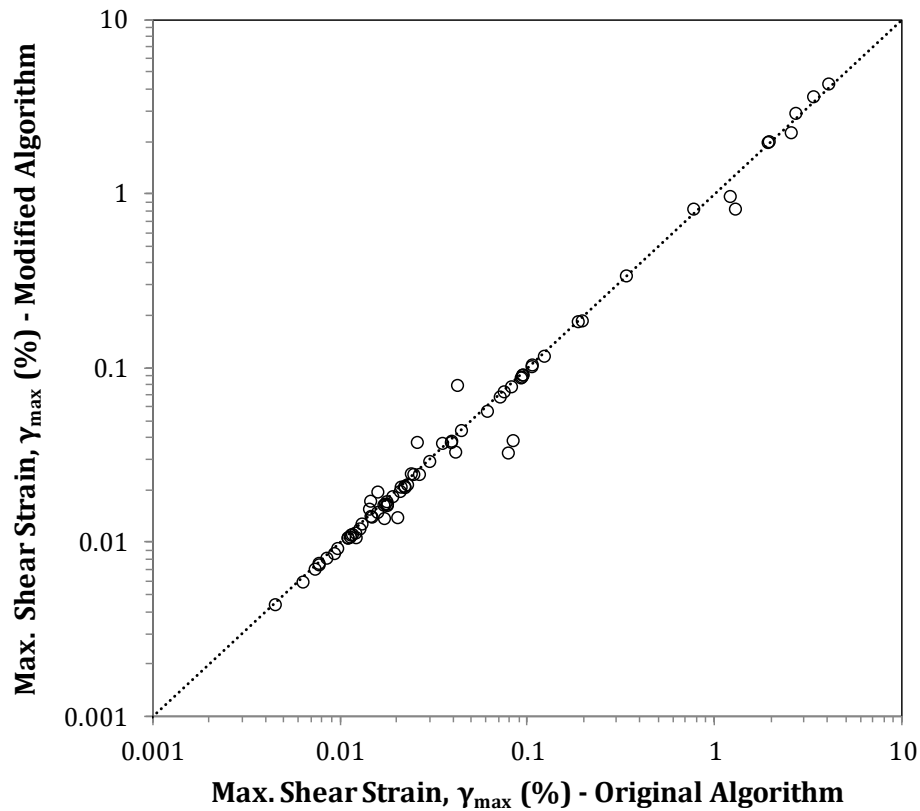


Figure 8.13: Comparison of maximum shear strains (γ_{max}) computed using the original and the modified EQL-FD algorithm, for IBRH13 borehole array

ctrum for the IBRH13 vertical array. As it can be readily seen from *FIGURE 8.13*, performing the EQL-FD iterations after the initial EQL iterations does not significantly alter the computed γ_{max} values. Consequently, the *mean* prediction residuals using these two approaches are very similar (*FIGURE 8.14*). As observed in *FIGURE 8.14*, the proposed modification to the EQL-FD approach results in essentially identical results with the original approach for PGA_{base} of 0.01 *g*, 0.06 *g*, and 0.11 *g*, while only a minimal change in the prediction residuals at $T < 0.07$ *s* is observed for $PGA_{base} = 0.20$ *g*. Note that the example provided in *FIGURES 8.13* and *8.14* involves the response of the IBRH13 site prior to the application of the strength correction procedure described in [Section 8.2](#).

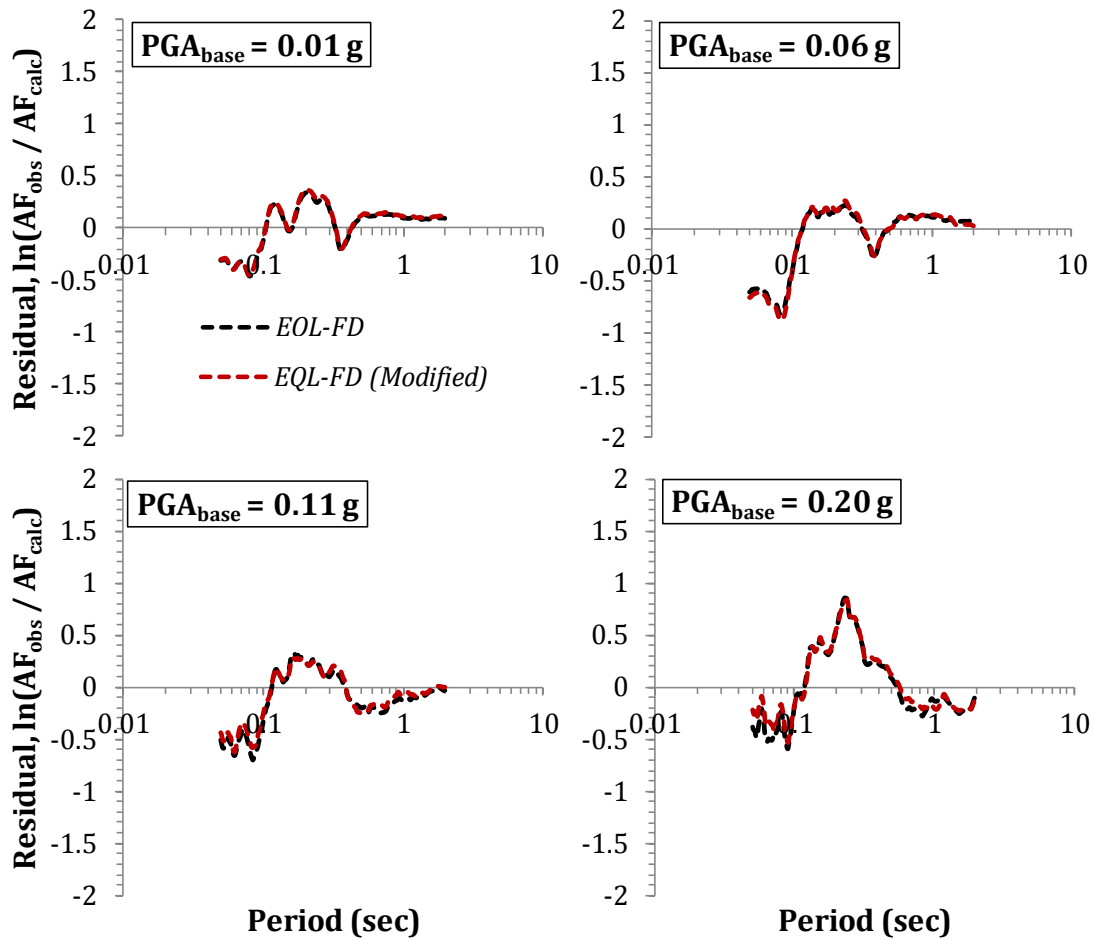


Figure 8.14: Mean prediction residuals for the original and for the modified EQL-FD models, for IBRH13 borehole array

8.3.2. Utilization of Complete Shear Strain Spectrum

The EQL-FD approach presented by Assimaki and Kausel (2002) is based on the utilization of material properties that are selected based on shear strains that are smoothed over frequency (*Chapter 2*). More specifically, the Assimaki and Kausel (2002) procedure develops shear strain frequency spectra ($\gamma(f)$) by fitting a smooth function to the computed Fourier Amplitude Spectrum of shear strains (FAS_γ) and scaling this smooth function to match, at low frequencies, the maximum

calculated shear strain (γ_{max}). Nonetheless, the smoothing process may lead to a misrepresentation of important characteristics of the frequency content of the shear strains. In the following paragraphs we investigate the possibility of an improvement in the accuracy of the EQL-FD model by specifying the frequency-dependent material properties based on a “complete” and scaled shear strain spectrum ($\gamma(f)$) rather than a smoothed spectrum. The performance of EQL-FD computations based on a “complete” shear strain spectrum is feasible after the application of the proposed modification of the EQL-FD algorithm presented in [Section 8.3.1](#), i.e. the specification of frequency dependent material properties after the completion of an initial set of the EQL iterations.

Two alternative approaches to scaling the complete shear strain spectrum are considered herein. The main difference between the two alternatives is the scaling factor applied on the computed FAS_γ to match the γ_{max} . The scaling factor is necessary to convert the units of FAS_γ from (% – s) to (%), and thus obtain the “complete” shear strain spectrum ($\gamma(f)$). The computed and scaled $\gamma(f)$ is then used to map the soil properties (shear modulus reduction, G/G_{max} , and damping, D) into the frequency domain.

For the first approach, the scaling factor is selected such that the average value of the FAS_γ over a given frequency range is equal to γ_{max} . This scaling factor is the same as the one proposed by Assimaki and Kausel (2002), and it is represented by:

$$\gamma(f) = \left| \frac{FAS_\gamma}{\gamma_0} \right| \gamma_{max} \quad (8.2)$$

where γ_0 is the average FAS_γ at frequencies between 0 and the mean frequency, f_0 , and γ_{max} is the maximum calculated shear strain from the corresponding shear

strain time history. *FIGURE 8.15* shows the application of this scaling procedure to a FAS_γ . An important result of this approach is that the $\gamma(f)$ obtained based on Equation 8.2 yields $\gamma(f) > \gamma_{max}$ at some frequencies below f_0 .

An alternative complete and scaled shear strain spectrum is also considered. The alternate $\gamma(f)$ is obtained as:

$$\gamma(f) = \left| \frac{FAS_\gamma}{\max(FAS_\gamma)} \right| \gamma_{max} \quad (8.3)$$

where $\max(FAS_\gamma)$ is the maximum value of FAS_γ . In contrast with the $\gamma(f)$ from Equation 8.2, the computed $\gamma(f)$ based on Equation 8.3 gives a maximum $\gamma(f)$ value which is equal to the corresponding maximum value of the calculated $\gamma - t$, i.e. $\max(\gamma(f)) = \gamma_{max}$ (*FIGURE 8.15*). This approach essentially is a variation of the one proposed by Furumoto *et al.* (2000) (*Chapter 2*), the main difference being that the scaling parameter, C , introduced by Furumoto *et al.* (2000) (Equation 2.3) is not considered herein.

To demonstrate the effect of using the complete shear strain spectrum on the computed site response, four *single-events* recorded at the IBRH13 vertical array are used. Relevant information regarding the four selected single events is shown in *TABLE 8.2*. Note that the considered input motions induce significantly different levels of shear strain. Using these input motions, EQL and EQL-FD site response analyses are performed. The original EQL-FD algorithm (i.e., Assimaki and Kausel, 2002) as well as the aforementioned two alternative modifications are considered. Based on the results of our analyses, the selected four events produced shear strains ranging from less than 0.01 % (motion 1) to greater than 1.0 % (motion 4). At this point, it is worthwhile to note that the following analysis did not incorporate the

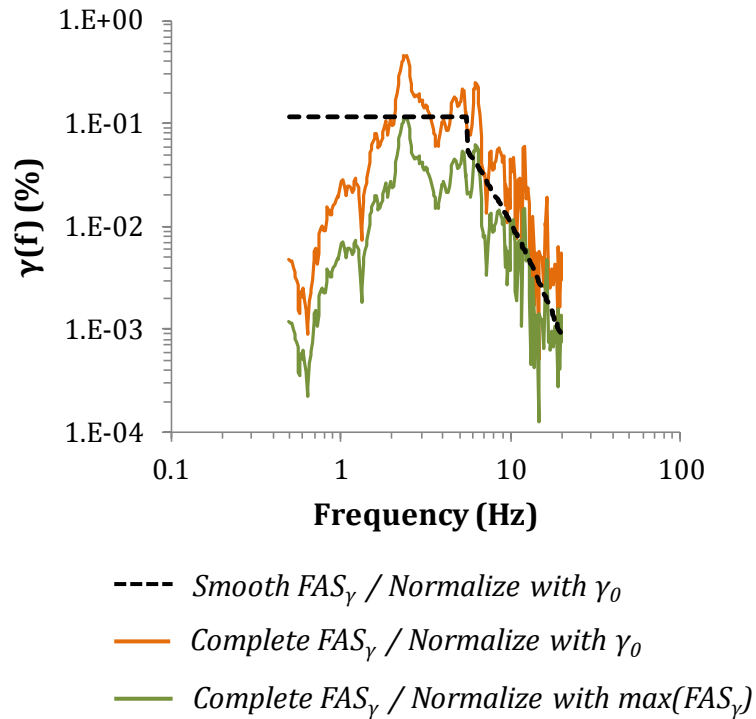


Figure 8.15: Example illustration of the two approaches to scaling the complete shear strain spectrum

modification in the modulus reduction curve made due to the strength correction procedure presented in [Section 8.2](#).

The site-specific evaluation is made by comparing the computed and observed surface spectral accelerations (S_a). The performance of the different models is associated to the frequency dependence of the utilized shear strains ($\gamma(f)$) and the corresponding frequency dependence of the utilized damping. The Fourier Amplitude Spectrum of shear strains (FAS_γ), based upon which $\gamma(f)$ is computed, is obtained for the soil layer where the maximum shear strain, γ_{max} , was calculated. Specifically, at IBRH13 site, γ_{max} was observed at a depth of approximately 2 m. *FIGURES 8.16 to 8.19* present the results of our analyses for the four input motions considered. Note that the frequency dependence of shear strains

Table 8.2: Information regarding the four single-events recorded at IBRH13 vertical array used for the exemplified evaluation of the proposed modification to the EQL-FD approach

Motion No	Date	Time	PGA _{base} (g)	γ_{max} (%)
1	4/8/2003	20:57	0.007	≤ 0.01 %
2	5/5/2011	0:09	0.057	(0.01, 0.1]
3	3/19/2011	8:49	0.076	(0.1, 1.0]
4	3/19/2011	18:56	0.209	> 1.0 %

for the EQL approach is depicted as a flat, single-valued $\gamma(f)$ equal to a percentage (typically 65 %) of γ_{max} , at all frequencies.

The first observation one can make from *FIGURES 8.16 to 8.19* is that the normalization of FAS_γ by γ_0 (orange lines in *FIGURES 8.16 to 8.19*) produces poor results with respect to the observations across all shear strain levels. The computed spectral accelerations are substantially lower than from the other analyses, at all strain levels. This remark is explained by the fact that when the FAS_γ is normalized by γ_0 and subsequently scaled by γ_{max} , the resulting $\gamma(f)$ exceeds γ_{max} at some frequencies and the response is overdamped. Because this approach does not perform well, it will not be discussed further.

The alternative $\gamma(f)$ approach scales the computed FAS_γ by $\gamma_{max}/\max(FAS_\gamma)$ and therefore $\gamma(f)$ never exceeds γ_{max} . The computed response spectra for this approach are depicted by the green lines in *FIGURES 8.16 to 8.19*. At very low input intensities ($\gamma_{max} \leq 0.01$ % - *FIGURE 8.16*), this approach produces spectral accelerations which are almost identical with the EQL and the smooth $\gamma(f)$ EQL-FD approach (i.e., Assimaki and Kausel, 2002 approach) and very close to the observations. As shear strains increase, deviations between the $\max(FAS_\gamma)$ norma-

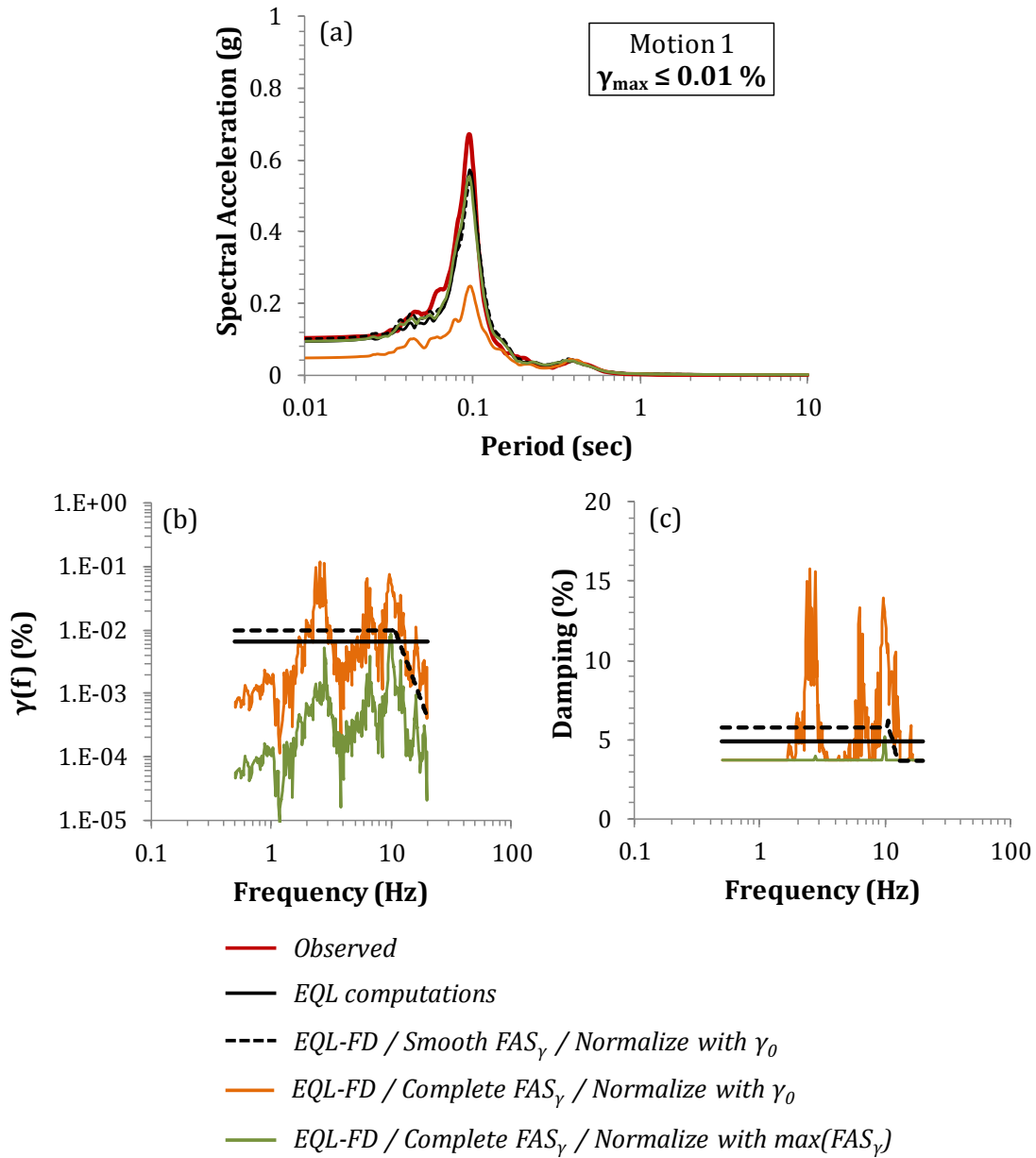


Figure 8.16: Evaluation of the performance of the site response models at IBRH13 site using Motion 1 (see *TABLE 8.2*); (a) computed and observed spectral accelerations, (b) incorporated shear strain spectra ($\gamma(f)$), and (c) corresponding frequency dependence of the damping.

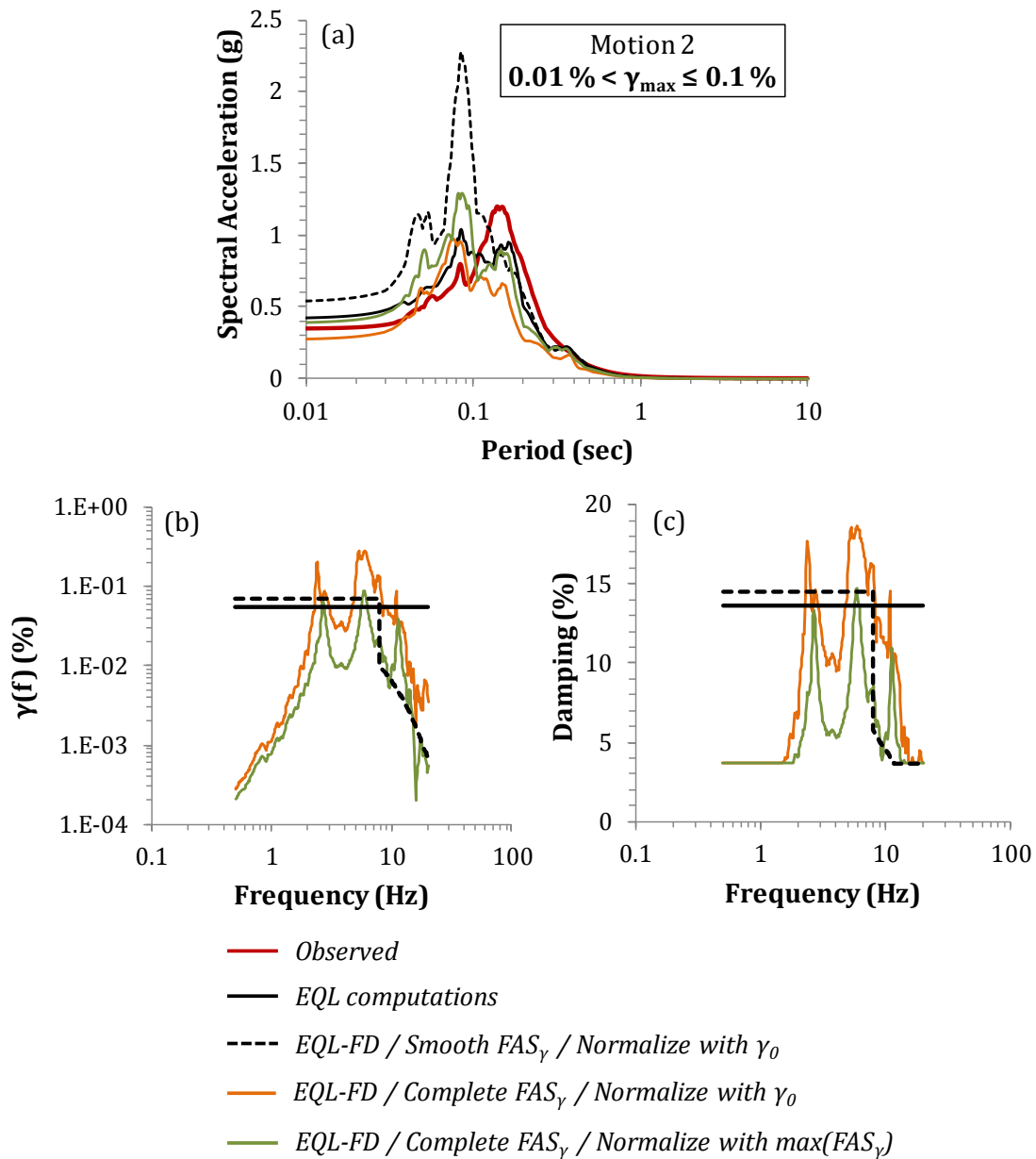


Figure 8.17: Evaluation of the performance of the site response models at IBRH13 site using Motion 2 (see *TABLE 8.2*); (a) computed and observed spectral accelerations, (b) incorporated shear strain spectra ($\gamma(f)$), and (c) corresponding frequency dependence of the damping.

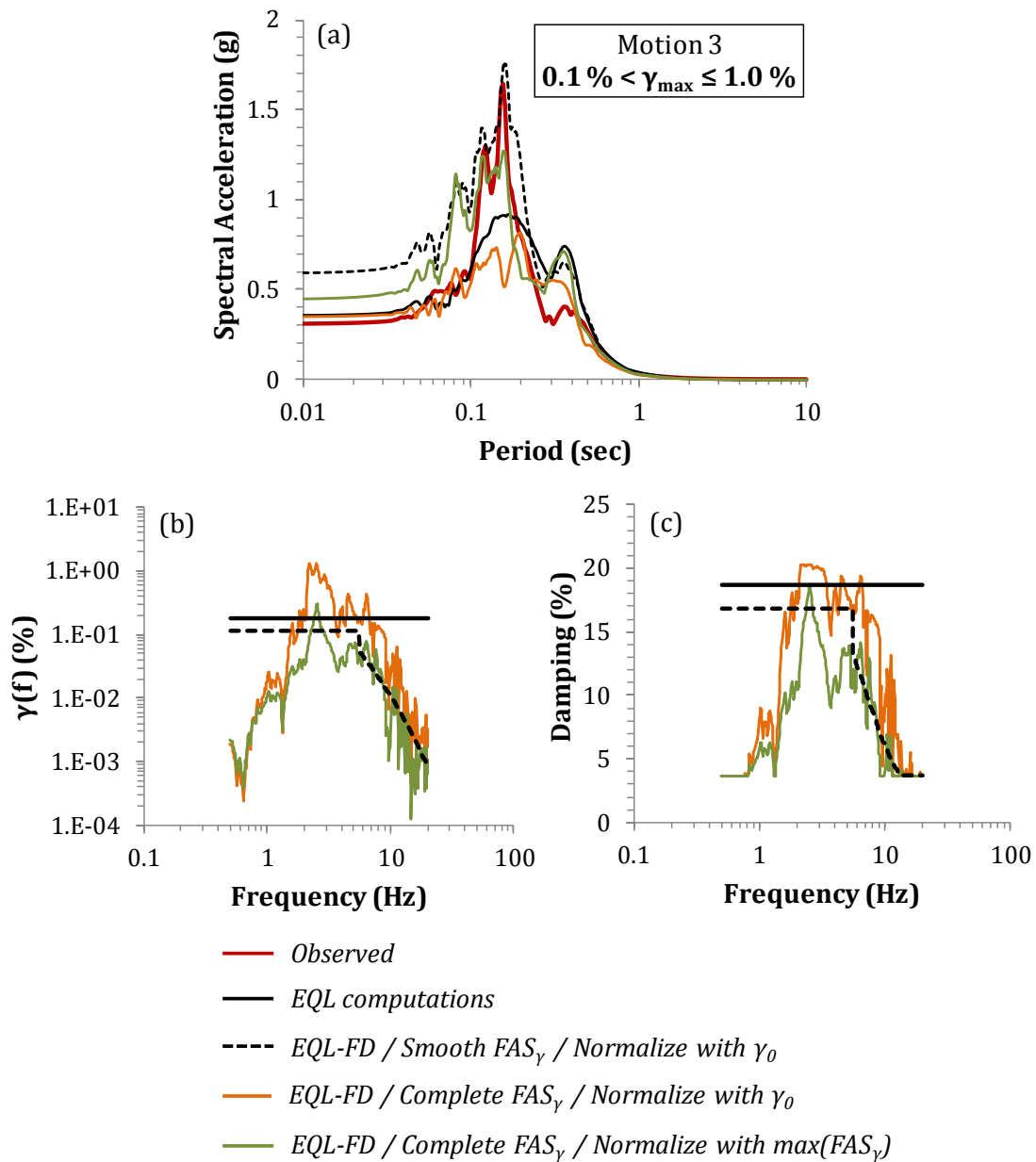


Figure 8.18: Evaluation of the performance of the site response models at IBRH13 site using Motion 3 (see *TABLE 8.2*); (a) computed and observed spectral accelerations, (b) incorporated shear strain spectra ($\gamma(f)$), and (c) corresponding frequency dependence of the damping.

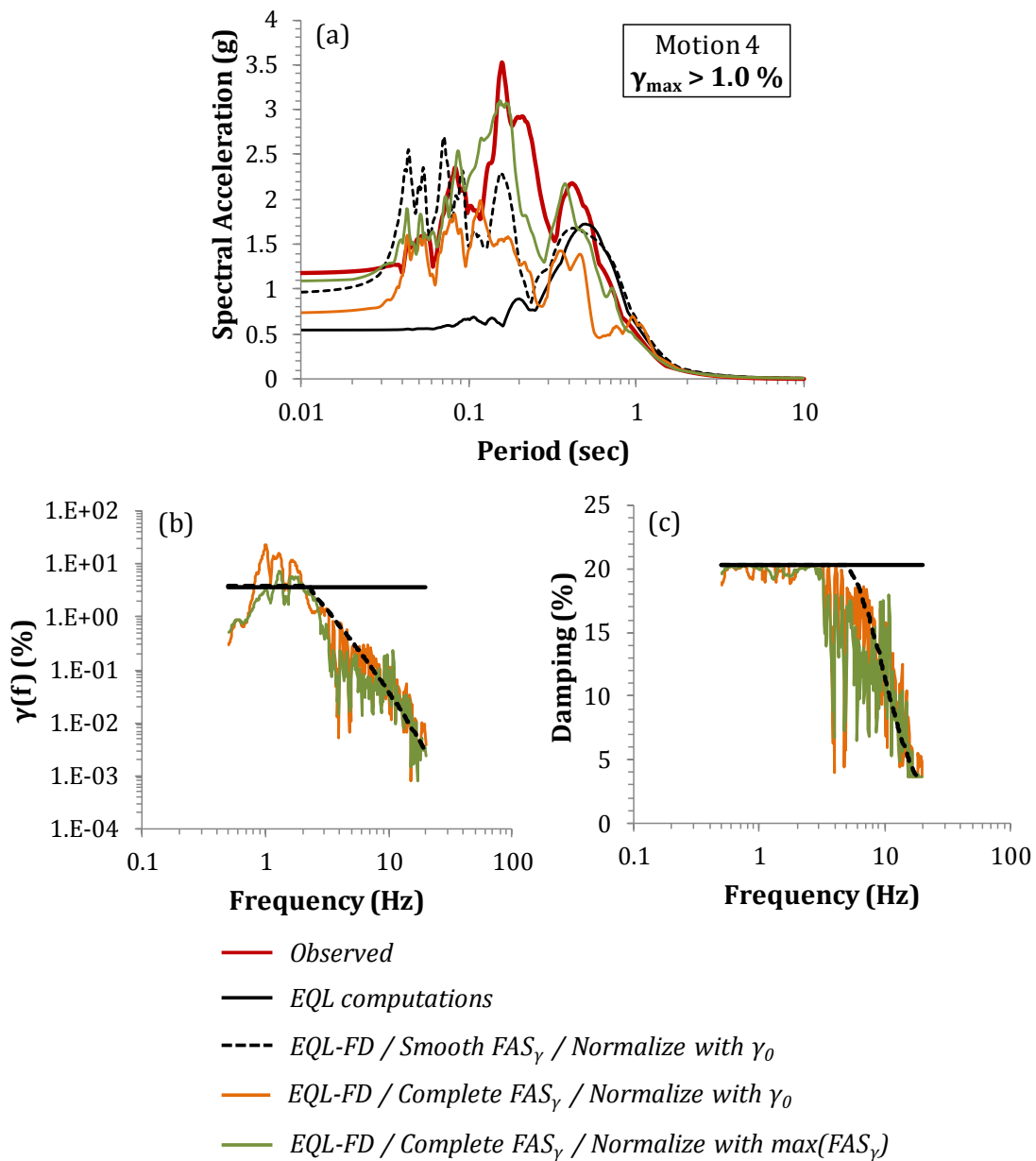


Figure 8.19: Evaluation of the performance of the site response models at IBRH13 site using Motion 4 (see *TABLE 8.2*); (a) computed and observed spectral accelerations, (b) incorporated shear strain spectra ($\gamma(f)$), and (c) corresponding frequency dependence of the damping.

lization and the other approaches can be seen. Specifically, at $\gamma_{max} \sim 0.08\%$ (FIGURE 8.17), the $\max(FAS_\gamma)$ normalization yields significantly smaller spectral accelerations than the smooth spectrum at periods less than 0.1 s. Consequently, the over-prediction of the high frequency response is reduced by a factor of 2. This result is explained by the fact that at frequencies greater than about 10 Hz, the $\max(FAS_\gamma)$ normalization incorporates greater shear strains than the smooth spectrum. Therefore, more damping is introduced in the analysis and the computed amplification is reduced. At $\gamma_{max} \sim 0.3\%$ (FIGURE 8.18), the response spectrum obtained via $\max(FAS_\gamma)$ normalization differs slightly from the one obtained from the smooth spectrum. Here, the $\max(FAS_\gamma)$ normalization generally predicts a smaller response than the smooth spectrum at periods less than 0.1 s because of the incorporation of smaller strains. Finally, at the highest input intensity, where $\gamma_{max} \sim 5.0\%$ (FIGURE 8.19), the $\max(FAS_\gamma)$ normalization produces an improved response at periods smaller than 0.5 s. At these periods, the $\max(FAS_\gamma)$ normalization approach produces spectral accelerations that are in very good agreement with the observations. At frequencies between 2 Hz and 10 Hz (i.e., periods between 0.1 s and 0.5 s), the $\max(FAS_\gamma)$ normalization incorporates smaller shear strains, and thus less damping, and the computed spectral accelerations are increased. On the other hand, at frequencies greater than 10 Hz, the $\max(FAS_\gamma)$ normalization utilizes slightly larger shear strains and thus the over-prediction of the spectral accelerations is reduced.

The results presented in FIGURES 8.16 to 8.19 indicate that specifying $\gamma(f)$ through the full FAS_γ scaled by $\gamma_{max}/\max(FAS_\gamma)$ can generate surface ground motions more similar to observations. To validate this conclusion, the performance of this modification to the EQL-FD approach across different sites was evaluated.

Site response analyses were performed using the original and the modified modulus reduction curves, as discussed in [Section 8.2](#), and the complete shear strain spectrum ($\gamma(f)$) derived from scaling FAS_γ by $\gamma_{max}/\max(FAS_\gamma)$, and the results were compared with the observations. As mentioned earlier, MYGH02 and TTRH02 sites are not considered for these analyses, and thus the following discussion does not include them.

To evaluate the accuracy of the modified EQL-FD method, prediction residuals in the computed amplification factors ($y = \ln(AF^{obs}/AF^{calc})$) were obtained. The residuals were evaluated at different spectral periods (T) and maximum calculated shear strains (γ_{max}). To solely examine the effect of the utilization of a complete shear strain spectrum on the computed response, [FIGURE 8.20](#) presents the prediction residuals computed before the application of the strength correction procedure ([Section 8.2](#)) using both the smooth shear strain spectrum approach (i.e., original EQL-FD) and the complete shear strain approach (i.e., modified EQL-FD). Once again, to ensure that our main observations are based solely on statistically meaningful measures, *mean* residuals are depicted only at γ_{max} bins that contain at least 4 observations. [FIGURE 8.20](#) shows that, before the strength correction, the modified EQL-FD approach provides AF values that are in very good agreement with the observations at $0.01\% < \gamma_{max} < 0.2\%$ and $\gamma_{max} > 1.0\%$, at $T < 0.2$ s. This result is a notable improvement with regards to the original EQL-FD approach and consistent with the observations made regarding the single event examples presented in [FIGURES 8.17](#) and [8.19](#).

To further evaluate the performance of the modified EQL-FD model, the computed maximum shear strains obtained using the modified EQL-FD approach are compared with those from the original EQL-FD approach with a smooth strain

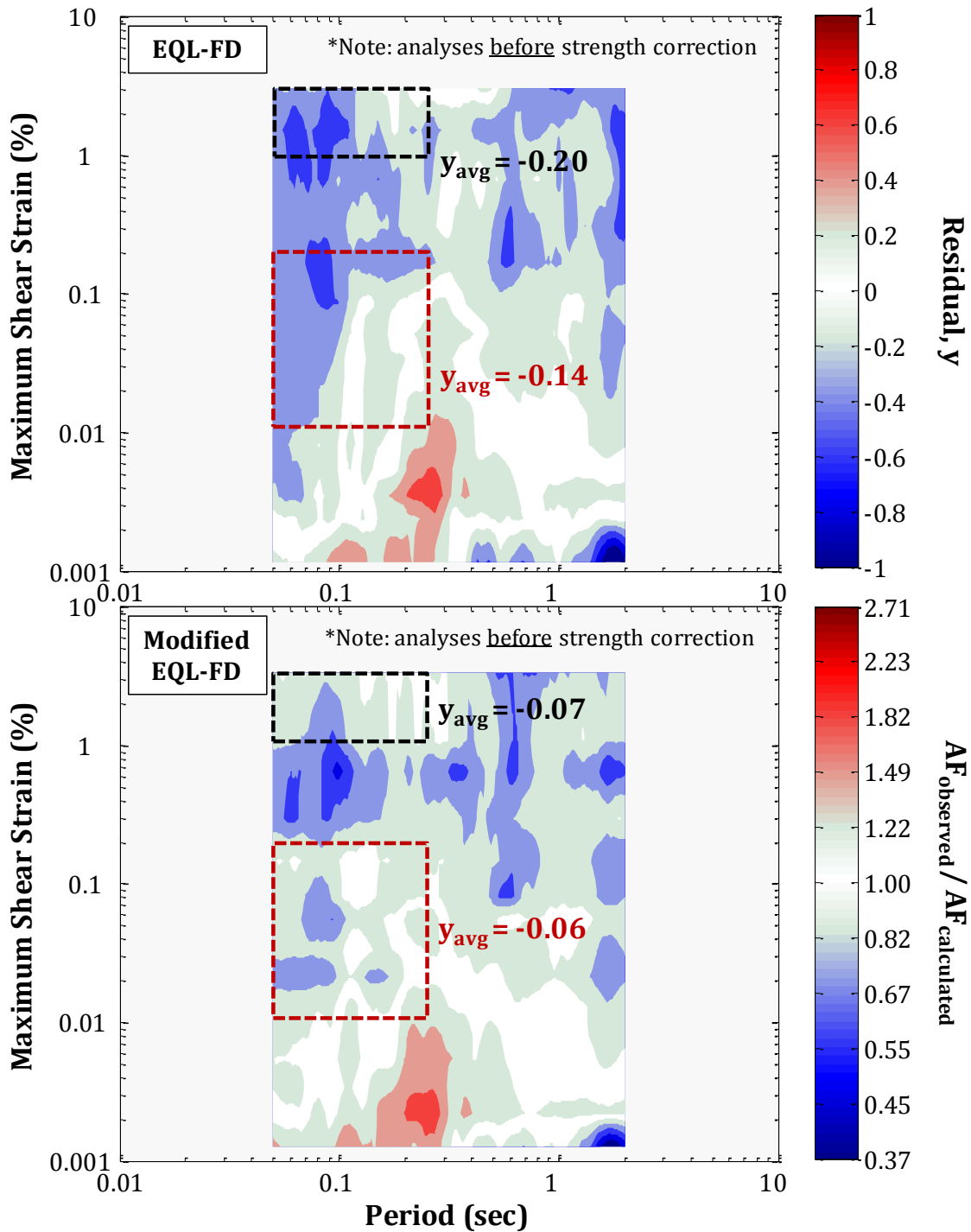


Figure 8.20: Contour plots of *mean* prediction residuals vs maximum calculated shear strains (γ_{max}) vs spectral period (T) obtained using the original and the modified EQL-FD approaches

spectrum and with those from the EQL approach (*FIGURE 8.21*). Now, all analyses incorporate a strength correction for the modulus reduction curves (*Section 8.2*). From *FIGURE 8.21*, it can be observed that the computed maximum shear strains (γ_{max}) obtained by the modified EQL-FD approach are reduced from those predicted by the original EQL-FD approach, particularly for strains exceeding 0.1 %. Moreover, the proposed modification results in γ_{max} values that are in better agreement with those obtained using the EQL approach. This is due to the fact that the scaling factor utilized in the original EQL-FD algorithm (Assimaki and Kausel, 2002) artificially increases the calculated shear strains over a wide range of frequencies (*FIGURE 8.15*).

FIGURE 8.22 presents the corresponding computed mean prediction residuals at different spectral periods (T) and maximum calculated shear strains (γ_{max}) for the modified EQL-FD, the original EQL-FD and the EQL approaches. Based on *FIGURE 8.22* it is evident that the proposed modifications to the EQL-FD method lead to a notable improvement in the performance of the model (i.e., residuals closer to 0.0). Two effects can be identified. First, the calculated shear strains are significantly reduced, i.e. the computed maximum γ_{max} decreased from about 1.3 % to almost 0.6 % (*FIGURE 8.22*). Indeed, the calculated maximum γ_{max} value for the modified EQL-FD approach is very similar to the maximum γ_{max} value calculated by the EQL model. The proposed modification to the EQL-FD approach modestly reduces the substantial over-prediction observed at $0.2 \% < \gamma_{max} < 0.6 \%$ and $T < 0.2 - 0.3 s$, with y_{avg} changing from 0.27 (25 % over-prediction) to 0.21 (20% over-prediction). The second effect of the proposed modification on the computed AF can be seen by examining the prediction residuals at $0.01 \% < \gamma_{max} < 0.10 \%$ (*FIGURE 8.22*). At these strain levels, a substantial reduction in the over-prediction of the response at

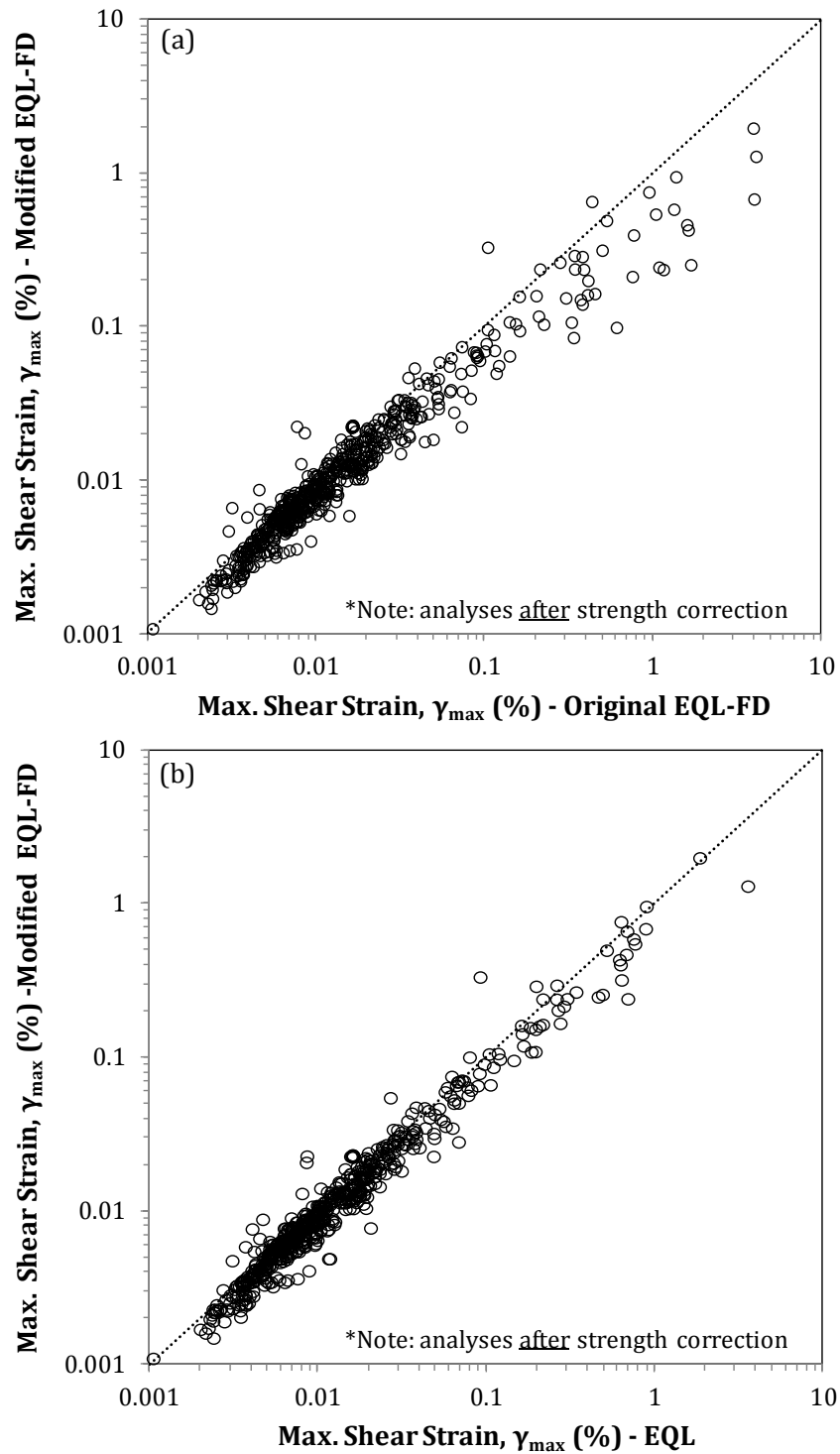


Figure 8.21: Comparison of computed maximum shear strains (γ_{max}) between: (a) the original (Assimaki and Kausel, 2002) and the modified EQL-FD approaches, and (b) the EQL and the modified EQL-FD approaches

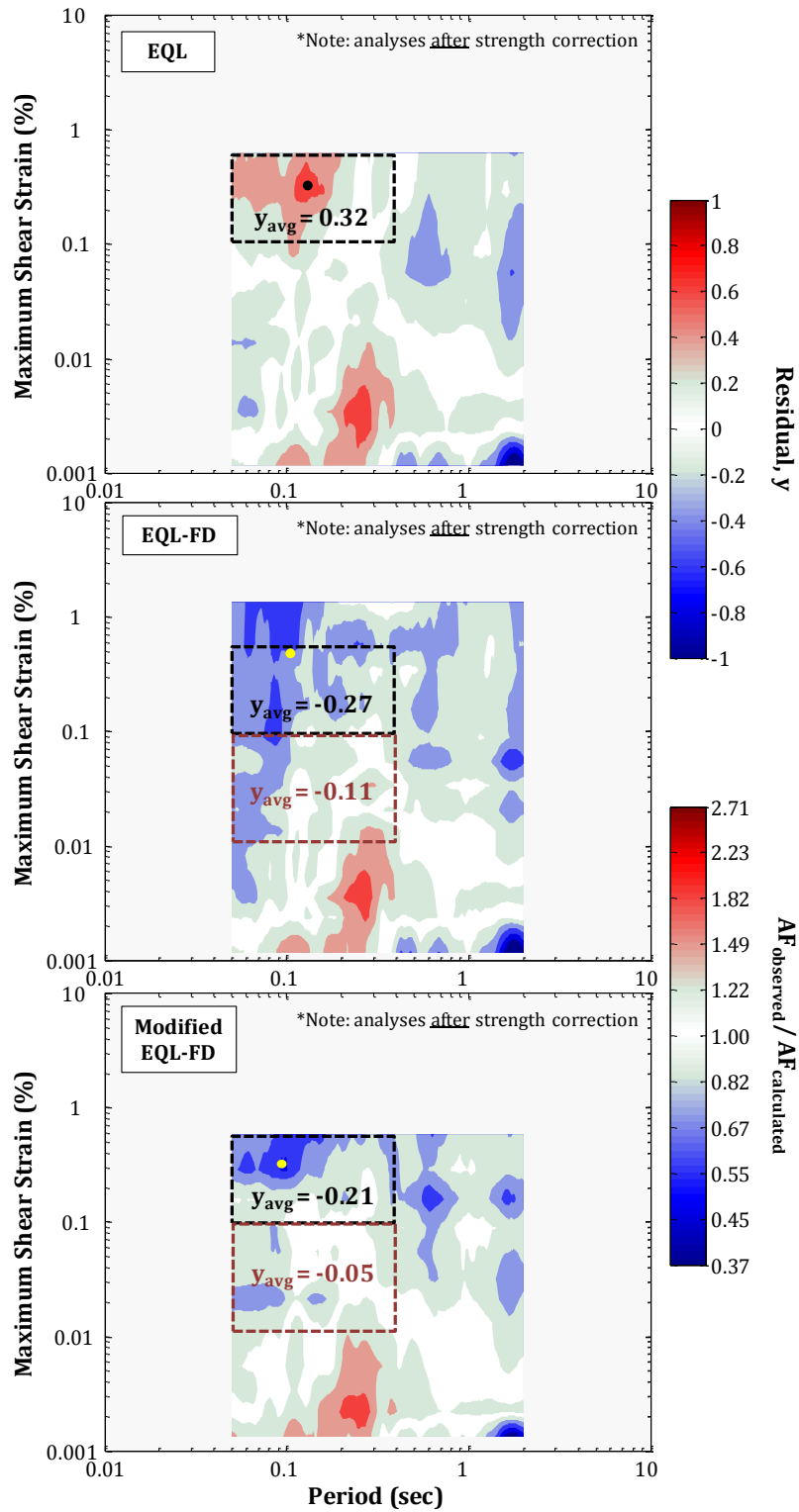


Figure 8.22: Mean residuals vs T vs γ_{max} contour plots obtained using the EQL, the original EQL-FD (Assimaki and Kausel, 2002) and the modified EQL-FD models

$T < 0.15$ s is observed. More specifically, it can be concluded that, at $0.01\% < \gamma_{max} < 0.10\%$, the amplification factors from the modified EQL-FD approach fall within $\pm 20\%$ of the observed AF values.

Finally, we present the *mean* prediction residuals as a function of T/T_{site} by normalizing the spectral period (T) by the T_{site} of each vertical array. *FIGURE 8.23* shows the resulting contour plots of the *mean* residuals computed using the EQL, the original EQL-FD (Assimaki and Kausel, 2002) and the modified EQL-FD approaches. *FIGURE 8.23* emphasizes the influence of the proposed modification on the site response, particularly at strains between 0.01% and 0.2% and $T/T_{site} < 0.5$. In this range of $T/T_{site} - \gamma_{max}$, the AF values computed using the modified EQL-FD model are characterized by smaller *mean* residuals (i.e., higher amplification).

8.4. Discussion of Results

The results presented in this chapter indicate that the strength correction procedure improves the performance of EQL and NL site response analyses (*Section 8.2*). Nonetheless, both theoretical models still predict site amplification at high frequencies and large strains that are 30% to 50% smaller than observed. In particular, the poor performance of the NL method even after the strength correction (*FIGURE 8.9*) is a surprising result that contradicts the general perception within the engineering profession regarding the accuracy of the NL method at large strains. Indeed, the results of this study indicate that the NL method produces larger under-prediction of the high frequency response at large strains than the less rigorous EQL approach. This observation indicates that the inability of site response analysis to accurately predict the surface response at large strains may be related to

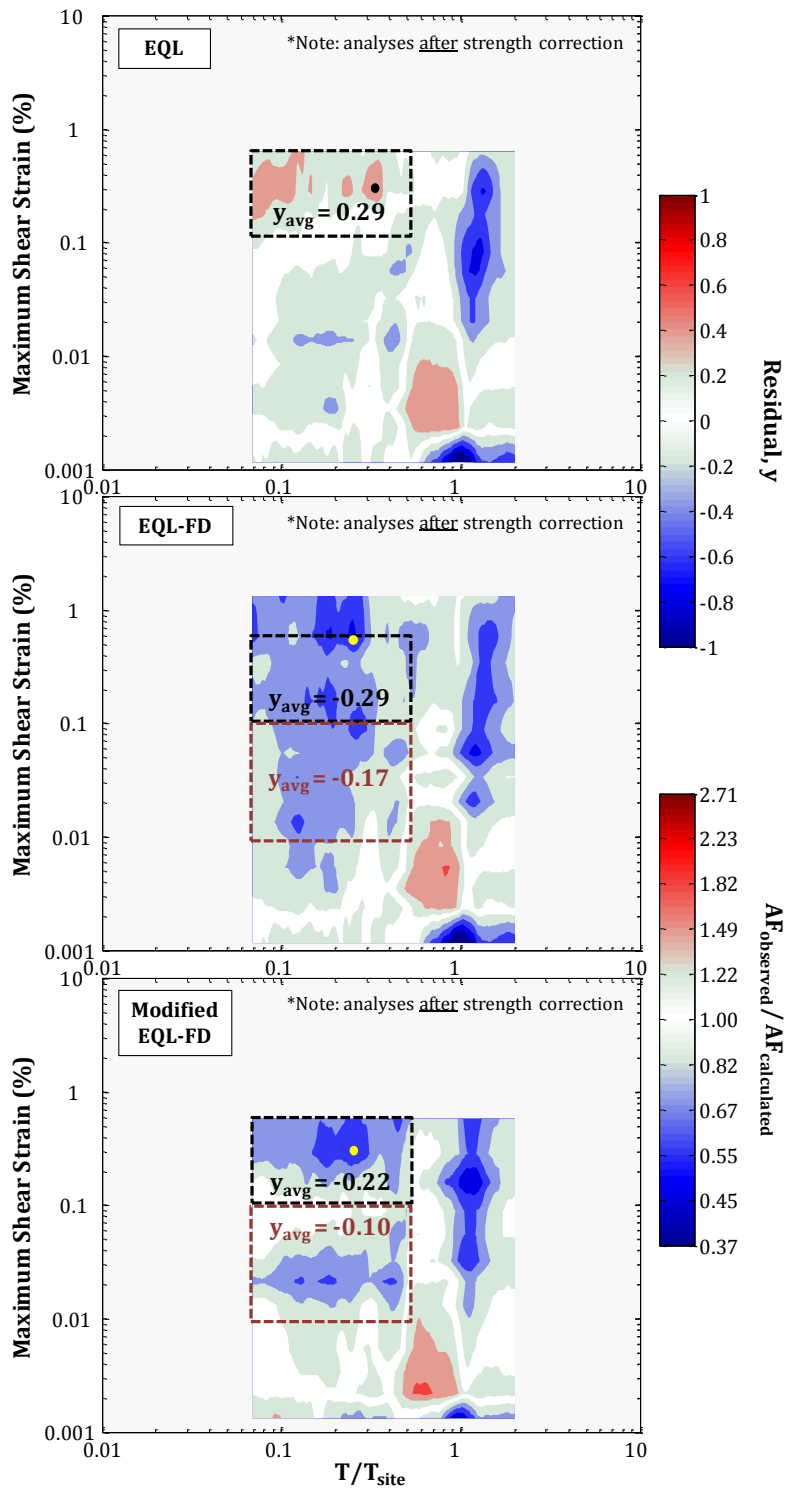


Figure 8.23: Mean residuals vs T/T_{site} vs γ_{max} contour plots obtained using the EQL, the EQL-FD (Assimaki and Kausel, 2002) and the modified EQL-FD models

the use of the one-dimensional modeling approach. In particular, the base isolation effect associated with a limiting shear stress on a horizontal plane that limits the peak acceleration at the ground surface. This issue is independent of whether or not the response of the vertical arrays at small strains is well represented by the one-dimensional assumption.

To investigate this hypothesis, we perform EQL and NL site response analyses for the IWTH26 site using a record from the Loma Prieta (1989) earthquake (*FIGURE 8.24*). This input record is scaled to obtain different peak ground accelerations varying from 0.05 g to 1.0 g ; each motion is propagated through the site, and peak ground accelerations and response spectra are computed at the surface of the IWTH26 site. For these analyses, the stress-corrected modulus reduction and damping curves associated with a friction angle of 29° are used.

Before showing the site response results, we can estimate the limiting peak ground acceleration from the maximum shear stress using Newton's 2nd law. This analysis is the same approach commonly used for the prediction of earthquake induced shear stresses (Seed and Idriss, 1971). Assuming a one-dimensional, level ground site and vertical propagation of horizontally polarized shear waves, Seed and Idriss (1991) proposed that the maximum shear stress at depth z ($\tau_{max}(z)$) of a deformable soil column can be obtained as:

$$\tau_{max}(z) = \frac{PGA}{g} \cdot \sigma_v(z) \cdot r_d(z) \quad (8.4)$$

where PGA is the maximum ground surface acceleration, $\sigma_v(z)$ is the total vertical stress at depth z , and r_d is depth-dependent shear stress reduction coefficient that accounts for the deformability of the assumed soil column.

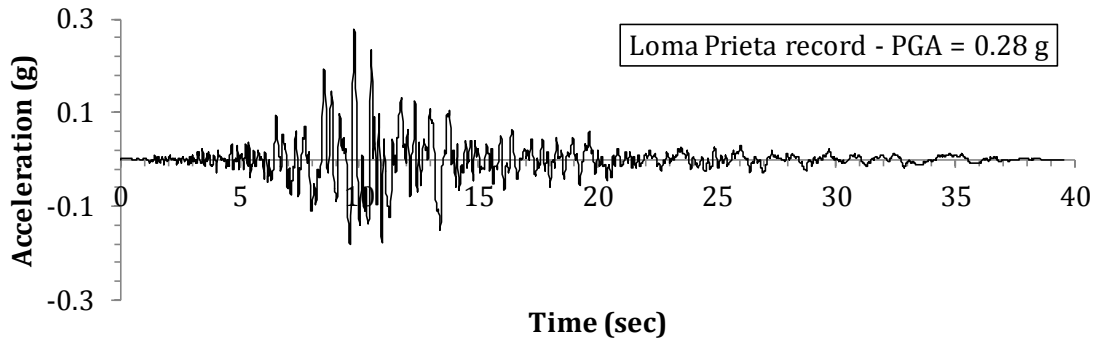


Figure 8.24: Earthquake record used for the evaluation of the 1-D modeling approach

FIGURE 8.25 shows a schematic illustration of the determination of the maximum shear stress (τ_{max}) at depth z based on Equation 8.4. As it can be seen in FIGURE 8.25, the shear stress reduction coefficient, r_d , takes a value of 1 at the surface and smaller values at greater depths. Based on Equation 8.4, if the maximum shear stress (τ_{max}) at a specific depth is known, then the PGA at the surface can be calculated, as:

$$\frac{PGA}{g} = \frac{\tau_{max}(z)}{\sigma_v(z) \cdot r_d(z)} \quad (8.5)$$

Equation 8.5 can, therefore, be used to estimate a limiting value of PGA at the surface of the IWTH26 site. Specifically, we utilized the information provided in FIGURE 8.2 (Section 8.2) regarding the maximum shear stress ($\tau_{max} = 34 \text{ kPa}$) and total vertical stress $\sigma_v = 59.5 \text{ kPa}$ at a depth of 3.5 m of the IWTH26 array. Based on data from Seed and Idriss (1971), a reasonable value of $r_d = 0.97$ was assumed. The resulting limiting value of PGA is 0.59 g.

FIGURE 8.26a shows the surface peak ground accelerations ($PGA_{surface}$) computed using the EQL and NL site response methods for each of the input intensities (PGA_{base}) analyzed. It can be observed that the computed $PGA_{surface}$ values from both the EQL and NL analyses become saturated with increasing values

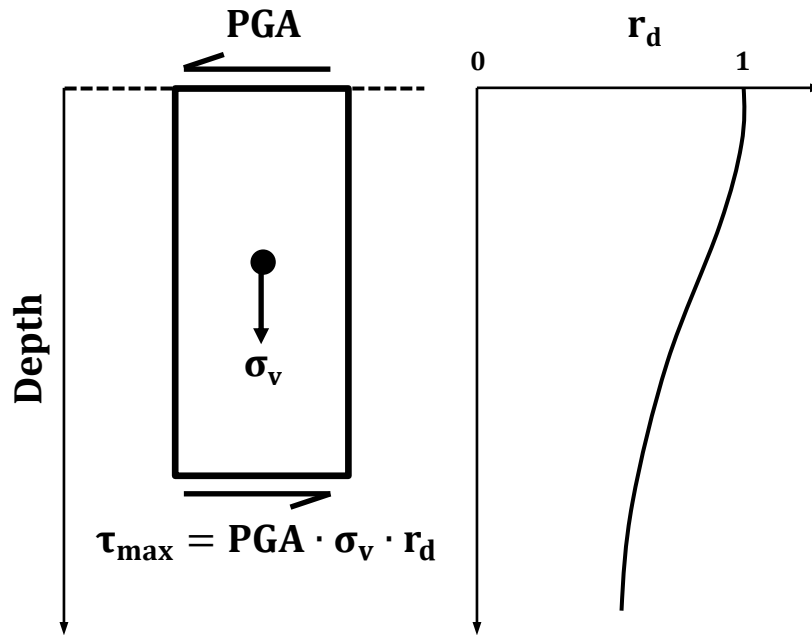


Figure 8.25: Schematic illustration of the determination of the maximum shear stress (τ_{max}) at depth of a one-dimensional soil column

of PGA_{base} . More specifically, the computed $PGA_{surface}$ values start to level off at $PGA_{base} > 0.4 g$. For the NL approach, the computed limiting value of $PGA_{surface}$ is approximately $0.7 g$ which is about 20 % larger than predicted by the simplified analysis (shown by the red dotted line in *FIGURE 8.26a*). The limiting $PGA_{surface}$ value is about $1.2 g$ for EQL analysis. Larger PGA values can be sustained by the EQL analysis because the linear-elastic, strain-compatible shear modulus associated with the effective strain ($\gamma_{eff} \sim 0.65 \cdot \gamma_{max}$) allows for shear stresses larger than the shear strength to be mobilized.

FIGURE 8.26a shows the entire surface response spectra for analyses performed with different PGA_{base} . The limiting motions also are observed here, with the computed spectral accelerations for input motions with $PGA_{base} = 0.8 g$ and $1.0 g$ being very similar. The fact that the computed response becomes sa-

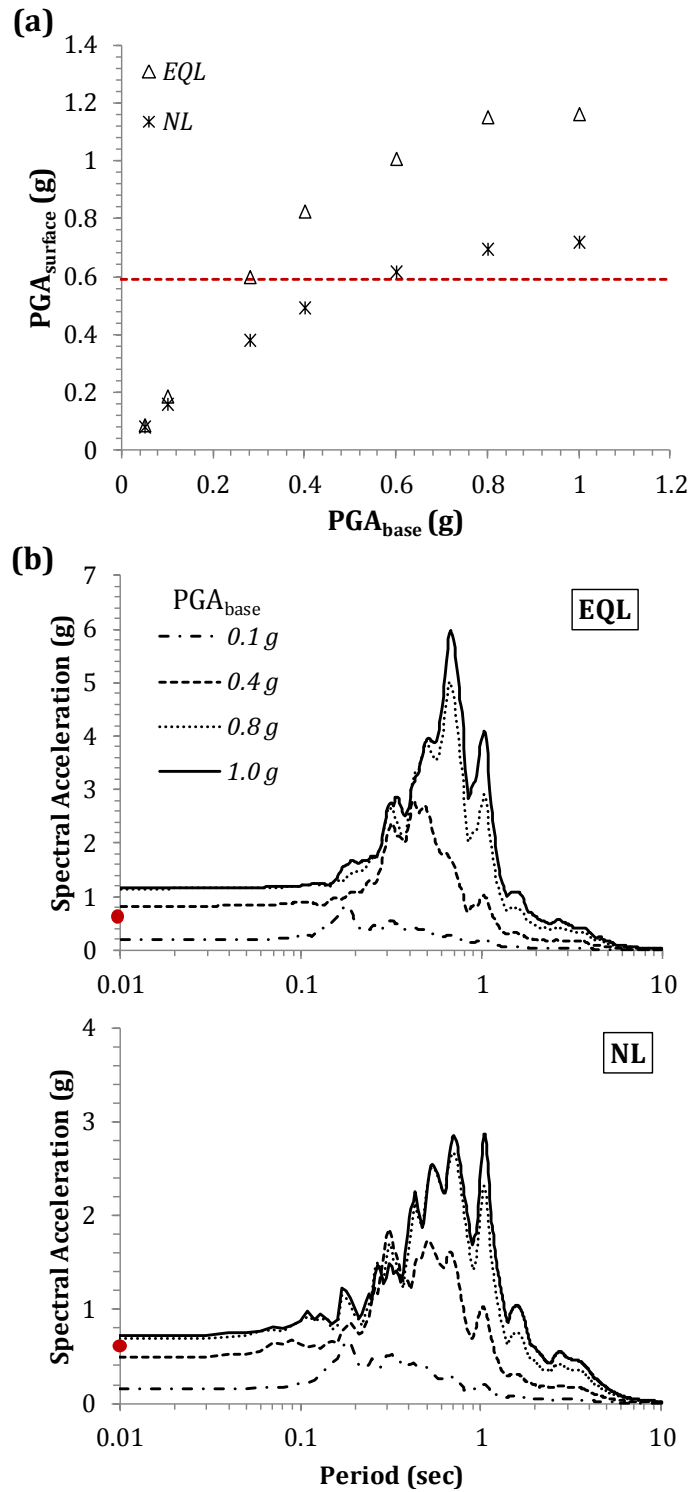


Figure 8.26: (a) Computed and predicted $PGA_{surface}$ versus PGA_{base} , and (b) surface spectral accelerations, for the EQL and NL site response methods

turated at high input intensities may be explained by the base isolation effect within the one-dimensional soil column once the shear strength is reached. When the induced shear strains within a soil layer become large enough to almost fully mobilize the shear strength, the material does not allow the motion to be fully propagated to the surface. It is not clear at this time whether field recordings at sites with weaker layers show this base isolation effect. Time histories at sites that have liquefied (e.g., Wildlife site in California) certainly have shown a significant drop in peak acceleration after the initiation of liquefaction (Holzer and Youd, 2007), something that supports the concept of a base isolation effect. However, the shear strength of liquefied soil is very small compared to those considered here and the geologic setting of a liquefaction site lends itself to horizontal continuity. Both of these issues would make the base isolation effect more likely to happen. However, only a small amount of lateral variability in terms of stiffness could minimize the base isolation effect. If in-situ lateral variability minimizes the base isolation, this could help explain why the observed high frequency site amplification at large strains was consistently larger than the predicted site amplification from one-dimensional EQL and NL analyses. Nonetheless, more research is needed regarding the response of sites at large strains.

The base isolation effect should also be relevant for the one-dimensional EQL-FD approach. *FIGURE 8.27* presents the computed surface spectral accelerations for the EQL-FD method at the IWTH26 site for the same input motions used for the EQL and NL analyses presented in *FIGURE 8.26*. *FIGURE 8.27* shows that the EQL-FD response also becomes saturated at high input intensities, i.e., the responses for $PGA_{base} = 0.8 g$ and $1.0 g$ are very similar. Nevertheless, comparing the EQL-FD results with those of the EQL approach (*FIGURE 8.25b*), it is evident that now the sa-

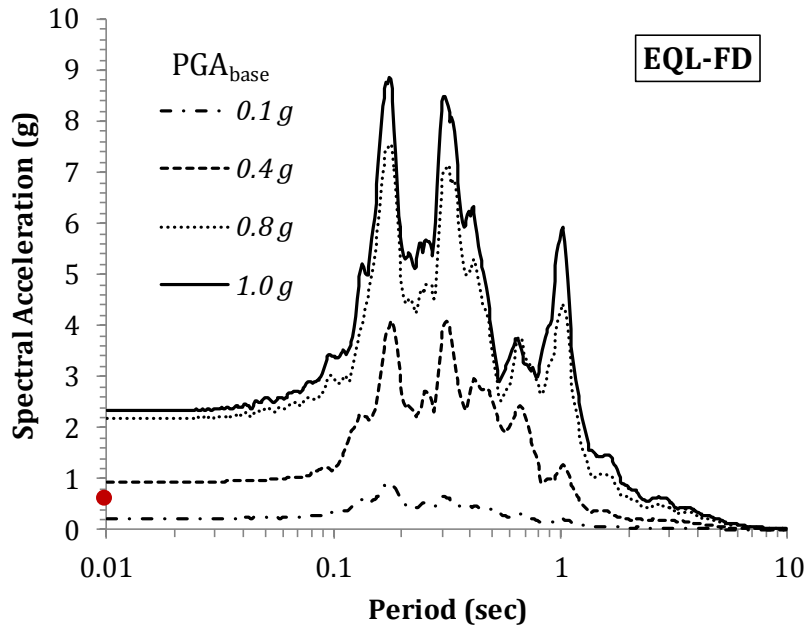


Figure 2.27: Surface spectral accelerations for the EQL-FD method

turation occurs at much larger spectral acceleration levels, particularly at short periods. This is due to the fact that at short periods the EQL-FD model is primarily sensitive to the incorporated small-strain damping values and not by the shear strength at large strains. Consequently, the definition of appropriate damping values at small strains becomes a critical aspect of the performance of the EQL-FD method. For example, *FIGURE 8.28* illustrates the effect of the different small strain damping (D_{min}) definitions on the short period response of the modified EQL-FD approach. The computed and observed surface spectral accelerations at the IBRH13 site for a motion recorded on 3/19/2011, 18:56 (motion 4 in *TABLE 8.2*) are depicted. From *FIGURE 8.28*, it can be observed that the incorporation of minimum damping (D_{min}) values based on the Darendeli (2001) model leads to higher spectral accelerations at short periods and thus larger response is observed. Therefore, the appropriate value of minimum damping is an important issue to consider in EQL-FD analyses.

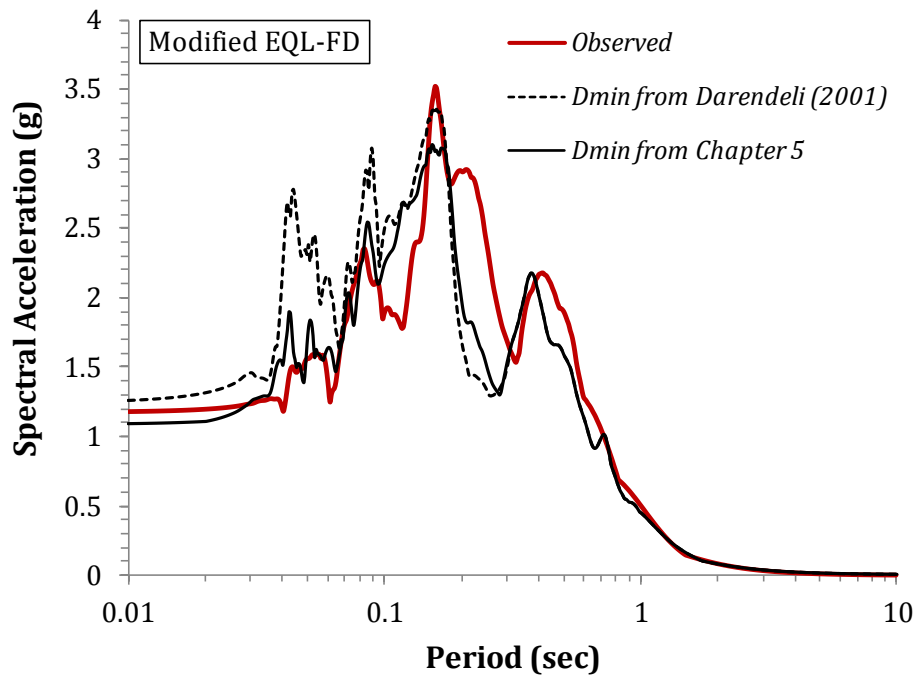


Figure 8.28: Effect of the different minimum damping (D_{min}) definitions on the computed response by the modified EQL-FD method at the IBRH13 site and for an input motion recorded on 3/19/2011, 18: 56 (motion 4 in TABLE 8.2)

8.5. Summary

In this chapter, several procedures that can be used to improve the accuracy of the one-dimensional EQL, EQL-FD and NL site response analyses, were presented. First, an attempt to take into account the shear strength of the soil materials at large shear strains was made. The procedure developed by Hashash *et al.* (2010) was applied to the vertical arrays considered in this study. The utilized modulus reduction curves ($G/G_{max} - \log \gamma$) of all layers within the upper 50 m of the soil profiles and with a shear wave velocity of less than 500 m/s were altered to match a target shear strength. Due to the limited geotechnical site investigation at the Kik-Net arrays, a target friction angle, ϕ , of 29° was assumed for all layers that were strength corrected. Overall, the results from the present study indicate that the

application of a strength correction procedure reduces the under-prediction by the EQL and NL one-dimensional site response analyses, but significant under-prediction still remains. On the other hand, the EQL-FD approach is only modestly affected by the strength correction.

Second, several numerical refinements of the EQL-FD approach were proposed. First, we proposed the performance of the EQL-FD computations after the completion of the initial EQL iterations. Then, we modified the numerical procedure of the EQL-FD approach by selecting the frequency dependent material properties (G/G_{max} and damping, D) based on the complete and scaled shear strain Fourier Amplitude Spectrum ($\gamma(f)$) rather than a smoothed variation of $\gamma(f)$ (e.g., Assimaki and Kausel, 2002). The proposed modifications were evaluated against recordings from the borehole arrays.

Chapter 9

Summary and Conclusions

9.1. Summary and Conclusions

The main objective of this study was to compare and evaluate the 1-D equivalent-linear (EQL), equivalent-linear with frequency dependent soil properties (EQL-FD), and nonlinear (NL) time series site response methodologies. To investigate the accuracy of the modeling techniques with respect to recorded ground motions during earthquake shaking, recordings from instrumented borehole arrays were utilized.

The NIED Kik-Net database in Japan was selected as the main source of borehole array data for this study. A total of thirteen borehole arrays (11 Kik-Net plus the La Cienega array in California and the Lotung array in Taiwan) were selected based on the availability of a large number of recordings and recordings with large intensity. The $V_{S,30}$ for the selected sites ranges from 184 m/s to 371 m/s , while the depth to the downhole sensor varies from less than 100 m to more than 200 m . Some of the sites exhibit a strong impedance contrast within the top 50 m of the profile.

Low intensity input motions with $PGA_{base} \leq 0.05 g$ were used to evaluate common assumptions regarding the boundary conditions used in one-dimensional site response analysis (i.e., “within” versus “incoming only” wavefield). Comparison of theoretical linear-elastic transfer functions and observed transfer functions indicated that the “within” boundary condition accurately captured the response of

sites with a base sensor installed at depths less than or equal to about 100 *m*. The sites with a deeper base sensor were better modeled with the “incoming only” boundary condition. Nonetheless, subsequent analyses were performed using the “within” boundary conditions to achieve consistency across all sites. Assuming a “within” boundary condition, we identified the small-strain damping profiles for each site that provided the best-fit to the observed transfer functions. The best-fit damping values generally were larger than those predicted by empirical models derived from laboratory testing. These larger values are a result of the field recordings being affected by both material damping and attenuation from wave scattering, whereas laboratory testing only measures materials damping.

The performance of the different site response approaches was evaluated by comparing the observed and computed response spectral amplification factors (*AF*). To compare the results across sites, the residuals in the predictions (i.e. $y = \ln(AF^{obs} / AF^{calc})$) at each site were computed and the strain dependence of the mean amplification residuals examined. At computed maximum strain levels (γ_{max}) less than 0.01 %, all three site response approaches performed well with the average predicted site amplification within $\pm 20\%$ of the observations. At larger strain values ($\gamma_{max} > 0.1\%$), the EQL and NL approaches both under-predict the observed amplification, predominantly at periods less than about 0.3 *s* to 0.5 *s*. The predicted amplification can be as small as one-third to one-half of the observed amplification at strains greater than 0.4 %. Surprisingly, the NL approach did not provide more accurate predictions than the EQL approach. For the EQL-FD approach, the amplification predictions are generally larger than the observations. At periods less than 0.2 *s* and strains larger than 0.1 %, the predicted amplification from the EQL-FD approach may be as much as 60 % larger than observations.

Investigating the variability in the predicted amplification relative to the observations at small strains indicates that the total standard deviation is approximately 0.5 at periods less than 1.0 s for all three site response approaches. The inter-site and intra-site standard deviations contribute almost equally to the total standard deviation at these periods. At larger strains ($\gamma_{max} > 0.1\%$), the total variability increases to about 0.65 – 0.8 at periods less than 1.0 s. At these strain levels, the inter-site component of variability dominates across all spectral periods, with the intra-site standard deviation being smaller. However, with fewer data at large strains these variability estimates are more uncertain.

When considering site amplification at large strains, it is important that the nonlinear soil properties model realistic shear strengths at large strains. The empirical modulus reduction curves used in the previous analyses were modified at large strains to be consistent with a large strain friction angle of 29° . In general, this modification increased the shear stress that could be transmitted at large strains. The use of the modified modulus reduction curves improved the performance of both the EQL and NL approaches at large strains. The improvement is a result of two factors: *i)* a reduction in the induced level of shear strain for the motions considered, and *ii)* the mobilization of larger shear stresses at the induced level of strain. Generally, the first factor was most influential in improving the predictions of site amplification, with the computed maximum strain across all motions decreasing from 2 – 4 % to 0.5 – 1.0 %. Within this strain range, EQL analysis under-predicts amplification by 30 % on average, and by as much as 50 %, for periods less than 0.5 s. For NL analysis, the under-prediction at large strains is 45 % on average, and as much as 70 %, over the same strain range, for periods less than 0.5 s.

For the EQL-FD approach, the modification of the modulus reduction curves did not significantly improve the amplification predictions relative to the observations. Further modifications were incorporated to the EQL-FD approach. Specifically, the full shear strain spectrum, rather than a smooth spectrum, was used to define the frequency dependent material properties. This modification removed any systematic over-prediction by the EQL-FD method for strains less than 0.1 % and periods less than 0.5 s, and reduced the over-prediction to 25 % on average over strains between 0.1 % and 0.6 %.

9.2. Recommendations for Future Work

The results from this study indicate that the EQL, EQL-FD and NL site response methodologies are all unable to accurately predict the high frequency response of soil deposits, when large shear strains are experienced. The proposed modification in the material properties (i.e., shear strength correction) and the proposed modifications to the EQL-FD method only partly alleviate the observed inaccuracies. Therefore, future research efforts should focus on identifying and mitigating the primary causes for the poor performance of one-dimensional site response models at high frequencies and at large strains. Based on the experience gained through this work, the following recommendations can be made regarding possible steps forward:

- 1.** In this study the incorporation of additional small strain attenuation mechanisms, such as wave scattering, was made by simply applying a factor on the depth-dependent D_{min} profiles obtained from the Darendeli (2001) model. A more thorough investigation of the simultaneous frequency and

depth dependence of wave scattering should be performed. This investigation could utilize data from extensively instrumented geotechnical borehole arrays (i.e., accelerometers installed at various depths). By comparing the linear elastic transfer functions computed at different depths with the corresponding observed transfer functions, the depth and frequency dependence of wave scattering and associated attenuation can be better constrained.

2. The effect of the strength correction procedure on the computed EQL and NL responses should be evaluated in more detail using site-specific data. Data from static or dynamic shear strength tests can be used to develop target shear strength values for the soil layers at different depths. Moreover, the robustness of the strength correction procedure can be increased by developing an automated algorithm for the modification of the G/G_{max} curve at large strains.
3. The main theoretical justification for the strength correction is based on the errors associated with the extrapolation of laboratory measurements of G/G_{max} at large strains. Since the same errors are incorporated into the extrapolation of laboratory measurements of damping, one could logically argue that the $D - \log \gamma$ need to be modified at large strains as well. Therefore, the development of a relevant and theoretically solid procedure seems to be necessary.
4. The assumption of one-dimensional wave propagation may be one of the main causes for the observed inaccuracies at high frequencies and large strains in the site response approaches studied. The influence of 2-D and 3-D

soil heterogeneity on the response of level ground sites at large strains may provide insights into this issue.

Appendix

A.1. Boring Logs for the Selected Kik-Net Vertical Arrays

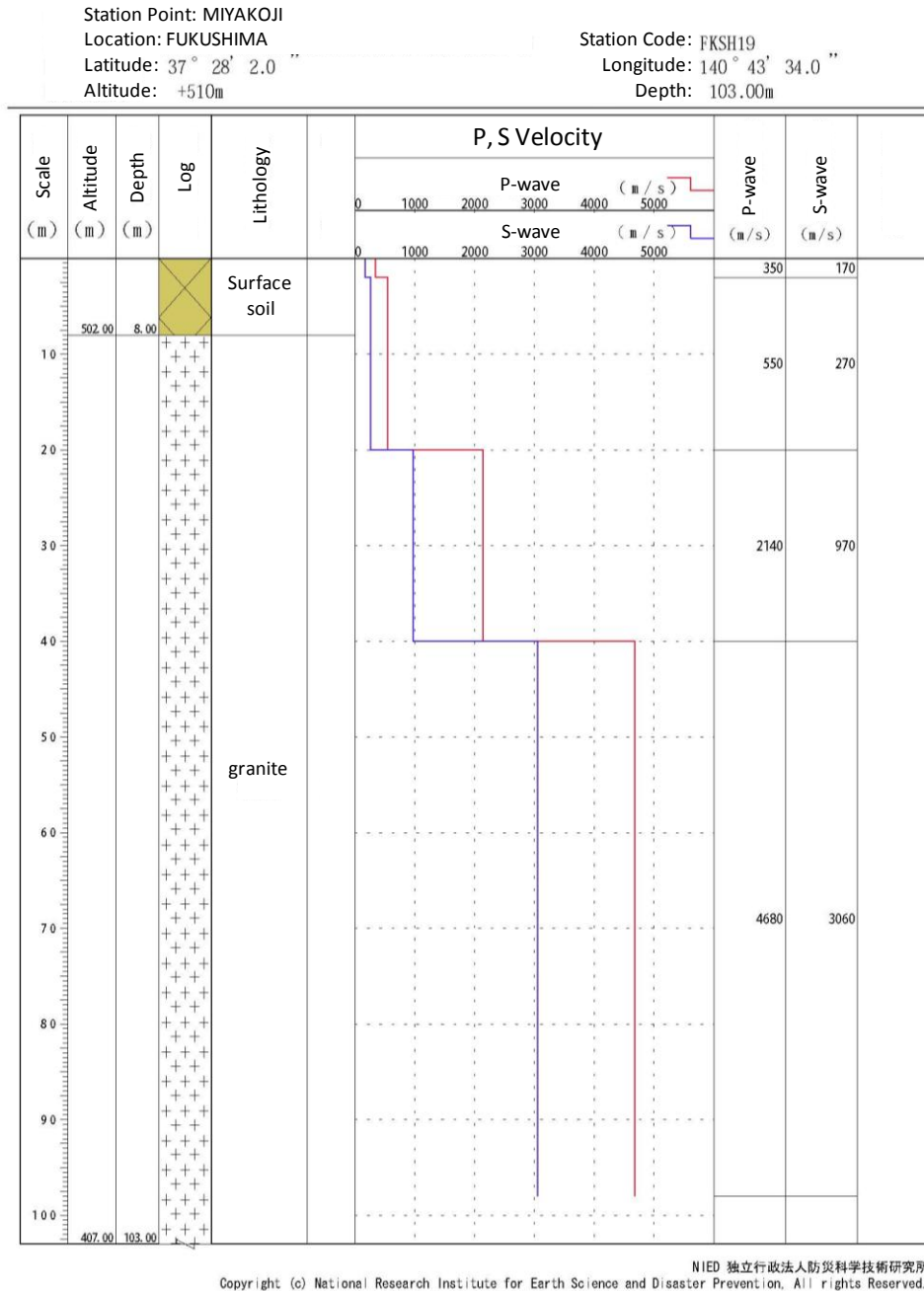
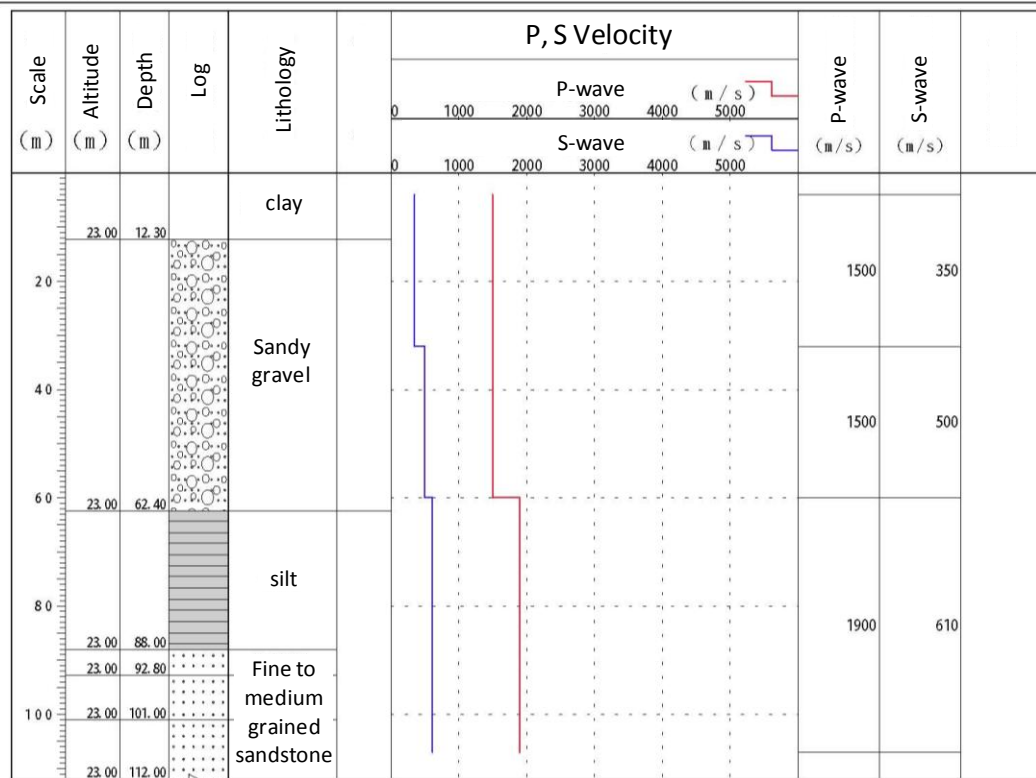


Figure A.1: Boring log reported by NIED Kik-Net database, for the FKSH19 array (translated from the original Japanese version)

Station Point: NAMIE
 Location: FUKUSHIMA
 Latitude: 37° 29' 17.0''
 Altitude: +23m

Station Code: FKSH20
 Longitude: 140° 59' 26.0''
 Depth: 112.00m



NIED 独立行政法人防災科学技術研究所
 Copyright (c) National Research Institute for Earth Science and Disaster Prevention. All rights Reserved.

Figure A.2: Boring log reported by NIED Kik-Net database, for the **FKSH20** array (translated from the original Japanese version)

Station Point: IWASE

Location: IBARAKI

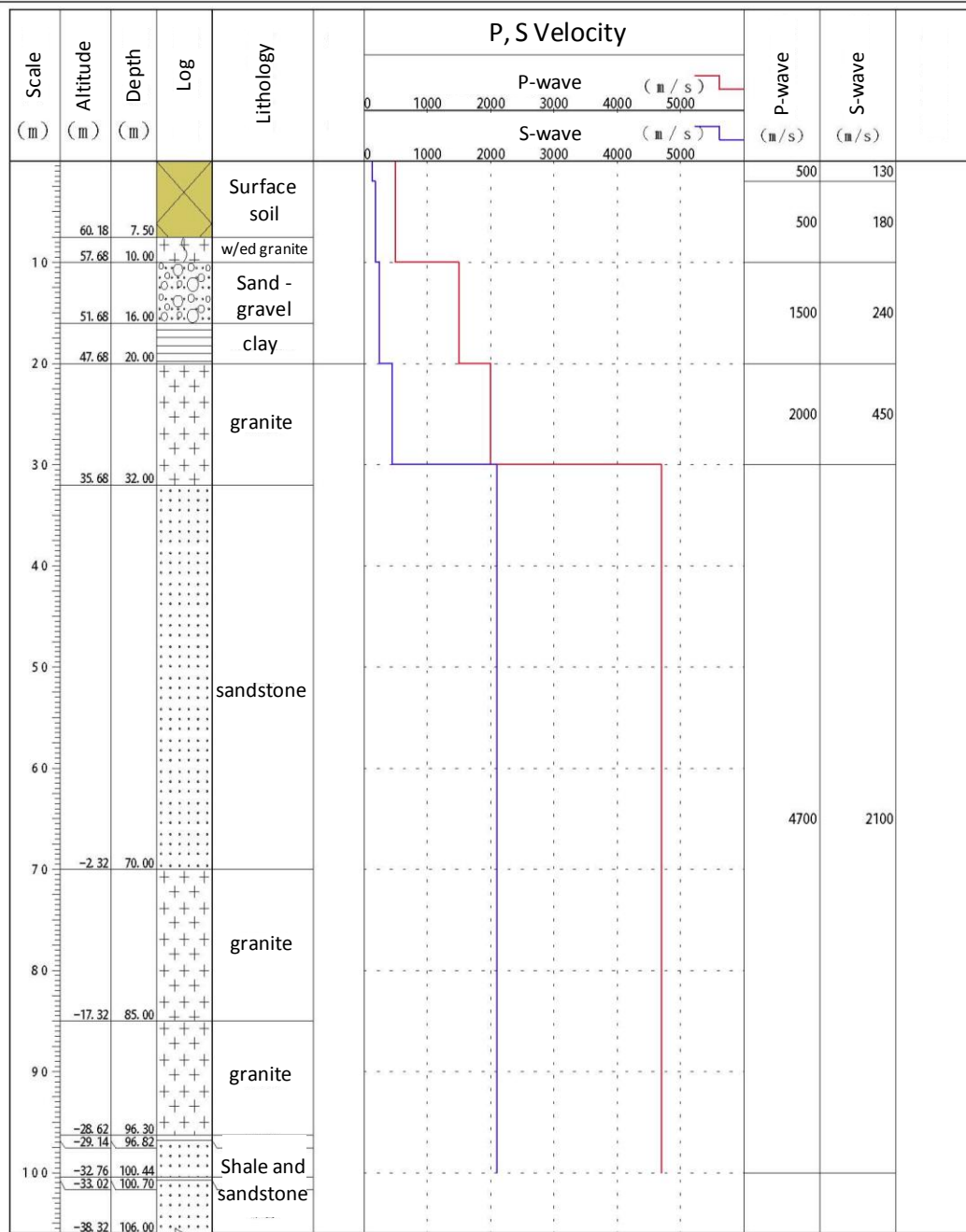
Latitude: 36° 22' 2.0 "

Altitude: +68m

Station Code: IBRH11

Longitude: 140° 8' 37.0 "

Depth: 106.00m



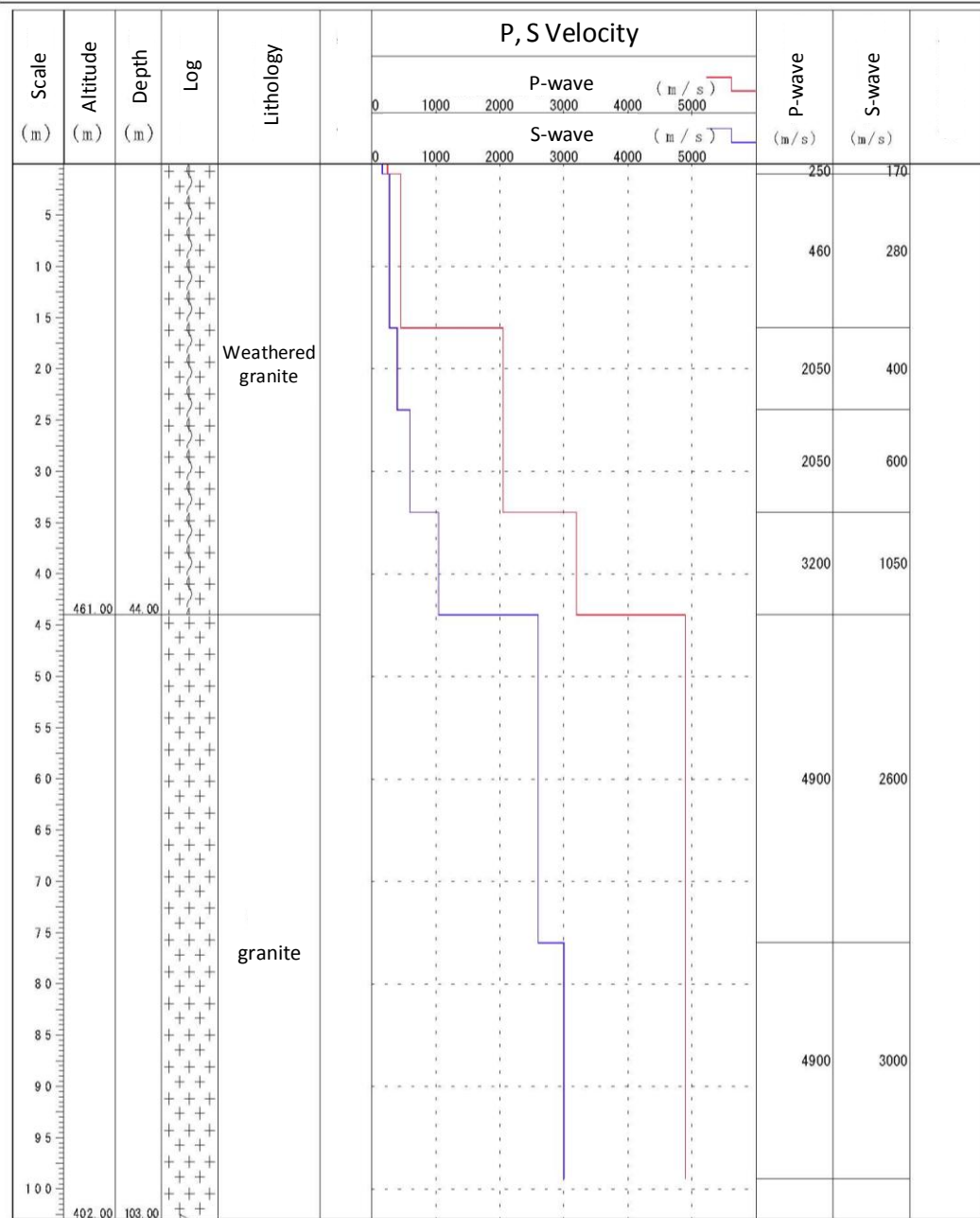
NIED 独立行政法人防災科学技術研究所

Copyright (c) National Research Institute for Earth Science and Disaster Prevention. All rights Reserved.

Figure A.3: Boring log reported by NIED Kik-Net database, for the IBRH11 array (translated from the original Japanese version)

Station Point: TAKAHAGI
 Location: IBARAKI
 Latitude: 36° 47' 32.6"
 Altitude: +505m

Station Code: IBRH13
 Longitude: 140° 34' 42.2"
 Depth: 103.00m



NIED 独立行政法人防災科学技術研究所
 Copyright (c) National Research Institute for Earth Science and Disaster Prevention. All rights Reserved.

Figure A.4: Boring log reported by NIED Kik-Net database, for the IBRH13 array (translated from the original Japanese version)

Station Point: ICHINOSEKI-E

Location: IWATE

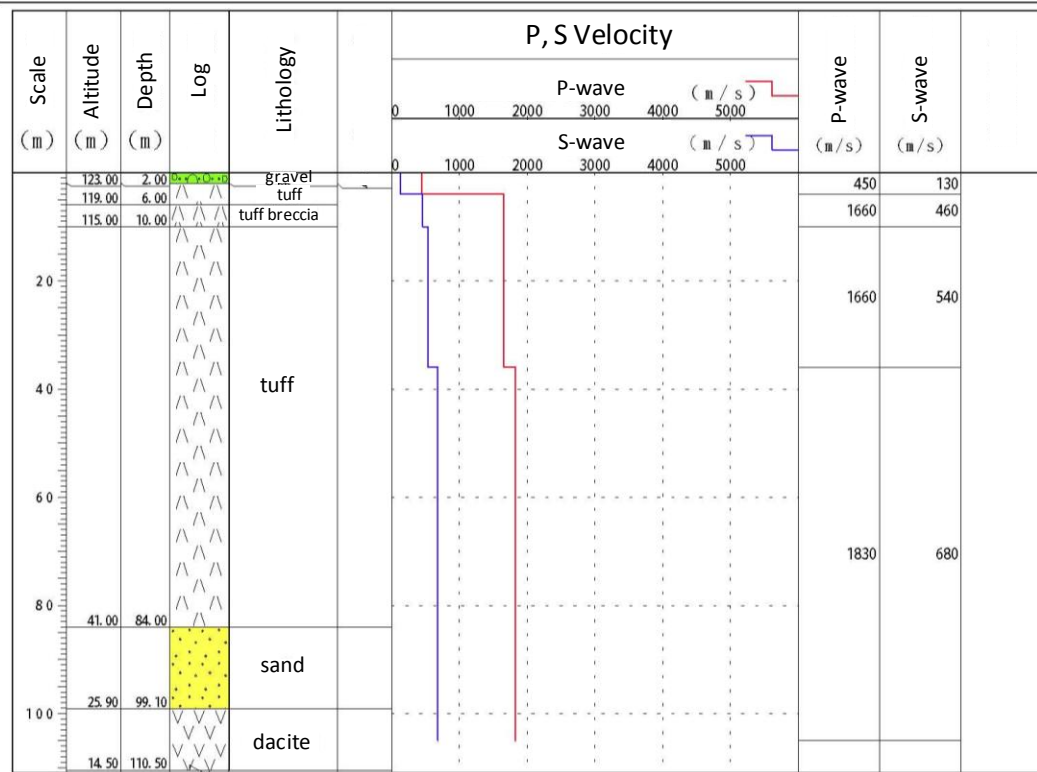
Latitude: 38° 57' 58.0"

Altitude: +125m

Station Code: IWTH26

Longitude: 141° 0' 17.0"

Depth: 110.50m



NIED 独立行政法人防災科学技術研究所

Copyright (c) National Research Institute for Earth Science and Disaster Prevention, All rights Reserved.

Figure A.5: Boring log reported by NIED Kik-Net database, for the IWTH26 array (translated from the original Japanese version)

Station Point: TSURUI-E

Location: HOKKAIDO

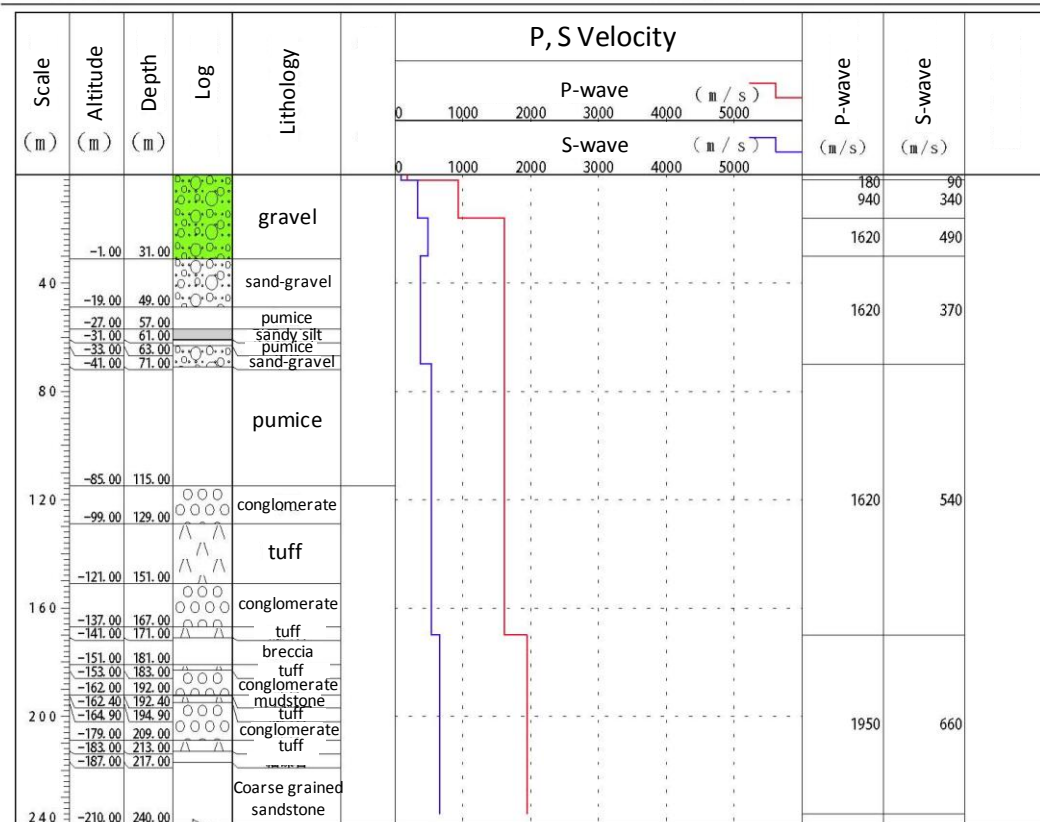
Latitude: 43° 13' 3.0 "

Altitude: +30m

Station Code: KSRH06

Longitude: 144° 25' 57.0 "

Depth: 240.00m



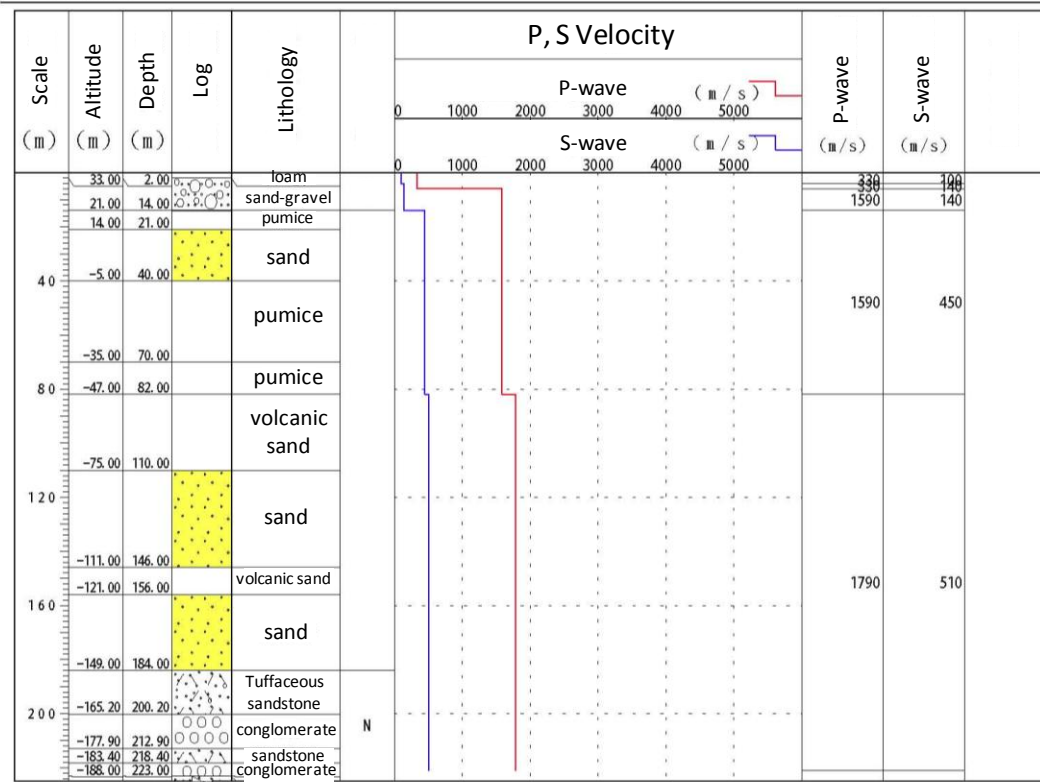
NIED 独立行政法人防災科学技術研究所

Copyright (c) National Research Institute for Earth Science and Disaster Prevention. All rights Reserved.

Figure A.6: Boring log reported by NIED Kik-Net database, for the KSRH06 array (translated from the original Japanese version)

Station Point: TSURUI-S
 Location: HOKKAIDO
 Latitude: 43° 7' 60.0"
 Altitude: +35m

Station Code: KSRH07
 Longitude: 144° 19' 53.0"
 Depth: 225.00m



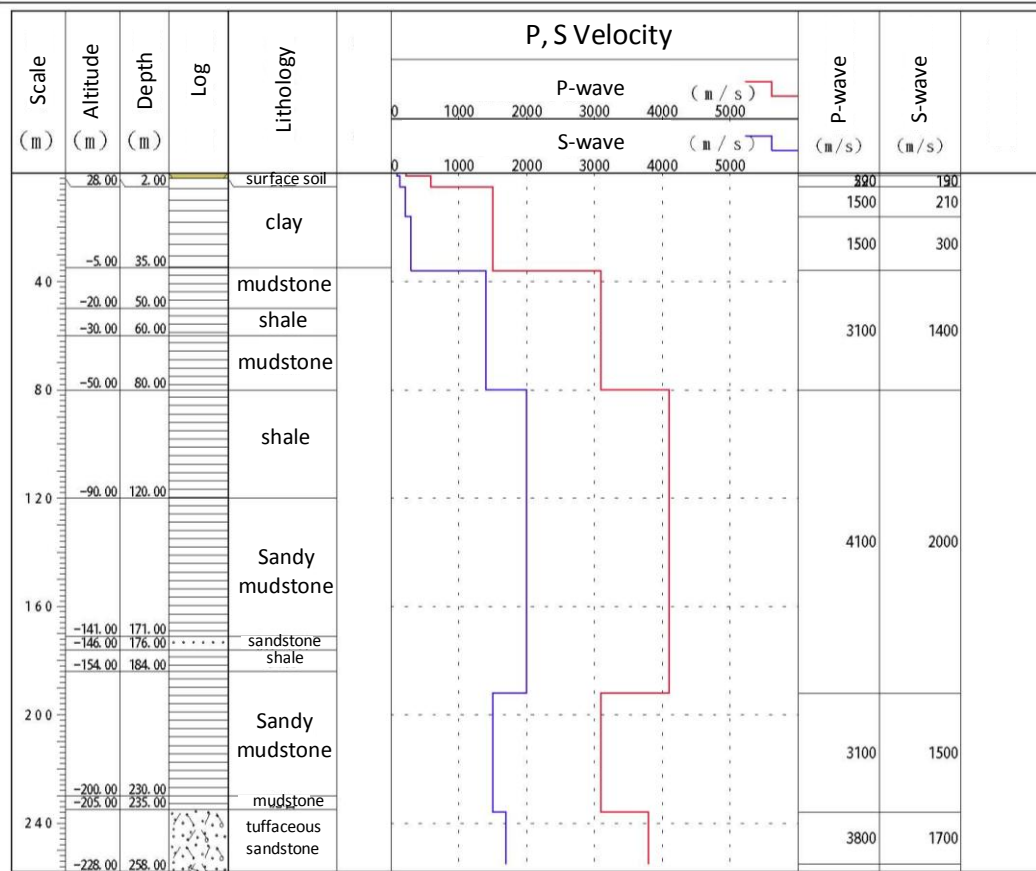
NIED 独立行政法人防災科学技術研究所

Copyright (c) National Research Institute for Earth Science and Disaster Prevention. All rights Reserved.

Figure A.7: Boring log reported by NIED Kik-Net database, for the **KSRH07** array (translated from the original Japanese version)

Station Point: HAMANAKA
 Location: HOKKAIDO
 Latitude: 43° 12' 21"
 Altitude: +30m

Station Code: KSRH10
 Longitude: 145° 7' 15"
 Depth: 258.00m

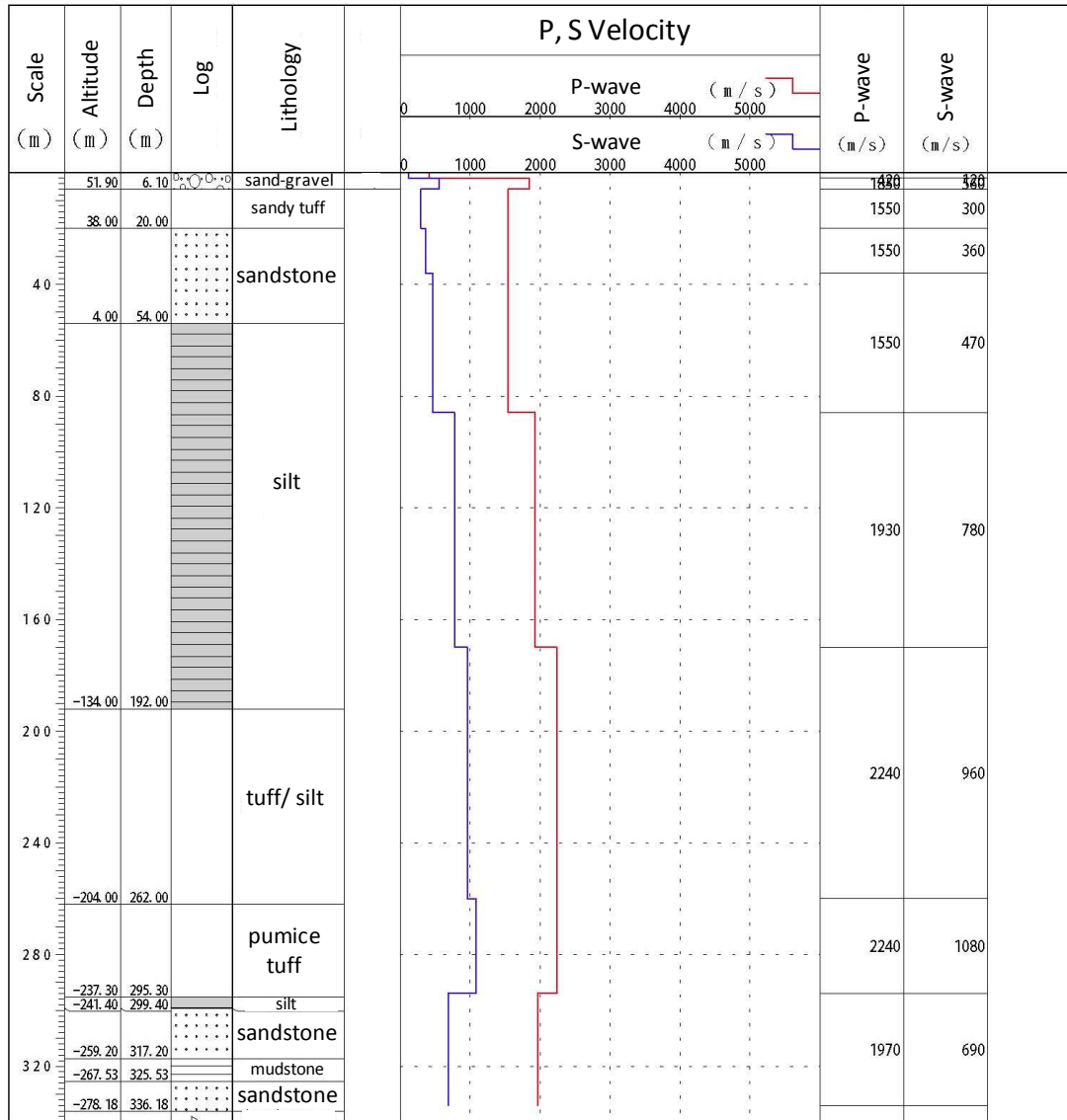


NIED 独立行政法人防災科学技術研究所
 Copyright (c) National Research Institute for Earth Science and Disaster Prevention. All rights Reserved.

Figure A.8: Boring log reported by NIED Kik-Net database, for the **KSRH10** array (translated from the original Japanese version)

Station Point: ONODA
 Location: MIYAGI
 Latitude: 38° 34' 35.0''
 Altitude: +58m

Station Code: MYGH05
 Longitude: 140° 47' 2.0''
 Depth: 340.00m



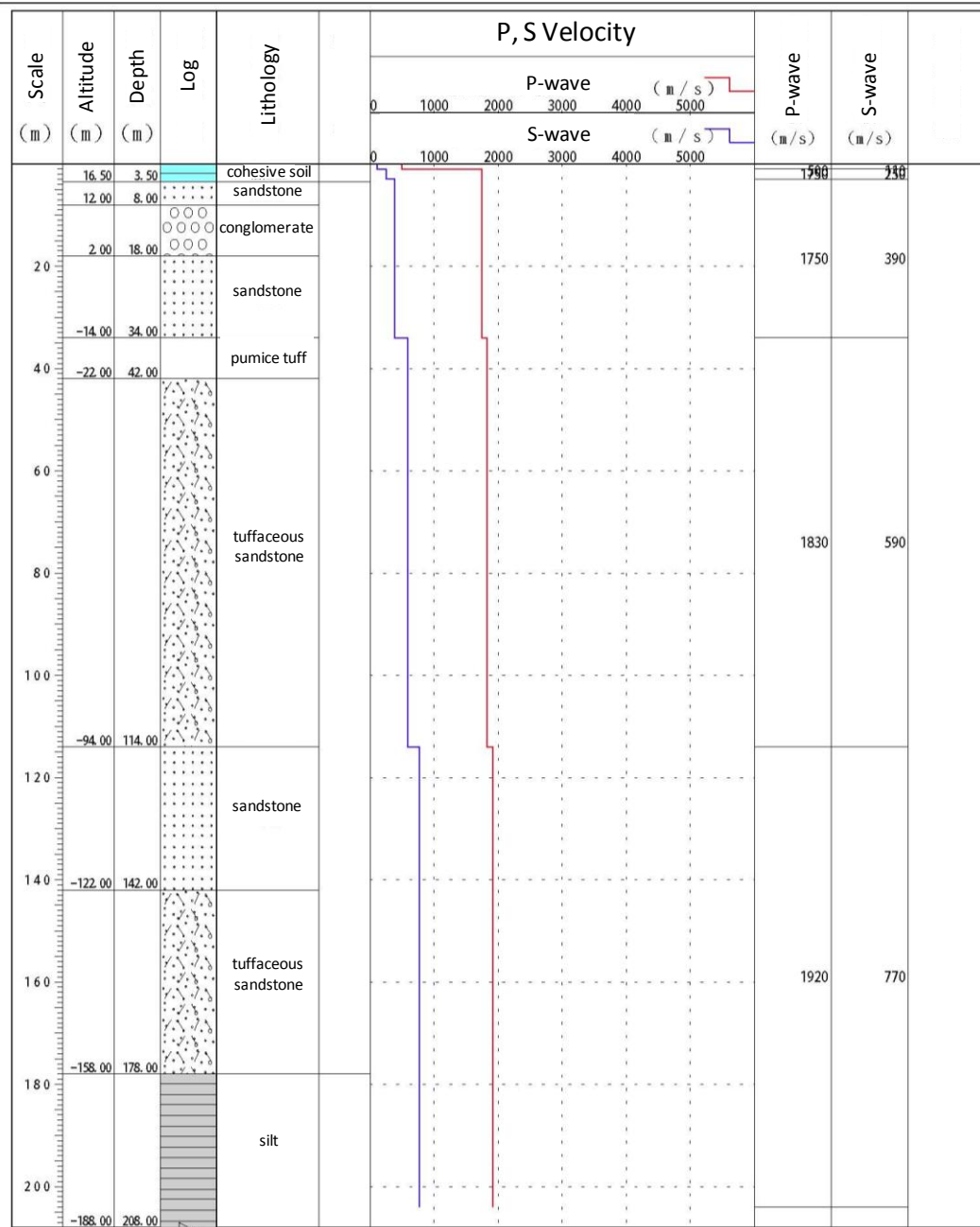
NIED 独立行政法人防災科学技術研究所

Copyright (c) National Research Institute for Earth Science and Disaster Prevention, All rights Reserved.

Figure A.9: Boring log reported by NIED Kik-Net database, for the **MYGH05** array (translated from the original Japanese version)

Station Point: YAMAMOTO
 Location: MIYAGI
 Latitude: 37° 56' 17.0"
 Altitude: +20m

Station Code: MYGH10
 Longitude: 140° 53' 45.0"
 Depth: 208.00m

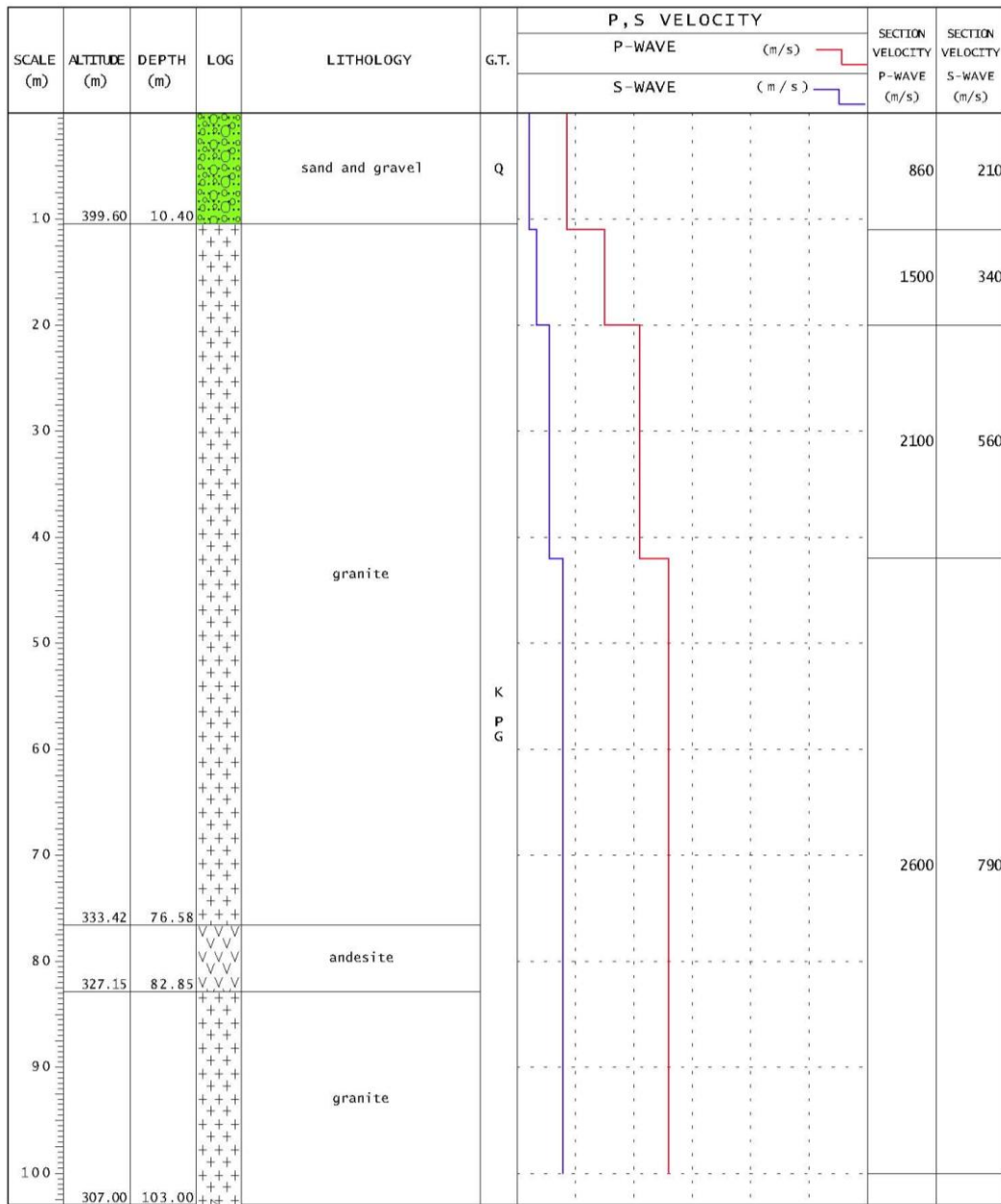


NIED 独立行政法人防災科学技術研究所
 Copyright (c) National Research Institute for Earth Science and Disaster Prevention. All rights Reserved.

Figure A.10: Boring log reported by NIED Kik-Net database, for the **MYGH10** array (translated from the original Japanese version)

Station Point: HINO
 Location : TOTTORIKEN HINOGUN HINOCHO SHIMOKUROSAKA 1251-2
 Latitude : 35 deg 14 ' 40.0 "
 Altitude : +410m

Station Code: TTRH02
 Longitude : 133 deg 23 ' 37.0 "
 Depth : 103.00m



NIED 独立行政法人防災科学技術研究所
 Copyright (c) National Research Institute for Earth Science and Disaster Prevention, All rights Reserved.

Figure A.11: Boring log reported by NIED Kik-Net database, for the TTRH02 array

A.2. Strong Ground Motions Utilized

Table A.1: Utilized strong motion records at each vertical array

Site	Date	Time	Distance (km)	Depth (km)	Magnitude	PGA _{base} (g)	
						EW	NS
FKSH19	11/16/2000	18:31:00	76.97	51	5.0	0.006	0.008
FKSH19	2/5/2001	4:17:00	20.57	77	4.3	0.005	0.008
FKSH19	10/2/2001	17:20:00	99.81	41	5.4	0.015	0.008
FKSH19	5/26/2003	18:24:00	170.61	71	7.0	0.025	0.015
FKSH19	1/23/2004	18:01:00	41.90	66	5.3	0.011	0.011
FKSH19	1/1/2005	5:14:00	78.88	89	5.0	0.021	0.013
FKSH19	8/16/2005	11:46:00	155.76	42	7.2	0.034	0.031
FKSH19	10/19/2005	20:44:00	123.79	48	6.3	0.005	0.005
FKSH19	10/22/2005	22:12:00	55.33	52	5.6	0.007	0.007
FKSH19	6/14/2008	8:43:00	174.07	8	7.2	0.010	0.021
FKSH19	7/24/2008	0:26:00	263.85	108	6.8	0.008	0.007
FKSH19	1/3/2009	16:13:00	59.65	51	4.8	0.005	0.006
FKSH19	2/1/2009	6:52:00	96.53	47	5.8	0.005	0.007
FKSH19	8/9/2009	19:56:00	526.72	333	6.8	0.003	0.004
FKSH19	3/13/2010	21:46:00	67.41	78	5.5	0.017	0.013
FKSH19	3/14/2010	17:08:00	99.91	40	6.7	0.016	0.010
FKSH19	6/13/2010	12:33:00	94.38	40	6.2	0.027	0.016
FKSH19	2/10/2011	22:03:00	69.11	48	5.4	0.004	0.007
FKSH19	3/11/2011	14:46:00	200.09	24	9.0	0.337	0.117
FKSH19	3/11/2011	14:54:00	53.07	36	5.8	0.017	0.009
FKSH19	3/11/2011	15:13:00	87.31	27	6.1	0.013	0.011
FKSH19	3/11/2011	15:15:00	158.45	43	7.7	0.009	0.008
FKSH19	3/11/2011	15:26:00	368.77	34	7.5	0.006	0.006
FKSH19	3/11/2011	16:29:00	220.28	36	6.5	0.005	0.007
FKSH19	3/11/2011	16:30:00	50.88	27	6.0	0.020	0.021
FKSH19	3/11/2011	17:41:00	52.03	27	6.1	0.027	0.023
FKSH19	3/12/2011	10:14:00	62.04	20	4.5	0.008	0.005
FKSH19	3/12/2011	22:15:00	68.39	40	6.2	0.008	0.013
FKSH19	3/14/2011	15:18:00	59.63	30	5.3	0.013	0.016
FKSH19	3/16/2011	13:14:00	85.67	20	5.6	0.013	0.011

Table A.1: Utilized strong motion records at each vertical array (cont'd)

Site	Date	Time	Distance (km)	Depth (km)	Magnitude	PGA _{base} (g)	
						EW	NS
FKSH19	3/17/2011	21:55:00	99.15	30	5.8	0.006	0.008
FKSH19	3/19/2011	18:56:00	77.37	5	6.1	0.013	0.016
FKSH19	3/20/2011	10:30:00	80.78	20	5.7	0.006	0.007
FKSH19	3/21/2011	4:54:00	45.49	30	4.7	0.009	0.009
FKSH19	3/22/2011	18:19:00	103.57	10	6.3	0.020	0.016
FKSH19	3/23/2011	7:12:00	43.00	8	6.0	0.010	0.005
FKSH19	3/23/2011	7:36:00	45.06	7	5.8	0.013	0.016
FKSH19	3/30/2011	22:19:00	88.59	50	5.0	0.003	0.007
FKSH19	4/3/2011	16:38:00	82.99	47	5.4	0.009	0.005
FKSH19	4/7/2011	23:32:00	132.73	66	7.1	0.045	0.034
FKSH19	4/9/2011	18:42:00	128.69	58	5.4	0.005	0.004
FKSH19	4/11/2011	17:16:00	58.27	6	7.0	0.025	0.026
FKSH19	4/11/2011	20:42:00	56.48	11	5.9	0.006	0.005
FKSH19	4/12/2011	14:07:00	46.78	15	6.4	0.033	0.033
FKSH19	4/18/2011	11:08:00	42.73	8	4.2	0.004	0.004
FKSH19	4/20/2011	4:29:00	60.53	47	4.4	0.006	0.004
FKSH19	4/22/2011	1:11:00	63.88	48	5.6	0.009	0.009
FKSH19	4/23/2011	0:25:00	52.74	21	5.4	0.005	0.006
FKSH19	4/28/2011	18:28:00	92.90	44	5.7	0.006	0.009
FKSH19	5/1/2011	11:48:00	42.48	29	4.6	0.005	0.007
FKSH19	5/17/2011	0:53:00	51.06	35	4.6	0.007	0.005
FKSH19	5/20/2011	16:28:00	66.48	41	5.2	0.007	0.006
FKSH19	6/4/2011	1:00:00	67.97	30	5.5	0.008	0.007
FKSH19	6/18/2011	20:31:00	97.54	28	6.0	0.013	0.015
FKSH19	6/20/2011	3:58:00	84.60	46	4.3	0.006	0.006
FKSH19	7/8/2011	3:35:00	54.15	55	5.6	0.014	0.012
FKSH19	7/25/2011	3:51:00	83.46	46	6.3	0.026	0.015
FKSH19	7/31/2011	3:54:00	76.36	57	6.5	0.027	0.027
FKSH19	8/12/2011	3:22:00	67.29	52	6.1	0.020	0.018
FKSH19	8/19/2011	14:36:00	96.18	51	6.5	0.016	0.017
FKSH19	10/10/2011	11:46:00	66.76	47	5.6	0.010	0.008
FKSH19	1/1/2012	14:28:00	700.28	397	7.0	0.005	0.005
FKSH19	1/23/2012	20:45:00	61.04	52	5.1	0.014	0.011
FKSH19	3/25/2012	22:22:00	97.78	50	5.2	0.005	0.008
FKSH19	4/1/2012	23:04:00	56.09	53	5.9	0.014	0.013
FKSH19	6/28/2012	14:52:00	51.07	60	5.2	0.005	0.004
FKSH20	11/16/2000	18:31:00	54.00	51	5.0	0.043	0.018
FKSH20	9/6/2001	10:40:00	45.00	52	4.5	0.010	0.025
FKSH20	10/2/2001	17:20:00	77.34	41	5.4	0.011	0.013
FKSH20	5/26/2003	18:24:00	158.63	71	7.0	0.033	0.034

Table A.1: Utilized strong motion records at each vertical array (cont'd)

Site	Date	Time	Distance (km)	Depth (km)	Magnitude	PGA _{base} (g)	
						EW	NS
FKSH20	11/12/2003	17:27:00	597.94	398	6.5	0.009	0.014
FKSH20	11/15/2003	3:44:00	118.56	48	5.8	0.007	0.010
FKSH20	1/23/2004	18:01:00	27.99	66	5.3	0.030	0.020
FKSH20	5/29/2004	12:47:00	92.75	38	5.9	0.013	0.012
FKSH20	1/1/2005	5:14:00	78.06	89	5.0	0.031	0.013
FKSH20	4/4/2005	2:57:00	68.60	44	5.3	0.012	0.018
FKSH20	8/16/2005	11:46:00	134.97	42	7.2	0.028	0.027
FKSH20	7/24/2008	0:26:00	255.74	108	6.8	0.012	0.017
FKSH20	2/1/2009	6:52:00	89.45	47	5.8	0.011	0.059
FKSH20	2/17/2009	9:13:00	41.42	48	4.9	0.022	0.021
FKSH20	2/21/2010	9:57:00	51.05	45	4.8	0.010	0.008
FKSH20	3/13/2010	21:46:00	44.71	78	5.5	0.018	0.060
FKSH20	3/14/2010	17:08:00	77.40	40	6.7	0.040	0.060
FKSH20	6/13/2010	12:33:00	71.82	40	6.2	0.035	0.063
FKSH20	2/10/2011	22:03:00	52.08	48	5.4	0.017	0.061
FKSH20	3/11/2011	14:46:00	177.97	24	9.0	0.399	0.174
FKSH20	3/11/2011	14:54:00	30.03	36	5.8	0.053	0.047
FKSH20	3/11/2011	15:15:00	155.39	43	7.7	0.017	0.024
FKSH20	3/11/2011	15:26:00	345.72	34	7.5	0.010	0.012
FKSH20	3/11/2011	16:30:00	29.06	27	6.0	0.050	0.046
FKSH20	3/11/2011	17:41:00	29.70	27	6.1	0.080	0.076
FKSH20	6/28/2012	14:52:00	37.02	60	5.2	0.018	0.068
IBRH11	8/15/2000	3:55:00	20.14	52	3.9	0.014	0.007
IBRH11	1/19/2001	8:11:00	43.17	57	3.8	0.007	0.007
IBRH11	3/6/2001	14:32:00	80.37	52	4.6	0.013	0.015
IBRH11	5/31/2001	8:59:00	35.78	55	4.5	0.007	0.011
IBRH11	7/20/2001	6:02:00	35.95	56	4.8	0.009	0.014
IBRH11	10/18/2001	6:30:00	40.37	49	4.3	0.017	0.014
IBRH11	2/12/2002	22:44:00	87.74	48	5.5	0.024	0.025
IBRH11	6/14/2002	11:42:00	22.34	57	4.9	0.020	0.033
IBRH11	7/13/2002	21:45:00	41.06	65	4.8	0.006	0.004
IBRH11	7/27/2002	17:59:00	43.82	58	4.5	0.008	0.010
IBRH11	3/13/2003	12:13:00	40.03	47	4.8	0.012	0.011
IBRH11	5/12/2003	0:57:00	55.71	47	5.2	0.004	0.005
IBRH11	5/26/2003	18:24:00	303.36	71	7.0	0.007	0.006
IBRH11	8/4/2003	20:57:00	43.04	58	4.9	0.014	0.016
IBRH11	9/20/2003	12:55:00	128.58	70	5.8	0.003	0.004
IBRH11	11/12/2003	17:27:00	453.36	398	6.5	0.005	0.005
IBRH11	1/27/2004	2:43:00	130.31	56	3.7	0.005	0.010
IBRH11	4/4/2004	8:02:00	90.81	49	5.8	0.007	0.007

Table A.1: Utilized strong motion records at each vertical array (cont'd)

Site	Date	Time	Distance (km)	Depth (km)	Magnitude	PGA _{base} (g)	
						EW	NS
IBRH11	7/10/2004	20:07:00	39.26	48	4.7	0.011	0.011
IBRH11	10/6/2004	23:40:00	42.39	66	5.7	0.018	0.012
IBRH11	11/6/2004	10:25:00	35.55	58	3.9	0.009	0.008
IBRH11	1/1/2005	5:14:00	88.22	89	5.0	0.010	0.008
IBRH11	2/8/2005	11:29:00	25.72	67	4.8	0.007	0.006
IBRH11	2/16/2005	4:46:00	42.97	45	5.4	0.013	0.014
IBRH11	4/4/2005	2:57:00	181.86	44	5.3	0.004	0.004
IBRH11	5/14/2005	0:14:00	39.83	57	4.4	0.007	0.009
IBRH11	7/28/2005	19:15:00	37.74	51	5.0	0.014	0.013
IBRH11	10/16/2005	16:05:00	40.87	47	5.1	0.009	0.014
IBRH11	6/2/2007	14:43:00	27.73	50	4.6	0.014	0.016
IBRH11	3/8/2008	1:55:00	43.28	57	5.2	0.020	0.015
IBRH11	4/4/2008	19:02:00	39.27	53	5.0	0.006	0.007
IBRH11	5/8/2008	1:45:00	132.39	51	7.0	0.020	0.061
IBRH11	7/5/2008	16:49:00	78.75	50	5.2	0.019	0.026
IBRH11	8/20/2008	15:13:00	40.64	45	4.6	0.006	0.010
IBRH11	8/22/2008	19:59:00	43.32	56	5.2	0.016	0.021
IBRH11	2/1/2009	6:52:00	108.86	47	5.8	0.021	0.061
IBRH11	8/9/2009	19:56:00	393.66	333	6.8	0.021	0.061
IBRH11	10/16/2009	6:56:00	41.56	56	3.9	0.004	0.008
IBRH11	12/18/2009	5:41:00	37.98	78	5.1	0.005	0.005
IBRH11	2/22/2010	18:53:00	40.23	56	4.4	0.007	0.009
IBRH11	3/14/2010	17:08:00	211.86	40	6.7	0.022	0.062
IBRH11	6/13/2010	12:33:00	186.37	40	6.2	0.022	0.062
IBRH11	8/3/2010	7:31:00	43.95	82	4.6	0.008	0.006
IBRH11	10/24/2010	13:50:00	42.99	45	4.4	0.013	0.012
IBRH11	3/11/2011	14:46:00	308.59	24	9.0	0.156	0.222
IBRH11	3/11/2011	15:15:00	104.93	43	7.7	0.035	0.035
IBRH11	3/11/2011	15:26:00	452.03	34	7.5	0.009	0.009
IBRH11	3/11/2011	17:41:00	157.46	27	6.1	0.023	0.062
IBRH11	3/12/2011	4:45:00	187.34	30	5.2	0.009	0.009
IBRH11	3/14/2011	10:02:00	88.72	32	6.2	0.013	0.012
IBRH11	3/14/2011	15:52:00	111.62	40	5.2	0.006	0.004
IBRH11	3/16/2011	12:52:00	90.54	10	6.1	0.023	0.062
IBRH11	3/16/2011	13:14:00	187.34	20	5.6	0.006	0.005
IBRH11	3/17/2011	21:55:00	110.06	30	5.8	0.010	0.009
IBRH11	3/19/2011	18:56:00	60.12	5	6.1	0.024	0.062
IBRH11	3/22/2011	18:19:00	194.15	10	6.3	0.023	0.062
IBRH11	3/23/2011	7:12:00	98.30	8	6.0	0.023	0.062
IBRH11	3/23/2011	7:36:00	95.62	7	5.8	0.023	0.062

Table A.1: Utilized strong motion records at each vertical array (cont'd)

Site	Date	Time	Distance (km)	Depth (km)	Magnitude	PGA _{base} (g)	
						EW	NS
IBRH11	3/24/2011	8:56:00	22.88	52	4.8	0.027	0.015
IBRH11	3/30/2011	22:19:00	85.29	50	5.0	0.014	0.010
IBRH11	4/2/2011	16:56:00	23.90	54	5.0	0.013	0.016
IBRH11	4/4/2011	20:46:00	28.24	49	4.1	0.005	0.006
IBRH11	4/7/2011	23:32:00	257.82	66	7.1	0.011	0.014
IBRH11	4/9/2011	3:57:00	23.22	52	4.1	0.011	0.011
IBRH11	4/9/2011	17:02:00	16.09	54	4.3	0.007	0.009
IBRH11	4/11/2011	6:36:00	99.54	53	5.1	0.011	0.008
IBRH11	4/11/2011	17:16:00	79.89	6	7.0	0.030	0.062
IBRH11	4/11/2011	18:05:00	86.81	12	5.1	0.023	0.062
IBRH11	4/11/2011	20:42:00	79.72	11	5.9	0.008	0.007
IBRH11	4/12/2011	8:08:00	118.19	26	6.4	0.004	0.004
IBRH11	4/12/2011	14:07:00	88.39	15	6.4	0.014	0.013
IBRH11	4/13/2011	10:08:00	79.20	5	5.7	0.009	0.012
IBRH11	4/14/2011	12:09:00	88.70	11	5.4	0.005	0.004
IBRH11	4/16/2011	11:19:00	17.72	79	5.9	0.032	0.023
IBRH11	4/19/2011	23:10:00	37.16	53	5.0	0.015	0.013
IBRH11	4/26/2011	21:12:00	34.67	46	5.0	0.010	0.014
IBRH11	5/20/2011	17:53:00	42.40	64	4.6	0.005	0.005
IBRH11	5/28/2011	11:14:00	42.65	56	4.4	0.010	0.015
IBRH11	7/8/2011	3:35:00	119.75	55	5.6	0.005	0.005
IBRH11	7/10/2011	9:57:00	350.98	34	7.3	0.005	0.004
IBRH11	7/15/2011	21:01:00	23.25	66	5.4	0.013	0.011
IBRH11	7/31/2011	3:54:00	113.25	57	6.5	0.023	0.062
IBRH11	8/12/2011	3:22:00	112.88	52	6.1	0.023	0.062
IBRH11	8/17/2011	9:23:00	48.29	78	4.3	0.003	0.003
IBRH11	8/19/2011	0:39:00	24.45	50	4.0	0.006	0.014
IBRH11	8/19/2011	14:36:00	204.78	51	6.5	0.006	0.007
IBRH11	9/10/2011	15:00:00	49.96	53	4.8	0.009	0.006
IBRH11	9/21/2011	22:30:00	56.71	9	5.2	0.005	0.006
IBRH11	11/20/2011	10:23:00	55.22	9	5.3	0.005	0.004
IBRH11	1/1/2012	14:28:00	568.18	397	7.0	0.006	0.006
IBRH11	1/17/2012	12:30:00	41.94	46	4.7	0.005	0.004
IBRH11	2/19/2012	14:54:00	58.44	7	5.2	0.007	0.005
IBRH11	2/28/2012	14:20:00	76.29	23	5.1	0.003	0.008
IBRH11	3/1/2012	7:32:00	44.12	56	5.3	0.019	0.021
IBRH11	3/10/2012	2:25:00	57.38	7	5.4	0.007	0.005
IBRH11	3/14/2012	21:05:00	99.10	15	6.1	0.009	0.010
IBRH11	4/1/2012	23:04:00	118.53	53	5.9	0.006	0.007
IBRH11	5/18/2012	17:18:00	37.27	51	4.8	0.008	0.009

Table A.1: Utilized strong motion records at each vertical array (cont'd)

Site	Date	Time	Distance (km)	Depth (km)	Magnitude	PGA _{base} (g)	
						EW	NS
IBRH11	5/18/2012	17:19:00	28.42	50	4.8	0.008	0.009
IBRH11	5/29/2012	1:36:00	63.15	80	5.2	0.006	0.003
IBRH11	6/1/2012	17:48:00	36.67	50	5.2	0.008	0.007
IBRH11	6/17/2012	16:13:00	22.41	50	4.6	0.022	0.014
IBRH13	8/4/2003	20:57:00	39.49	58	4.9	0.007	0.004
IBRH13	7/5/2008	16:49:00	37.51	50	5.2	0.013	0.012
IBRH13	8/3/2010	7:31:00	24.39	82	4.6	0.005	0.008
IBRH13	3/11/2011	14:46:00	248.60	24	9.0	0.110	0.116
IBRH13	3/11/2011	14:54:00	102.95	36	5.8	0.180	0.121
IBRH13	3/11/2011	15:15:00	98.09	43	7.7	0.022	0.023
IBRH13	3/14/2011	10:02:00	61.61	32	6.2	0.022	0.015
IBRH13	3/19/2011	8:49:00	10.72	10	5.3	0.035	0.076
IBRH13	3/19/2011	18:56:00	1.47	5	6.1	0.106	0.210
IBRH13	3/23/2011	7:12:00	37.07	8	6.0	0.009	0.008
IBRH13	3/23/2011	7:36:00	34.39	7	5.8	0.062	0.035
IBRH13	3/30/2011	22:19:00	38.80	50	5.0	0.009	0.007
IBRH13	4/2/2011	19:22:00	2.89	6	4.4	0.033	0.039
IBRH13	4/5/2011	18:08:00	1.71	7	4.4	0.064	0.021
IBRH13	4/6/2011	21:56:00	7.24	7	4.9	0.018	0.018
IBRH13	4/7/2011	23:32:00	196.39	66	7.1	0.009	0.010
IBRH13	4/11/2011	17:16:00	18.70	6	7.0	0.108	0.066
IBRH13	4/11/2011	18:05:00	25.41	12	5.1	0.007	0.008
IBRH13	4/11/2011	18:36:00	14.84	8	4.8	0.011	0.007
IBRH13	4/11/2011	20:42:00	19.55	11	5.9	0.013	0.016
IBRH13	4/12/2011	14:07:00	29.17	15	6.4	0.025	0.041
IBRH13	4/13/2011	10:08:00	17.66	5	5.7	0.030	0.026
IBRH13	4/14/2011	7:35:00	1.94	9	5.1	0.113	0.105
IBRH13	4/30/2011	5:21:00	4.70	10	3.7	0.009	0.018
IBRH13	5/5/2011	0:09:00	2.95	7	4.1	0.058	0.022
IBRH13	5/5/2011	19:20:00	5.91	8	4.5	0.013	0.021
IBRH13	5/14/2011	1:28:00	6.44	6	4.3	0.010	0.013
IBRH13	5/26/2011	19:56:00	9.49	6	4.8	0.011	0.013
IBRH13	7/31/2011	3:54:00	58.44	57	6.5	0.043	0.031
IBRH13	8/7/2011	12:33:00	7.62	7	4.7	0.014	0.009
IBRH13	8/12/2011	3:22:00	55.31	52	6.1	0.015	0.021
IBRH13	8/14/2011	16:38:00	5.56	9	4.3	0.010	0.014
IBRH13	8/16/2011	19:16:00	1.99	10	4.6	0.043	0.052
IBRH13	8/27/2011	11:35:00	10.72	20	4.3	0.011	0.010
IBRH13	9/21/2011	22:30:00	10.38	10	5.3	0.054	0.063
IBRH13	11/5/2011	0:45:00	1.99	10	4.2	0.039	0.060

Table A.1: Utilized strong motion records at each vertical array (cont'd)

Site	Date	Time	Distance (km)	Depth (km)	Magnitude	PGA _{base} (g)	
						EW	NS
IWTH26	5/26/2003	18:24:00	61.68	71	7.0	0.096	0.077
IWTH26	7/26/2003	7:13:00	64.49	12	6.2	0.020	0.012
IWTH26	8/16/2005	11:46:00	143.94	42	7.2	0.045	0.047
IWTH26	6/14/2008	8:43:00	12.05	8	7.2	0.208	0.268
IWTH26	6/14/2008	11:55:00	10.27	9	3.8	0.012	0.047
IWTH26	6/14/2008	23:42:00	9.69	10	4.8	0.011	0.024
IWTH26	6/16/2008	23:14:00	13.92	11	5.3	0.043	0.049
IWTH26	7/24/2008	0:26:00	101.08	108	6.8	0.039	0.042
IWTH26	6/3/2010	7:39:00	13.92	7	4.4	0.013	0.009
IWTH26	7/4/2010	4:33:00	9.49	7	5.2	0.047	0.036
IWTH26	3/11/2011	14:46:00	188.57	24	9.0	0.118	0.081
IWTH26	3/11/2011	16:29:00	111.17	36	6.5	0.014	0.015
IWTH26	3/24/2011	17:21:00	118.19	34	6.2	0.015	0.013
IWTH26	3/31/2011	16:15:00	94.66	47	6.1	0.014	0.020
IWTH26	4/7/2011	23:32:00	117.07	66	7.1	0.137	0.093
KSRH06	4/29/2003	20:43:00	29.45	97	4.2	0.009	0.011
KSRH06	9/11/2003	4:32:00	74.54	97	4.9	0.012	0.009
KSRH06	9/26/2003	4:50:00	162.43	42	8.0	0.114	0.107
KSRH06	9/26/2003	8:11:00	64.54	46	4.8	0.010	0.010
KSRH06	9/27/2003	17:06:00	54.19	59	5.2	0.013	0.010
KSRH06	10/8/2003	18:07:00	75.18	51	6.4	0.009	0.011
KSRH06	10/20/2003	8:27:00	63.47	96	4.7	0.008	0.009
KSRH06	4/12/2004	3:06:00	62.82	47	5.8	0.021	0.027
KSRH06	4/12/2004	14:15:00	66.93	48	4.8	0.015	0.009
KSRH06	11/29/2004	3:32:00	74.92	48	7.1	0.160	0.194
KSRH06	11/30/2004	14:55:00	76.20	48	4.3	0.016	0.008
KSRH06	12/6/2004	23:15:00	84.85	46	6.9	0.103	0.112
KSRH06	1/18/2005	23:09:00	59.98	50	6.4	0.043	0.034
KSRH06	3/12/2005	3:47:00	41.75	61	5.1	0.032	0.023
KSRH06	5/19/2005	1:33:00	40.66	58	4.8	0.017	0.011
KSRH06	9/21/2005	11:25:00	167.84	103	6.0	0.015	0.010
KSRH06	1/10/2006	10:21:00	70.54	85	4.2	0.007	0.005
KSRH06	7/1/2007	13:12:00	52.90	132	5.8	0.016	0.014
KSRH06	4/28/2009	20:21:00	88.40	38	5.4	0.063	0.049
KSRH06	12/28/2009	9:13:00	17.98	85	5.0	0.065	0.049
KSRH06	4/9/2010	3:41:00	41.02	57	4.8	0.065	0.050
KSRH06	9/4/2010	6:15:00	102.78	61	5.1	0.066	0.050
KSRH06	6/14/2011	21:49:00	76.25	73	5.1	0.067	0.050
KSRH07	4/27/2001	2:49:00	126.16	83	5.9	0.014	0.015
KSRH07	12/1/2002	18:57:00	60.17	103	5.4	0.010	0.007

Table A.1: Utilized strong motion records at each vertical array (cont'd)

Site	Date	Time	Distance (km)	Depth (km)	Magnitude	PGA _{base} (g)	
						EW	NS
KSRH07	9/11/2003	4:32:00	62.13	97	4.9	0.038	0.042
KSRH07	9/26/2003	4:50:00	151.80	42	8.0	0.196	0.218
KSRH07	9/27/2003	17:06:00	44.26	59	5.2	0.019	0.020
KSRH07	9/29/2003	11:37:00	87.86	43	6.5	0.015	0.017
KSRH07	10/8/2003	18:07:00	68.94	51	6.4	0.009	0.009
KSRH07	4/12/2004	3:06:00	63.53	47	5.8	0.014	0.012
KSRH07	6/7/2004	13:14:00	66.34	78	4.9	0.017	0.017
KSRH07	11/11/2004	19:03:00	117.76	39	6.3	0.015	0.009
KSRH07	11/29/2004	3:32:00	79.49	48	7.1	0.055	0.045
KSRH07	12/6/2004	23:15:00	88.28	46	6.9	0.030	0.040
KSRH07	1/18/2005	23:09:00	61.63	50	6.4	0.024	0.021
KSRH07	5/19/2005	1:33:00	39.57	58	4.8	0.012	0.014
KSRH07	7/1/2007	13:12:00	65.30	132	5.8	0.019	0.013
KSRH07	7/24/2008	0:26:00	439.82	108	6.8	0.012	0.013
KSRH07	3/20/2009	15:52:00	61.58	64	5.0	0.012	0.011
KSRH07	7/8/2010	21:23:00	64.33	59	4.7	0.020	0.014
KSRH07	6/14/2011	21:49:00	83.61	73	5.1	0.013	0.028
KSRH10	12/11/2001	18:40:00	71.52	69	4.6	0.007	0.013
KSRH10	8/30/2003	9:31:00	34.65	47	4.7	0.010	0.004
KSRH10	9/26/2003	4:50:00	180.52	42	8.0	0.096	0.128
KSRH10	10/8/2003	18:07:00	80.34	51	6.4	0.010	0.015
KSRH10	4/12/2004	3:06:00	43.25	47	5.8	0.027	0.027
KSRH10	4/12/2004	14:15:00	37.62	48	4.8	0.019	0.014
KSRH10	11/29/2004	3:32:00	31.93	48	7.1	0.069	0.095
KSRH10	11/29/2004	17:00:00	34.28	48	4.9	0.010	0.009
KSRH10	7/12/2004	11:31:00	36.49	48	4.3	0.011	0.009
KSRH10	12/22/2004	0:34:00	44.76	45	5.7	0.019	0.020
KSRH10	1/18/2005	23:09:00	37.97	50	6.4	0.022	0.028
KSRH10	1/28/2005	4:49:00	36.56	48	4.5	0.017	0.017
KSRH10	3/12/2005	3:47:00	30.26	61	5.1	0.011	0.017
KSRH10	6/16/2005	23:42:00	48.26	43	4.7	0.014	0.008
KSRH10	9/21/2005	11:25:00	117.43	103	6.0	0.010	0.012
KSRH10	7/1/2007	13:12:00	40.86	132	5.8	0.018	0.027
KSRH10	4/28/2009	20:21:00	69.14	38	5.4	0.018	0.032
MYGH05	12/2/2001	22:02:00	100.48	122	6.4	0.017	0.018
MYGH05	5/26/2003	18:24:00	82.10	71	7.0	0.177	0.240
MYGH05	7/26/2003	0:13:00	37.00	12	5.5	0.021	0.024
MYGH05	7/26/2003	7:13:00	38.91	12	6.2	0.041	0.031
MYGH05	8/16/2005	11:46:00	138.93	42	7.2	0.064	0.041
MYGH05	10/8/2010	15:53:00	15.53	10	4.2	0.016	0.014

Table A.1: Utilized strong motion records at each vertical array (cont'd)

Site	Date	Time	Distance (km)	Depth (km)	Magnitude	PGA _{base} (g)	
						EW	NS
MYGH05	3/11/2011	14:46:00	188.87	24	9.0	0.193	0.148
MYGH05	3/11/2011	15:06:00	149.38	27	6.4	0.020	0.025
MYGH05	3/11/2011	16:29:00	139.44	36	6.5	0.054	0.058
MYGH05	3/11/2011	20:37:00	172.19	24	6.7	0.027	0.022
MYGH05	3/12/2011	15:19:00	164.24	10	5.4	0.079	0.099
MYGH05	3/24/2011	17:21:00	147.53	34	6.2	0.080	0.100
MYGH05	4/7/2011	23:32:00	107.67	66	7.1	0.144	0.167
MYGH10	10/2/2001	17:20:00	83.60	41	5.4	0.009	0.009
MYGH10	12/2/2001	22:02:00	165.37	122	6.4	0.017	0.014
MYGH10	5/26/2003	18:24:00	118.14	71	7.0	0.071	0.066
MYGH10	7/26/2003	0:13:00	59.68	12	5.5	0.010	0.012
MYGH10	7/26/2003	7:13:00	57.04	12	6.2	0.021	0.018
MYGH10	1/23/2004	18:01:00	77.89	66	5.3	0.018	0.017
MYGH10	8/16/2005	11:46:00	122.95	42	7.2	0.087	0.054
MYGH10	10/22/2005	22:12:00	97.58	52	5.6	0.025	0.016
MYGH10	6/14/2008	8:43:00	121.21	8	7.2	0.047	0.044
MYGH10	7/24/2008	0:26:00	209.39	108	6.8	0.030	0.021
MYGH10	2/17/2009	9:13:00	67.74	48	4.9	0.010	0.012
MYGH10	3/13/2010	21:46:00	61.91	78	5.5	0.051	0.017
MYGH10	3/14/2010	17:08:00	84.01	40	6.7	0.028	0.026
MYGH10	6/13/2010	12:33:00	99.25	40	6.2	0.037	0.044
MYGH10	3/11/2011	14:46:00	172.67	24	9.0	0.172	0.238
MYGH10	3/11/2011	14:54:00	61.66	36	5.8	0.025	0.029
MYGH10	3/11/2011	14:58:00	93.43	23	6.4	0.022	0.018
MYGH10	3/11/2011	15:06:00	179.01	27	6.4	0.013	0.015
MYGH10	3/11/2011	15:13:00	105.67	27	6.1	0.022	0.023
MYGH10	3/11/2011	15:15:00	206.05	43	7.7	0.011	0.013
MYGH10	3/11/2011	15:26:00	350.57	34	7.5	0.014	0.014
MYGH10	3/11/2011	17:41:00	67.83	27	6.1	0.032	0.051
MYGH10	3/12/2011	22:15:00	94.50	40	6.2	0.051	0.021
MYGH10	3/22/2011	18:19:00	106.42	10	6.3	0.051	0.021
MYGH10	3/24/2011	17:21:00	179.20	34	6.2	0.051	0.023
MYGH10	3/28/2011	7:24:00	133.61	31	6.5	0.019	0.015
MYGH10	4/3/2011	16:38:00	74.54	47	5.4	0.051	0.040
MYGH10	4/6/2011	22:55:00	68.10	46	5.3	0.051	0.025
MYGH10	4/7/2011	23:32:00	94.03	66	7.1	0.118	0.121
MYGH10	4/9/2011	18:42:00	86.97	58	5.4	0.013	0.013
MYGH10	4/11/2011	17:16:00	112.24	6	7.0	0.027	0.027
MYGH10	4/12/2011	14:07:00	101.09	15	6.4	0.012	0.009
MYGH10	4/16/2011	13:20:00	68.54	46	4.4	0.008	0.010

Table A.1: Utilized strong motion records at each vertical array (cont'd)

Site	Date	Time	Distance (km)	Depth (km)	Magnitude	PGA _{base} (g)	
						EW	NS
MYGH10	4/22/2011	1:11:00	67.98	48	5.6	0.024	0.027
MYGH10	4/23/2011	0:25:00	89.43	21	5.4	0.026	0.014
MYGH10	4/28/2011	18:28:00	96.98	44	5.7	0.018	0.023
MYGH10	5/8/2011	19:43:00	68.41	46	4.7	0.011	0.013
MYGH10	5/15/2011	8:51:00	67.68	48	5.1	0.009	0.011
MYGH10	5/20/2011	16:28:00	74.51	41	5.2	0.010	0.011
MYGH10	6/18/2011	20:31:00	88.38	28	6.0	0.051	0.021
MYGH10	6/23/2011	19:35:00	85.30	57	5.3	0.010	0.007
MYGH10	6/30/2011	19:22:00	89.70	43	4.8	0.005	0.009
MYGH10	7/8/2011	3:35:00	95.65	55	5.6	0.014	0.016
MYGH10	7/25/2011	3:51:00	68.79	46	6.3	0.048	0.069
MYGH10	7/31/2011	3:54:00	118.61	57	6.5	0.026	0.025
MYGH10	8/12/2011	3:22:00	110.27	52	6.1	0.020	0.018
MYGH10	8/19/2011	14:36:00	85.16	51	6.5	0.053	0.063
MYGH10	10/10/2011	11:46:00	70.31	47	5.6	0.051	0.029
MYGH10	3/25/2012	22:22:00	83.37	50	5.2	0.052	0.022
MYGH10	3/30/2012	13:38:00	68.87	46	5.1	0.013	0.014
MYGH10	4/1/2012	23:04:00	97.90	53	5.9	0.021	0.016
MYGH10	6/28/2012	14:52:00	86.22	60	5.2	0.026	0.015
TTRH02	10/6/2000	13:30:00	6.47	11	7.3	0.610	0.410
TTRH02	10/9/2000	1:14:00	1.26	13	3.4	0.024	0.027
TTRH02	10/17/2000	22:17:00	5.63	12	4.2	0.032	0.051
TTRH02	10/28/2000	20:08:00	6.55	9	3.3	0.016	0.036
TTRH02	11/5/2000	3:00:00	5.72	12	3.8	0.037	0.027
TTRH02	11/7/2000	0:38:00	0.21	7	3.3	0.023	0.022
TTRH02	1/16/2001	18:06:00	6.12	9	3.4	0.026	0.045
TTRH02	3/6/2002	7:12:00	7.76	15	4.5	0.011	0.014
La Cienega	10/16/1999	2:46:45	203.90	6	7.1	0.012	0.014
La Cienega	9/9/2001	4:59:18	4.30	7.9	4.0	0.160	0.240
La Cienega	1/23/2009	7:42:44	10.30	7	3.4	0.001	0.004
La Cienega	3/16/2010	4:04:00	28.60	18	4.4	0.004	0.005
Lotung	11/7/1985	5:25:00	60.69	46	4.9	0.010	0.010
Lotung	1/16/1986	13:04:00	58.38	46	6.1	0.170	0.180
Lotung	3/29/1986	7:17:00	79.04	46	3.9	0.020	0.020
Lotung	4/8/1986	2:15:00	103.91	46	4.9	0.010	0.010
Lotung	5/20/1986	5:26:00	141.58	46	6.2	0.080	0.010
Lotung	7/11/1986	18:25:00	78.12	46	3.7	0.030	0.020
Lotung	7/16/1986	23:50:00	79.94	46	3.7	0.010	0.020
Lotung	7/17/1986	12:03:00	73.23	46	4.3	0.050	0.060

A.3. Supplementary Documentation

Table A.2: Percentage contribution of each array to the overall residual depicted in *FIGURE 6.16* – EQL method

γ_{\max} (%)	from	to	Percentage Contribution (%)													Total Number of Motions	
			FKSH20	IWTH26	TTRH02	Lotung	FKSH19	IBRH11	IBRH13	KSRH10	KSRH06	KSRH07	MYGH05	MYGH10	La Cienega		
0.001	0.002	-	-	-	-	-	-	-	16.7	-	-	-	-	-	33.3	50.0	6
0.002	0.003	8.7	-	-	-	34.8	8.7	-	-	-	-	-	4.3	43.5	-	-	23
0.003	0.004	5.6	-	-	2.8	44.4	13.9	-	6.9	1.4	-	-	1.4	23.6	-	-	72
0.004	0.007	11.9	-	0.7	3.5	20.3	37.1	1.4	6.3	3.5	2.8	0.7	11.9	-	-	-	143
0.007	0.011	5.0	1.7	3.9	1.1	17.9	34.1	5.0	3.4	5.6	2.2	6.1	14.0	-	-	-	179
0.011	0.017	5.3	1.8	3.5	0.9	11.4	31.6	13.2	1.8	11.4	7.0	-	10.5	1.8	-	-	114
0.017	0.027	9.7	5.4	1.1	1.1	9.7	26.9	12.9	3.2	4.3	8.6	4.3	12.9	-	-	-	93
0.027	0.043	3.6	5.5	1.8	1.8	10.9	21.8	20.0	5.5	5.5	12.7	3.6	7.3	-	-	-	55
0.043	0.069	5.6	16.7	-	-	5.6	11.1	16.7	5.6	16.7	11.1	-	5.6	5.6	5.6	5.6	18
0.069	0.110	-	11.8	-	5.9	-	5.9	41.2	5.9	5.9	-	5.9	11.8	5.9	11.8	5.9	17
0.110	0.220	5.6	16.7	-	16.7	-	-	11.1	11.1	5.6	11.1	16.7	5.6	-	-	-	18
0.220	0.440	-	20.0	-	-	-	-	40.0	10.0	10.0	10.0	-	10.0	-	10.0	-	10
0.440	0.880	-	12.5	-	-	25.0	-	25.0	-	12.5	12.5	12.5	-	-	-	-	8
0.880	2.000	10.0	20.0	-	-	-	10.0	20.0	-	30.0	10.0	-	-	-	-	-	10
2.000	10.000	-	36.4	18.2	-	-	9.1	27.3	-	-	-	9.1	-	-	-	-	11

Table A.3: Percentage contribution of each array to the overall residual depicted in *FIGURE 6.16* – EQL-FD method

Y _{max} (%)		Percentage Contribution (%)													Total Number of Motions
from	to	FKSH20	IWTH26	TTRH02	Lotung	FKSH19	IBRH11	IBRH13	KSRH10	KSRH06	KSRH07	MYGH05	MYGH10	La Cienega	
0.001	0.002	-	-	-	-	-	-	-	25.0	-	-	-	-	75.0	4
0.002	0.003	10.0	-	-	-	30.0	-	-	-	-	-	5.0	55.0	-	20
0.003	0.004	4.1	-	-	2.7	45.9	13.5	-	8.1	-	-	1.4	24.3	-	74
0.004	0.007	12.4	-	0.8	3.9	24.8	31.8	1.6	5.4	3.1	2.3	0.8	13.2	-	129
0.007	0.011	5.8	1.2	3.5	1.2	15.7	37.2	3.5	4.1	7.6	2.9	5.8	11.6	-	172
0.011	0.017	4.3	1.7	3.4	0.9	11.1	34.2	12.8	1.7	6.0	6.8	0.9	14.5	1.7	117
0.017	0.027	10.7	5.8	1.9	1.0	6.8	26.2	16.5	2.9	8.7	7.8	2.9	8.7	-	103
0.027	0.043	4.3	4.3	2.1	2.1	12.8	21.3	10.6	6.4	4.3	14.9	4.3	12.8	-	47
0.043	0.069	3.8	7.7	-	-	19.2	23.1	11.5	3.8	11.5	3.8	-	7.7	7.7	26
0.069	0.110	-	12.0	-	4.0	-	12.0	44.0	4.0	8.0	4.0	4.0	8.0	-	25
0.110	0.220	7.1	21.4	-	7.1	-	7.1	21.4	7.1	-	14.3	7.1	7.1	-	14
0.220	0.440	-	23.1	-	7.7	7.7	-	7.7	15.4	15.4	7.7	15.4	-	-	13
0.440	0.880	-	14.3	-	14.3	14.3	-	14.3	-	-	14.3	28.6	-	-	7
0.880	2.000	-	-	10.0	-	-	-	40.0	-	40.0	-	-	10.0	-	10
2.000	10.000	6.3	37.5	6.3	-	-	12.5	25.0	-	-	6.3	6.3	-	-	16

Table A.4: Percentage contribution of each array to the overall residual depicted in *FIGURE 6.16* – NL method

Y_{\max} (%)	from	to	Percentage Contribution (%)														Total Number of Motions			
			FKSH20	IWTH26	TTRH02	Lotung	FKSH19	IBRH11	IBRH13	KSRH10	KSRH06	KSRH07	MYGH05	MYGH10	La Cienega					
0.001	0.002	-	-	-	-	-	-	-	11.1	-	-	-	-	-	-	-	-	66.7	22.2	9
0.002	0.003	6.7	-	-	-	40.0	10.0	-	3.3	-	-	-	-	-	6.7	-	-	33.3	-	30
0.003	0.004	8.1	-	-	1.2	46.5	12.8	1.2	5.8	1.2	-	-	-	1.2	1.2	-	-	22.1	-	86
0.004	0.007	11.3	-	1.4	2.8	18.4	36.9	2.1	5.0	4.3	1.4	-	-	2.8	13.5	-	-	13.5	-	141
0.007	0.011	3.7	2.1	3.2	1.6	16.6	35.3	5.3	4.3	7.5	3.7	-	-	3.7	12.8	-	-	12.8	-	187
0.011	0.017	6.5	0.9	3.7	1.9	6.5	34.6	16.8	0.9	9.3	8.4	-	-	0.9	7.5	1.9	-	7.5	-	107
0.017	0.027	10.8	6.0	1.2	1.2	10.8	24.1	13.3	3.6	3.6	8.4	-	-	3.6	13.3	-	-	13.3	-	83
0.027	0.043	-	8.5	2.1	2.1	10.6	23.4	12.8	6.4	6.4	12.8	-	-	4.3	6.4	4.3	-	6.4	4.3	47
0.043	0.069	-	7.1	-	-	-	14.3	21.4	7.1	21.4	14.3	-	-	7.1	7.1	-	-	7.1	-	14
0.069	0.110	-	30.8	-	-	-	-	46.2	7.7	-	-	-	-	7.7	7.7	-	-	7.7	-	13
0.110	0.220	6.3	18.8	-	18.8	6.3	-	25.0	6.3	-	12.5	-	-	6.3	-	-	-	-	-	16
0.220	0.440	-	12.5	-	6.3	-	-	18.8	12.5	12.5	6.3	-	-	18.8	12.5	-	-	12.5	-	16
0.440	0.880	-	7.7	-	-	7.7	15.4	30.8	-	23.1	15.4	-	-	-	-	-	-	-	-	13
0.880	2.000	-	33.3	-	-	-	-	50.0	-	16.7	-	-	-	-	-	-	-	-	-	6
2.000	10.000	16.7	50.0	33.3	-	-	-	-	-	-	-	-	-	-	-	-	-	-	-	6

A.4. Strength Corrected Soil Layers at Each Site

FKSH19

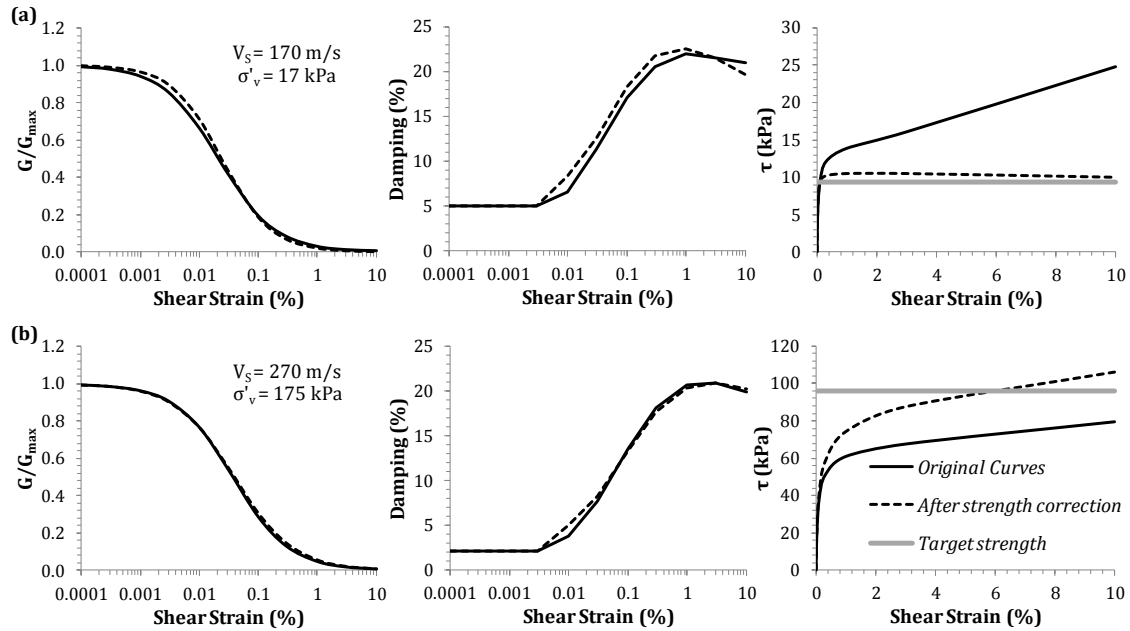


Figure A.12: Original and modified modulus reduction and damping curves and the associated stress strain relationships for the strength corrected layers: (a) $V_S = 170 \text{ m/s}$ and $\sigma'_v = 17 \text{ kPa}$, and (b) $V_S = 270 \text{ m/s}$ and $\sigma'_v = 175 \text{ kPa}$ – FKSH19 array

FKSH20

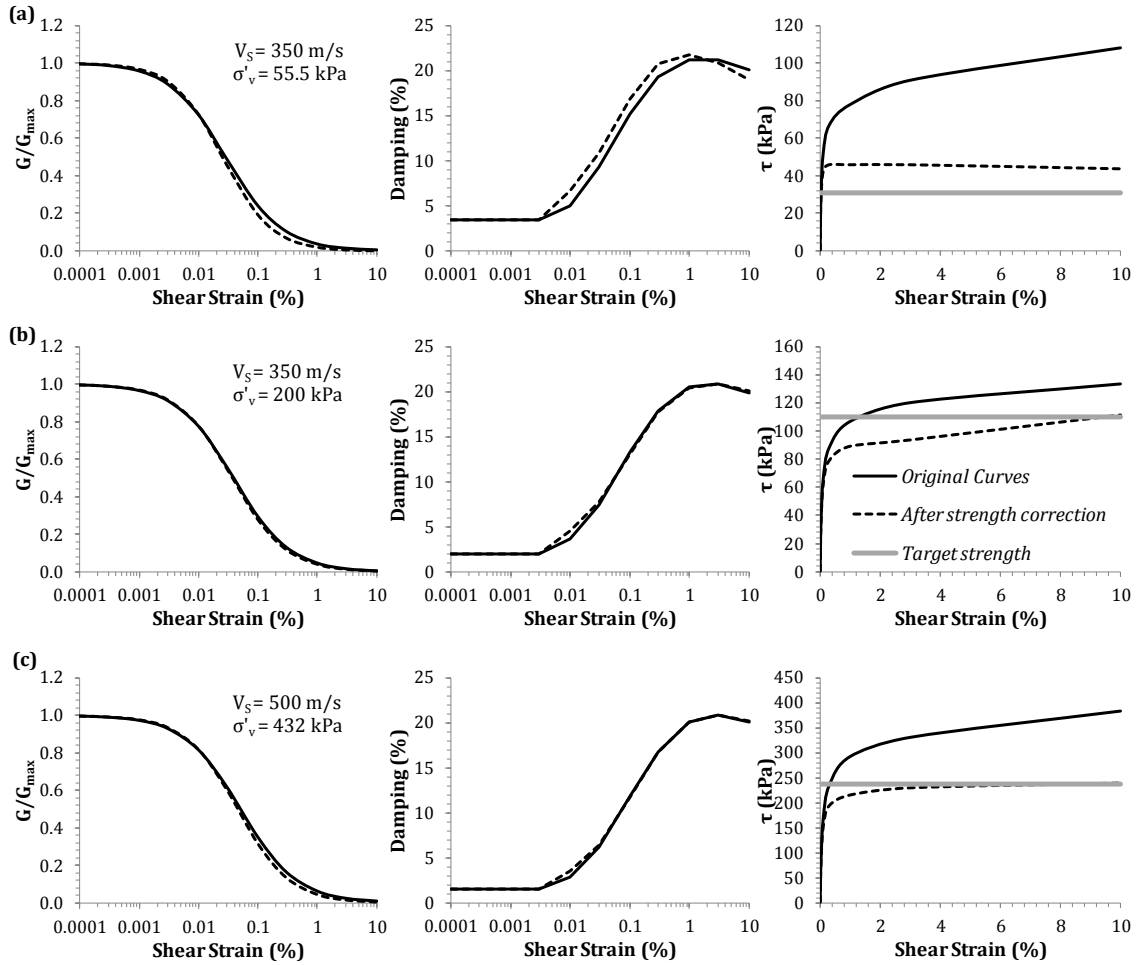


Figure A.13: Original and modified modulus reduction and damping curves and the associated stress strain relationships for the strength corrected layers: (a) $V_s = 350 \text{ m/s}$ and $\sigma'_v = 55.5 \text{ kPa}$, (b) $V_s = 350 \text{ m/s}$ and $\sigma'_v = 200 \text{ kPa}$, and (c) $V_s = 500 \text{ m/s}$ and $\sigma'_v = 432 \text{ kPa}$ - FKSH20 array

IBRH11

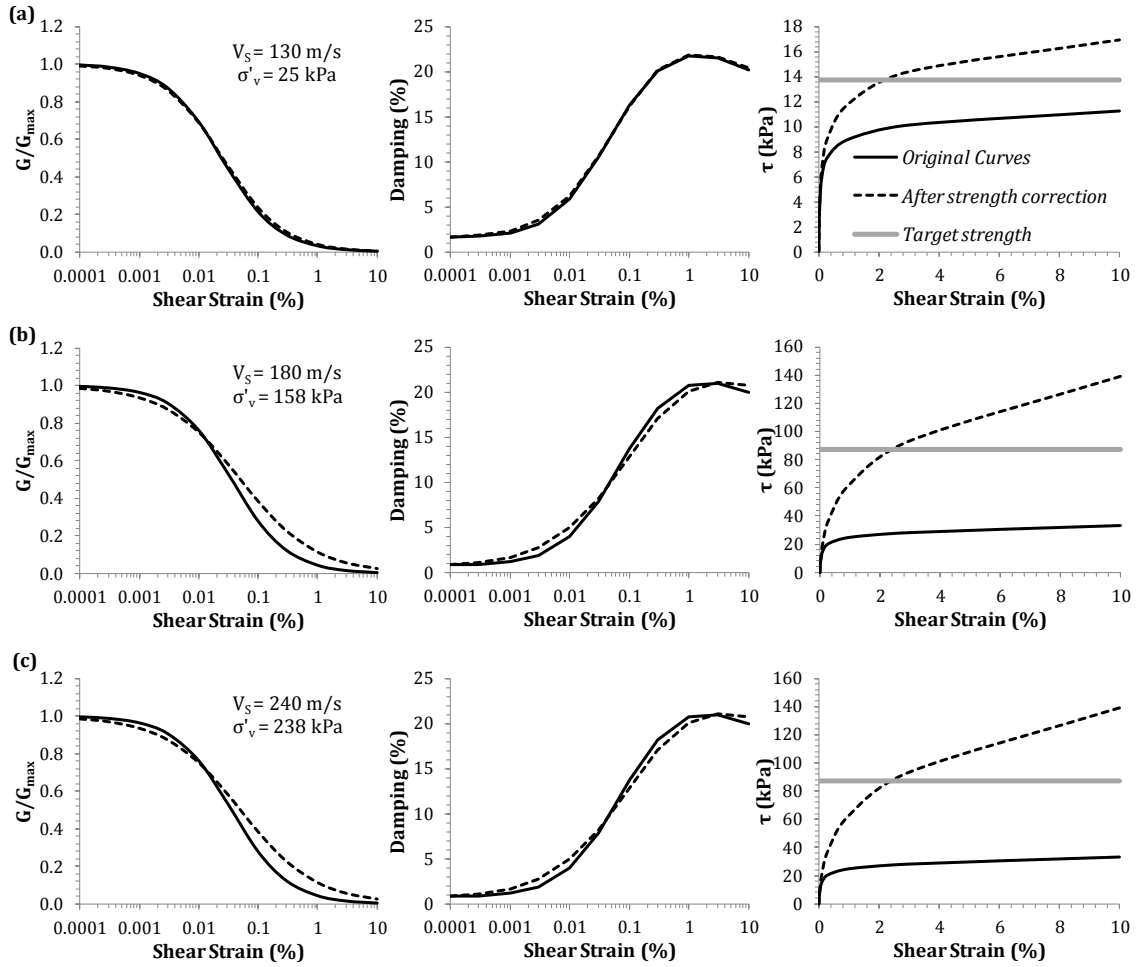


Figure A.14: Original and modified modulus reduction and damping curves and the associated stress strain relationships for the strength corrected layers: (a) $V_s = 130 \text{ m/s}$ and $\sigma'_v = 25 \text{ kPa}$, (b) $V_s = 180 \text{ m/s}$ and $\sigma'_v = 158 \text{ kPa}$, and (c) $V_s = 240 \text{ m/s}$ and $\sigma'_v = 238 \text{ kPa}$ - **IBRH11** array

IBRH13

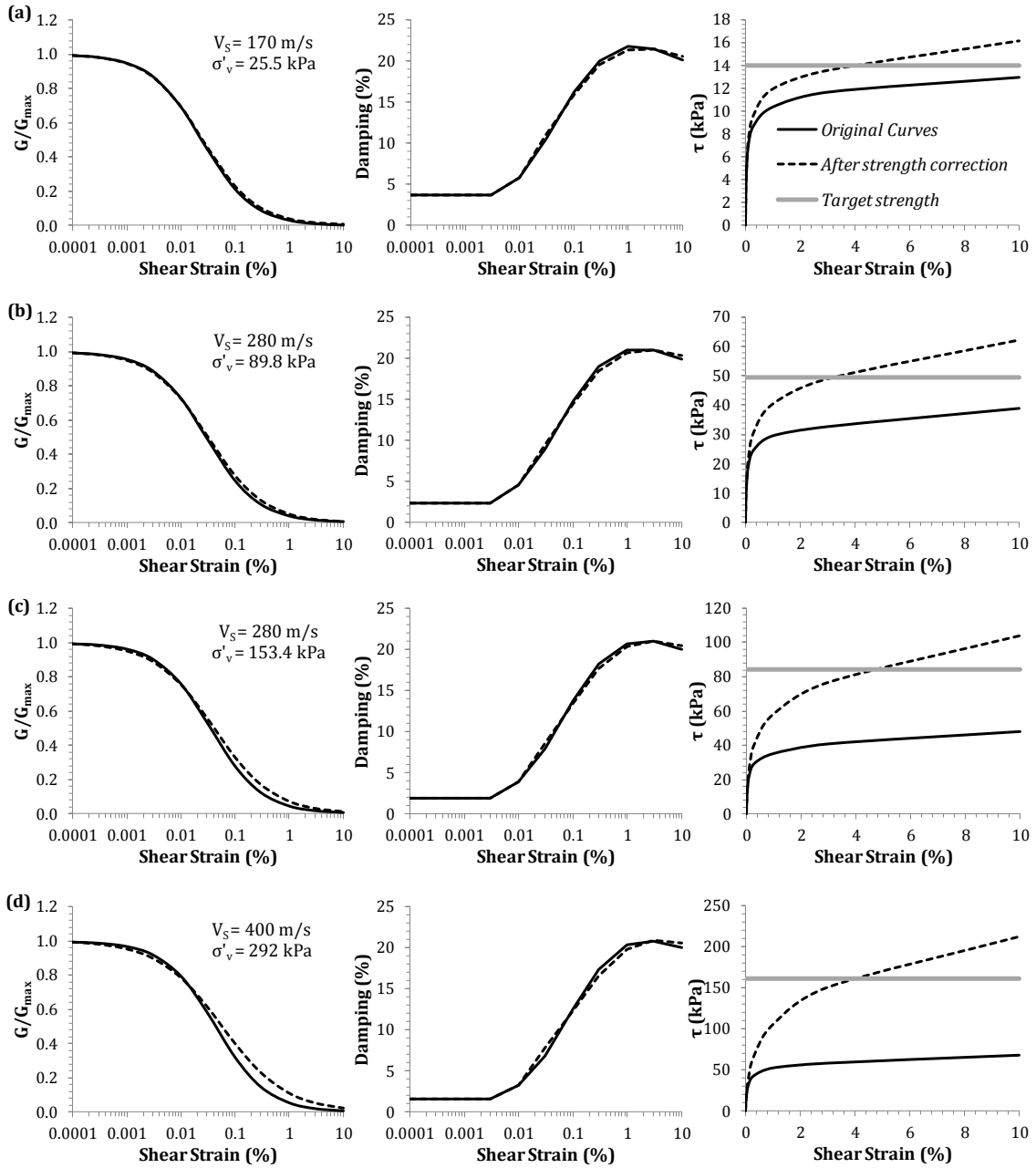


Figure A.15: Original and modified modulus reduction and damping curves and the associated stress strain relationships for the strength corrected layers: (a) $V_S = 170$ m/s and $\sigma'_v = 25.5$ kPa, (b) $V_S = 280$ m/s and $\sigma'_v = 89.8$ kPa, (c) $V_S = 280$ m/s and $\sigma'_v = 153.4$ kPa, and (d) $V_S = 400$ m/s and $\sigma'_v = 292$ kPa - IBRH13 array

IWTH26

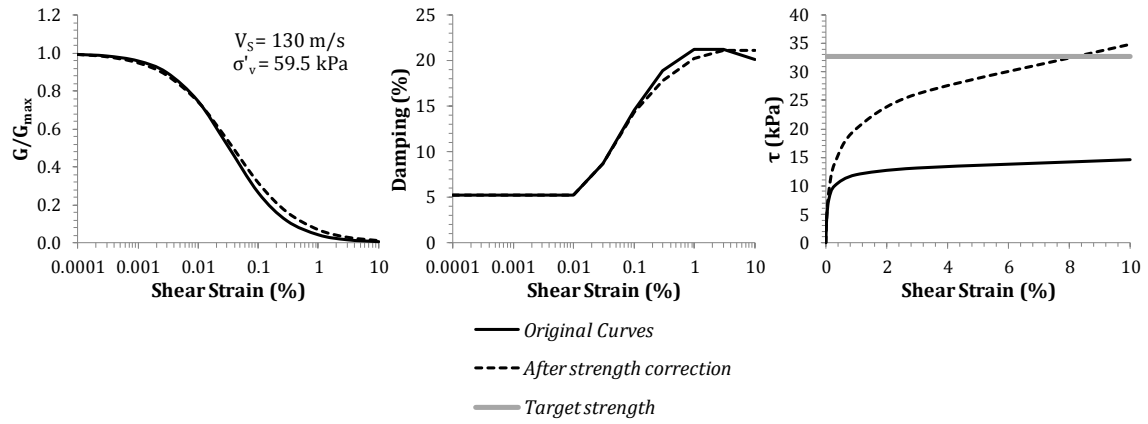


Figure A.16: Original and modified modulus reduction and damping curves and the associated stress strain relationships for the strength corrected layer with $V_s = 130$ m/s and $\sigma'_v = 59.5$ kPa - IWTH26 array

KSRH06

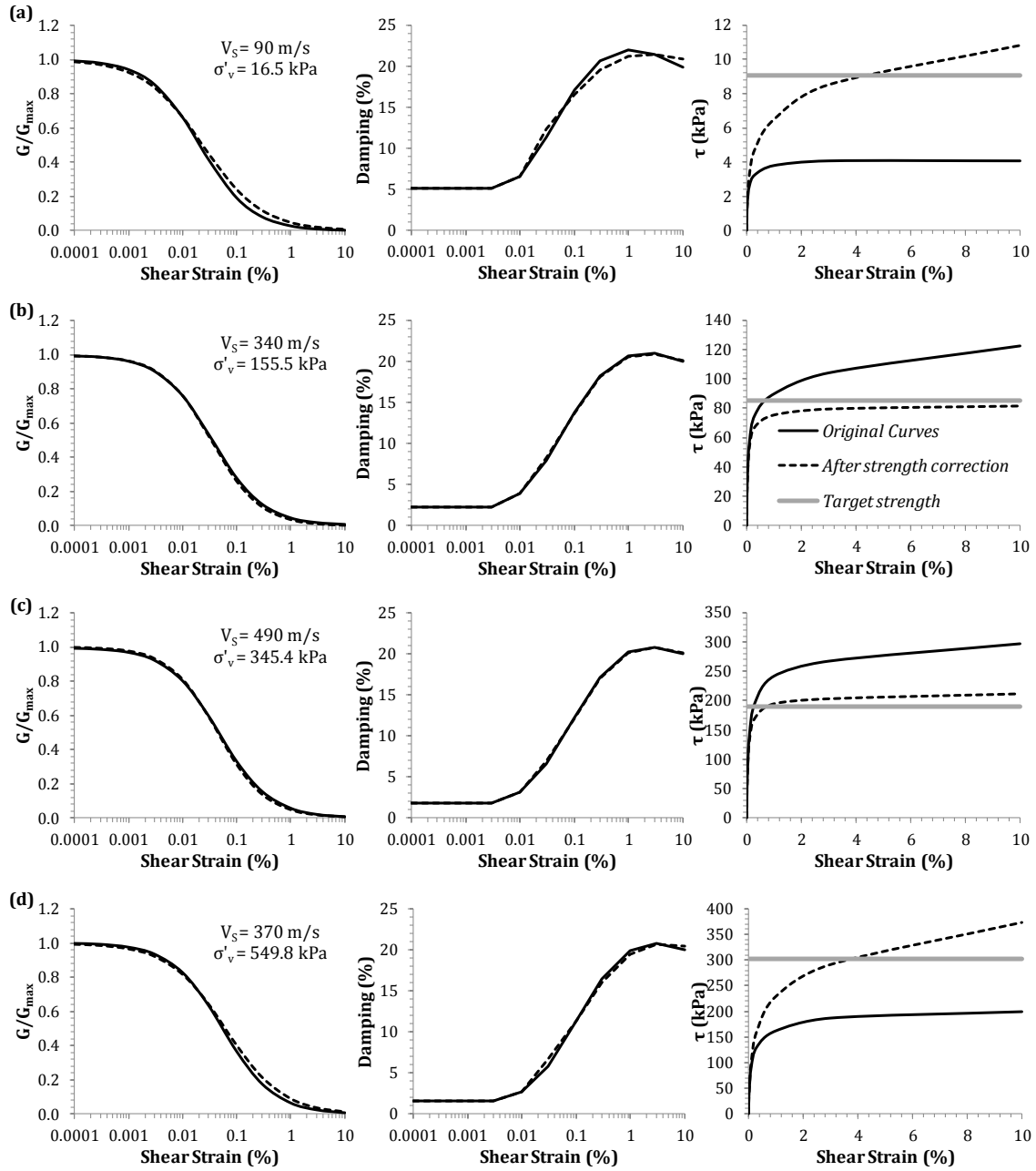


Figure A.17: Original and modified modulus reduction and damping curves and the associated stress strain relationships for the strength corrected layers: (a) $V_S = 90 \text{ m/s}$ and $\sigma'_v = 16.5 \text{ kPa}$, (b) $V_S = 340 \text{ m/s}$ and $\sigma'_v = 155.8 \text{ kPa}$, (c) $V_S = 490 \text{ m/s}$ and $\sigma'_v = 345.4 \text{ kPa}$, and (d) $V_S = 370 \text{ m/s}$ and $\sigma'_v = 549.8 \text{ kPa}$ – KSRH06 array

KSRH07

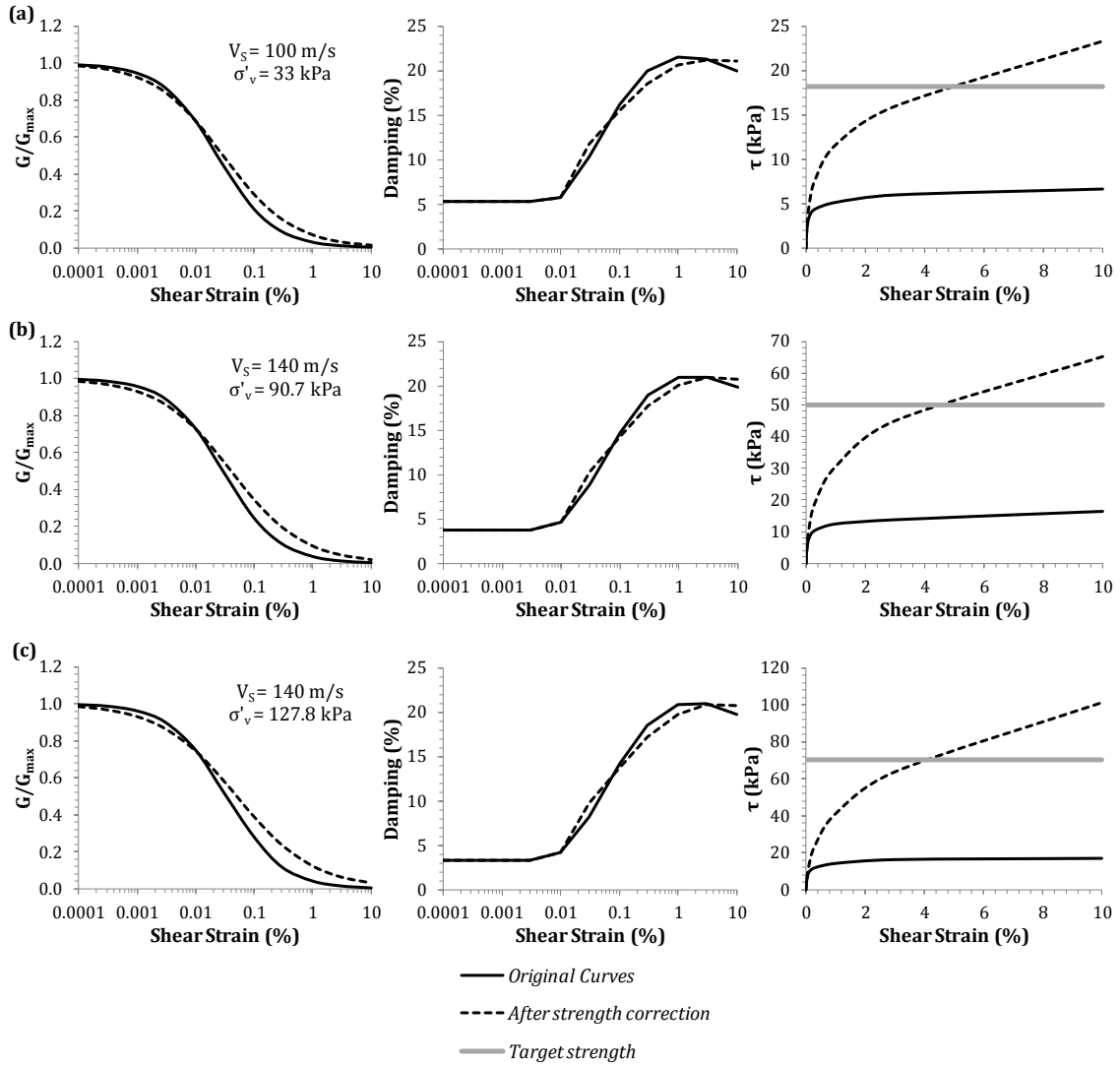


Figure A.18: Original and modified modulus reduction and damping curves and the associated stress strain relationships for the strength corrected layers: (a) $V_S = 100 \text{ m/s}$ and $\sigma'_v = 33 \text{ kPa}$, (b) $V_S = 140 \text{ m/s}$ and $\sigma'_v = 90.7 \text{ kPa}$, and (c) $V_S = 140 \text{ m/s}$ and $\sigma'_v = 127.8 \text{ kPa}$ - **KSRH07** array

KSRH10

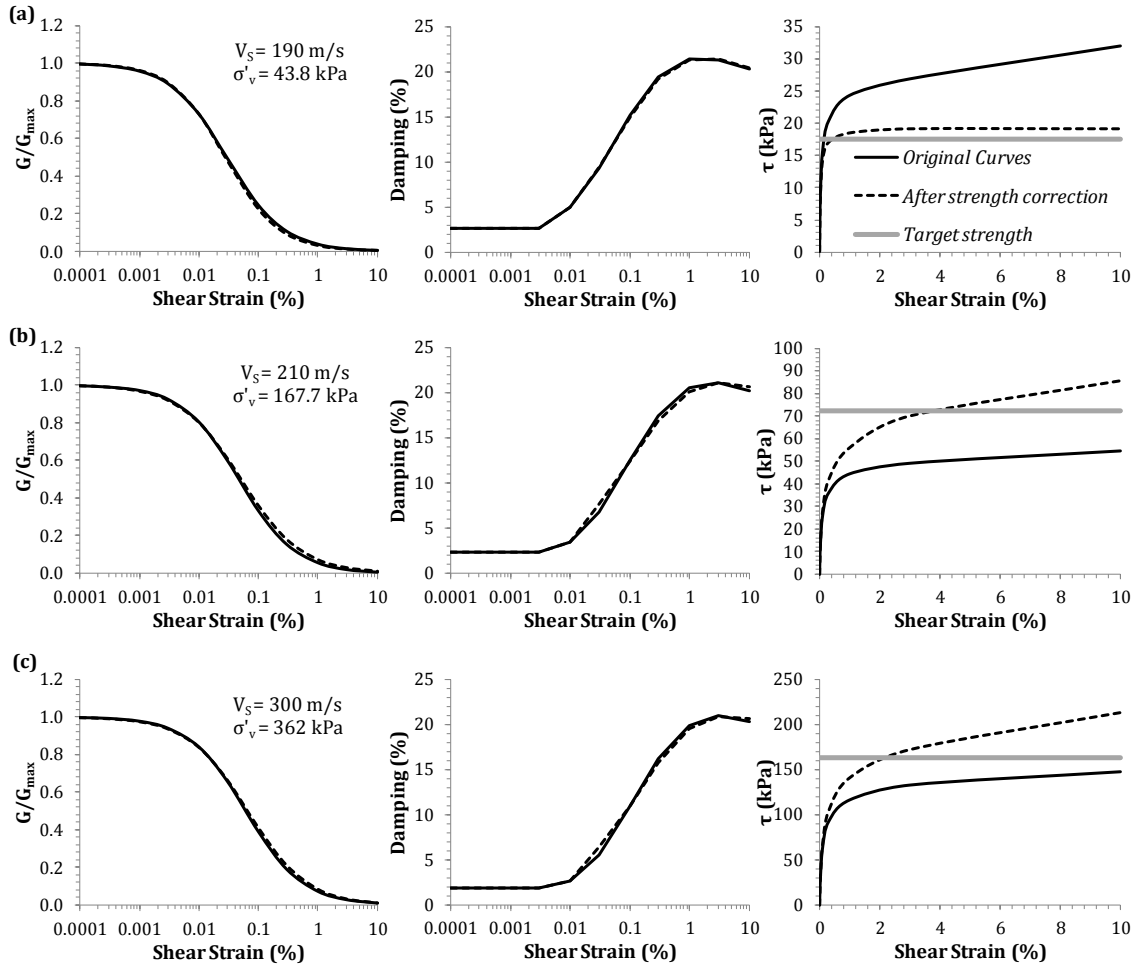


Figure A.19: Original and modified modulus reduction and damping curves and the associated stress strain relationships for the strength corrected layers: (a) $V_S = 190$ m/s and $\sigma'_v = 43.8$ kPa, (b) $V_S = 210$ m/s and $\sigma'_v = 167.7$ kPa, and (c) $V_S = 300$ m/s and $\sigma'_v = 362$ kPa - **KSRH10** array

MYGH05

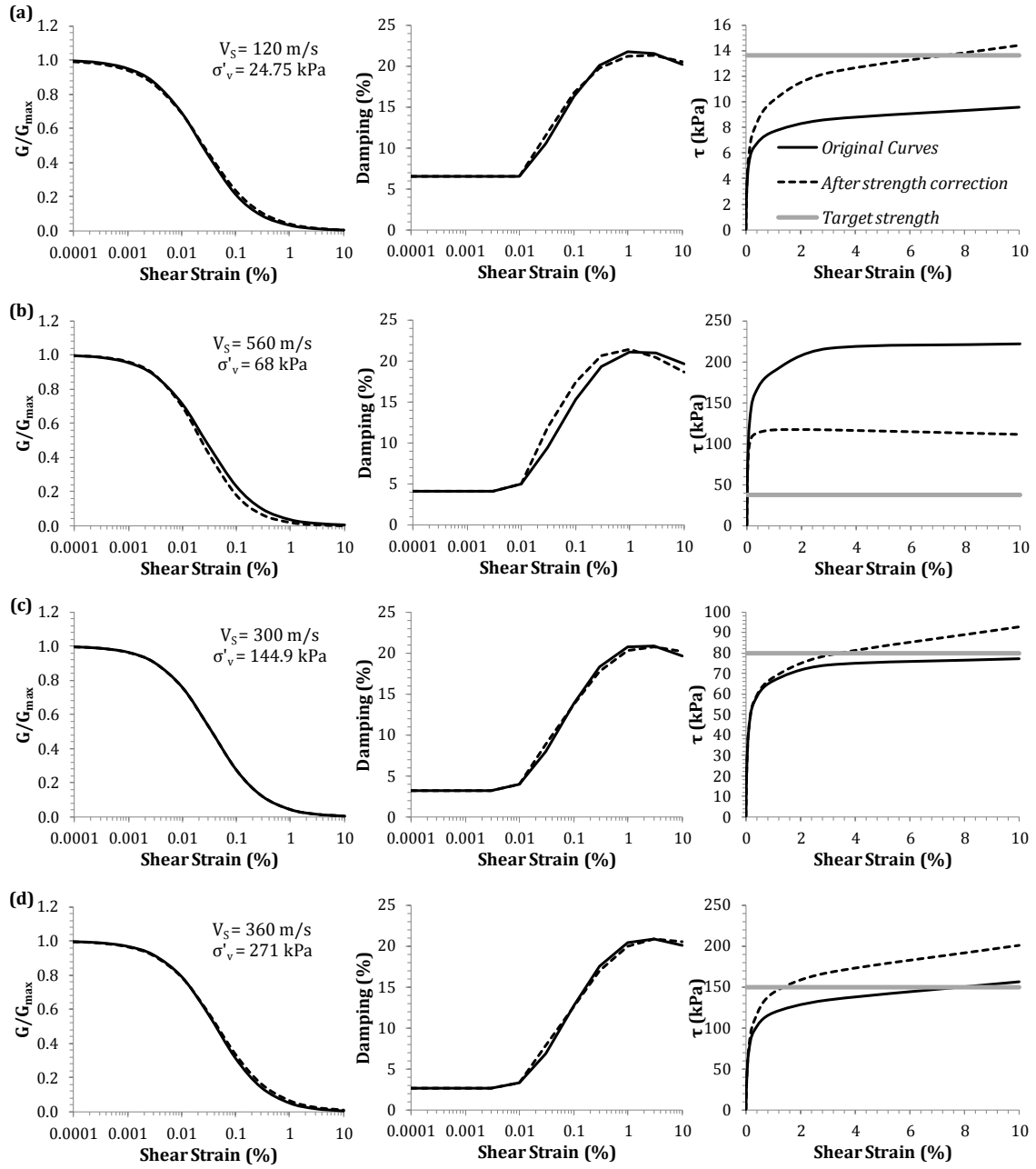


Figure A.20: Original and modified modulus reduction and damping curves and the associated stress strain relationships for the strength corrected layers: (a) $V_s = 120 \text{ m/s}$ and $\sigma'_v = 24.75 \text{ kPa}$, (b) $V_s = 560 \text{ m/s}$ and $\sigma'_v = 68.8 \text{ kPa}$, (c) $V_s = 300 \text{ m/s}$ and $\sigma'_v = 144.9 \text{ kPa}$, and (d) $V_s = 360 \text{ m/s}$ and $\sigma'_v = 271 \text{ kPa}$ - MYGH05 array

Bibliography

- Abrahamson, N. A., P. G. Somerville, and C. Cornell (1990), "Uncertainty in Numerical Strong Motion Predictions," *Proceedings of the Fourth US National Conference on Earthquake Engineering*, volume **1**, 407-416
- Aki, K., P. G. Richards (2002), "Quantitative Seismology", *second edition*, *University Science Books*, , Sausalito, CA
- Al Atik, L., N. Abrahamson, J. J. Bommer, F. Scherbaum, F. Cotton, and N. Kuehn (2010), "The Variability of Ground-Motion Prediction Models and Its Components", *Seismological Research Letters*, **81**(5), 794-801
- Archuleta, R. J., and J. H. Steidl (1998). "ESG studies in the United States: Results from Borehole arrays", *Proceedings of the International Symposium on Effects of Surface Geology on Seismic Motion*, Yokohama, Japan. **1**, 3-14
- Assimaki, D., and E. Kausel (2002), "An Equivalent Linear Algorithm with Frequency-and-Pressure-Dependent Moduli and Damping for Seismic Analysis of Deep Sites," *Soil Dynamics and Earthquake Engineering*, **22**, 959-965
- Assimaki, D., and W. Li (2012), "Site-and-Ground Motion-Dependent Nonlinear Effects in Seismological Model Predictions", *Soil Dynamics and Earthquake Engineering*, **32**, 143-151
- Assimaki, D., and J. Steidl (2007), "Inverse Analysis of Weak and Strong Motion Downhole Array Data from the M_w 7.0 Sanriku-Minami Earthquake", *Soil Dynamics and Earthquake Engineering*, **27**, 73-92
- Assimaki, D., J. Steidl, and P. C. Liu (2006), "Attenuation and Velocity Structure for Site Response Analyses via Downhole Seismogram Inversion", *Pure and Applied Geophysics*, **163**, 81-118

- Beresnev, I. A., A M. Nightengale, W. J. Silva (2002), "Properties of Vertical Ground Motions", *Bulletin of Seismological Society of America*, **92**, 3152-3164
- Beresnev, I. A., K-L Wen, and Y. T. Yeh (1995), "Seismological Evidence for Nonlinear Elastic Ground Behavior during Large Earthquakes", *Soil Dynamics and Earthquake Engineering*, **14**, 103-114
- Boaga, J., S. Renzi, G. Vignoli, R. Deiana, G. Cassiani (2012), "From Surface Wave Inversion to Seismic Site Response Prediction: Beyond the 1D Approach", *Soil Dynamics and Earthquake Engineering*, **36**, 38-51
- Bonilla, L. F., J. H. Steidl, J.-C. Gariel, and R. J. Archuleta (2002), "Borehole Response Studies at the Garner Valley Downhole Array, Southern California," *Bulletin of Seismological Society of America*, **92**(6), 3165-3179
- Borja, R. I., H. Y. Chao, F. J. Montans, C. Lin (1999), "Nonlinear Ground Response at Lotung LSST site," *Journal of Geotechnical and Geoenvironmental Engineering*, **125**(3), 187-197
- Borja, R. I., C-H. Lin, K. M. Sama, and G. M. Masada (2000), "Modelling Non-linear Ground Response of Non-liquefiable Soils", *Earthquake Engineering and Structural Dynamics*, **29**, 63-83
- Bradley, B. A. (2011), "A Framework for Validation of Seismic Response Analyses using Seismometer Array Recordings", *Soil Dynamics and Earthquake Engineering*, **31**, 512-520
- Chiu, P., D. E. Pradel, A. O.-L. Kwok, and J. P. Stewart (2008), "Seismic Response Analyses for the Silicon Valley Rapid Transit Project." *Geotechnical Earthquake Engineering and Soil Dynamics IV (GSP 181)*, Sacramento, CA
- Dafalias, Y.F. and E.P. Popov (1979), "A Model for Nonlinearly Hardening Materials for Complex Loading," *Acta Mechanica*, **21**(3), 173-192

- Darendeli, M. B. (2001), "Development of a New Family of Normalized Modulus Reduction and Material Damping Curves," *Ph.D. Dissertation, The University of Texas at Austin*, Austin, Texas, 396 pp.
- Deng, N., and F. Ostadan (2008), "Random Vibration Theory Based Seismic Site Response Analysis", *Proceedings of the 14th World Conference on Earthquake Engineering*, paper 04-02-0024, Beijing, China
- Elgamal, A., T. Lai, Z. Yang, and L. He (2001), "Dynamic soil properties, seismic downhole arrays and applications in practice", *Proceedings of the 4th International Conference on Recent Advances in Geotechnical Earthquake Engineering and Soil Dynamics*, San Diego, California
- EPRI (1993), "Guidelines for Determining Design Basis Ground Motions", *Report TR-102293, Electrical Power Research Institute (EPRI)*, Palo Alto, CA
- Finn, W. D. L., K. W. Lee, and G. R. Martin (1977), "An effective stress model for liquefaction", *Journal of the Geotechnical Engineering Division*, **103**(GT6), 517-533
- Foerster, E., H. Modaressi (2007), "Nonlinear Numerical Method for Earthquake Site Response Analysis II – Case Studies", *Bulletin of Earthquake Engineering*, **5**, 325-345
- Furumoto, Y., M. Sugito, M., and A. Yashima (2000), "Frequency-Dependent Equivalent Linearized Technique for FEM Response Analysis of Ground", *Proceedings of the 12th World Conference on Earthquake Engineering*, Auckland, New Zealand
- Gerolymos, N., and G. Gazetas (2005), "Constitutive Model for 1D Cyclic Soil Behavior Applied to Seismic Analysis of Layered Deposits", *Soils and Foundations*, **45**(3), 147-159
- Google Inc. (2013). Google Earth (Version 7.1.2.2041) [Software]

- Hardin, B. O., and V. P. Drnevich (1972a), "Shear Modulus and Damping in Soils: Design Equations and Curves", *Journal of Soil Mechanics and Foundations*, **98**(SM7), 289-324
- Hardin, B. O., and V. P. Drnevich (1972b), "Shear Modulus and Damping in Soils: Measurement and Parameter Effects." *Journal of Soil Mechanics and Foundation Engineering Division*, **98**(SM6), 603-624
- Hashash, Y. M. (2002), "Viscous Damping Formulation and High Frequency Motion Propagation in Nonlinear Site Response Analysis", *Soil Dynamics and Earthquake Engineering*, **22**(7), 611-624
- Hashash, Y. M. A. (2012), "DEEPSOIL V 5.1: User Manual and Tutorial", *University of Illinois at Urbana-Champaign*, Urbana, Illinois, www.illinois.edu/~deepsoil.
- Hashash, Y. M. A., and D. Park (2001), "Nonlinear One-Dimensional Seismic Ground Motion Propagation in the Mississippi Embayment", *Engineering Geology*, **62**(1-3), 185-206
- Hashash, Y., S. Pezeshk, and D. Park (2003), "Final Report: Non-linear Seismic Site Response of Deep Deposits in West Tennessee", *Technical Report, Tennessee Department of Transportation*
- Hashash, Y. M. A., C. Phillips, and D. R. Groholski (2010), "Recent Advances in Non-linear Site Response Analysis", *Proceedings of the Fifth International Conference on Recent Advances in Geotechnical Earthquake Engineering and Soil Dynamics*, San Diego, California
- Holzer, T. L., and T. L. Youd (2007), "Liquefaction, Ground Oscillation and Soil Deformation at the Wildlife Array, California", *Bulletin of Seismological Society of America*, **72**(3), 961-976
- Idriss, I. M., and J. I. Sun (1993), "User's Manual for SHAKE91: A Computer Program for Conducting Equivalent Linear Seismic Response Analyses of Horizontally

- Layered Soil Deposits”, *Technical report, Center for Geotechnical Modeling, University of California, Davis*
- Joyner, W. B. and A.T.F. Chen (1975), “Calculation of Nonlinear Ground Response in Earthquakes,” *Bulletin of Seismological Society of America*, **65**(5), 1315–1336
- Kaklamanos, J., B. A. Bradley, E. M. Thompson, and L. G. Baise (2013), “Critical Parameters Affecting Bias and Variability in Site Response Analyses using Kik-net Downhole Array Data,” *Bulletin of the Seismological Society of America*, **103**(3), 1733-1749
- Kaklamanos, J. (2012), “Quantifying Uncertainty in Earthquake Site Response Models using the Kik-Net Database”, *Ph.D. Dissertation, Department of Civil and Environmental Engineering, Tufts University, Medford, Massachusetts, 301 pp.*
- Kausel, E., and D. Assimaki (2002), “Seismic Simulation of Inelastic Soils via Frequency-Dependent Moduli and Damping”, *Journal of Engineering Mechanics*, 128:1(34)
- Kik-net, *Kiban-kyoshin network*, URL <http://kik.bosai.go.jp/>.
- Kokusho, T., K. Sato (2008), “Surface-to-base Amplification Evaluated from Kik-Net Vertical Array Strong Motion Records”, *Soil Dynamics and Earthquake Engineering*, **28**, 707-716
- Kondner, R. L., and J. S. Zelasko (1963), "Hyperbolic Stress-Strain Formulation of Sands", *Second pan-American Conference on Soil Mechanics and Foundation Engineering*, Sao Paulo, Brazil, 289-324
- Kottke, A. (2010), “A Comparison of Seismic Site Response Methods,” *Ph.D Dissertation, Unverisity of Texas at Austin, Austin, Texas, 326 pp.*

- Kottke, A., and E. Rathje (2008), "Technical Manual for Strata," *Report 2008/10, Pacific Earthquake Engineering Research (PEER) Center, Berkeley, California, 2008b*
- Kramer, S. L. (1996), "Geotechnical Earthquake Engineering," *Prentice-Hall, New Jersey, pp. 653*
- Kwak, D-Y., C-G. Jeong, D. Park, and S. Park (2008), "Comparison of Frequency Dependent Equivalent Linear Analysis Methods", *Proceedings of the 14th World Conference on Earthquake Engineering, Beijing, China*
- Kwok, A. O. L., Stewart J. P., Hashash Y. M. A. (2008), "Nonlinear Ground-Response Analysis of Turkey Flat Shallow Stiff-Soil Site to Strong Ground Motion", *Bulletin of Seismological Society of America, 98(1), 331-343*
- Kwok, O. L. A., J. P. Stewart, Y. M. A. Hashash, N. Matasovic, R. M. Pyke, Z. Wang, and Z. Yang (2007), "Use of Exact Solutions of Wave Propagation Problems to Guide Implementation of Nonlinear Seismic Ground Response Analysis Procedures", *Journal of Geotechnical and Geoenvironmental Engineering, 133:11 (1385)*
- Lee, C-P., Y-B. Tsai, and K-L. Wen (2006), "Analysis of Nonlinear Site Response using the LSST Downhole Accelerometer Array Data", *Soil Dynamics and Earthquake Engineering, 26, 435-460*
- Li, W., and D. Assimaki (2010), "Site and Motion-Dependent Parametric Uncertainty of Site-Response Analyses in Earthquake Simulations", *Bulletin of Seismological Society of America, 100(3), 954-968*
- Lin, P.-S., B. Chiou, N. Abrahamson., M. Walling, C.-T. Lee, and C.-T. Cheng (2011), "Repeatable Source, Site, and Path Effects on the Standard Deviation for Ground-Motion Prediction," *Bulletin of Seismological Society of America, 101, 2281-2295*

- Matasovic, N. and M. Vucetic (1993a), "Cyclic Characterization of Liquefiable Sands," *Journal of Geotechnical Engineering*, ASCE, **119**(11), 1805-1822
- Matasovic, N. and M. Vucetic (1993b), "Seismic Response of Horizontally Layered Soil Deposits," *Report No. ENG 93-182*, University of California, Los Angeles
- Mroz, Z. (1967), "On the Description of Anisotropic Work Hardening", *Journal of the Mechanics and Physics of Solids*, **15**, 163-175
- Ordóñez, G. (2002), "User's Manual for Shake91: A Computer Program for Conducting Equivalent Linear Seismic Response Analyses of Horizontally Layered Soil Deposits", *Technical report*, GeoMotions
- Park, D., and Y. M. A. Hashash (2004), "Estimation of Non-linear Seismic Site Effects for Deep Deposits of the Mississippi Embayment", *Technical Report, Natinal Science Foundation, Mid America Earthquake Center*
- Phillips, C. and Y. M. Hashash (2009), "Damping Formulation for Nonlinear 1D Site Response Analysis", *Soil Dynamics and Earthquake Engineering*, **29**(7), 1143-1158
- Pitilakis, K. (2004), "EUROSEISTEST and CORSSA experimental test sites in Greece", In P. de Alba, R. L. Nigbor, J. H. Steidl, and J. C. Stepp, editors, *International Workshop for Site Selection, Installation, and Operation of Geotechnical Strong-Motion Arrays*, pages 45-50, Richmond, CA, COSMOS
- Prevost, J. H. (1977). "Mathematical Modeling of Monotonic and Cyclic Undrained Clay Behavior." *International Journal of Numerical and Analytical Methods in Geomechanics*, **1**(2), 195-216
- Pyke, R. M. (1979), "Nonlinear Soil Models for Irregular Cyclic Loadings", *Journal of the Geotechnical Engineering Division*, **105**(GT6), 715-726

- Ramberg, W., and W. R. Osgood (1943), "Description of Stress-Strain Curves by Three Parameters." *Technical Note No. 902, National Advisory Committee For Aeronautics*, Washington DC
- Rayleigh, J., and R. Lindsay (1945), "The theory of sound", *Dover Publications*, New York, 1st american edition
- Rathje, E. M., N. Abrahamson, and J. D. Bray 1998, "Simplified Frequency Content Estimates of Earthquake Ground Motions", *Journal of Geotechnical Engineering*, **124**(2), 150-159
- Rodriguez-Marek A., G. A. Montalva, F. Cotton, and F. Bonilla (2011), "Analysis of Single-Station Standard Deviation using the Kik-net data," *Bulletin of Seismological Society of America*, **101**, 1242-1258
- Roscoe, K.H. and J.B. Burland (1968), "On the generalized stress-strain behavior of 'wet' clay", *Engineering Plasticity*, University Press, Cambridge, 535-609
- Roscoe, K.H. and A.N. Schofield (1963), "Mechanical Behavior of an Idealized 'Wet' Clay," *Proc. of 2nd European Conference on Soil Mechanics*, Wiesbaden, Germany, Vol. **1**, 47-54
- ROSRINE. Resolution Of Site Response Issues from the Northridge Earthquake, URL <http://gees.usc.edu/ROSRINE/>
- Schnabel, P. B., J. Lysmer, and H. B. Seed (1972), "SHAKE: A Computer Program for Earthquake Response Analysis of Horizontally Layered Sites," *Report UCB/EERC-71/12, Earthquake Engineering Research Center, University of California*, Berkeley, California, 102 pp.
- Seed, H. B., and I. M. Idriss (1971), "Simplified Procedure for Evaluating Soil Liquefaction Potential", *Journal of Soil Mechanics and Foundations Div.*, ASCE **97**(SM9), 1249-273

- Silva, W., N. Abrahamson, G. Toro, and C. Costantino (1996), "Description and Validation of the Stochastic Ground Motion Model", *Report 770573, Brookhaven National Laboratory*, Upton, New York.
- Silva, W. J., and K. Lee (1987), "WES RASCAL Code for Synthesizing Earthquake Ground Motions", *Report 24, U.S. Army Corps of Engineers Waterways Experiment Station*
- Steidl, J., H (2006), "Inventory of Existing Strong-Motion Geotechnical Arrays". In P. de Alba, R. L. Nigbor, J. H. Steidl, and J. C. Stepp, editors. *Proceedings of the International Workshop for Site Selection, Installation, and Operation of Geotechnical Strong-Motion Arrays*, La Jolla, California
- Stein, S., and Wysession, M. (2003), "An Introduction to Seismology, Earthquakes, and Earth Structure", *Blackwell Publishing*, Massachusetts, pp. 498
- Stewart, J., and A. O. L. Kwok (2008), "Nonlinear Seismic Ground Response Analysis: Code Usage Protocols and Verification Against Vertical Array Data", *Geotechnical Earthquake Engineering and Soil Dynamics IV Congress 2008 - Geotechnical Earthquake Engineering and Soil Dynamics*, GSP 181
- Stewart, J. P., A. O.-L. Kwok, Y. M. Hashash, N. Matasovic, R. Pyke, Z. Wang, and Z. Yang (2008), "Benchmarking of Nonlinear Geotechnical Ground Response Analysis Procedures", *Report 2008/04, Pacific Earthquake Engineering Research (PEER) Center*, Berkeley, California.
- Sugito, M. (1995), "Frequency-dependent equivalent strain for earthquake response analysis of soft ground", *Proceedings of IS-Tokyo '95, The First International Conference on Earthquake Geotechnical Engineering*, Tokyo, pp.655-660
- Thompson, E., L. Baise, R. Kayen, and B. Guzina (2009), "Impediments to Predicting Site Response: Seismic Property Estimation and Modeling Simplifications," *Bulleting of Seismological Society of America*, **99**(5), 2927-2949

- Thompson, E. M., L. G. Baise, Y. Tanaka, and R. E. Kayen (2012), "A Taxonomy of Site Response Complexity", *Soil Dynamics and Earthquake Engineering*, **41**, 32-43
- Trifunac, M. D., and V. W. Lee (1996), "Peak Surface Strains During Strong Earthquake Motion", *Soil Dynamics and Earthquake Engineering*, **15**(5), 311-319
- Yoshida, N., S. Kobayashi, I. Suetomi, and K. Miura (2002), "Equivalent Linear Method Considering Frequency Dependent Characteristics of Stiffness and Damping," *Soil Dynamics and Earthquake Engineering*, **22**, 205-222
- Visone, C., and F. S. de Magistris (2010), "Comparative Study on Frequency and Time Domain Analyses for Seismic Site Response", *Electronic Journal of Geotechnical Engineering*, **15**
- Vucetic, M. (1990), "Normalized Behavior of Clay under Irregular Cyclic Loading." *Canadian Geotechnical Journal*, **27**, 29-46
- Vucetic, M. and R. Dobry (1991), "Effect of Soil Plasticity on Cyclic Response," *Journal of Geotechnical Engineering*, **117**, 89-107
- Wang, Z. L., C.-Y. Chang, and C. M. Mok (2001), "Evaluation of Site Response using Downhole Array Data from a Liquefied Site," *Proceedings of 4th International Conference on Recent Advances in Geotechnical Earthquake Engineering and Soil Dynamics*
- Wilson, C. R. (2011), "Geophysical Data Processing Essentials", *Course Notes, Department of Geological Sciences, University of Texas at Austin, Austin, Texas*
- Yang, Z. (2000), "Numerical Modeling of Earthquake Site Response Including Dilation and Liquefaction", *Columbia University, NY, New York.*
- Zalachoris, G., and E. M. Rathje (2013), "Evaluating One-Dimensional Site Response Analysis using Borehole Arrays", *Proceedings of 10th International Conference*

on Urban Earthquake Engineering, March 1-2, Tokyo Institute of Technology,
Tokyo, Japan

Zeghal, M., A.-W. Elgamal, H. T. Tang, and J. C. Stepp (1995), "Lotung Downhole Array. ii: Evaluation of Soil Nonlinear Properties", *ASCE Journal of Geotechnical Engineering*, **121**(4), 363-378

Ziotopoulou, A. (2007), "Non-Linear Seismic Response Analysis of Soil Deposits and Piles and Proposed Unique Bi-Normalized Design Spectrum", *Diploma Thesis, National Technical University of Athens*, Athens, Greece, pp. 276

Vita

Georgios Zalachoris was born in Athens, Greece on September 28, 1984, the second child of Vasilios Zalachoris and Maria-Elissavet Zalachori-Meramveliotaki. After completing his studies at Tositsio Arsakio high school, Ekali, Athens, Greece, in 2002 he entered the National Technical University of Athens (NTUA). He received his Diploma in Civil Engineering in November 2007. In August 2008, he entered the Graduate Program of the Cockrell College of Engineering at The University of Texas at Austin. He earned his Masters of Science in Civil Engineering in August 2010 by writing a thesis on “Field measurements of linear and nonlinear shear moduli of solid municipal waste using a dynamically loaded surface footing”. The aforementioned thesis was supervised by Prof. Kenneth H. Stokoe, II.

Permanent address: Kifisou 18, Kifisia, Athens, Greece, 14564

This dissertation was typed by Georgios Zalachoris.